

Development of 3D printing technologies for manufacturing microfluidic devices for bioengineering applications

Francesc Subirada

ADVERTIMENT. La consulta d'aquesta tesi queda condicionada a l'acceptació de les següents condicions d'ús: La difusió d'aquesta tesi per mitjà del servei TDX (**www.tdx.cat**) i a través del Dipòsit Digital de la UB (**diposit.ub.edu**) ha estat autoritzada pels titulars dels drets de propietat intel·lectual únicament per a usos privats emmarcats en activitats d'investigació i docència. No s'autoritza la seva reproducció amb finalitats de lucre ni la seva difusió i posada a disposició des d'un lloc aliè al servei TDX ni al Dipòsit Digital de la UB. No s'autoritza la presentació del seu contingut en una finestra o marc aliè a TDX o al Dipòsit Digital de la UB (framing). Aquesta reserva de drets afecta tant al resum de presentació de la tesi com als seus continguts. En la utilització o cita de parts de la tesi és obligat indicar el nom de la persona autora.

ADVERTENCIA. La consulta de esta tesis queda condicionada a la aceptación de las siguientes condiciones de uso: La difusión de esta tesis por medio del servicio TDR (**www.tdx.cat**) y a través del Repositorio Digital de la UB (**diposit.ub.edu**) ha sido autorizada por los titulares de los derechos de propiedad intelectual únicamente para usos privados enmarcados en actividades de investigación y docencia. No se autoriza su reproducción con finalidades de lucro ni su difusión y puesta a disposición desde un sitio ajeno al servicio TDR o al Repositorio Digital de la UB. No se autoriza la presentación de su contenido en una ventana o marco ajeno a TDR o al Repositorio Digital de la UB (framing). Esta reserva de derechos afecta tanto al resumen de presentación de la tesis como a sus contenidos. En la utilización o cita de partes de la tesis es obligado indicar el nombre de la persona autora.

WARNING. On having consulted this thesis you're accepting the following use conditions: Spreading this thesis by the TDX (**www.tdx.cat**) service and by the UB Digital Repository (**diposit.ub.edu**) has been authorized by the titular of the intellectual property rights only for private uses placed in investigation and teaching activities. Reproduction with lucrative aims is not authorized nor its spreading and availability from a site foreign to the TDX service or to the UB Digital Repository. Introducing its content in a window or frame foreign to the TDX service or to the UB Digital Repository is not authorized (framing). Those rights affect to the presentation summary of the thesis as well as to its contents. In the using or citation of parts of the thesis it's obliged to indicate the name of the author.

Doctoral Thesis

Development of 3D printing technologies for manufacturing microfluidic devices for bioengineering applications

Francesc Subirada



UNIVERSITAT DE BARCELONA

Development of 3D printing technologies for manufacturing microfluidic devices for bioengineering Applications

Memòria presentada per optar al grau de doctor per la Universitat de Barcelona

Programa de doctorat en Biomedicina

Autor: Francesc Subirada

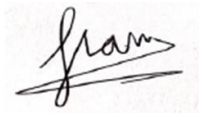
Director/a: Dr. Josep Samitier i Dr. Romén Rodriguez

Tutor/a: Dr. Josep Samitier

Tesi realitzada a l'Institut de Bioenginyeria de Catalunya (IBEC)

IBEC
Institute for Bioengineering of Catalonia

PhD Candidate



Francesc Subirada

Directors



Josep Samitier



Romén Rodriguez

UNIVERSITAT DE BARCELONA

Abstract

Advancements in 3D printing have revolutionized microfluidic device fabrication, offering unprecedented flexibility and precision in the design and production of complex geometries. This thesis presents a comprehensive study utilizing a custom-made DLP-SLA 3D printer and commercially available resins to develop and evaluate microfluidic devices for applications in particle separation and fluid mixing under laminar flow conditions. A detailed analysis of printing errors was conducted, highlighting the challenges posed by over-curing effects, which significantly impact the ability to fabricate closed microchannels with high dimensional accuracy.

The research involved a dual approach of computational simulations and experimental validations to optimize device performance. Spiral microfluidic devices were designed and tested for particle separation, achieving efficient separation of particles larger than 75 µm under laminar flow conditions, with Reynolds numbers carefully analyzed to ensure optimal performance. Additionally, staggered herringbone mixers were developed to enhance mixing efficiency through chaotic advection. The results demonstrated effective mixing of fluids, confirming the versatility of these devices in achieving homogenous mixing even at low Reynolds numbers.

This work underscores the potential of DLP-SLA 3D printing in fabricating both open molds for PDMS replication and fully enclosed microchannels, offering a scalable and customizable alternative to traditional lithographic methods. The findings contribute to advancing the field of microfluidics, providing insights into the interplay between fabrication techniques, material properties, and device functionality. Future applications of these devices extend to biomedical diagnostics, chemical synthesis, and lab-on-a-chip systems, highlighting their relevance and impact in both research and industry.

Resumen

Los avances en la impresión 3D han revolucionado la fabricación de dispositivos microfluídicos, ofreciendo una flexibilidad y precisión sin precedentes en el diseño y producción de geometrías complejas. Esta tesis presenta un estudio exhaustivo que utiliza una impresora 3D DLP-SLA personalizada y resinas comerciales para desarrollar y evaluar dispositivos microfluídicos destinados a la separación de partículas y la mezcla de fluidos en condiciones de flujo laminar. Se realizó un análisis detallado de los errores de impresión, destacando los desafíos planteados por los efectos de sobrecurado, que afectan significativamente la capacidad de fabricar micro canales cerrados con alta precisión dimensional.

La investigación combinó simulaciones computacionales y validaciones experimentales para optimizar el rendimiento de los dispositivos. Se diseñaron y probaron dispositivos microfluídicos espirales para la separación de partículas, logrando una separación eficiente de partículas mayores de 75 µm en condiciones de flujo laminar, con un análisis cuidadoso de los números de Reynolds para garantizar un rendimiento óptimo. Además, se desarrollaron mezcladores herringbone para mejorar la eficiencia de mezcla mediante advección caótica. Los resultados demostraron una mezcla efectiva de fluidos, confirmando la versatilidad de estos dispositivos para lograr mezclas homogéneas incluso en números de Reynolds bajos.

Este trabajo subraya el potencial de la impresión 3D DLP-SLA para fabricar tanto moldes para la replicación en PDMS como micro canales completamente cerrados, ofreciendo una alternativa escalable y personalizable a los métodos litográficos tradicionales. Los hallazgos contribuyen al avance del campo de la microfluídica, proporcionando información sobre la interacción entre las técnicas de fabricación, las propiedades de los materiales y la funcionalidad de los dispositivos. Las aplicaciones futuras de estos dispositivos incluyen diagnósticos biomédicos, síntesis química y sistemas de laboratorio en chip, destacando su relevancia e impacto tanto en la investigación como en la industria.

Resum

Els avenços en la impressió 3D han revolucionat la fabricació de dispositius microfluídics, oferint una flexibilitat i precisió sense precedents en el disseny i producció de geometries complexes. Aquesta tesi presenta un estudi exhaustiu que utilitza una impressora 3D DLP-SLA personalitzada i resines comercials per desenvolupar i avaluar dispositius microfluídics destinats a la separació de partícules i la barreja de fluids en condicions de flux laminar. S'ha realitzat un anàlisi detallat dels errors d'impressió, destacant els desafiaments plantejats pels efectes de sobre curat, que afecten significativament la capacitat de fabricar micro canals tancats amb alta precisió dimensional.

La investigació realitzada combina simulacions computacionals i validacions experimentals per optimitzar el rendiment dels dispositius. Es van dissenyar i provar dispositius microfluídics espirals per a la separació de partícules, aconseguint una separació eficient de partícules més grans de 75 µm en condicions de flux laminar, amb una anàlisi acurat dels nombres de Reynolds per garantir un rendiment òptim. A més, s'han desenvolupat mescladors herringbone per millorar l'eficiència de barreja mitjançant advecció caòtica. Els resultats han demostrat una barreja efectiva de fluids, confirmant la versatilitat d'aquests dispositius per aconseguir barreges homogènies fins i tot amb nombres de Reynolds baixos.

Aquest treball remarca el potencial de la impressió 3D DLP-SLA per fabricar tant motlles per a la replicació en PDMS com micro canals completament tancats, oferint una alternativa escalable i personalitzable als mètodes litogràfics tradicionals. Les troballes contribueixen a l'avenç del camp de la microfluídica, proporcionant informació sobre la interacció entre les tècniques de fabricació, les propietats dels materials i la funcionalitat dels dispositius. Les aplicacions futures d'aquests dispositius inclouen diagnòstics biomèdics, síntesi química i sistemes de laboratori en xip, destacant la seva rellevància i impacte tant en la recerca com en la indústria.

Paraules clau: Impressió 3D, Microfluidica, Separació (Tecnologia), Metodes de simulació.

Aknowledgments

I would like to express my gratitude to all the people who have supported me during this journey, whether academically or, equally or even more importantly, in life.

First and foremost, I wish to thank my supervisor and director, Prof. Josep Samitier, for giving me the opportunity to join his lab and undertake this thesis. The experience has allowed me to learn about a wide range of interdisciplinary topics. I am deeply grateful for all his guidance, advice, and recommendations throughout this process. I would also like to extend my sincere thanks to my co-director, Romén Rodriguez, for his valuable assistance and all his work. I truly appreciate the support from both of them, knowing how challenging it can be to find time in their busy schedules.

I am also grateful to the entire Nanobioengineering lab at IBEC, led by Prof. Samitier, for making these four years so enjoyable. Their willingness to help whenever possible, despite the lab's highly interdisciplinary nature and the diverse specializations of its members, has been invaluable and greatly enriched my experience.

A special thanks to my family—my parents, Francesc and Pepa—for always encouraging me to take the most responsible and studious path, even though I'm sure I haven't made it easy for them over the years. To my brother Joaquin and my partner Laura, who may not have directly contributed to the academic side of this work but have been crucial in helping me endure these challenging doctoral years. Thank you both; your support has been even more important.

I also wish to thank Jessica and Sujey for their assistance with the microscopes, and my friends Jaume Gabarrella and Santi P. Altes for their help with design software and macro programming. My thanks go as well to Jordi Comellas from Elena Martínez's group at IBEC for his help with the fluorescence microscope, and to Aina Anton from the Hospital Clínic for her support with the confocal experiments.

Finally, I am incredibly grateful to my friends and my hockey team, Barcelona Tsunamis, for providing much needed distractions and enjoyment during my free time.

Thank you all for making these years not only possible but also memorable!

List of Abbreviations

2D Two-Dimensional

3D Three-Dimensional

ABS Acrylonitrile Butadiene Styrene

α Absorption Coefficient

CAD Computer-Aided Design

CFD Computational Fluid Dynamics

COMSOL Multiphysics Simulation Software

CT Computed Tomography

CTC Circulating Tumor Cell

DLP Digital Light Processing

DNA Deoxyribonucleic Acid

De Dean Number

FDM Fused Deposition Modeling

Ha Penetration Depth

I0 Initial Irradiance

LED Light Emitting Diode

LOC Lab-on-a-Chip

mL Milliliter

OOC Organ-on-a-Chip

PBS Phosphate Buffered Saline

PCR Polymerase Chain Reaction

PD Penetration Depth

PDMS Polydimethylsiloxane

PLA Polylactic Acid

PS Polystyrene

RBC Red Blood Cell

Re Reynolds Number

RPM Revolutions Per Minute

SEM Scanning Electron Microscopy

SLA Stereolithography

TPP Two-Photon Polymerization

UV Ultraviolet

V Voltage

WBC White Blood Cell

h Hour

µL Microliter

µm Micrometer

s Second

Table of Contents

Abstract ____ 3

Resumen ____ 4

Resum ____ 5

Aknowledgments ____ 6

List of Abbreviations ____ 7

List of Figures ____ 13

List of Tables ____ 14

List of Equations ____ 15

Chapter 1: Introduction ____ 16

1.1Microfluidics and Its Importance in Bioengineering ____ 16

1.1.1 Applications of Microfluidics ____ 17

1.2Traditional Methods for Fabrication of Microfluidic Devices ____ 19

1.2.1 Soft Lithography ____ 19

1.2.2 Injection Molding ____ 22

1.2.3 Hot Embossing ____ 23

1.2.4 Micromachining ____ 25

1.2.5 Limitations of Traditional Methods ____ 25

1.2.6 Transition to 3D Printing in Microfluidics ____ 26

1.3 Emergence of 3D Printing in Microfluidics ____ 27

1.3.1 Stereolithography (SLA) ____ 27

1.3.2 Digital Light Processing (DLP) ____ 30

1.3.3 Two-Photon Polymerization (2PP) ____ 32

1.3.4 Fused Deposition Modeling (FDM) ____ 34

1.3.5 Photopolymer Inkjet Printing ____ 35

1.3.6 Selective Lasers Sintering (SLS) ____ 37

1.3.5 Advantages of 3D Printing for Microfluidics ____ 39

1.4 Fabrication of 3D-Printed Microfluidic Devices and its Applications ____ 39

1.4.1 Customized 3D Printing Protocols ____ 40

1.4.2 Custom Resin Compositions for DLP-SLA 3D Printing for Microfluidics ____ 42

1.4.3 Advanced Commercial Resins for DLP-SLA 3D Printing for Microfluidics ____ 43

1.4.4 Light Dose absorption for a resin – Mathematical model optical analysis ____ 44

1.4.5 3D Printing Molds for PDMS Replica ____ 49

1.4.6 3D Printing Closed Channels ____ 50

1.4.7 Potential of DLP-SLA in Achieving Unique Geometries ____ 52

1.5. Theory of Laminar Flow in Microchannels 54
1.5.1 Laminar Flow vs. Turbulent Flow 54
1.5.2 Mixing in Laminar Flow 55
1.5.3 Inertial Forces in Microfluidic Devices 56
1.6 Computational Fluid Dynamics (CFD) Simulations 57
1.6.1 Using COMSOL Multiphysics to Simulate Microfluidic Flows 57
1.6.2 Impact of Viscosity on Mixing and Flow Dynamics 59
1.6.3 Optimizing Microfluidic Device Design with CFD Simulations 60
1.7 Methods to Improve Mixing in Microchannels 61
1.7.1 Passive Mixing Techniques 61
1.7.2 Active Mixing Techniques 62
1.7.3 Optimizing Microchannel Design for Efficient Mixing 63
Chapter 2: Objectives 64
Chapter 3 Materials and Methods 67
3.1 Fabrication of Microfluidic Devices 68
3.1.1 Custom Stereolithography 3D Printer 68
3.1.2 3D Printing Protocol 72
3.1.3 Post-procesing 75
3.1.4 3D Printed Molds Fabrication and PDMS Replica 77
3.1.5 Bonding and chip manufacturing 77
3.1.6 Resins Used and Absorbance Test 78
3.1.7 Approaches for Printing Closed Channels and Integrating Internal Structures 79
3.2 Dimensional Characterization 80
3.2.1 Lateral Dimensional Characterization 80
3.2.2 Vertical Dimensional Characterization 80
3.2.3 Cross-Sectional Analysis 81
3.2.4 Surface Roughness Characterization 81
3.2.5 Sidewall Roughness 81
3.3 Design of Microfluidic Devices 82
3.4 Comsol Simulations 84
3.4.1 General Setup 84
3.4.2 Governing Equations 85
3.4.3 Particle Separation Simulation in Spiral Structures 86
3.4.4 Fluid Mixing Simulation in Herringbone Structures 87
3.5 Particle Separation Experimental Validation 88
3.5.1 Device Setup and Preparation 88

3.5.2 Particle Type and Characteristics 88
3.5.3 Fluid Properties and Experimental Conditions 89
3.5.4 Validation and Separation Performance Analysis 90
3.5.5 Experimental Validation using Blood and Beads 90
3.6 Mixing Analysis Experimental Validation 91
3.6.1 Device Setup and Experimental Conditions 91
3.6.2 Confocal Microscope Setup 92
3.6.3 Image Processing and analysis with Fiji 93
3.6.4 Mixing Efficiency Calculation/formula 93
Chapter4: 3D Printing Results and Discussion 96
4.1 Introduction to 3D Printing Performance in Microfluidics 96
4.2 Projector Irradiance Calibration 97
4.3 Absorbance Characterization of Resins 98
4.4 Optimization of Exposure Settings for 3D Printed Microstructures 100
4.4.1 Preliminary Exposure Range Test 100
4.4.2 Iterative Adjustment of Printing Parameters 109
4.5 Dimensional Accuracy 112
4.5.1 Width Dimensioning 112
4.5.2 Z-Dimensioning 118
4.6 Closed Channel Fabrication 120
4.6.1 Printing of Inclined Closed Channels 129
4.6.2 Integration of Input and Output Ports in One-Step Printed Channels 131
4.7 Surface Roughness Characterization 132
4.7.1 Horizontal Surface Roughness 132
4.7.2 Internal Channel Roughness 133
4.7.3 Lateral Roughness 134
4.8 Dimensional Error Analysis for Microfluidic Features Inside Channels 137
4.8.1 Experimental Design and Methodology 137
4.8.2 Dimensional Accuracy of Printed Microstructures 138
4.8.3 Capabilities and Challenges of DLP-SLA 3D Printing for Internal Microfluidic Features 141
Chapter 5: Spiral Microfluidic devices 143
5.1 Introduction 143
5.2 Spiral Design for Leveraging Lift and Dean Forces 145
5.3 Particle Separation Simulations 147
5.4 Fabrication of the Spiral Microfluidic Device 158

5.4.1 Mold-Based PDMS Devices 158
5.4.2 Embossed 3D-Printed Devices with Direct Assembly 161
5.4.3 Dimensional Accuracy: Resin and Method Comparison 163
5.4.4 Microfluidic Devices Fabrication Using 3D Printed Closed Channels 164
5.5 Experimental Results 165
5.5.1 EXPERIMENTAL RESULTS OBTAINED IN COLLABORATION 170
5.6 Design and fabrication of two spiral microfluidic devices to increase the separation efficiency 173
Chapter 6: Herringbone Mixer Results and Discussion 176
6.1 Introduction 176
6.2 Design 178
6.3 Fabrication 179
6.3.1 Mold-Based PDMS Devices 179
6.3.2 Directly Printed Closed-Channel Devices 180
6.4 Computational Simulations 181
6.5 Experimental Analysis 186
6.5.1 Experimental Setup 186
6.5.2 Experimental Results 188
Chapter 7: General Discussion 195
7.1 Evaluation of Printing Parameters and Resolution 195
7.2 Study of Spiral Device for size-based Particle Separation 198
7.3 Study of Herringbone Device for Fluid Mixing under Laminar Flow 199
Chapter 8: Conclusions 203
Statement of Originality 205
Bibliography 206

List of Figures

Figure 1. Fabrication of an SU-8 master mould for PDMS replica. 21
Figure 2 Schematic of the injection molding 22
Figure 3 Schematic representation of the hot embossing 24
Figure 4: Schematic of SLA 3D printing. 29
Figure 5: Schematic of DLP 3D printing. 31
Figure 6: Visual representation of a DLP-printed structure. 32
Figure 7: Schematic of the 2PP process. 33
Figure 8: Schematic of the FDM 35
Figure 9: Photopolymer inkjet printing process) 36
Figure 10: SLS process schematic 38
Figure 11: Schematic representation of Beer's law 45
Figure 12: Step-by-step illustration of the layer-by-layer fabrication 47
Figure 13: Normalized dose as a function of depth 48
Figure 14: Cross-sectional view of layer-by-layer UV light exposure 51
Figure 15: Overview of the 3D printer's electronic system.. 69
Figure 16: The Wintech PRO6500 DLP projector. 70
Figure 17: The resin vat, with a Fluorinated Ethylene Propylene (FEP) 71
Figure 18: Touchscreen interface integrated into the 3D printer 72
Figure 19: Example of insufficient burn-in exposure during the 3D printing process. 74
Figure 20: Washing and Curing Machine from CREALITY 76
Figure 21: Step-by-step process for fabricating a PDMS device using a 3D-printed mold 78
Figure 22: Example of a 3D printed part and its sidewall roughness 82
Figure 23: Top view of the 3D spiral microfluidic device 83
Figure 24: Detailed view of the herringbone structure within the microfluidic device 84
Figure 25: Irradiance calibration results 97
Figure 26: View of the VAT containing resin 98
Figure 27: Graph presenting the absorbance for three commercial resins. 99
Figure 28: View of the test structure to evaluate the effect of exposure time on accuracynsity. 101
Figure 29: Test structure used to optimize exposure settings. 109
Figure 30: Figure of the parametric design made with Inventor from Autodesk. (B) Picture of one of the 3D printed piece obtained, for the design of 600 µm height and the resin from Asiga. 112
Figure 31: Pictures of the parts printed with Detax, Asiga and Keyprint 114
Figure 32: Graphic from the error obtained for 600 µm 115
Figure 33: Graphic from the error obtained for 400 µm. 116
Figure 34: Graphic from the error obtained for 200 µm 117
Figure 35: Profilometric analysis of a 3D-printed structure 120
Figure 36: Design of the printed channels 122
Figure 37: This graphic shows the thickness of the cover. 125
Figure 38: CAD design and results of printed rectangular channels 127
Figure 39: Designs and experimental results for the inclined channel configuration 130
Figure 40: 3D model of a cylindrical adapter 131
Figure 41: Fi gure obtained with the AFM 132
Figure 42: Superior internal part of the cover channel 133
Figure 43: Plot of the irradiance 135
Figure 44: 3D printed part created using Detax resin 139
Figure 45: Design and manufacture of the spiral microfluidic device 147
Figure 46: Results obtained in COMSOL 149
Figure 47: Comparison of theoretical particle separation diameters 150
Figure 48: Particle trajectories and separation. 152
Figure 49: Plasma cleaner used for the oxygen plasma treatment. 160

Figure 50: 3D printed result with Detax resin of the extruded spira 161
Figure 51: 3D printed result with Detax resin of the embossed spiral 162
Figure 52:3D printed device, a spiral with a channel of 1.4 mm width and 600 μm height. 165
Figure 53: Processed stack subsets and fluorescence microscopy 167
Figure 54: Design of the single spiral. 170
Figure 55: Microfluidic setup for the separation of CTCs from leukocyte-bead complexes. 171
Figure 56: Characterization of polystyrene particles binding to CD45-antibody 173
Figure 57: Design of the two interconnected spirals. 174
Figure 58: View of a microfluidic device that combines two spirals. 174
Figure 59: The figure shows two different views of the section of the double-spiral device 175
Figure 60: Concentration distribution of water-based fluorophore (mol/m^3) 182
Figure 61: Schematic representation of the concentration measurement 184
Figure 62: Simulated mixing profiles 185
Figure 63: Fully 3D-printed herringbone device 189
Figure 64: Experimental vortex formations 190
Figure 65: Experimental results of fluorescein mixing 192
Figure 66: Comparison between the simulated and experimental mixing 194

List of Tables

Table 1: Relation of PWM with Voltage and LED Intensity. 71
Table 2: Definitions of the spiral device. 83
Table 3: Simulation Conditions for Particle Separation 87
Table 4: Physical properties of water and dextran used in simulations. 87
Table 5: Exposure times tested. 102
Table 6: Summary of exposure conditions for Detax with 50 μm layers. 103
Table 7: Summary of exposure conditions for Detax with 100 μm layers. 103
Table 8: Summary of exposure conditions for Asiga with 50 μm layers 104
Table 9: Summary of exposure conditions for Asiga with 100 μm layers. 104
Table 10: Summary of exposure conditions for Keyprint with 50 μm layers 105
Table 11: Summary of exposure conditions for Keyprint with 100 μm layers 105
Table 12: Minimum ilumination time conditions. 107
Table 13: Polymerization Efficiency Calculation 107
Table 14: Alpha and ha. 108
Table 15: Optimal settings empirically determined for the different resins tested. 110
Table 16: Height error for every resin type and every different height design. 118
Table 17: The values of the thickness of the covers of the channels showed in Figure 36. 125
Table 18: Cover sizes as a function of layer thickness and channel size. All values in μm. 128
Table 19: Dimensional errors 140
Table 20: Reynolds Numbers for Simulated Channel Heights and Flow Rates. 151
Table 21: Percentage of particles of each size exiting through the Inner Output for 540μm. 153
Table 22: Percentage of particles of each size exiting through the Inner Output for 640μm 154
Table 23: Percentage of particles of each size exiting through the Inner Output for 740μm. 155
Table 24: Percentage of 100 μm and 75 μm particles recovered at the Inner Output and contamination levels for different flow rates for the Device of 540 μm. 156
Table 25: Percentage of 100 μm and 75 μm particles recovered at the Inner Output and contamination levels for different flow rates for the Reverse Device of 540 μm. 156
Table 26: Percentage of 100 μm and 75 μm particles recovered at the Inner Output and contamination levels for different flow rates for the Device of 640 μm. 156

Table 27: Percentage of 100 µm and 75 µm particles recovered at the Inner Output and contamination levels for different flow rates for the Reverse Device of 640 µm. *157*
Table 28: Percentage of 100 µm and 75 µm particles recovered at the Inner Output and contamination levels for different flow rates for the Device of 740 µm. *157*
Table 29: Percentage of 100 µm and 75 µm particles recovered at the Inner Output and contamination levels for different flow rates for the Reverse Device of 740 µm. *157*
Table 30: Width and height error for extruded and embossed spiral *163*
Table 31: Experimental Results for Channel Height: 540 µm. Sample with Particles 760 ul/min and Seath Flow 6840 ul/min. *168*
Table 32: Experimental Results for Channel Height: 640 µm. Sample with Particles 760 ul/min and Seath Flow 6840 ul/min. Reverse Configuration. *169*
Table 33: Reynolds number (Re) comparison for two different fluid combinations: water + water (fluorophore solution) and dextran + water (fluorophore solution). *188*

List of Equations

Equation 1: Energy Dose. *45*
Equation 2:Critical Energy Dose. *45*
Equation 3: Critical Time. *46*
Equation 4: Reynolds Number. *54*
Equation 5: Fick's First Law of Diffusion. *55*
Equation 6: Particle Reynolds Number (3) *56*
Equation 7: Dean Number. *56*
Equation 8: Drag Force. *56*
Equation 9: Lift Force. *57*
Equation 10: Navier-Stokes *58*
Equation 11: Continuity Equation for Incompressible Fluids. *58*
Equation 12: Convection-Diffusion. *59*
Equation 13: Sidewall Roughness. *81*
Equation 14: Mixing Efficiency. *94*
Equation 15: Polymerization Efficiency. *107*
Equation 16: Ln Polymerization Efficiency. *107*
Equation 17: Theoretical Cuttoff for Particle Separation. *147*
Equation 18: Hydraulic Diameter. *147*

Chapter 1: Introduction

1.1 Microfluidics and Its Importance in Bioengineering

Microfluidics, an interdisciplinary field bridging engineering, physics, chemistry, and biology, has rapidly become an indispensable tool in bioengineering. It enables the precise manipulation and control of fluids at the microscale, typically within channels measuring a few to hundreds of micrometers. This unique capability facilitates applications in biological analysis, chemical reactions, and diagnostic technologies, revolutionizing how experiments and clinical processes are conducted. At its core, microfluidics integrates various laboratory functions onto a single miniaturized platform, often referred to as a lab-on-a-chip (LOC). These systems not only improve efficiency but also open new possibilities in research and clinical diagnostics by providing tools that are smaller, faster, and more precise than conventional methods.

One of the most critical advantages of microfluidics lies in its ability to drastically reduce the volume of samples and reagents required for experiments. This feature is particularly valuable in bioengineering, where expensive or limited materials such as cells, Deoxyribonucleic Acid (DNA), or proteins are often used(1). By reducing reagent consumption by several orders of magnitude compared to traditional techniques, microfluidic devices minimize operational costs and waste while accelerating reaction times. Additionally, their small scale allows for more efficient screening and parallel processing, enabling researchers to perform multiple experiments simultaneously and thus accelerating discovery and development processes (2,3).

Microfluidics is particularly adept at replicating physiological conditions, offering controlled environments that are difficult to achieve using traditional methods. These systems can maintain defined concentration gradients or apply precise shear forces, both of which are crucial for cell-based assays and tissue engineering. For instance, in drug delivery research or organ-on-a-chip (OOC) technologies, microfluidic devices mimic the complex architecture and function of human organs, providing new insights into disease mechanisms and drug responses. By offering unparalleled control over the experimental environment, microfluidics allows researchers to design more accurate in vitro models that closely mimic in vivo conditions (4,5).

Another fundamental advantage of microfluidic systems is their capacity to handle biological fluids with high precision. Blood, cell suspensions, and other biological samples often require precise flow rates and controlled mixing to ensure proper interactions between components. The microscale laminar flow inherent in microfluidics ensures that fluid streams flow in parallel without turbulent mixing. This property is particularly advantageous for applications that require accurate spatial and

temporal delivery of reagents or cells, such as cell culture experiments that rely on gradients of oxygen or nutrients to mimic physiological conditions (6,7) .

The ability to integrate multiple laboratory processes into a single device further highlights the utility of microfluidic systems. Lab-on-a-chip technologies combine functions such as sample preparation, mixing, separation, and detection on a single platform. This integration not only streamlines experimental workflows but also reduces the risk of contamination, a common issue in traditional benchtop assays requiring multiple handling steps. Furthermore, the compact size of these devices enhances portability, enabling applications such as point-of-care diagnostics and field testing in resource-limited settings. Their adaptability makes microfluidics a versatile tool, whether for diagnosing diseases in remote areas or for conducting high-throughput screenings in state-of-the-art laboratories (8).

Finally, the precision and efficiency of microfluidics have led to its application across a wide array of bioengineering fields, including diagnostics, cell biology, drug delivery, and organ-on-a-chip technologies. These systems enable researchers to explore complex biological phenomena with a level of control and efficiency unattainable by traditional methods. Organ-on-a-chip devices, for example, replicate human organ structures and functions on a microscale, providing powerful tools to study disease mechanisms and test drug efficacy. By combining minimal reagent consumption, precise control of fluid dynamics, and the ability to replicate complex biological conditions, microfluidics continues to redefine bioengineering, offering transformative solutions for challenges in healthcare, research, and beyond (9,10).

1.1.1 Applications of Microfluidics

Building on its foundational capabilities, microfluidics has become integral to numerous scientific and industrial applications, offering unparalleled precision and efficiency. Its transformative impact is particularly evident in diagnostics, particle separation, fluid mixing, and filtration.

In diagnostics, microfluidic platforms facilitate rapid, cost-effective, and highly sensitive assays. These devices streamline complex analytical processes, enabling nucleic acid amplification techniques such as polymerase chain reaction (PCR) on a microscale. This miniaturization accelerates disease detection, including viral infections and genetic disorders, making microfluidic diagnostics a cornerstone of early intervention strategies. Additionally, the portability of these systems allows for the development of point-of-care diagnostic tools capable of delivering immediate results in clinical or resource-limited settings, addressing global health disparities.

Particle separation is another critical application, particularly in biomedical and industrial contexts. Microfluidic devices utilize unique designs to segregate particles by size, density, or other properties with high precision. Spiral channels and trapezoidal geometries are particularly effective for separating cells or other particles, achieving efficient filtration and sample preparation without requiring extensive external equipment. This capability is invaluable for isolating cells in cancer research, purifying biological samples, or preparing reagents for downstream processes.

Mixing at the microscale, a traditionally challenging task due to laminar flow, is also revolutionized by microfluidic technology. Advanced mixers, such as chaotic and serpentine designs, enable efficient and homogeneous fluid mixing. These devices are crucial for applications requiring rapid and consistent reagent distribution, such as chemical synthesis, drug screening, and cellular assays. Moreover, the ability to precisely manipulate fluid streams at this scale enhances reaction kinetics, reducing time and resource consumption.

Filtration, often coupled with particle separation, is optimized through microfluidic systems, offering high-throughput and high-resolution solutions. Devices incorporating microfilters effectively remove unwanted particulates from biological or chemical samples, ensuring the purity and reliability of downstream analyses. This integration of filtration and separation is pivotal in diagnostics, biomanufacturing, and environmental monitoring.

Another exciting application of microfluidics is its OOC technology, a field that promises to revolutionize drug testing and personalized medicine. OOC devices use microfluidic channels to simulate the architecture and function of human tissues or organs in vitro, allowing researchers to study disease progression, organ function, and drug responses in a controlled and replicable environment. These devices are often made using microfluidic platforms because they can mimic the microenvironment of living tissues, including fluid flow, shear stress, and mechanical stretching, which are all critical factors for cell function and differentiation. (11,12)

In conclusion, the versatility of microfluidic systems has established them as very useful tools across diagnostics, particle separation, mixing, and filtration. By leveraging their precision, scalability, and efficiency, microfluidics continues to drive innovation in bioengineering and beyond, offering solutions to some of the most pressing challenges in healthcare, research, and industry(13,14). (15–18). (19,20) (21–25)

1.2Traditional Methods for Fabrication of Microfluidic Devices

The fabrication of microfluidic devices is a critical aspect of microfluidic research, as the accuracy, reproducibility, and functionality of the devices depend heavily on the fabrication method used. Over the years, several fabrication techniques have been developed, each with its own strengths and limitations. Traditional methods, such as soft lithography, injection molding, hot embossing, and micromachining, have been widely used, particularly in early-stage research. However, they often require specialized facilities, and their ability to create complex three-dimensional (3D) structures is limited. More recently, 3D printing has emerged as a flexible and versatile alternative that overcomes many of the limitations of traditional methods.

Traditional fabrication methods have been foundational in the development of microfluidics, enabling the precise manufacturing of microscale structures essential for a range of applications in diagnostics, biological studies, and chemical analysis. Techniques such as soft lithography, injection molding, hot embossing, and micromachining, largely adapted from the semiconductor industry, provided the initial tools to manipulate fluids at microscale dimensions, thus establishing the groundwork for modern microfluidics.

The significance of these methods lies in their ability to produce controlled geometries and multilayered structures with various materials, facilitating early advancements in LOC systems and other microfluidic technologies. However, despite their critical role, these techniques come with inherent limitations, including high production costs, long processing times, and limited design flexibility. The complexity and requirement for specialized facilities, like clean rooms and precision equipment, restrict rapid prototyping and complex geometries, prompting a search for more versatile alternatives(26,27).

1.2.1 Soft Lithography

Soft lithography is one of the most widely used techniques in microfluidic device fabrication. It involves creating a master mold, typically from silicon or glass, using photolithography. In this process, a photoresist, such as SU-8, is spin-coated onto a substrate, and a photomask is used to pattern microchannels onto the photoresist. After exposing the photoresist to UV light, areas exposed through the photomask undergo a chemical change, becoming solidified. During the development step that follows, the unexposed regions of the photoresist are dissolved, leaving behind the hardened microchannel structures on the mold surface. Finally, a polymer, most commonly PDMS, is poured over the mold to create a replica of the patterned microchannels.

PDMS material is highly popular in microfluidics due to its transparency, biocompatibility, and gas permeability, making it ideal for biological applications like cell culture and organ-on-a-chip systems. Additionally, PDMS is flexible, allowing it to bond easily to glass or other PDMS layers through plasma treatment to form enclosed microchannels.

(28,29)

Figure 1 illustrates the fabrication process of microfluidic devices using soft lithography, highlighting the key steps involved in creating a PDMS-based microfluidic chip. Panel A depicts the mould fabrication process, starting with the application of a negative SU-8 photoresist on a substrate, followed by spin-coating, soft baking, and UV light exposure through a photomask to define the desired patterns. After development, baking, and rinsing, a mould with hardened photoresist structures is obtained. Panel B outlines the PDMS device fabrication, where liquid PDMS is cast onto the mould, thermally annealed, and peeled off to replicate the microfluidic features. The final steps include creating inlets and sealing the device through plasma treatment and pressure bonding to form functional microchannels. Panel C shows the completed device in operation, demonstrating its application for fluid flow experiments. This figure provides a comprehensive overview of the soft lithography technique, a widely used approach for microfluidic device fabrication due to its simplicity, precision, and reproducibility.

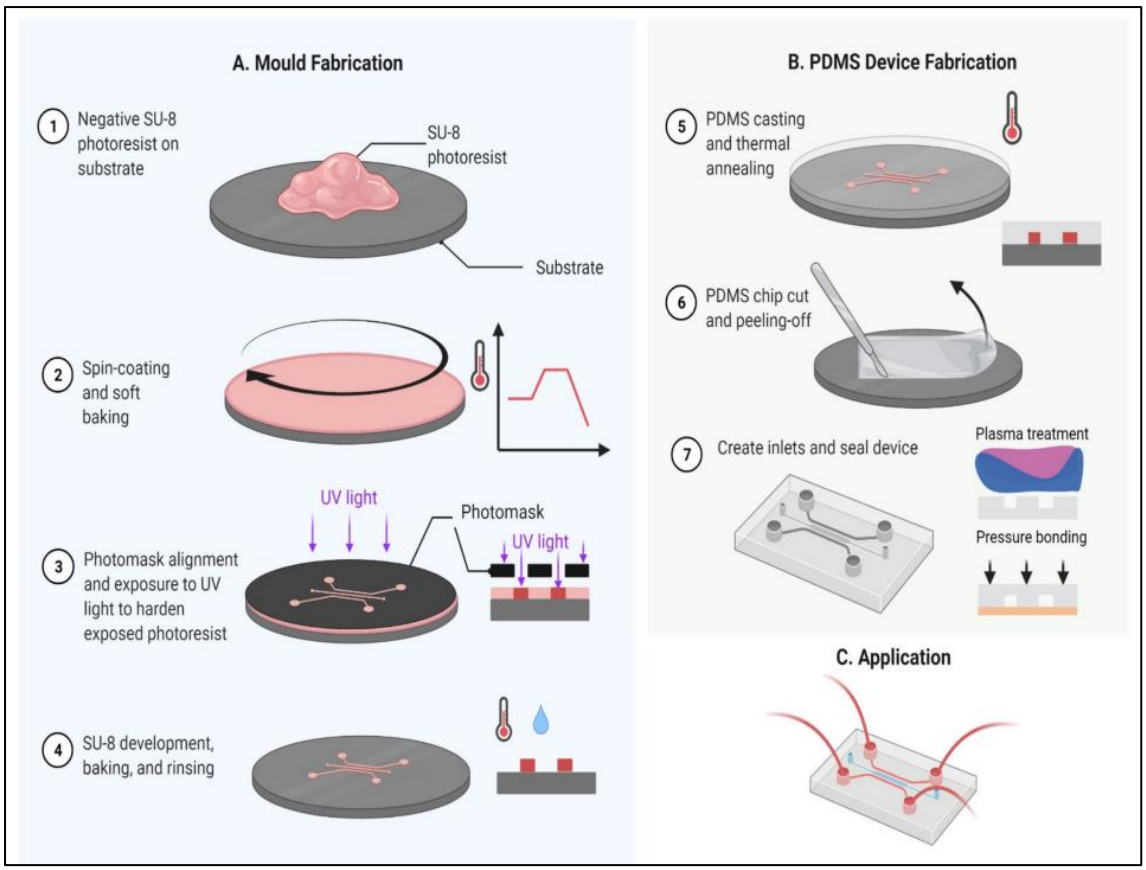


Figure 1(A) Fabrication of an SU-8 master mould; (B) casting of polydimethylsiloxane (PDMS) on the mould, plasma treatment, and contact pressure bonding; (C) integrating PDMS microfluidic device with world to chip interfaces for application.(26)

Advantages:

Soft lithography offers several advantages in microfluidic device fabrication. The technique allows for high-resolution patterning, enabling precise microchannel designs essential for controlled fluid flow. PDMS, the most commonly used polymer, provides transparency, biocompatibility, and gas permeability, which are highly beneficial for biological applications such as cell culture and organ-on-a-chip systems. Additionally, PDMS's flexibility allows for easy bonding with glass or additional PDMS layers through plasma treatment, enabling the formation of enclosed microchannels.

Limitations:

Despite its benefits, soft lithography has notable limitations. The initial creation of the master mold is costly, requiring cleanroom facilities and specialized photolithographic equipment, making it challenging for laboratories without such infrastructure. Furthermore, the process is generally restricted to planar designs, complicating the fabrication of complex three-dimensional microstructures. This limitation reduces the versatility of soft lithography, especially for applications needing intricate 3D geometries, such as advanced mixers or particle separators (28,29).

1.2.2 Injection Molding

Injection molding is a well-established method for the mass production of plastic components, and it has been adapted for the fabrication of microfluidic devices. In this process, a polymer material is heated until it becomes liquid and is then injected into a metal mold under high pressure. The polymer solidifies upon cooling, taking the shape of the mold. This method is particularly useful for producing large quantities of devices with high precision and reproducibility, making it popular in industrial settings.

While injection molding is effective for mass production, it is not suited for early-stage research or prototyping due to the high cost and time involved in fabricating the metal molds. Once a mold is created, design modifications are costly and time-consuming. Additionally, injection molding is primarily limited to two-dimensional (2D) or shallow 3D designs, and it lacks the flexibility required for creating complex microfluidic structures with intricate internal geometries(30–32).

Figure 2 illustrates the injection molding process, a widely used technique for fabricating polymer-based microfluidic devices. The process consists of four key steps: plastification, injection, cooling and demolding.

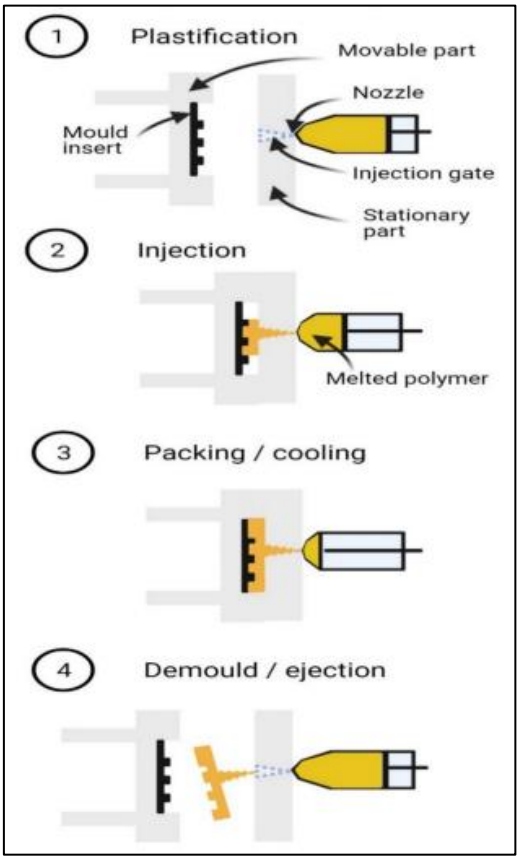


Figure 2 Schematic of the injection molding process used in the fabrication of microfluidic devices. Figure adapted from (26)

Advantages:

Injection molding is highly advantageous for the mass production of microfluidic devices, offering high precision and reproducibility, essential for industrial applications. This method allows for the rapid manufacturing of large quantities, making it efficient and cost-effective once the initial mold is created. Additionally, it supports a wide variety of polymers, expanding material options for different applications.

Limitations:

However, injection molding is less suitable for early-stage research and prototyping due to the high cost and time required to fabricate metal molds. Once a mold is made, design changes become expensive and time-consuming. The technique is also restricted to primarily two-dimensional or shallow 3D designs, limiting its flexibility for producing complex internal geometries needed in certain microfluidic applications.

1.2.3 Hot Embossing

Hot embossing is another method that has been adapted for microfluidic fabrication. It involves heating a polymer substrate until it becomes soft, and then pressing it against a prefabricated mold to imprint the desired microchannel patterns. The polymer is allowed to cool and harden, retaining the pattern of the mold.

This technique is useful for creating microfluidic devices in materials like polycarbonate or COC (cyclic olefin copolymer), which are more rigid than PDMS and can provide better mechanical properties for certain applications. Like injection molding, hot embossing is more suited for mass production rather than prototyping due to the need for precise molds, which are costly and difficult to modify once fabricated (32).

Figure 3 shows the hot embossing process. This technique combines heat and pressure to imprint micro-scale patterns onto polymer substrates, offering precision and cost-effectiveness for device fabrication.

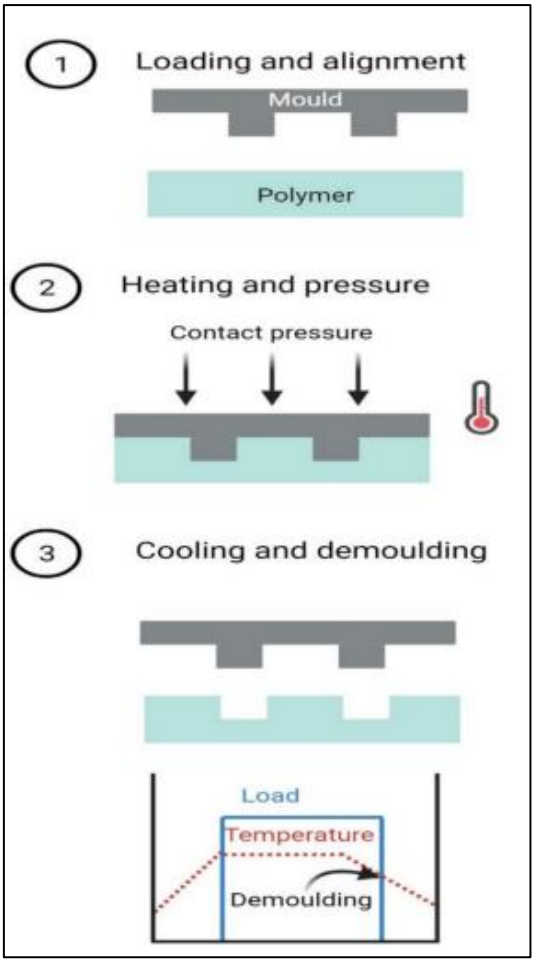


Figure 3 Schematic representation of the hot embossing process for microfluidic device fabrication. Figure adapted from (26)

Advantages:

Hot embossing is an effective method for microfluidic device fabrication, especially suited for materials like polycarbonate or COC that require higher rigidity and mechanical stability than PDMS. The technique is beneficial for producing devices with defined, durable structures, making it ideal for applications where mechanical strength is essential. It also supports efficient, repeatable mass production once the mold is fabricated.

Limitations:

Despite its benefits, hot embossing is less ideal for prototyping and early research due to the high cost and difficulty of modifying molds after fabrication. Like injection molding, it is best suited for two-dimensional or relatively shallow 3D designs, limiting its flexibility for more complex or intricate microfluidic geometries.

1.2.4 Micromachining

Micromachining, also known as micro-milling, involves using mechanical or laser-based tools to carve microchannels and structures directly into a material. It offers high precision and flexibility, allowing for the fabrication of complex and deep microstructures that are difficult to achieve with other methods. Micromachining is particularly useful for creating custom devices with intricate designs, as it does not require a mold, allowing for rapid modifications to the design.

However, micromachining is a slow and expensive process, especially for producing large quantities of devices. The surface quality of micromachined devices can also be rougher compared to other methods, which may affect the behavior of fluid flow within the channels. Despite its high precision, micromachining is not ideal for mass production due to its low throughput and high costs(33,34).

Advantages:

Micromachining, or micro-milling, provides high precision and flexibility in microfluidic fabrication. It allows for the creation of complex and deep microstructures that are challenging to achieve with other methods. Unlike mold-based techniques, micromachining enables rapid design changes, making it ideal for custom devices with intricate features without requiring extensive tooling.

Limitations:

However, micromachining is time-consuming and costly, especially for large-scale production, making it less suitable for mass manufacturing. Additionally, the surface finish of micromachined devices can be rougher than that of other methods, potentially impacting fluid flow behavior within channels. The low throughput and high costs limit its practicality for producing large quantities of microfluidic devices.

1.2.5 Limitations of Traditional Methods

While traditional fabrication methods like soft lithography, injection molding, and micromachining have been highly effective for many microfluidic applications, they have several limitations:

- **High Costs**: These methods require expensive cleanroom facilities and specialized equipment, making them inaccessible for smaller laboratories. Although PDMS itself is low-cost, the process of creating master molds and performing photolithography can be expensive.
- **Design Flexibility**: Once molds are created, modifying designs is difficult and costly. This makes traditional methods less suited for iterative prototyping, which is often necessary in early-stage research.

- **Complex 3D Structures**: Traditional methods are largely limited to two-dimensional or shallow three-dimensional structures, making them inadequate for fabricating devices with complex internal geometries. This restricts their use in advanced applications such as chaotic mixers or multi-functional microfluidic devices.
- **Time-Consuming**: Fabricating molds or setting up micromachining processes can take a significant amount of time, which limits the speed at which new designs can be tested and iterated.

1.2.6 Transition to 3D Printing in Microfluidics

The limitations of traditional microfabrication methods such as high costs, limited design flexibility, and challenges in creating complex 3D structures have led to the exploration of alternative fabrication technologies. One of the most promising solutions to these challenges is 3D printing. Over the past decades, additive manufacturing technologies have advanced significantly, allowing researchers and engineers to fabricate highly complex microfluidic devices with remarkable efficiency and precision(35,36).

3D printing offers several advantages over traditional methods. First, it allows for rapid prototyping and iterative design. Unlike soft lithography or injection molding, where modifying a mold can be costly and time-consuming, 3D printing enables immediate modifications to the design file, which can be implemented in a matter of hours. This flexibility is particularly useful in the research and development phase, where designs often need to be tested and optimized based on experimental results(14,37).

Additionally, 3D printing can create fully three-dimensional structures with complex internal geometries that are difficult or impossible to achieve with traditional methods. This capability is especially beneficial for applications requiring integrated features, such as spiral channels for particle separation or herringbone mixers for fluid mixing. The ability to fabricate such intricate designs in a single fabrication step eliminates the need for multi-step processes like bonding or assembly, reducing the risk of defects, minimizing human error, and improving device reliability(38,39).

Moreover, 3D printing offers cost-effective fabrication. While traditional methods often require expensive cleanroom facilities and specialized equipment, 3D printers can operate in standard laboratory environments with minimal setup. This significantly reduces the barriers to entry for laboratories without access to cleanroom infrastructure.

As 3D printing technologies, such as stereolithography (SLA) and fused deposition modeling (FDM), have matured, their resolution and material options have improved, making them suitable for

microfluidic applications. In particular, the development of transparent, biocompatible resins has made it possible to fabricate devices that allow real-time optical monitoring of fluid flow and biological processes(40–42).

Given these advantages, 3D printing has emerged as a game-changing technology in the field of microfluidics, offering a flexible, rapid, and cost-effective alternative to traditional methods. The following section will explore the emergence of 3D printing in microfluidics, discussing its impact on the field and how it addresses the limitations of traditional fabrication techniques(27,43).

1.3 Emergence of 3D Printing in Microfluidics

As traditional fabrication methods have shown significant limitations, the need for more flexible, cost-effective, and rapid manufacturing solutions in microfluidics has become evident. In response, 3D printing, also known as additive manufacturing, has revolutionized the way microfluidic devices are fabricated. It enables the creation of intricate and complex structures with unparalleled design freedom, offering substantial benefits over conventional methods, particularly in terms of customization, time efficiency, and cost reduction.

Additive manufacturing operates by building devices layer-by-layer, directly from a digital model, thus eliminating the need for molds or masks. This technique enables rapid prototyping, allowing for quick iteration of designs, and has made it possible to fabricate 3D microfluidic structures in a single fabrication step. Below are the key 3D printing technologies relevant to microfluidics, along with a detailed explanation of their working principles, advantages, and limitations(39,44,45).

1.3.1 Stereolithography (SLA)

SLA is currently one of the most widely used 3D printing technologies in microfluidics due to its high resolution and precision. It operates by using a light source, typically in the ultraviolet (UV) range, to selectively cure a photopolymer resin, solidifying it layer by layer to build the desired structure. This process is controlled by a digital light processing (DLP) system or a laser that traces the pattern of each layer on the resin vat. The printer's build platform is submerged in the resin, and the UV light cures one layer at a time, with the platform gradually lifting out of the vat as each successive layer is cured. SLA offers several advantages for microfluidic applications, including high resolution, with feature sizes as small as 10–20 microns, allowing for the production of intricate microchannels and internal features,

such as herringbone mixers, that would be difficult to fabricate with traditional methods. It also provides material versatility, as a wide range of photopolymer resins can be used, including transparent and biocompatible resins that are essential for biological and diagnostic applications, enabling real-time observation of fluid flow and biological processes within the channels. Additionally, SLA facilitates the fabrication of fully three-dimensional structures in a single step, allowing for complex geometries such as spiral channels for particle separation or intricate multi-layered devices without the need for assembly or bonding.

However, SLA does present challenges, particularly in the fabrication of closed microchannels. The light used to cure the resin may penetrate deeper than desired, causing partial curing within the channel itself. To address this, post-processing steps such as flushing uncured resin from the channels and additional UV curing are often required to ensure the integrity of the microchannels. With proper optimization of curing parameters and resin selection, SLA remains one of the most promising techniques for fabricating high-resolution microfluidic devices. SLA has been successfully applied to fabricate herringbone mixers, which enhance fluid mixing in laminar flow by generating chaotic advection, as well as spiral channels for particle separation based on particle size, demonstrating the technique's capability to create complex, functional microfluidic devices(46–49).

Figure 4 illustrates the working principle of SLA, a widely used 3D printing technique that utilizes a laser to selectively cure liquid photopolymer resin into solid layers. This process allows for high-precision fabrication of microfluidic devices and other complex geometries.

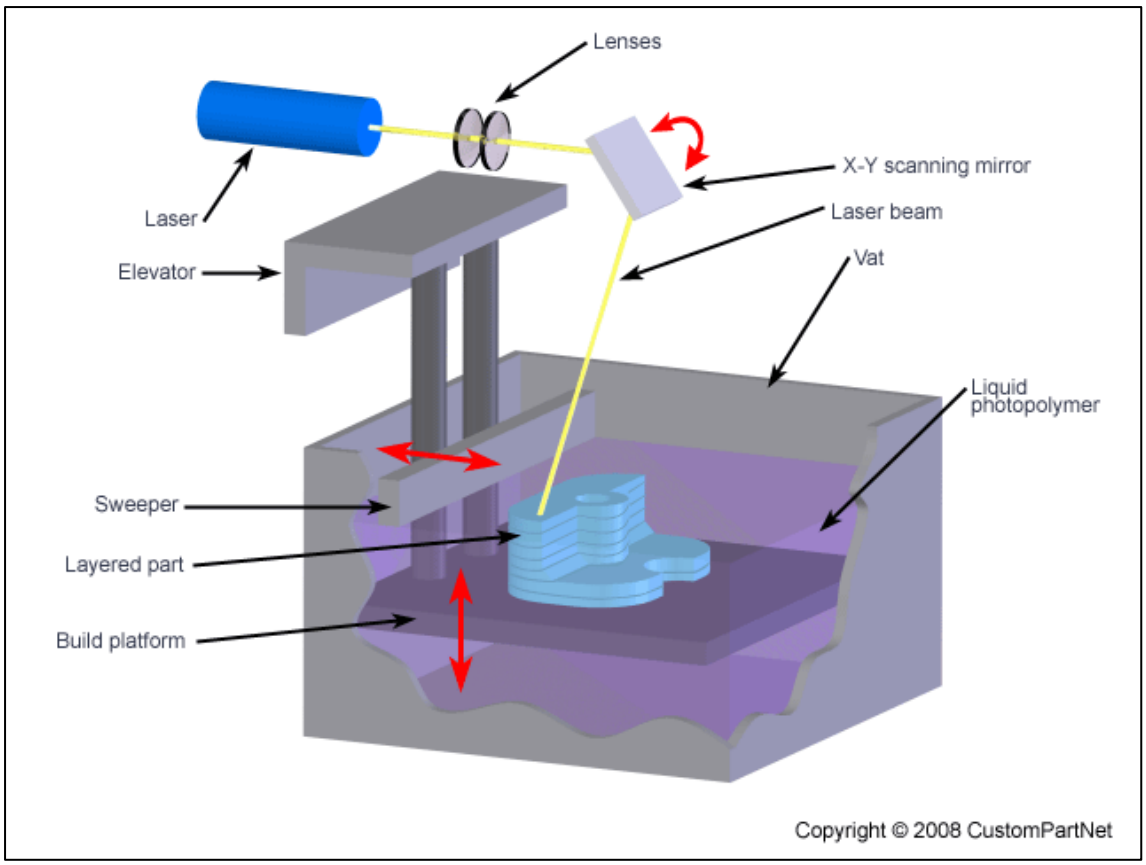


Figure 4: Schematic of SLA 3D printing. A laser selectively cures liquid photopolymer resin layer by layer to create the final structure.(50)

Advantages:

SLA provides high resolution, enabling the fabrication of intricate microchannel designs essential for advanced microfluidic applications. It supports a variety of photopolymer resins, including biocompatible and transparent options, making it suitable for biological and diagnostic uses. Additionally, SLA allows for the creation of complex, fully 3D structures in a single step, which eliminates the need for assembly or bonding processes.

Limitations:

Despite its benefits, SLA faces challenges in fabricating closed microchannels, as the curing light can penetrate deeper than intended, causing partial curing within channels. This often requires additional post-processing, such as flushing out uncured resin and further UV curing, to ensure proper channel integrity. These limitations make SLA less straightforward for some applications, though careful optimization can mitigate these issues.

1.3.2 Digital Light Processing (DLP)

DLP is a type of SLA 3D printing technique, with key distinctions in speed and precision. Like SLA, DLP uses a UV light source to cure a photopolymer resin layer by layer; however, instead of relying on a laser to trace each layer's pattern point by point, DLP employs a digital micromirror device (DMD) that projects the entire layer's pattern onto the resin simultaneously. This approach allows DLP to achieve faster print speeds than traditional SLA, as each layer is cured in a single step. DLP offers several advantages for microfluidic fabrication, including increased speed, since entire layers are cured at once, making it particularly efficient for complex designs. It also provides high resolution, comparable to or slightly better than SLA, which is essential for applications requiring precise microchannel patterns. Figures 5 and 6 present the schematic of DLP 3D printing allowing versatile design options, enabling the printing of complex three-dimensional structures with intricate internal geometries, such as interwoven channels or sophisticated mixing designs.

However, DLP, like SLA, faces challenges in producing closed microchannels, as the curing process may leave residual resin within the channels. This often requires additional post-processing steps, such as flushing out uncured resin and further UV curing, to ensure clear and functional channels(51,52).

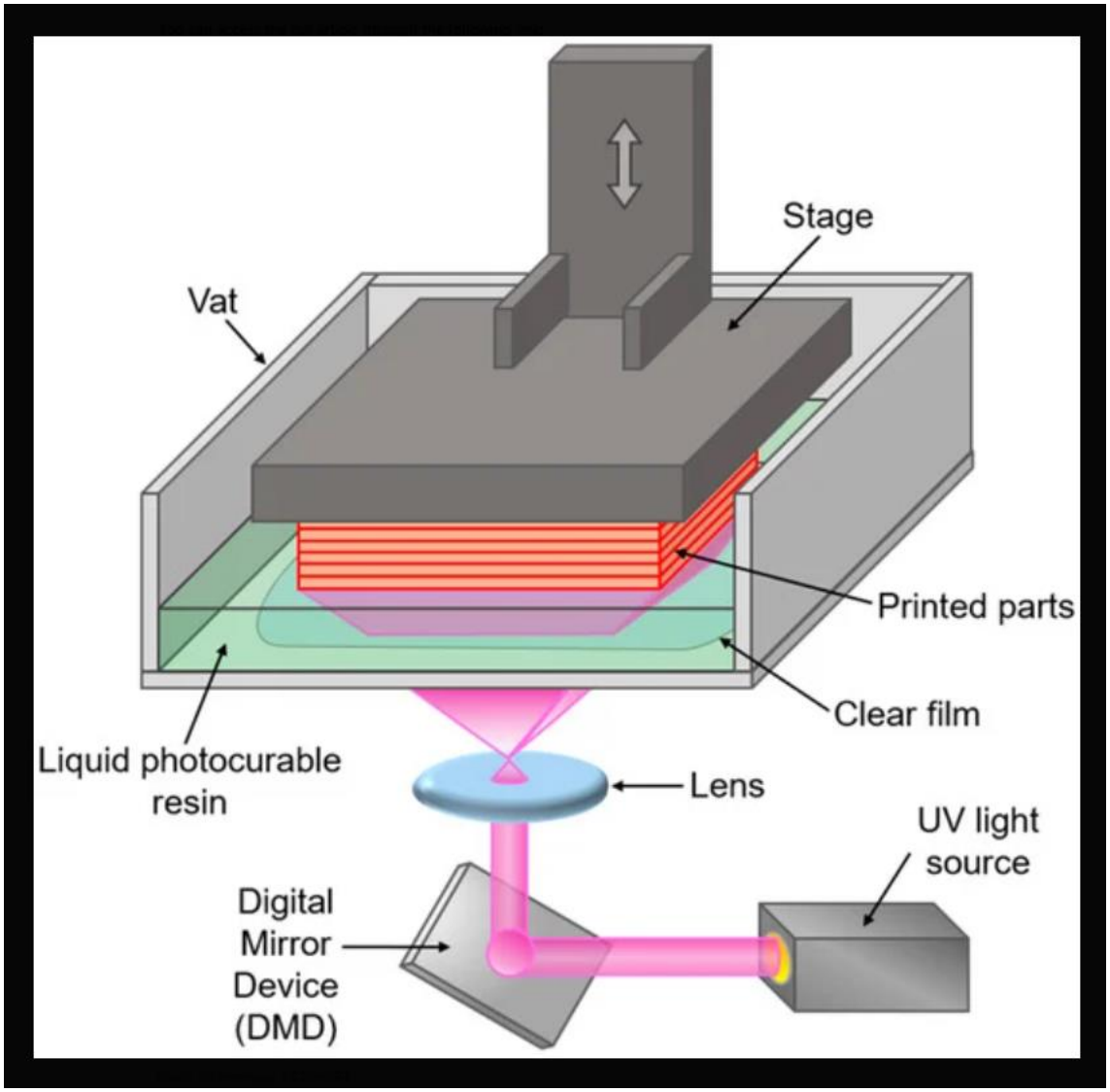


Figure 5: Schematic of DLP 3D printing. A UV light source and digital mirror device project light onto a liquid resin, solidifying entire layers at once to build the printed part. (53)

Figure 6 showcases a visual representation of a 3D-printed structure produced through DLP, where the printed part is lifted from the resin vat during the layer-by-layer curing process.

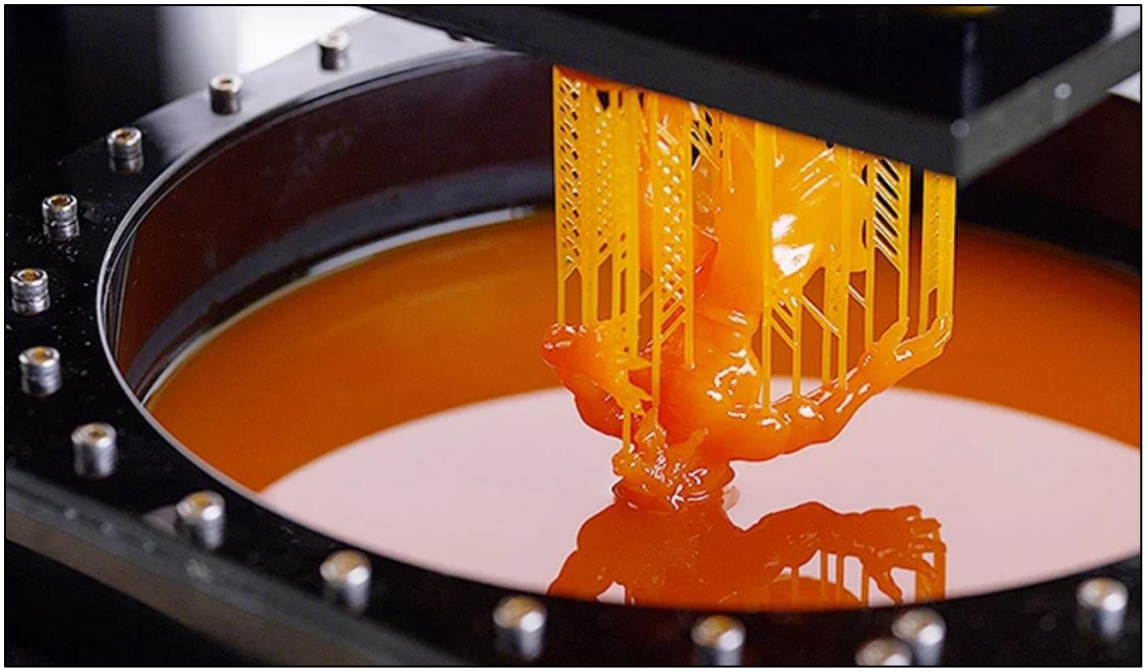


Figure 6: Visual representation of a DLP-printed structure.(54)

Advantages:

DLP offers increased printing speed by curing entire layers at once, making it ideal for complex designs. Its resolution is comparable to or slightly better than SLA, and it allows for versatile 3D designs, enabling complex internal structures suitable for microfluidic applications.

Limitations:

Despite its speed and versatility, DLP encounters similar challenges to SLA in fabricating closed microchannels, as residual resin may remain in channels, necessitating additional post-processing to clear and cure the structures fully.

1.3.3 Two-Photon Polymerization (2PP)

Two-Photon Polymerization (2PP) is an advanced 3D printing technology that utilizes femtosecond lasers to initiate polymerization at the precise focal point of the laser beam, where two photons are absorbed simultaneously. This process enables the fabrication of structures with nanometer resolution (200-300 nm), far exceeding the capabilities of SLA and DLP. The standout feature of 2PP is its ability to produce extremely fine and intricate structures, making it particularly valuable for high-precision microfluidic applications that require ultra-small channels or specialized features. With feature sizes reaching down to a few hundred nanometers, 2PP offers exceptional resolution for creating nanoscale structures within microfluidic devices. Additionally, 2PP supports true 3D fabrication, as it is not limited

by layer-by-layer processing, allowing for the creation of highly complex and detailed microfluidic systems.

However, despite its high resolution, 2PP faces challenges in terms of slow print speeds and high operational costs. This technique is therefore best suited for applications demanding extreme precision, such as nanoscale biological studies or custom mixing devices, but is less practical for large-scale or high-throughput production(55).

Figure 7 illustrates the working principle of 2PP. The focused femtosecond laser (fs-laser) selectively polymerizes material on the donor film, transferring patterned features to the receptor substrate with precise control over positioning.

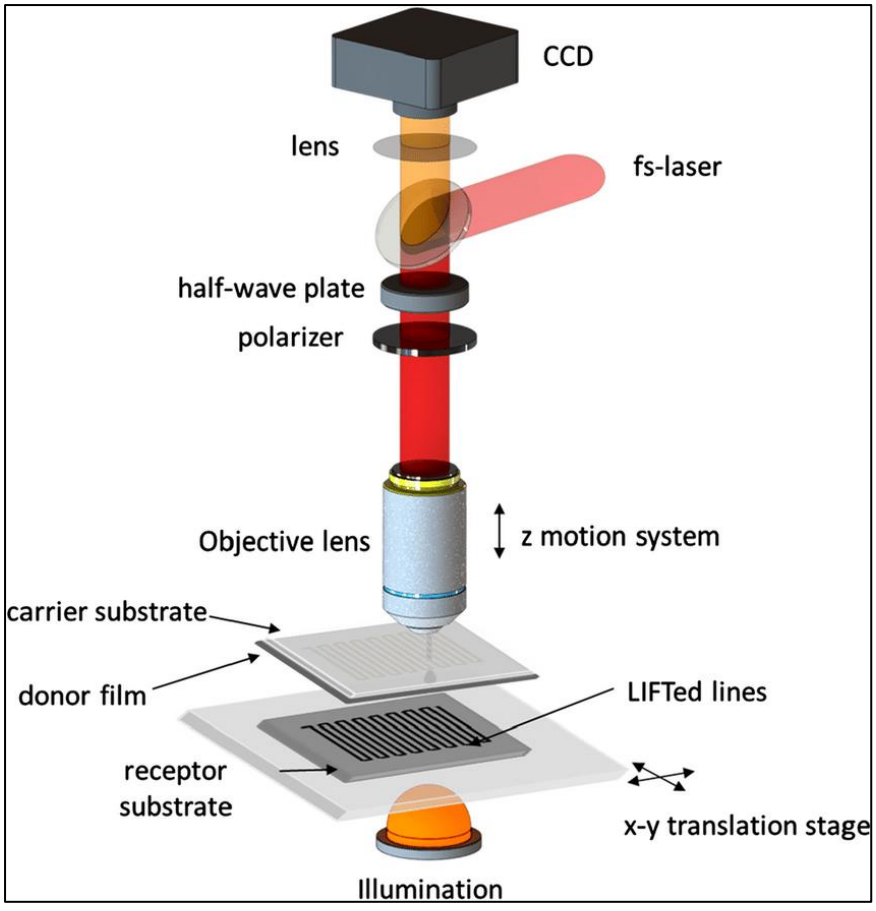


Figure 7: Schematic of the 2PP process, illustrating the laser setup and material transfer to create precise microstructures. From (56).

Advantages:

2PP offers unmatched resolution, with feature sizes as small as a few hundred nanometers, ideal for nanoscale structures in microfluidics. Its true 3D fabrication capabilities enable the creation of intricate designs without the restrictions of layer-by-layer processing, making it highly adaptable for complex, detailed systems.

Limitations:

While 2PP provides exceptional detail, it is limited by slow print speeds and high costs, making it less suitable for large-scale or high-throughput manufacturing. It is most practical for specialized applications requiring extremely fine resolution and intricate designs.

1.3.4 Fused Deposition Modeling (FDM)

Fused Deposition Modeling (FDM) is a widely available and affordable 3D printing technology often used for larger-scale fabrication. This process involves heating and extruding a thermoplastic filament, like Polylactic Acid (PLA) or Acrylonitrile Butadiene Styrene (ABS) , layer by layer to build the desired structure. While FDM is less commonly used for microfluidic applications due to its lower resolution, typically in the range of 100–200 microns, recent advances in nozzle design and material formulations have allowed for its use in creating macroscale microfluidic components, such as device housings or larger flow channels. FDM offers several advantages, notably its cost-effectiveness, as it is one of the most affordable 3D printing technologies, making it accessible for laboratories with limited resources. Additionally, FDM supports printing with durable thermoplastics, which are suitable for producing robust casings or larger channels that do not require high resolution.

However, FDM's primary limitation in microfluidics is its relatively low resolution, which restricts its ability to fabricate fine microchannels or intricate internal geometries. Despite this limitation, FDM can still be used in conjunction with other methods, like SLA, to create hybrid devices that benefit from the strengths of each technology(42,57–59).

Figure 8 shows the FDM process, where thermoplastic filaments are heated, melted, and extruded through a nozzle to build parts layer by layer. Support structures are printed as needed to maintain the stability of complex designs.

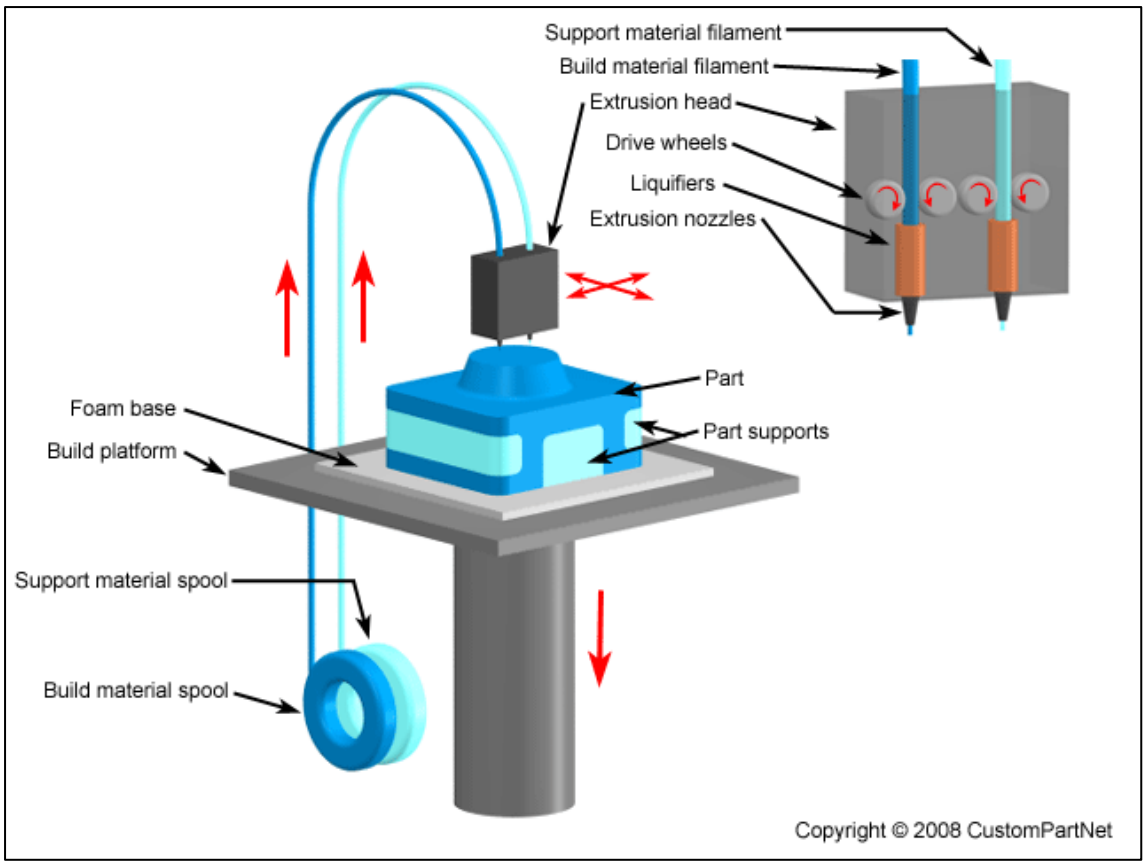


Figure 8: Schematic of the FDM process showing the extrusion of build and support materials to create a 3D-printed part layer by layer. (60)

Advantages:

FDM is cost-effective and accessible, making it ideal for laboratories with budget constraints. It also allows for the use of robust thermoplastics, suitable for creating durable device casings or larger channels where fine resolution is unnecessary.

Limitations:

The main drawback of FDM for microfluidic applications is its low resolution, limiting its use in creating intricate microchannels. However, it can complement higher-resolution methods, such as SLA, in hybrid devices that combine the advantages of both technologies.

1.3.5 Photopolymer Inkjet Printing

Photopolymer inkjet printing, also referred to as PolyJet or MultiJet Modeling (MJM), is an advanced 3D printing technology that utilizes inkjet nozzles to precisely deposit liquid photopolymer droplets layer by layer onto a build platform. Each layer is immediately cured by ultraviolet (UV) light, solidifying the material and allowing for the creation of highly detailed and complex structures. Unlike other 3D printing methods, this technique supports the use of multiple materials within a single print, enabling

the fabrication of components with diverse mechanical properties, such as rigid and flexible segments in the same part. Additionally, photopolymer inkjet printing achieves smooth surface finishes and high-resolution features, making it ideal for applications requiring intricate details or aesthetic accuracy. Commonly used in industries such as healthcare, this technology has been employed to produce highly detailed anatomical models for surgical planning, educational tools, and complex prototypes.

Figure 9 illustrates the process of photopolymer inkjet printing, where liquid photopolymer materials are deposited in layers using inkjet print heads. Heated reservoirs supply the build and support materials, which are solidified as they are deposited to create the desired 3D structure. This method allows for high precision and smooth surface finishes.

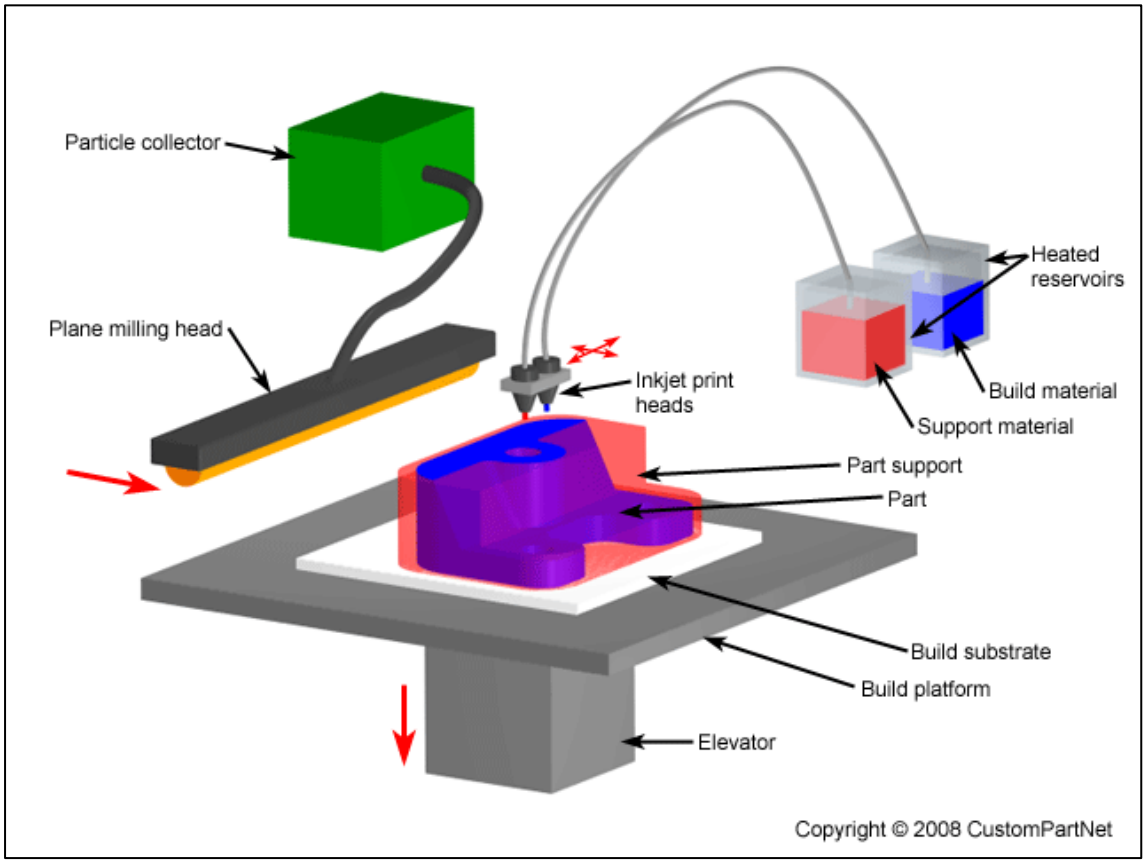


Figure 9: Photopolymer inkjet printing process showing the deposition of materials through inkjet heads, with support and build materials solidified layer by layer. From (61)

Advantages:

Photopolymer inkjet printing offers unparalleled multi-material versatility, enabling the simultaneous use of rigid and flexible materials within a single part. This capability simplifies the creation of complex, functional designs that would otherwise require post-assembly. The technology also delivers high resolution and smooth surface finishes, making it suitable for applications demanding intricate details,

such as anatomical models for surgical planning or advanced prototypes. Additionally, the immediate UV curing of each layer allows for faster production times compared to methods like SLA or FDM, further enhancing its efficiency for rapid prototyping and design validation.

Limitations:

Despite its advantages, photopolymer inkjet printing has notable drawbacks. The reliance on proprietary photopolymers significantly increases material costs, making it less accessible for users with budget constraints. Moreover, the mechanical properties of the printed parts are often insufficient for functional or end-use applications, limiting their use to prototyping and visual models. The bio- and cytocompatibility of the available materials is also limited, restricting the technology's application in certain biomedical and biological fields. These limitations must be addressed to expand its usability beyond prototyping and non-functional modeling.

1.3.6 Selective Lasers Sintering (SLS)

Selective Laser Sintering (SLS) is a versatile and widely used 3D printing technology that relies on a laser to sinter powdered materials, layer by layer, to create a three-dimensional object. In SLS, the precursor material, typically a polymer, metal, ceramic, or composite powder, is evenly spread across a build platform. A focused laser beam selectively heats the powder to fuse particles together, defining the geometry of each layer. After the layer is completed, the build plate lowers, and a roller deposits a new layer of powder on top of the previous one. This process is repeated until the entire object is formed. Unlike other methods such as SLA or FDM, SLS does not require support structures, as the unsintered powder surrounding the object provides natural support during printing. At the end of the process, the object is retrieved from the powder bed, and excess powder is removed, often with compressed air or other cleaning methods.

SLS is particularly advantageous for its ability to process a wide range of materials, from biopolymers to metals and ceramics, enabling the fabrication of functional parts with properties comparable to those made using traditional manufacturing techniques. Its applications are vast, ranging from creating anatomically accurate scaffolds for bone tissue engineering and prosthetics to printing patient specific surgical models derived from Magnetic Resonance Imaging (MRI) or Computed Tomography (CT) data.

SLS is also used for industrial prototyping and the production of high-performance components, such as customized implants made from biocompatible metals like titanium or advanced composite materials for aerospace and automotive applications.

Figure 10 shows the SLS process, where a laser selectively fuses powder particles layer by layer to form a solid part. Powder feed pistons supply the material, and a leveling roller spreads it evenly across the build area before laser sintering occurs.

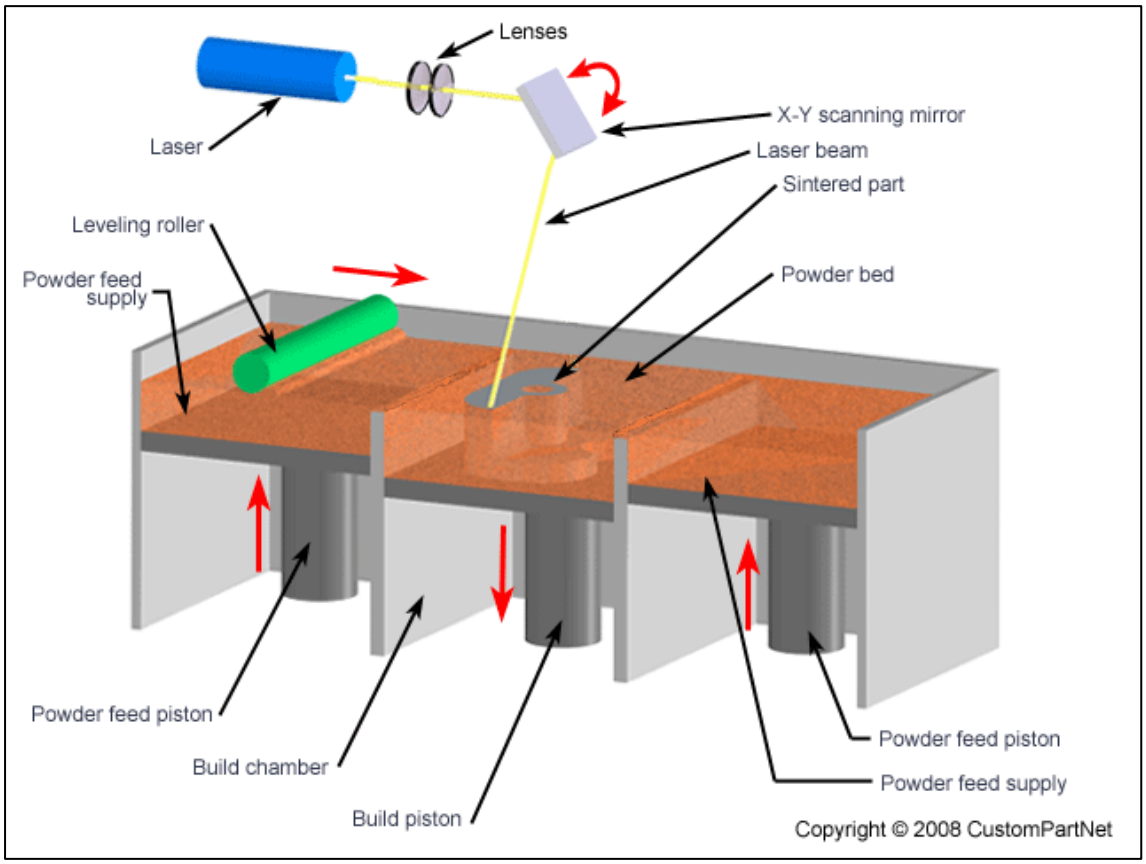


Figure 10: SLS process schematic highlighting the laser sintering of powder layers to create solid parts. From (62)

Advantages:

SLS offers significant benefits in 3D printing, primarily due to its material versatility and the high quality of its output. The technique allows for the fabrication of complex geometries without the need for support structures, reducing post-processing requirements. Furthermore, the sintered materials exhibit high purity and mechanical properties comparable to those produced through traditional manufacturing methods, making them suitable for demanding applications such as biomedical implants and aerospace components. SLS also supports multi-material printing, enabling the integration of different functionalities within a single device. This flexibility has made it the go-to method for rapid prototyping and the creation of highly realistic industrial prototypes.

Limitations:

Despite its advantages, SLS has some limitations. The need for precise control over laser parameters and powder quality makes the process complex and often expensive. Additionally, post-processing steps such as powder removal and surface finishing can be time-consuming, especially for intricate designs. The cost of SLS-compatible materials, particularly metals like titanium, can be prohibitively high for some applications. Lastly, while the unsintered powder acts as a natural support during printing, it must be carefully handled and recycled to minimize material waste and cost. These challenges highlight the need for continued research and development to improve the accessibility and efficiency of SLS for a broader range of applications.

1.3.5 Advantages of 3D Printing for Microfluidics

In summary, the key advantage of 3D printing in microfluidics lies in its ability to fabricate complex, multi-functional devices in a single manufacturing step. Unlike traditional methods that require bonding or assembly, 3D printing can produce integrated microfluidic devices with features such as herringbone mixers, spiral channels for particle separation, and multi-layered designs for more complex fluidic control. This significantly simplifies the fabrication process, reduces the risk of misalignment during assembly, and improves the overall functionality and precision of the devices.

Furthermore, 3D printing allows for rapid prototyping, which is essential in research and development. Researchers can quickly iterate designs, fabricate new prototypes within hours, and immediately test their performance. This drastically shortens the development cycle, enabling faster innovation and optimization of microfluidic devices.

3D printing has become an indispensable tool in the field of microfluidics, providing design flexibility, cost efficiency, and the ability to create devices with complex internal geometries that were previously impossible with traditional methods. The continued advancements in 3D printing materials, resolution, and speed will further expand the possibilities of microfluidic device fabrication, making it a cornerstone technology for future innovations in bioengineering, diagnostics, and fluid dynamics (37,44,63–65).

1.4 Fabrication of 3D-Printed Microfluidic Devices and its Applications

The advancement of 3D printing has introduced innovative approaches for fabricating microfluidic devices, enabling the creation of complex and customized geometries previously unattainable with traditional methods. Two primary strategies have emerged: the use of 3D-printed molds for PDMS replication and the direct 3D printing of closed microchannels. Each method offers unique

opportunities but also presents specific challenges that underscore the need for continued research and optimization(44).

3D-printed molds provide a versatile and accessible route for fabricating PDMS-based microfluidic devices. This approach combines the design flexibility of 3D printing with the material advantages of PDMS, such as transparency, biocompatibility, and gas permeability. The ability to inspect and clean the PDMS replica before bonding it to a glass substrate adds a critical layer of quality control, minimizing the risk of obstructions and ensuring precise flow characteristics. However, the reliance on additional molding and bonding steps introduces variability and can increase fabrication time, especially when achieving precise alignment or sealing is challenging.

Direct 3D printing of closed microchannels offers a more integrated alternative, where the entire device, including the top layer, is fabricated in a single process. This approach eliminates the need for bonding and produces more robust devices, ideal for applications requiring pressure-driven fluid flow or sealed environments. Despite its advantages, this method faces significant challenges, particularly in controlling UV light penetration during SLA and DLP printing processes. Over curing within the channels can cause blockages or distortions, complicating the printing of functional microchannels. Strategies such as optimizing exposure settings, adjusting channel dimensions to account for light penetration, and employing sacrificial structures have been developed to address these issues. However, these techniques require precise control and remain limited by their reproducibility and the delicate nature of post-processing steps (11,12,66,67).

Both approaches demonstrate the transformative potential of 3D printing in microfluidics, but their limitations highlight critical areas for improvement(68–70).

1.4.1 Customized 3D Printing Protocols

In addition to the advancements in materials, significant efforts have been made to optimize the printing protocols to ensure the highest possible performance of 3D-printed microfluidic devices. These protocols focus on achieving precise control over the printing process, ensuring that microchannels are formed with the required dimensions, smoothness, and fluid dynamics(19,71–78).

Key parameters in these customized protocols include:

- **Layer thickness**: Thinner layers result in smoother channels and higher Z-axis resolution, reducing rugosity artifacts that can disrupt fluid flow. However, the balance between resolution and print time must be optimized depending on the application.
- **UV exposure time and intensity**: In SLA and DLP printing, controlling UV exposure time and intensity is critical to prevent over curing, which can cause blockages in closed channels by

distorting the intended shape of the microchannels. However, if the exposure time or intensity is insufficient, the material may not solidify properly, leading to poor layer adhesion and delamination during the printing process. Optimal exposure settings are therefore essential to ensure that microchannels maintain their designed structure and integrity throughout the device.

- **Post-processing**: Techniques such as UV curing and solvent flushing are essential for fully curing the resin and ensuring that the channels remain open and functional after printing.

These protocols are often tailored to the specific requirements of each device, allowing for rapid iteration and refinement during the development process. By continuously optimizing these protocols, researchers can ensure that 3D-printed devices meet the high precision and performance standards necessary for biomedical applications.

Despite the significant advances in 3D printing for microfluidics, certain technical limitations remain that must be addressed to further improve device functionality.

Limitations:

- **Resolution in the Z-axis**: While SLA and DLP offer high lateral resolution, the Z-axis resolution is often less precise, leading to layering artifacts that can affect the internal smoothness of microchannels. These artifacts can interfere with fluid flow and reduce the efficiency of mixing or separation processes.
- **Closed channels printing challenges**: Achieving defect-free closed channels remains a challenge. UV light can penetrate and partially cure the internal resin, causing blockages. While techniques like sacrificial materials help mitigate this, the complexity of fabricating intricate closed-channel geometries still limits some applications.

The continuous advancement in 3D printing technologies has led to significant improvements in how microfluidic devices are designed and integrated. These innovations are centered around the development of advanced resins and customized printing protocols that enhance both the performance and biocompatibility of the devices, making them more suitable for a wide range of biomedical applications(79,80).

1.4.2 Custom Resin Compositions for DLP-SLA 3D Printing for Microfluidics

Custom resins provide a tailored solution that enhances the capabilities of 3D printing, opening the door to more advanced and versatile microfluidic devices. These formulations offer a great flexibility in achieving the desired material properties and printing performance. By tailoring the resin composition, researchers can overcome challenges such as limited resolution, insufficient mechanical strength, or inadequate chemical compatibility for specific microfluidic applications.

Custom resins consist of three primary components, each fulfilling a critical role in the DLP-SLA process. Photoinitiators are responsible for initiating the polymerization reaction upon exposure to UV light, converting the liquid resin into solid structures with high precision and accuracy. Optical absorbers, on the other hand, play a crucial role in controlling the penetration depth of the curing light, ensuring that only the intended layer is solidified. This prevents over curing, which can distort fine features or block internal channels, and reduces unwanted light scattering that might affect the fidelity of printed structures. Finally, monomers serve as the foundational building blocks of the resin, directly influencing the mechanical, chemical, and optical properties of the final printed object. The type and concentration of monomers determine whether the structure will be rigid or flexible, transparent or opaque, and whether it can meet specific requirements such as biocompatibility or chemical resistance.

The ability to customize these components allows for precise control over the behavior and properties of the resin during and after printing. For example, by adjusting the concentration of optical absorbers, researchers can regulate the curing process to achieve sharper layer boundaries and prevent polymerization in unintended regions. Similarly, selecting specific monomers enables the creation of devices with enhanced durability, transparency, or flexibility, depending on the application's needs. This customization is particularly valuable in microfluidics, where intricate geometries and precise fluid flow dynamics require materials with specific characteristics (63,81–88).

Polymer and Monomer Selection

Photocurable resins typically consist of multifunctional acrylate or epoxy monomers, which create a dense cross-linked network when cured. Acrylates, including poly(ethylene glycol) diacrylate (PEG-DA), are often chosen for SLA-based microfluidics due to their compatibility with UV curing, transparency, and suitability for biocompatible applications. Adjusting the ratios of these monomers helps control resin viscosity and polymerization rate, impacting both print resolution and surface smoothness. For example, high-viscosity resins can provide finer details, which are essential for printing complex microfluidic channels and internal structures (13,89,90).

Photoinitiators and Their Role

Photoinitiators (PIs) play a crucial role in initiating polymerization upon exposure to specific wavelengths of light. Common UV cured resins employ photoinitiators like Irgacure 819 and phenylbis(2,4,6-trimethylbenzoyl) phosphine oxide (TPO) for their efficiency in curing and high conversion rates. However, traditional UV based photoinitiators may limit the thickness of each layer due to shallow penetration depth, which can increase print time for larger or more complex geometries.

Advances in photoinitiator technology have led to the development of photoinitiators that absorb longer wavelengths of light (often referred to as red-shifted photoinitiators), which are sensitive to visible light rather than UV. This adaptation helps reduce energy demands and minimizes potential damage to sensitive components, which is particularly useful in applications that involve live cells. A common example is isopropyl thioxanthone (ITX), which allows for efficient curing with visible light, resulting in better penetration and smoother layer bonding without the drawbacks of high UV exposure(13,91)

Optical Absorbers for Enhanced Precision

Optical absorbers are critical for controlling light penetration depth within the resin, which helps achieve high Z-axis resolution and prevents unintended curing in areas beyond the target layer. By reducing UV over curing in confined spaces like closed microchannels, absorbers help avoid blockages and ensure the precision of layer thickness. Compounds such as Sudan I dye and other light-absorbing additives can be incorporated into resins to limit light scattering, enhancing the layer-by-layer control that is essential for fabricating complex microfluidic channel networks.

Custom resin formulations provide significant advantages in 3D printing for microfluidics by enabling precise control over mechanical, optical, and chemical characteristics tailored to specific device requirements. By adjusting the proportions of polymers, photoinitiators, and optical absorbers, researchers can optimize resin performance for enhanced resolution, stability, and functional suitability in complex microfluidic applications(84,92).

1.4.3 Advanced Commercial Resins for DLP-SLA 3D Printing for Microfluidics

Commercial resins provide a reliable and accessible alternative for DLP-SLA printing, offering formulations with predefined proportions of polymer, photoinitiator, and optical absorber that are already tested and functional. Suddenly, the use of standardized commercial resins enhances

comparability across studies, as researchers working on similar applications can achieve more comparable results when using similar resins. Nowadays, the advances in using commercial photocurable resins in dental applications facilitate their use for other 3D printing applications. These resins are increasingly gaining prominence in the dental sector, as they have become widely used in recent years for applications such as dental prosthetics, aligners, and surgical guides.

These resins can be transparent and biocompatible, making them suitable for a wide range of applications in microfluidics. Transparency enables real time observation of fluid dynamics within microchannels, a critical feature for applications such as optical assays, cell culture, or biomarker detection. Biocompatibility ensures that the material does not adversely affect live cells or biological samples, expanding the utility of commercial resins to areas like drug discovery, tissue engineering, and organ-on-a-chip systems.

While commercial resins offer convenience and reliability, they also come with limitations. Their proprietary formulations do not allow for adjustments to the concentrations of components such as the optical absorber or photoinitiator. For example, if a specific print requires higher light absorption to prevent over curing in internal channels, this cannot be achieved by modifying a commercial resin. This lack of flexibility can pose challenges for highly specialized applications or novel device designs.

In summary, commercial resins simplify the initial stages of DLP-SLA printing by eliminating the need to develop and test custom formulations. Their proven compositions provide a reliable starting point for many applications. However, their fixed ratios can be a limitation, as they don't allow for adjustments, such as increasing the concentration of optical absorbers for specific designs. This highlights the balance between the convenience of starting with tested materials and the flexibility required for more specialized designs in microfluidic applications (27,93,94).

1.4.4 Light Dose absorption for a resin – Mathematical model optical analysis

As illustrated in Figure 11, the image shows the distribution of light intensity within the resin as a function of its position along the Z-axis. The amount of light received at each point determines whether the resin at that location will polymerize, based on whether it accumulates enough energy to trigger the polymerization process. The characteristic penetration depth, denoted as h_a, represents the maximum distance into the resin where sufficient energy is delivered for polymerization to occur. This is governed by the resin's absorption coefficient, α, and follows the principles of Beer's law, with the light intensity decreasing exponentially with depth.

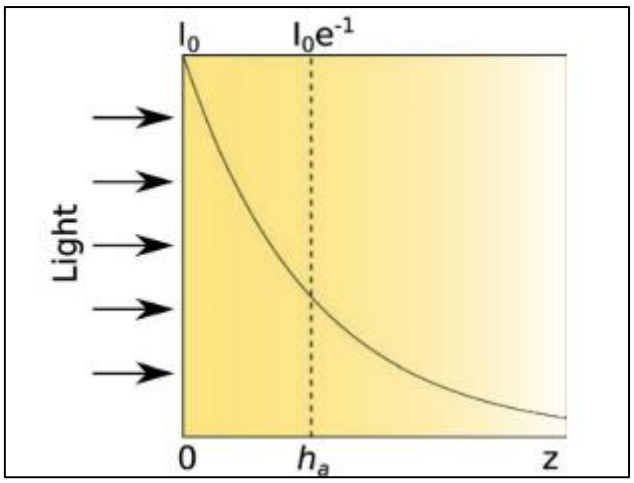


Figure 11: Schematic representation of Beer's law showing light attenuation through a material and the definition of the penetration depth ha. From (80)

In a photopolymerization process, the amount of light a resin receives at a specific depth z and exposure time t is referred to as the dose, D(z,t), and is expressed in units of J/cm^{-2}. This dose depends on the optical irradiance I(z) (the amount of light reaching a position z) and the exposure time t. It can be calculated as:

Equation 1: Energy Dose.

$$D(z,t) = t * I(z) = t * I_0 * e^{-z/ha}$$

Where:

- I_0: The initial irradiance at the resin surface (at z=0).
- h_a=1/α: The characteristic penetration depth of the light, where α is the resin's absorption coefficient.

This equation describes how the light intensity decreases exponentially with depth zzz due to absorption within the resin, following Beer's Law. The resin will only polymerize if the dose received at a certain position z exceeds a critical dose Dc.

The critical dose Dc is the minimum energy threshold required for the resin to solidify or reach a sufficiently solid state. This value depends on the material properties and the optical source being used. The critical dose at a given depth zp is calculated as:

Equation 2:Critical Energy Dose.

$$Dc = t_p * I_0 * e^{-zp/ha}$$

Where:

- tp: The exposure time required to reach the critical dose at depth zp.
- zp: The depth where the critical dose is achieved.

The relationship between tp and zp is significant because it defines a family of paired values: knowing the exposure time allows you to calculate the polymerization depth and vice versa. By increasing tp, the polymerization depth zp can be extended. However, this also introduces the risk of over curing, where unwanted regions polymerize due to excessive light penetration.

The critical time Tc represents the minimum time required to achieve the critical dose Dc at the resin surface (z=0). It is expressed as:

Equation 3: Critical Time.

$$Tc = \frac{Dc}{I_0}$$

In conclusion, the critical time Tc serves as a fundamental parameter for controlling the photopolymerization process in DLP-SLA printing. By defining the minimum exposure time required to achieve solidification at the resin surface, Tc ensures precise control over layer curing while minimizing over curing.

Figure 12 illustrates the layer-by-layer fabrication process of a 3D printed microfluidic device with a closed channel. In this process, the part is printed upside down, with light selectively curing each layer of resin as it passes through a transparent window in the resin tray. The final completed part is then flipped right side up, as shown in panel D.

In Figure 12A, the process begins with the printing of the base layer, where the entire region is exposed to light, solidifying the resin to form a solid foundation for the device. This step ensures structural stability for the subsequent layers.

In Figure 12B, layer 5 introduces the unexposed region that will form the flow channel. At this stage, the designed gap is left unexposed, keeping the resin in a liquid state within this region. This unexposed space will eventually serve as the internal microfluidic closed channel.

In Figure 12C, layer 7 is printed to close the channel. Here, light is projected across the entire layer, including the area directly above the unexposed channel. This creates the top boundary of the channel but simultaneously traps the liquid resin inside, risking over curing.

Finally, in Figure 12D, the part is flipped into its final orientation, revealing the designed closed channel within the printed device.

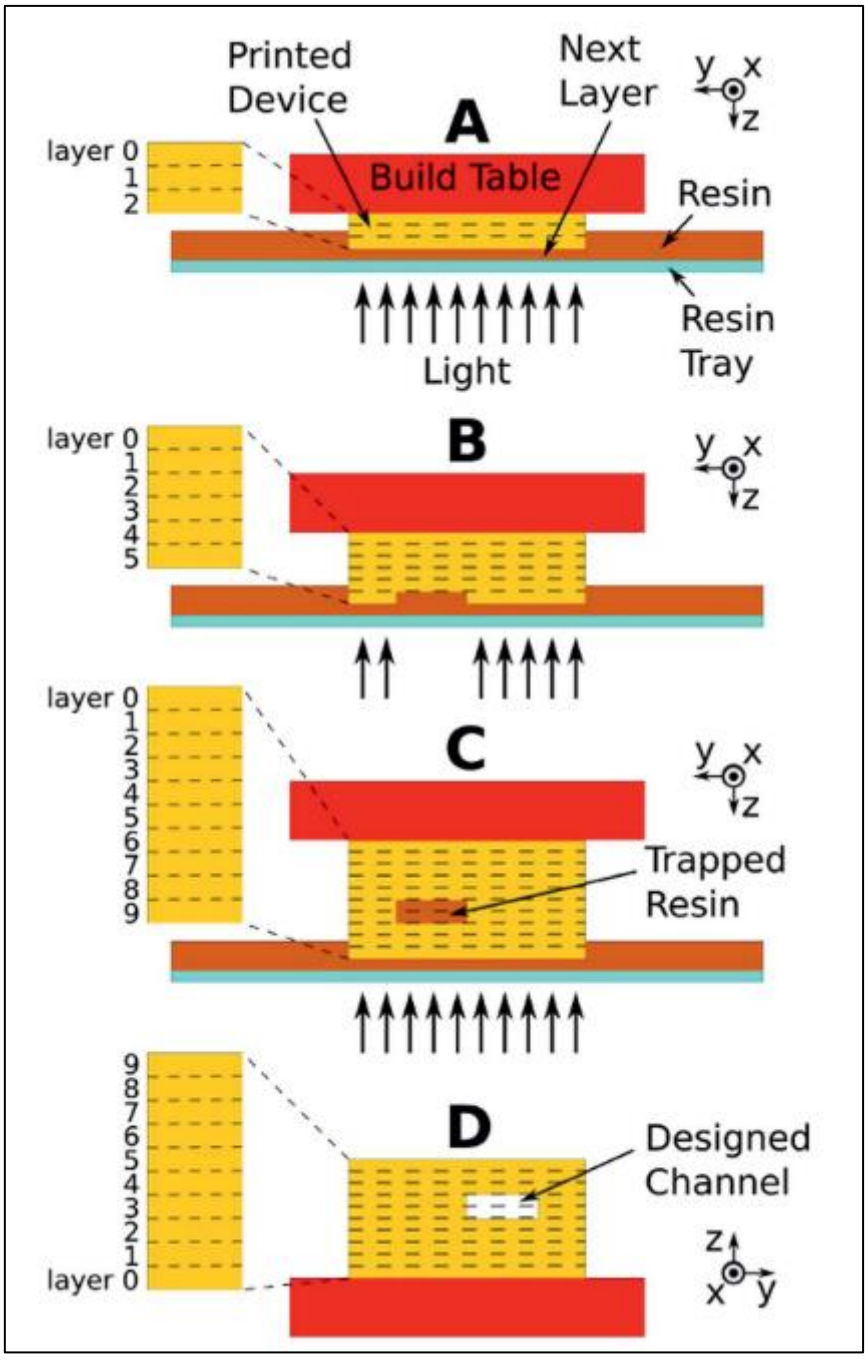


Figure 12: Step-by-step illustration of the layer-by-layer fabrication process for creating a simplified 3D-printed channel, showing the formation and trapping of resin in the channel region. From (80)

A key challenge in this process is the risk of trapped resin solidification. The trapped liquid resin can receive additional light exposure during the curing of subsequent layers, which can cause unwanted polymerization. Figure 8a shows the normalized energy dose delivered during a standard layer-by-layer printing process, where each layer receives a predictable and controlled dose of light. In contrast, Figure 8b illustrates the scenario when printing closed channels. In this case, layers 5 and 6 represent

the unexposed region intended for the flow channel. However, the trapped resin inside this channel still receives residual light exposure as subsequent layers are cured. If the cumulative light dose exceeds the critical dose Dc, the resin inside the channel may partially solidify, leading to blockages that compromise its functionality.

To avoid this issue, the channel height must be carefully designed to ensure that the total light dose absorbed by the trapped resin remains below the polymerization threshold. This constraint establishes an optical limit on the minimum channel height that can be fabricated successfully, as smaller channel heights are more prone to premature curing due to cumulative light exposure.

Figure 13 illustrates the normalized light dose distribution during layer-by-layer fabrication. Panel (a) shows the dose variation as a function of depth for five layers, where each layer receives a single exposure. Panel (b) highlights the total dose distribution for a 12-layer case, including unexposed layers 5 and 6, which form a flow channel.

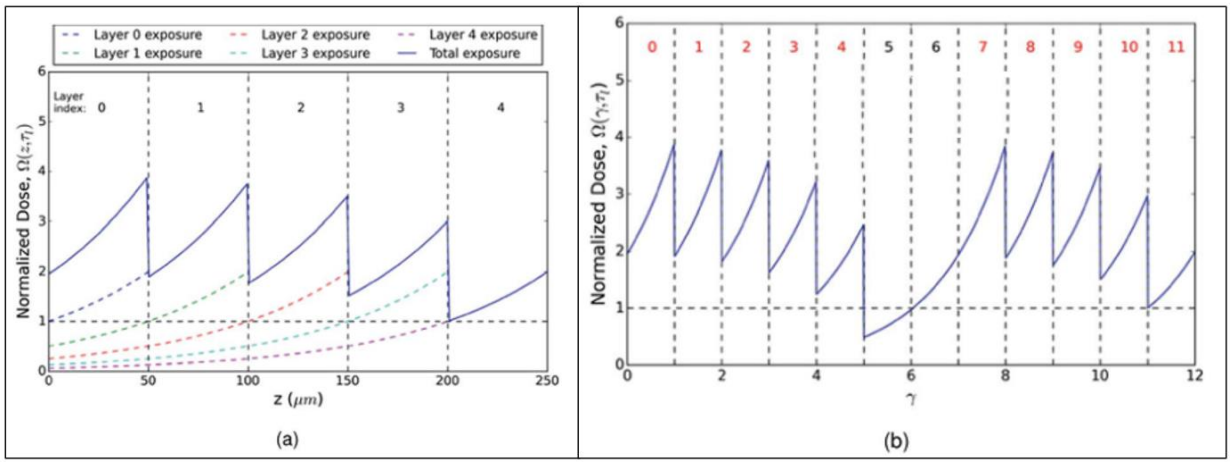


Figure 13: (a) Normalized dose as a function of depth z for five 3D printed layers, where each layer receives a single exposure. The solid line shows the total dose. (b) Normalized dose, for a 12-layer case with a closed channel formed in layers 5 and 6. Red and black layer numbers indicate exposure or no exposure, respectively. From (80)

1.4.5 3D Printing Molds for PDMS Replica

Fabricating microfluidic devices using 3D-printed molds has emerged as a versatile and accessible method for creating PDMS-based systems, leveraging the design flexibility of 3D printing to produce high-quality, functional devices. This approach involves printing a mold with intricate microchannel designs, which serves as a template for casting PDMS. Once cured, the PDMS replica is bonded to a glass substrate, forming the completed device with enclosed microchannels.

One of the key advantages of this method is the ability to inspect and clean the PDMS replica thoroughly before bonding. This additional quality control step minimizes the risk of obstructions in fluid flow, ensuring precise channel geometries critical for applications such as diagnostics, particle separation, and fluid mixing. The capability to inspect channels prior to final assembly also reduces the likelihood of manufacturing defects, a common challenge in enclosed channel fabrication.

The 3D-printed mold approach provides a practical solution to circumvent the technical challenges associated with directly printing enclosed microchannels. By casting open PDMS channels and sealing them through bonding to a cover layer—typically glass—this method simplifies fabrication while maintaining the desired channel integrity. PDMS offers additional advantages, including transparency for optical applications, biocompatibility for biological studies, and gas permeability, which is critical in applications such as cell culture and organ-on-a-chip devices.

Furthermore, the flexibility of 3D printing allows for the rapid prototyping of molds with complex channel geometries, enabling designs that would be challenging to achieve with traditional lithographic techniques. This includes features such as serpentine channels, sharp turns, and high-aspect-ratio structures, which are essential for advanced microfluidic applications. This adaptability makes the mold-based approach particularly attractive for research and development settings where iterative design and testing are required.

An alternative to this approach involves directly printing open channels using a negative extrusion method, bypassing the need for a mold entirely. However, this method is less commonly employed due to the challenges associated with aligning and bonding a top layer to achieve a functional device. Misalignments during the sealing process can compromise device integrity, making the PDMS replication method a more reliable choice for precise microfluidic applications.

Despite its advantages, the mold approach is not without limitations. The additional steps involved in casting and bonding increase fabrication time and introduce variability that could impact device performance. Imperfections in the bonding process, such as misalignment or incomplete sealing, may

compromise the device's structural integrity and fluidic performance. Addressing these challenges requires careful optimization of both the molding and bonding processes to ensure consistent results.

In summary, the use of 3D-printed molds for PDMS replication combines the design versatility of 3D printing with the material benefits of PDMS, providing a reliable and adaptable method for microfluidic device fabrication. While this approach offers significant advantages for creating intricate channel geometries and ensuring quality control, it also highlights the need for meticulous process optimization to overcome its inherent challenges. These advancements make mold-based fabrication a cornerstone in the development of next-generation microfluidic systems (95,96).

Challenges: The additional molding and bonding steps can introduce variability in device performance and increase total fabrication time. Misalignment or imperfect bonding between the PDMS replica and the glass substrate may lead to incomplete sealing, potentially compromising the device's structural integrity and resulting in leakage problems. These challenges underscore the need for precise alignment techniques and process optimization to ensure reliable and reproducible device fabrication.

1.4.6 3D Printing Closed Channels

Printing closed microchannels is one of the most advanced and ambitious approaches in microfluidic device fabrication, enabling the creation of fully enclosed fluidic pathways in a single 3D printing process. This method eliminates the need for bonding separate layers, significantly enhancing the structural integrity of the device. Closed channels are particularly advantageous for applications requiring sealed environments, where the risk of leaks or delamination at bonded interfaces could compromise functionality.

Despite its potential, the fabrication of closed microchannels poses significant technical challenges, primarily due to issues associated with over curing during the photopolymerization process. In SLA and DLP 3D printing, UV light is used to cure successive layers of resin, including the top cover layer that seals the channel. However, light penetration into the uncured resin within the channel can result in unwanted partial curing, leading to the formation of blockages or alterations in channel geometry. These effects disrupt fluid flow and compromise the precision required for microfluidic applications.

As illustrated in Figure 14, the UV light used for curing penetrates multiple layers, including the channel region intended to remain open. This penetration often causes partial polymerization of the resin inside the channel, as represented by the red zone in the figure. Such over curing creates blockages or narrows the channel dimensions, significantly impairing the flow characteristics critical for microfluidic

applications. This schematic emphasizes the complexity of managing light exposure to avoid these issues while ensuring the proper curing of surrounding layers.

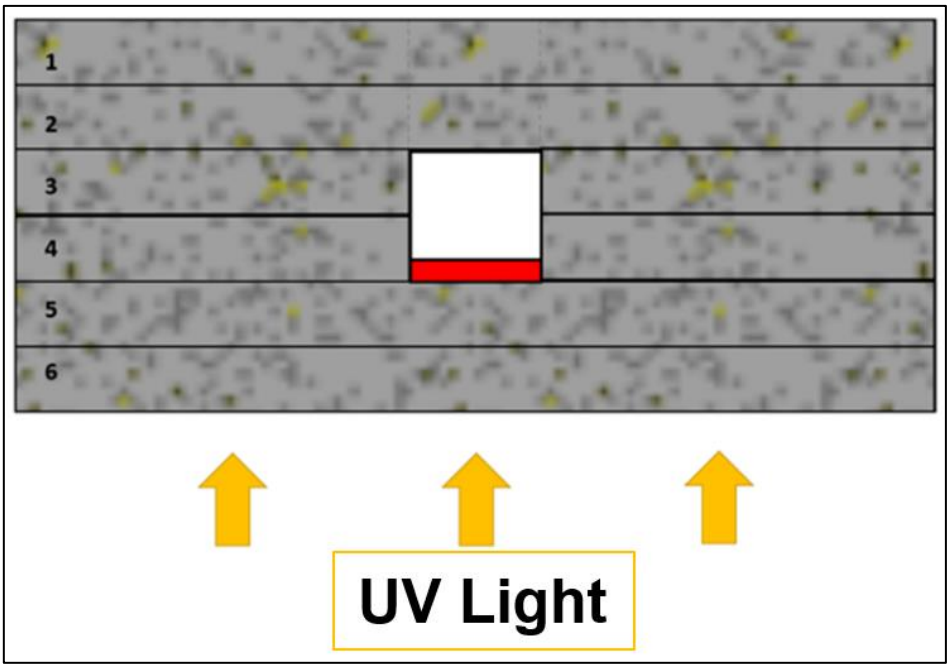


Figure 14: Cross-sectional view of layer-by-layer UV light exposure, showing a closed channel created by leaving specific layers (3 and 4) unexposed.

To address the issue of over curing, several strategies have been proposed, but each comes with its limitations. One approach involves optimizing the exposure time and light intensity during the printing process to minimize UV light penetration into the channel while ensuring the surrounding material cures adequately. Achieving this delicate balance is challenging, as insufficient curing could compromise the structural integrity of the outer layers, while excessive exposure could irreversibly block the channels.

Another strategy is to design channels with slightly larger cross-sectional dimensions than the intended size, accounting for potential resin polymerization within the channel. By predicting the degree of light penetration and over curing, the final printed channel dimensions can more closely match the theoretical design. While this approach improves dimensional accuracy, it requires precise modeling and iterative optimization for each device design, adding complexity to the fabrication process.

These challenges underscore the importance of advancing techniques for closed channel fabrication. While current methods have demonstrated promising results, they often require careful optimization, which can be time consuming and particular for each device. Overcoming these barriers is critical for unlocking the full potential of closed channel microfluidic devices, as they offer unparalleled design flexibility and functionality compared to traditional fabrication methods. This thesis aims to address

these challenges by exploring innovative approaches to optimize the curing process and improve the overall reliability and reproducibility of closed channel microfluidic devices.

In conclusion, while printing closed microchannels presents significant opportunities for advancing microfluidics, it remains a technically demanding process due to the inherent challenges of controlling photopolymerization. Further research into material properties, light management, and post processing techniques is essential to fully realize the potential of this fabrication method.

Challenges:

The fabrication of closed microchannels faces significant challenges, particularly due to over curing caused by UV light penetrating into the channels. Controlling this effect requires precise optimization of exposure settings, which can vary for each device design, making the process complex and time-consuming. Addressing these issues is essential to improve the reliability and reproducibility of closed channel microfluidic devices, and this thesis focuses on developing solutions to overcome these barriers.

1.4.7 Potential of DLP-SLA in Achieving Unique Geometries

The ability to fabricate unique and complex geometries is a critical frontier in microfluidic device development, and DLP-SLA presents an exciting avenue to overcome the limitations of traditional fabrication methods. While traditional techniques like soft lithography and injection molding have been foundational in microfluidics, their inherent constraints often make it challenging to achieve the intricate designs necessary for advanced fluid control and particle manipulation. DLP-SLA, with its potential for high resolution layer-by-layer fabrication, can overcome these challenges. However, achieving these geometries reliably and reproducibly remains a significant technical and scientific impediment, accentuating the importance of further research and innovation.

One of the most promising capabilities of DLP-SLA lies in its potential to create inclined microchannels. These designs, where either the cross-sectional height of the channel gradually changes or the channel itself rises along its path, offer transformative possibilities for microfluidic systems. Gradually sloped channels could enable the generation of controlled flow gradients, directing particle movement and establishing zones with varying shear stress. These features are essential for applications such as particle sorting, chemical gradient formation, and cell studies that require precise environmental control. However, ensuring the dimensional fidelity of such sloped geometries across the length of the

channel is a challenge that requires optimization of printing parameters, resin formulations, and post-processing techniques.

Another frontier in DLP-SLA based microfluidics is the fabrication of microchannels with complex wall profiles, such as curved, triangular, or rounded shapes. These profiles have the potential to reduce flow resistance, minimize stagnant zones, and improve particle transport efficiency. For example, curved walls could streamline fluid flow around bends, enhancing performance in mixing or reaction chambers. Despite these advantages, achieving these non-standard wall profiles with the precision needed for the performance of microfluidic devices remains a challenge. The development of reliable modeling tools and validation techniques is essential to bridge the gap between design and functional performance.

Internal structures within microchannels, such as posts, barriers, or patterned elements, represent another area where DLP-SLA could revolutionize microfluidic design. These features can introduce secondary flows or chaotic advection, dramatically improving mixing efficiency and enabling more sophisticated fluid handling. Traditional methods struggle to incorporate such intricate internal structures without additional fabrication steps, often limiting the integration of advanced functionalities into microfluidic devices. DLP-SLA, however, offers the potential to directly print these features as part of the initial fabrication process, significantly reducing complexity and assembly time. Yet, challenges such as ensuring structural stability, avoiding defects, and maintaining resolution at smaller scales must be addressed to fully harness this capability.

High-aspect-ratio channels, characterized by significantly greater height-to-width ratios, are another example of the unique geometries that DLP-SLA could potentially enable. Such channels are critical for certain microfluidic applications, such as creating stacked or multilayer devices that combine multiple functions in a compact footprint. However, maintaining the mechanical integrity of these channels, particularly during post-processing steps like cleaning or curing, remains a significant obstacle. Research into material properties, support structures, and post-processing protocols is crucial to overcome these limitations (97–99).

In summary, while DLP-SLA holds immense promise for advancing microfluidic device fabrication, achieving its full potential requires addressing significant challenges. The ability to fabricate inclined channels, complex wall profiles, internal structures, and high-aspect-ratio channels could enable groundbreaking applications in diagnostics, particle manipulation, and fluid mixing. However, achieving these geometries reliably and at scale demands further investigation into printer capabilities, resin chemistries, and process optimization. By focusing on these challenges, this work aims to contribute to the development of next-generation microfluidic devices that leverage the unique

advantages of DLP-SLA, pushing the boundaries of what is possible in bioengineering and beyond (100,101).

1.5. Theory of Laminar Flow in Microchannels

Microfluidics deals with the behavior, precise control, and manipulation of fluids confined to submillimeter channels. A fundamental concept in microfluidics is understanding the nature of fluid flow within these microchannels, particularly the distinction between laminar flow and turbulent flow, as well as the challenges associated with mixing in such confined environments (102).

1.5.1 Laminar Flow vs. Turbulent Flow

The behavior of fluid flow within a channel is characterized by the Reynolds number (Re), a dimensionless quantity that determines whether the flow is laminar or turbulent. The Reynolds number is defined as:

Equation 4: Reynolds Number.

$$Re = \frac{\rho U Dh}{\mu}$$

Where:

- ρ is the fluid density (kg/m³),
- U is the average fluid velocity (m/s),
- Dh is the hydraulic diameter of the channel (m),
- μ is the dynamic viscosity of the fluid (Pa·s).

In microchannels, the Reynolds number is typically very low (Re < 2000), which indicates laminar flow. In laminar flow, the fluid moves in parallel layers, with little to no mixing between them. The layers closest to the walls of the channel move more slowly due to friction (also called no-slip condition), while the fluid at the center of the channel moves more quickly. This results in a parabolic velocity profile across the channel.

For microfluidic systems, laminar flow is the dominant regime due to the small size of the channels and the relatively low velocities involved. This means that turbulent flow, which occurs at higher Reynolds numbers (Re > 4000) and is characterized by chaotic and irregular fluid motion, is rarely observed in microfluidics(103–105).

Flow Behavior in Microchannels:

- **Laminar Flow**: In laminar flow, the velocity at any given point remains constant over time, and there is minimal mixing between adjacent layers of fluid. This is beneficial for applications where precise control over the movement of fluid is required, such as in drug delivery or chemical analysis. However, it poses significant challenges for mixing, since the lack of turbulence prevents efficient interaction between different fluid streams.
- **Turbulent Flow**: In contrast, turbulent flow is characterized by irregular fluctuations and mixing. While turbulent flow enhances mixing and is often desirable in macroscopic systems, it is difficult to achieve in microchannels due to the low Reynolds numbers. Additionally, inducing turbulence in microfluidic systems often requires external forces or complex geometries, which can complicate the device design.

1.5.2 Mixing in Laminar Flow

One of the primary challenges in microfluidic systems is achieving efficient mixing. In a laminar flow regime, mixing between two or more fluids occurs predominantly through molecular diffusion, which is governed by Fick's Law of Diffusion:

Equation 5: Fick's First Law of Diffusion.

$$J = -D\frac{dC}{dx}$$

Where:

- J is the diffusion flux (mol/m²·s),
- D is the diffusion coefficient (m²/s),
- dC/dx is the concentration gradient (mol/m³).

Molecular diffusion is a slow process, especially for larger molecules or high-viscosity fluids, as the diffusion coefficient DDD decreases with increasing molecular size and viscosity. This makes it particularly difficult to achieve rapid mixing in laminar flow conditions. In microchannels, where the length scales are small, the lack of turbulence means that diffusion is the primary mechanism for mixing, which can be prohibitively slow for many applications that require fast, efficient mixing(106,107).

1.5.3 Inertial Forces in Microfluidic Devices

Inertial microfluidic devices operate within an intermediate Reynolds number range (typically between 1 and 100), where both inertial and viscous effects influence particle behavior, facilitating size-based particle separation without the need for labeling. In these devices, particles experience distinct forces, primarily the wall-effect lift force, which pushes particles away from channel walls, and the shear-gradient lift force, which directs particles toward the walls. These forces balance under specific conditions, allowing particles to achieve size-dependent equilibrium positions(34,108–110).

For a particle to reach inertial focusing, its diameter $a_p$relative to the channel hydraulic diameter D_h must satisfy ${}^{a_p}/_{D_h}$>0.07(Development of microflu…). This balance of forces can be represented using Reynolds numbers, specifically the channel Reynolds number (Re), already described in equation 4, and the particle Reynolds number (Re_p), calculated as follows:

Equation 6: Particle Reynolds Number (3)

$$Re_p = \frac{Reap2}{{D_h}^2} = \frac{\rho f U m {a_p}^2}{\mu D_h}$$

where ρf and μ are the fluid density and dynamic viscosity, Um is the maximum fluid velocity in the channel, and a_p and $D_h$represent the particle and hydraulic diameters, respectively.

In curved microchannels, an additional Dean flow is generated due to centrifugal forces, producing counter-rotating vortices across the channel's cross-section. This flow can be quantified using the Dean number (De), given by:

Equation 7: Dean Number.

$$De = Re\sqrt{\frac{D_h}{2r}}$$

where r is the radius of channel curvature. For Dean numbers below 50, two recirculating vortices are present, which influence particle positions across the channel. Larger particles are subject to stronger lift forces, pushing them toward the equilibrium zones within the channel, while smaller particles tend to follow the Dean flow vortices(111).

In spiral channels, this balance between lift and drag forces determines the equilibrium positions, with drag force (F_D) in the Stokes regime defined by:

Equation 8: Drag Force.

$$FD = 3\pi\mu a_p(u - u_p)$$

where u and up represent the fluid and particle velocities. The lift force (FL) can be calculated as:

Equation 9: Lift Force.

$$FL = fL(Re_{xp})\frac{\rho {U_F}^2 {a_p}^4}{{D_h}^2}$$

where fL is the lift coefficient, which depends on both Re and the particle's lateral position within the channel, xp. This force $\left(\frac{FL}{FD} \propto {a_p}^3\right)$ reveals that larger particles are more easily focused than smaller ones. Consequently, particles reach different equilibrium positions based on their diameter, enabling efficient, label-free size-based separation(110).

Computational modeling of these forces aids in optimizing channel design and operational parameters, improving particle separation by simulating different geometries and flow rates prior to fabrication.

1.6 Computational Fluid Dynamics (CFD) Simulations

In the field of microfluidics, Computational Fluid Dynamics (CFD) simulations are essential for understanding and predicting fluid behavior within microchannels. These simulations allow researchers to model complex fluid dynamics and optimize device designs before fabricating prototypes. One of the most widely used software tools for CFD in microfluidics is COMSOL Multiphysics, a versatile simulation platform that enables the modeling of fluid flow, heat transfer, and chemical reactions within microfluidic systems.

CFD simulations are critical in microfluidics because they help researchers identify potential issues with fluid flow, mixing, and particle separation, and optimize designs for maximum performance. The small scales involved in microfluidics mean that traditional methods of trial and error can be time-consuming and expensive, making CFD an invaluable tool for prototyping and testing new devices(112,113).

1.6.1 Using COMSOL Multiphysics to Simulate Microfluidic Flows

COMSOL Multiphysics is a powerful simulation tool that provides modules specifically designed for simulating fluid flow, such as the Laminar Flow module and the Transport of Diluted Species module. These modules allow for detailed modeling of fluid dynamics within microfluidic devices, enabling researchers to replicate experimental conditions, predict the behavior of fluids, and optimize device designs(114–116).

Laminar Flow Module

In microfluidic systems, where laminar flow is the dominant regime due to the low Reynolds numbers (Re < 2000), the Laminar Flow Module in COMSOL is frequently used to simulate the flow of incompressible fluids through channels. The behavior of fluids in laminar flow is governed by the Navier-Stokes equations, which describe the conservation of momentum, and the continuity equation, which ensures the conservation of mass. These are the fundamental equations used in COMSOL to simulate fluid dynamics:

- **Navier-Stokes Equation** for incompressible flow:

Equation 10: Navier-Stokes .

$$\rho(\frac{\partial u}{\partial t} + u \cdot \nabla u) = -\nabla p + \mu \nabla^2 u + F$$

Where:

- ρ is the fluid density,
- u is the velocity field,
- p is the pressure field,
- μ is the dynamic viscosity,
- F represents external forces, such as gravity.

- **Continuity Equation** (for conservation of mass):

Equation 11: Continuity Equation for Incompressible Fluids.

$$\nabla \cdot u = 0$$

These equations are solved numerically in COMSOL to predict how the fluid moves through the microchannels, allowing for the study of velocity profiles, pressure drops, and flow patterns. Given the small scales of microfluidic devices, these simulations are particularly useful for identifying potential areas where flow stagnation or high shear forces might occur, which can affect the performance of the device.

Transport of Diluted Species Module

In addition to modeling fluid flow, COMSOL's Transport of Diluted Species module is used to simulate the transport of solutes, particles, or other species within the flowing fluid. This module incorporates Fick's laws of diffusion and advection-diffusion equations to model how molecules or particles are

transported through the fluid. This is particularly important in microfluidics, where diffusion can play a significant role in mixing and reaction kinetics.

The advection-diffusion equation used in this module is:

Equation 12: Convection-Diffusion.

$$\frac{\partial C}{\partial t} + u \cdot \nabla C = D\nabla^2 C + R$$

Where:

- C is the concentration of the species,
- u is the velocity field of the fluid,
- D is the diffusion coefficient,
- R represents reaction terms if there are chemical reactions occurring.

By solving this equation, COMSOL can predict how species are transported through the fluid, where they will concentrate, and how fast they will diffuse. This is crucial for applications like drug delivery, diagnostics, or chemical reactions, where the concentration of substances within the fluid must be tightly controlled.

1.6.2 Impact of Viscosity on Mixing and Flow Dynamics

Viscosity plays a critical role in determining how fluids behave within microchannels, especially in microfluidic devices where different fluids often need to be mixed or separated. In COMSOL, the viscosity of the fluid is a key parameter that affects both the velocity profile and the mixing efficiency of the system.

For example, fluids with higher viscosity, such as dextran, exhibit a more pronounced parabolic velocity profile due to greater resistance to flow. This means that fluids with higher viscosity flow more slowly, which can impede mixing and reduce the formation of vortices that aid in chaotic advection. In contrast, fluids with lower viscosity, such as water, flow more freely and are more likely to form secondary flows that enhance mixing(107).

In microfluidic devices designed for mixing, such as those incorporating herringbone structures or serpentine channels, the viscosity of the fluid plays a crucial role in the formation of Dean vortices and secondary flows. These structures are intended to enhance mixing by generating complex flow patterns that disrupt the typical laminar flow within the channel. Low-viscosity fluids, such as water,

are more effective at generating vortices in curved or patterned channels, thus promoting mixing through secondary flows. In contrast, high-viscosity fluids, such as dextran solutions, tend to flow more smoothly, with fewer vortices forming, which can limit the mixing efficiency. For high-viscosity fluids, optimizing the channel geometry or increasing the flow rate may be necessary to promote effective mixing and compensate for the reduced secondary flow formation. COMSOL simulations allow researchers to explore how different fluids (e.g., water and dextran) behave in the same device. By adjusting the viscosity parameter, it is possible to model the flow profiles and predict how well the fluids will mix under different conditions. This enables researchers to fine-tune their designs for specific applications where the fluid properties may vary(117).

1.6.3 Optimizing Microfluidic Device Design with CFD Simulations

The use of CFD simulations, such as those provided by COMSOL Multiphysics, is invaluable for the optimization of microfluidic device designs. These simulations allow for the exploration of different design parameters, such as channel width, length, aspect ratio, and geometry, to determine the best configuration for achieving the desired fluid behavior(114,116).

Some key areas where CFD simulations help optimize device design include:

- **Minimizing pressure drop**: COMSOL simulations can predict how the geometry of the microchannels affects the pressure required to drive fluid through the device. This is crucial for ensuring that the device operates efficiently without requiring excessive power.
- **Maximizing mixing efficiency**: By simulating different channel geometries (e.g., herringbone, zigzag, serpentine), researchers can identify the designs that promote the most efficient mixing under laminar flow conditions.
- **Controlling fluid residence time**: In devices designed for chemical reactions or cell cultures, controlling how long the fluid remains in certain regions is important. COMSOL simulations can help optimize flow rates and channel dimensions to achieve the desired residence time.

In conclusion, COMSOL Multiphysics provides a comprehensive platform for simulating fluid dynamics in microfluidic devices, allowing researchers to model real-world experimental conditions, optimize designs, and predict fluid behavior with high accuracy. By incorporating parameters such as viscosity, channel geometry, and flow rate, COMSOL simulations can be used to design more efficient and functional microfluidic systems for a wide range of applications, from diagnostics to chemical analysis and biological research.

1.7 Methods to Improve Mixing in Microchannels

An ongoing challenge in microfluidics is achieving efficient mixing at the microscale. With typical flows in microfluidic channels characterized by low Reynolds numbers, mixing relies predominantly on molecular diffusion, a process that is often too slow and inefficient for many applications. Various strategies, such as passive mixing structures like herringbone mixers, have been introduced to induce chaotic advection and enhance mixing. However, optimizing these structures for reliable performance across various fluid types and flow rates remains challenging, particularly in applications that demand rapid and homogeneous mixing (118,119).

To overcome the limitations of laminar flow and enhance mixing in microchannels, researchers have developed various strategies that introduce secondary flows or induce chaotic advection to improve fluid mixing. These methods fall into two broad categories: passive mixers and active mixers(102,106,107,120–122).

1.7.1 Passive Mixing Techniques

Passive mixers rely on the geometry of the microchannels to generate secondary flows that enhance mixing without the need for external forces or energy input.

One of the most common passive mixing strategies is the use of herringbone mixers, which consist of grooves patterned along the bottom or walls of the microchannel. These grooves create chaotic advection, disrupting the laminar flow and promoting mixing between fluid layers. The herringbone structure generates secondary flows that push and rearrange the fluid layers, significantly enhancing mixing efficiency.

Another passive mixing method involves zigzag or serpentine channels, where the curved path of the channel induces secondary Dean flows. These flows occur due to centrifugal forces acting on the fluid as it moves through the curved sections of the channel, promoting mixing between the fluid layers(120,123–125).

Advantages of passive mixers:

- **No external energy required**: Passive mixers rely entirely on the channel geometry, making them energy-efficient and easy to integrate into microfluidic systems.
- **Scalability**: Passive mixers can be easily scaled down to microfluidic dimensions, allowing for efficient mixing in very small volumes of fluid.

Challenges:

- The effectiveness of passive mixers depends on the specific design of the channel, and optimizing these designs can be challenging.
- Mixing efficiency is still relatively slow compared to turbulent mixing in larger systems, so passive mixers are not always suitable for applications requiring rapid mixing.

1.7.2 Active Mixing Techniques

Active mixers, in contrast, use external forces such as electric fields, magnetic fields, or acoustic waves to enhance fluid mixing. These methods are often more complex than passive mixing but can achieve faster and more efficient mixing, especially in systems where molecular diffusion is too slow(126,127).

The main examples of active mixing techniques in microchannels are: Electrokinetic mixing applies an electric field to induce electroosmotic or electrophoretic flows, disrupting the laminar flow and promoting mixing. Magnetic mixing utilizes magnetic particles or ferrofluids in combination with an external magnetic field to create chaotic fluid motion, further enhancing the mixing process. Lastly, acoustic mixing employs ultrasonic waves to generate vibrations or oscillations within the fluid, facilitating rapid mixing by promoting interaction between fluid layers. Each of these techniques provides unique advantages for achieving efficient mixing in microfluidic systems.

Advantages of active mixers:

- **High mixing efficiency**: Active mixers can achieve much faster and more complete mixing than passive mixers, making them suitable for applications requiring rapid response times.
- **Control**: The mixing process can be precisely controlled by adjusting the external force, providing greater flexibility in tuning the mixing parameters.

Challenges:

- Active mixers require additional components and energy input, which can increase the complexity and cost of the microfluidic system.
- The integration of active mixing components can make the device bulkier and more difficult to miniaturize.

1.7.3 Optimizing Microchannel Design for Efficient Mixing

Regardless of whether passive or active mixing is employed, channel geometry plays a crucial role in determining the efficiency of fluid mixing. Optimizing the design of microchannels can significantly enhance mixing performance, especially in systems operating under laminar flow conditions. Some key design considerations include(123,124,128):

- **Channel width and depth**: Narrower and shallower channels promote faster diffusion due to the shorter distance over which the molecules must travel. However, this also increases the pressure required to drive fluid through the channel.
- **Aspect ratio**: The aspect ratio (height-to-width ratio) of the channel can be adjusted to influence the velocity profile and mixing efficiency.
- **Incorporation of obstacles**: Placing obstacles or geometric perturbations (such as pillars or ridges) within the channel can enhance mixing by disrupting the laminar flow and creating localized turbulence.

In summary, the dominance of laminar flow in microchannels presents significant challenges for fluid mixing, as the lack of turbulence means that mixing occurs predominantly through slow molecular diffusion. However, using passive and active mixing techniques, as well as the optimization of channel geometries, it is possible to enhance mixing efficiency in microfluidic systems. Understanding and addressing the limitations of laminar flow is crucial for developing high-performance microfluidic devices for applications such as chemical analysis, drug delivery, and biological assays.

Chapter 2: Objectives

This doctoral thesis is part of the Nanobioengineering Research Group at IBEC, dedicated to the development of microfluidic devices through 3D printing. Building on the foundational information presented in the introduction, and in consideration of the limitations associated with traditional and emerging fabrication techniques, this thesis aims to address critical challenges and push the boundaries of microfluidic device design and implementation. The proposed objectives are tailored to overcome the current technical barriers highlighted in the earlier sections, with a focus on enhancing precision, functionality, and applicability in bioengineering contexts:

1. **Design, Development and Optimization of a Custom 3D Printer for Microfluidic Applications**
   The primary objective is to develop a custom 3D printer based on DLP-SLA technology, specifically adapted to work with commercially available resins. This involves modifying and optimizing the printer's hardware and software settings to achieve precise control over the curing process, layer thickness, and feature resolution. Achieving these optimizations is crucial for creating detailed and accurate microfluidic channels. The design and optimization process will also include customizing the light exposure settings and adjusting the mechanical setup to minimize light scattering and over curing, which can affect the quality and functionality of the final printed channels. By tailoring the printer in this way, the goal is to establish a reliable and reproducible method for fabricating intricate microfluidic devices with clear and well-defined channel geometries.

2. **Evaluation of Printing Resolution and Size Control for Microfluidic Channel Fabrication**
   Once the printer has been optimized, an important objective is to thoroughly evaluate its resolution capabilities in micro-scale printing, specifically for microfluidic applications. This evaluation will involve printing test structures to determine the smallest achievable feature sizes and the precision of channel walls, curves, and internal structures. A detailed characterization of the printed features, such as channel height, width, and smoothness, will be conducted using imaging techniques like microscopy. Understanding these resolution limits is essential to assess the printer's suitability for producing functional microfluidic devices. Additionally, the study will explore how different commercial resins impact printing accuracy and resolution, as the choice of resin can affect the mechanical and optical properties of the final structures. By defining these parameters, the goal is to establish reliable guidelines for using the custom DLP-SLA printer in microfluidic fabrication.

3. **Fabrication of Fully Enclosed Microfluidic Channels with Internal Structures**

An additional objective is to explore the capabilities of the custom 3D printer to fabricate fully enclosed microfluidic channels, both plain and those incorporating internal features such as herringbone structures or other flow-modifying geometries. Achieving this involves overcoming challenges associated with overcuring, resin drainage, and internal feature resolution, which are critical for ensuring functionality and reliability in closed-channel systems. This objective will include:

3.1 Closed Channel Fabrication: Developing printing protocols that enable the creation of enclosed microchannels with consistent dimensional accuracy and minimal defects. This requires optimizing parameters such as exposure time, resin viscosity, and drainage techniques to eliminate uncured resin within the channel during fabrication.

3.2 Integration of Internal Structures: Printing enclosed microfluidic channels that incorporate complex internal geometries, such as staggered herringbone grooves or spiral separators, which require precise alignment and feature resolution. The aim is to demonstrate the feasibility of integrating functional elements within enclosed channels while maintaining structural integrity.

4 Application of the Optimized Printer in the Fabrication of Functional Microfluidic Devices

This objective involves leveraging the custom 3D printer to create two specific microfluidic applications, each with unique design and functional requirements:

4.1 Spiral Chip for Particle Separation Using Inertial Forces: Design, print, and test a spiral microfluidic chip intended for particle separation applications. This chip will build upon existing spiral channel designs, expanding their capabilities to accommodate larger channel dimensions, which will allow for increased flow capacity and the processing of higher sample volumes. By enabling the fabrication of larger channels, the objective is to enhance the chip's versatility and throughput for applications requiring higher flow rates while maintaining precise particle separation.

Additionally, this objective aims to develop interconnected spiral configurations, allowing for sequential separation processes within a single device. By combining multiple spiral channels in a chain-like arrangement, the design seeks to improve separation efficiency and target a broader range of particle sizes. Through careful

optimization of the device's geometry, flow parameters, and layout, the goal is to achieve effective particle separation across diverse operating conditions.

This application will also demonstrate the custom printer's ability to produce intricate microfluidic devices with controlled flow characteristics and functional reliability, showcasing its potential for advanced particle separation applications.

4.2 Herringbone Mixer Chip for Fluid Mixing under Laminar Flow: Develop a microfluidic device incorporating herringbone structures within the channel to facilitate efficient fluid mixing. The herringbone mixer is designed to disrupt laminar flow by inducing chaotic advection, which is crucial for applications requiring rapid and homogeneous mixing of two fluids. This objective includes optimizing the placement and dimensions of the herringbone patterns to maximize mixing efficiency, providing a proof-of-concept for the device's effectiveness in enhancing fluid interaction.

Building on existing designs, this work aims to fabricate herringbone mixers with larger channel dimensions than those typically reported in the literature. By increasing the channel size, the device will enable mixing at higher flow rates, expanding its applicability to scenarios where greater throughput is needed. This approach requires careful optimization to ensure that the larger-scale herringbone patterns maintain their ability to induce chaotic advection effectively, even under elevated flow conditions.

Successful fabrication of this device will not only validate the custom printer's capability to produce complex internal features but also demonstrate its potential to address the challenges of high-throughput microfluidic mixing applications.

Overall, these objectives aim to demonstrate that a custom DLP-SLA printer, specifically optimized for microfluidic applications, can achieve both the resolution and versatility required to create functional microfluidic devices. The outcomes of this work will provide valuable insights into how custom 3D printing approaches can expand the capabilities and applications of microfluidics in fields such as diagnostics, biomedical research, and chemical analysis.

Chapter 3 Materials and Methods

The present work focuses on the comprehensive development, characterization, and application of advanced microfluidic devices by utilizing 3D printing technologies, complemented by including biomedical diagnostics, chemical processing, and environmental monitoring, by enabling precise and controlled manipulation of fluids at the microscale. Despite its promise, the fabrication of intricate microfluidic devices, particularly those requiring complex internal geometries and functional integration, presents substantial challenges. This research addresses these obstacles by leveraging recent advancements in additive manufacturing and robust computational modeling to create devices with enhanced capabilities and precision.

Achieving the objectives of this thesis required the adoption of diverse fabrication methodologies, each selected for its distinct ability to fulfill specific design and functional criteria. A key aspect of this research is the use DLP-SLA 3D printing, a technique that allows the creation of highly customized and intricate microfluidic structures, including internal geometries such as staggered herringbone patterns. SLA technology not only facilitates the fabrication of complex, three-dimensional internal structures but also enables the integration of multiple functional features within a single device, overcoming the limitations of conventional soft lithography and other traditional fabrication approaches.

In parallel, replica molding techniques were employed to fabricate PDMS based devices. The use of PDMS replicas, derived from 3D-printed mold templates, allowed for rapid prototyping and integration of material properties that are essential for biological applications, such as transparency, flexibility, and biocompatibility. This hybrid fabrication strategy effectively combines the rapid customization and scalability of additive manufacturing with the material versatility and widespread acceptance of PDMS in microfluidic research. The approach ensures that the design process is adaptable, allowing for quick iterations and optimization based on specific experimental requirements.

To further refine the design and functionality of the fabricated devices, computational fluid dynamics (CFD) simulations were conducted using COMSOL Multiphysics®. These simulations played a crucial role in visualizing and understanding the behavior of fluid flow within the microchannels. The numerical approach provided a platform for the optimization of critical parameters, such as flow rate, pressure distribution, and concentration gradients, that are otherwise challenging to measure accurately in experimental setups. Through these simulations, the internal configurations could be systematically adjusted to maximize performance, ensuring that the devices operate as intended across a range of conditions.

This section outlines the methodologies utilized for the 3D printing, fabrication, characterization, material selection, and design of microfluidic devices. Each fabrication method, simulation technique, characterization approach, and experimental validation process was carefully chosen and executed to address the distinct requirements of the microfluidic applications investigated in this study. By integrating multiple state-of-the-art fabrication methods with advanced simulation tools and rigorous experimental validations, this thesis presents a comprehensive and scalable approach to microfluidic device development. The outcomes not only advance the precision and functionality of fluid manipulation at the microscale but also pave the way for broader applications in various scientific and industrial fields.

3.1 Fabrication of Microfluidic Devices

3.1.1 Custom Stereolithography 3D Printer

The customization of the 3D printer involved the careful selection of key components, including the DLP UV light projector, Z motors, plate holder, resin container, and open-source hardware solutions. The hardware system comprises two main parts: a Raspberry Pi® embedded computer and the open-source Reprap Universal Mega Board with Allegro driver (RUMBA) controller board, which was released under the GNU Public License (GPL) v2.0 by reprapdiscount.com. The Raspberry Pi® runs NanoDLP front-end and control software, downloadable from nanodlp.com, which provides full customization of the printing process, including slicing 3D models into layers and offering a remotely accessible web interface. The software communicates with the open-source Marlin firmware on the RUMBA board, responsible for controlling the movements of the printer. Marlin firmware, released under GPL v3.0, was configured to manage the two Z-axis motors through separate optical end-stops based on TCST2103 sensors manufactured by Vishay Semiconductor (Vishay Intertechnology, United States), ensuring reliable and precise alignment at each power cycle.

Figure 15 provides a visual representation of the printer's electronic components and their configuration. Panel A illustrates the complete electronics system of the printer, showcasing the integration of the Raspberry Pi® and RUMBA controller board. Panel B presents the schematic diagram of the Raspberry Pi®, highlighting its role as the central processing unit for NanoDLP software, which communicates with the printer's firmware.

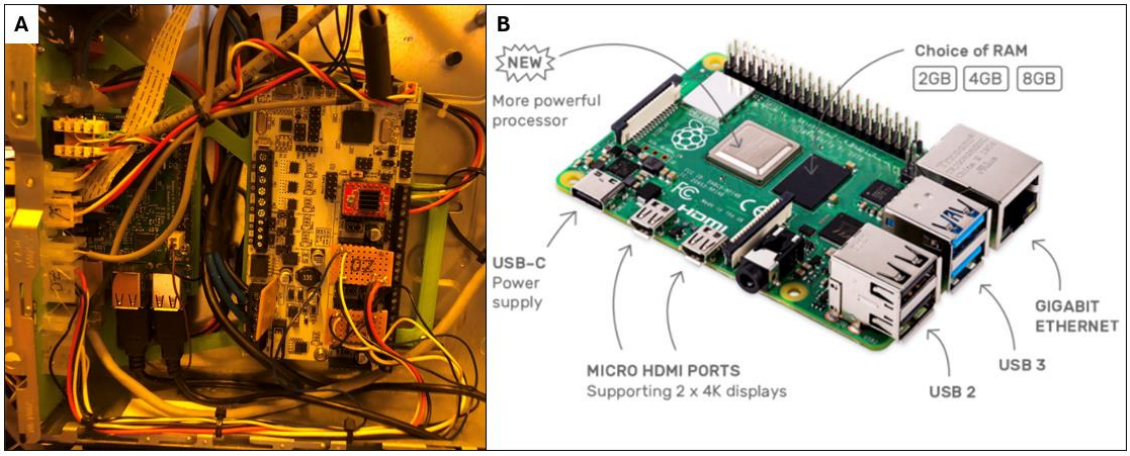


Figure 15: (A) Overview of the 3D printer's electronic system, illustrating the integration of the Raspberry Pi®, RUMBA controller board, and associated components. (B) Schematic of the Raspberry Pi® setup, detailing its configuration for running NanoDLP software and its role in controlling the printer via the Marlin firmware on the RUMBA board.

The DLP projector used in this setup is the Wintech PRO6500, based on the DLP6500 Digital Micromirror Device (DMD) by Texas Instruments® (Dallas, TX, USA). This UV DLP LED system features a resolution of 1920 × 1080 and a projected pixel size of 50 µm at a fixed working distance, with a peak wavelength of 384 nm. Standard interfaces, including HDMI, DisplayPort, USB, and I2C ports, allow for video input and precise projector control. Additionally, a custom program was developed to regulate the projector's LED status and intensity over the USB protocol, which was integrated into the NanoDLP software. The system uses an optical mirror, inclined at 45°, fixed by a mount fabricated by Edmund Optics, to reflect the projection accurately onto the bottom of the resin vat.

To enhance control over light exposure during the printing process, an electronically controlled shutter was included in the system. This shutter ensures that no extra light irradiates the resin during the time between layers by remaining closed during idle periods and opening only when the projector is actively projecting the next layer. The inclusion of this shutter prevents over-curing or unintended curing of the resin, thereby improving the reliability and precision of the printing process. The Shutter Settings control UV light exposure, with the servo motor operating at precise pulse widths (700 ms for closing and 1800 ms for opening) to align with layer curing phases, minimizing unintended exposure.

Figure 16 provides a detailed representation of the key components of this optical and projection setup. Panel A showcases the Wintech PRO6500 DLP projector, the core component generating the high-resolution UV light patterns required for layer-by-layer polymerization. Panel B illustrates the electronically controlled shutter mechanism, highlighting its critical role in preventing unnecessary light exposure between layers and maintaining precision during the printing process. Panel C shows the adjustable mount used to secure the 45° optical mirror. This mirror reflects the projector's light

precisely to the bottom of the resin vat, ensuring uniform and accurate curing of each layer. Together, these elements demonstrate the high degree of customization and integration employed to optimize the 3D printing system for microfluidic applications.

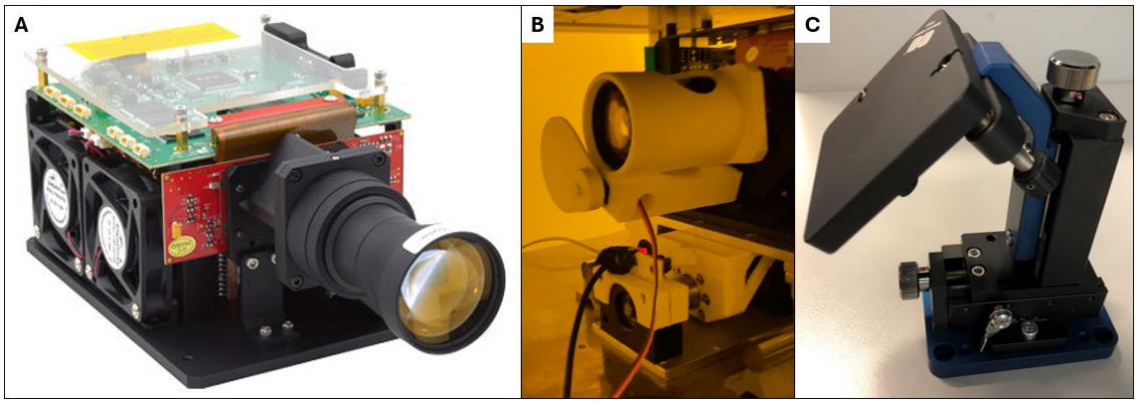


Figure 16: (A) The Wintech PRO6500 DLP projector, featuring a resolution of 1920 × 1080 and a pixel size of 50 µm at a peak wavelength of 384 nm, used for generating high-resolution UV light patterns. (B) Electronically controlled shutter mechanism, designed to block unintended light exposure between layers by closing during idle times and opening only during layer projection. (C) Adjustable mount with a 45° optical mirror, fabricated by Edmund Optics, used to reflect the projector's light accurately to the bottom of the resin vat, ensuring precise and uniform layer curing during the printing process.

The following table presents the relationship between PWM (Pulse Width Modulation), voltage, and the corresponding LED intensity in the UV projector used for 3D printing. PWM is a key parameter in controlling the brightness of the UV light, as it modulates the average power delivered to the LED by adjusting the duty cycle. The voltage values shown correspond to the electrical input driving the LED, while the LED intensity indicates the amount of UV light output, which directly affects resin curing during the printing process.

The resin container, shown in Figure 17A, is a “Resin Vat Anodized Aluminum” equipped with a Fluorinated Ethylene Propylene (FEP) Film, both sourced from ANYCUBIC. The plate holder, depicted in Figure 17B, was custom designed and fabricated with micromachining to securely hold a standard 50 × 75 mm glass slide during the printing process. This holder utilizes a central vacuum system to fix the glass slide in place through a central hole, while alignment pins and edge stops ensure precise positioning. The vacuum system creates a firm seal, preventing any movement of the slide during printing. Additionally, the plate holder was anodized with a matte black finish to minimize light reflection and avoid unwanted UV polymerization outside the designated print area. Once the print is complete, the vacuum system is deactivated, allowing the glass slide, with the printed structure adhered to its surface, to be easily removed. This facilitates the transition to the cleaning and post-curing steps.

Table 1: Relation of PWM with Voltage and LED Intensity.

PWM	Voltage (V)	LED Intensity (A)
0	0	0
15	8.3	3.6
20	10	4.4
25	11.4	5.2
30	14.4	6.4
35	15.7	7.2
40	17.9	8.4
45	19.2	9
50	20.3	9.6
60	22.4	10.6
70	25.1	11.9
80	27.6	13.1
90	28.7	13.8
100	30	14.4
120	33.4	16
140	36	17.2
150	37.1	17.9
155	37.8	18.1

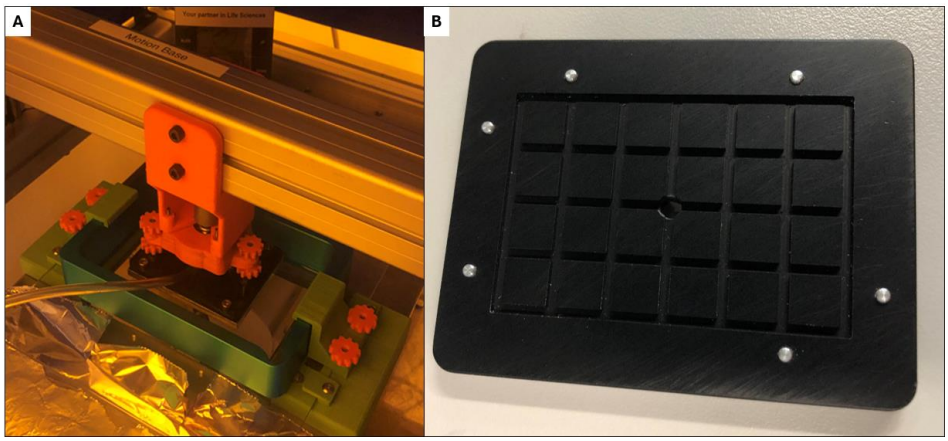


Figure 17: (A) The resin vat, made of anodized aluminum, with a Fluorinated Ethylene Propylene (FEP) film to contain the resin during the printing process. The upper bar of the plate holder, connected to the Z motors, ensures precise movement and alignment during printing. (B) The custom-designed plate holder, featuring a central vacuum system to securely fix a standard 50 × 75 mm glass slide in place. The alignment pins and edge stops enhance stability, while the matte black anodized finish prevents light reflection and unwanted UV polymerization.

Projector irradiance was calibrated using a Thorlabs Power and Energy meter with an S302C Thermal Power Sensor (190–2500 nm, max 2 W, 12 mm sensor diameter). The sensor was attached to the build platform adapter and positioned at the focus distance. Measurements were taken at various projector PWM settings (PWM = 20, 45, 50, 70, 100, 150) under two configurations: (i) no vat installed and (ii) with a vat containing new FEP film. A PWM setting of 35 was used for the 3D printing process.

As shown in figure 18, a touchscreen interface was incorporated into the 3D printing system to enable direct control of the printer's movements without the need for remote access. This addition allowed for convenient local adjustments, such as calibrating the Z-axis and regulating the position of the build plate. However, for safety reasons, the touchscreen was not used during the actual printing process to prevent potential exposure to UV. Instead, it proved highly effective for tasks like plate alignment and ensuring accurate positioning prior to starting a print.



Figure 18: Touchscreen interface integrated into the 3D printer, enabling local control for Z-axis calibration and build plate positioning. This setup was utilized exclusively for alignment purposes and not during the printing process for safety reasons.

3.1.2 3D Printing Protocol

All 3D printing procedures were conducted in a yellow-light room to prevent unintended UV light exposure, ensuring that the resin was only cured under the controlled conditions provided by the DLP UV projector. The models were designed using Autodesk Inventor and saved as STL files, a format compatible with the NanoDLP slicing software used for 3D printing. Once the design was completed,

the STL file was uploaded to the NanoDLP software via the printer's IP address, enabling precise control of the printing process. Before initiating a print, several critical steps were followed to ensure optimal conditions. The Raspberry Pi®, Z motors, and DLP projector were powered on, and all components were verified for proper functionality. The resin vat was filled to a consistent level to ensure an uninterrupted printing process, ensuring there is enough resin for printing the part, while the 50 × 75 mm glass slide, where the printed structure adheres, was carefully aligned in the plate holder. Alignment pins and a vacuum system secured the slide, ensuring accurate layer positioning and adhesion. The NanoDLP software settings were reviewed, confirming proper communication between the projector and the printer. Connection to the internet was also verified to allow for remote monitoring and adjustments. To maintain consistent resin properties, the printing chamber was preheated to 30°C, as fluctuations in temperature can alter resin viscosity and curing behavior(75) .

Ventilation and extraction systems were activated to mitigate exposure to resin fumes. All operations were conducted remotely from outside the yellow-light room, ensuring no unintended exposure to UV light. Protective UV glasses were used whenever direct access to the room was necessary.

The NanoDLP software played a central role in managing and optimizing the printing process. Several parameters were configured to ensure precision. Display Engine settings determined the resolution of the DLP projector (1920 × 1080 pixels), corresponding to an X/Y resolution of 50 µm, providing the precision required for microfluidic structures. A 30 second warmup time stabilized the projector's light intensity before printing began. Axis/Movement settings controlled Z-axis mechanics, with speeds set between 1000 µm/sec and 3000 µm/sec to ensure smooth transitions between layers. The motor step angle (1.08 degrees) and leadscrew pitch (1.001 mm) guaranteed micro-level accuracy in layer adjustments.

The exposure settings were divided into two categories: burn-in layers and normal layers. Burn-in layers are the initial layers exposed to prolonged UV light to ensure strong adhesion to the substrate. These layers are critical for preventing detachment during the printing process, as shown in Figure 19, where insufficient burn-in exposure led to poor adhesion. When adhesion is inadequate, the printed part does not form correctly and remains partially attached to the build plate, as seen in the image. In cases where the burn-in layer exposure is extremely insufficient, the entire piece fails to adhere to the plate and instead remains in the resin vat, rendering the print unsuccessful.



Figure 19: Example of insufficient burn-in exposure during the 3D printing process. Poor adhesion caused the printed part to hang partially from the build plate, compromising the print.

Normal layers followed the burn-in layers, with a reduced cure time compared to the initial layers. Since these layers adhere to previously cured layers of the same material, the risk of delamination is significantly reduced, requiring less energy for proper adhesion. Additionally, normal layers form the functional structures of the printed device, making dimensional accuracy critical. Over curing must be carefully controlled at this stage to avoid unintended polymerization that could compromise the design's dimensions and functionality. For burn-in layers, the platform lifted by 3 mm, while for normal layers, it lifted by 1.5 mm, with a 0.2-second wait time to allow the resin to settle evenly before curing the next layer. This lifting and waiting process ensures that the resin flows back into the printing area, completely covering the surface where the next layer will be printed. This step is crucial to prevent any gaps or areas lacking resin, allowing the next layer to form properly and ensuring consistent layer adhesion throughout the print.

Once the setup was complete, the slicing settings segmented the uploaded 3D model into printable layers. The Gcode settings were used to initiate the print sequence, with customized commands for booting, stopping, and resuming prints. The printing process was monitored remotely, ensuring consistent operation of the Z-axis motors and projector, with position sensors and a live camera respectively. Exposure times for each resin were optimized based on initial dose calibration experiments, as detailed in Chapter 4.

These settings, combined with controlled environmental factors, ensured the successful fabrication of complex microfluidic structures. This comprehensive approach to 3D printing, integrating NanoDLP's capabilities, enabled precise and reproducible results critical for advanced microfluidic applications.

3.1.3 Post-procesing

Once the printing process was completed, the printed piece was carefully removed from the plate holder for post-processing. The initial cleaning involved submerging the piece in 2-Propanol (IPA) for three minutes using the Washing and Curing Machine from CREALITY. This machine operates in two modes: in the first mode, the piece is placed in a bath of IPA, where a built-in fan circulates the IPA, enhancing its ability to remove any uncured resin from the surface. After this initial wash, compressed air was used to blow off residual resin and IPA from the surface of the piece, particularly from exposed features, ensuring that all external surfaces were thoroughly cleaned.

For pieces containing closed microfluidic channels, an additional critical step was implemented: IPA was carefully flushed through the channels using a syringe, ensuring that no uncured resin remained inside the channel. This was necessary because any residual resin would cure during the post-curing phase, leading to blockages that would compromise the functionality of the microfluidic channels.

After the initial cleaning, the piece was washed again in 2-Propanol for an additional three minutes under the same IPA circulation system of the CREALITY machine to ensure thorough removal of any remaining resin. Following this, the machine was switched to its second mode: UV curing mode, where the piece was placed on a reflective plate and exposed to UV light for a period of 2 to 5 minutes, depending on the size and geometry of the printed object. This final curing step ensured complete polymerization of the resin, achieving the desired mechanical properties and solidifying the structure.

The Washing and Curing Machine from CREALITY, used during the post-processing stage, is shown in Figure 20. In Figure 20A, the machine is depicted in washing mode, where the printed part is submerged in IPA for resin removal. In Figure 20B, the machine operates in UV curing mode, ensuring complete polymerization of the printed structures.

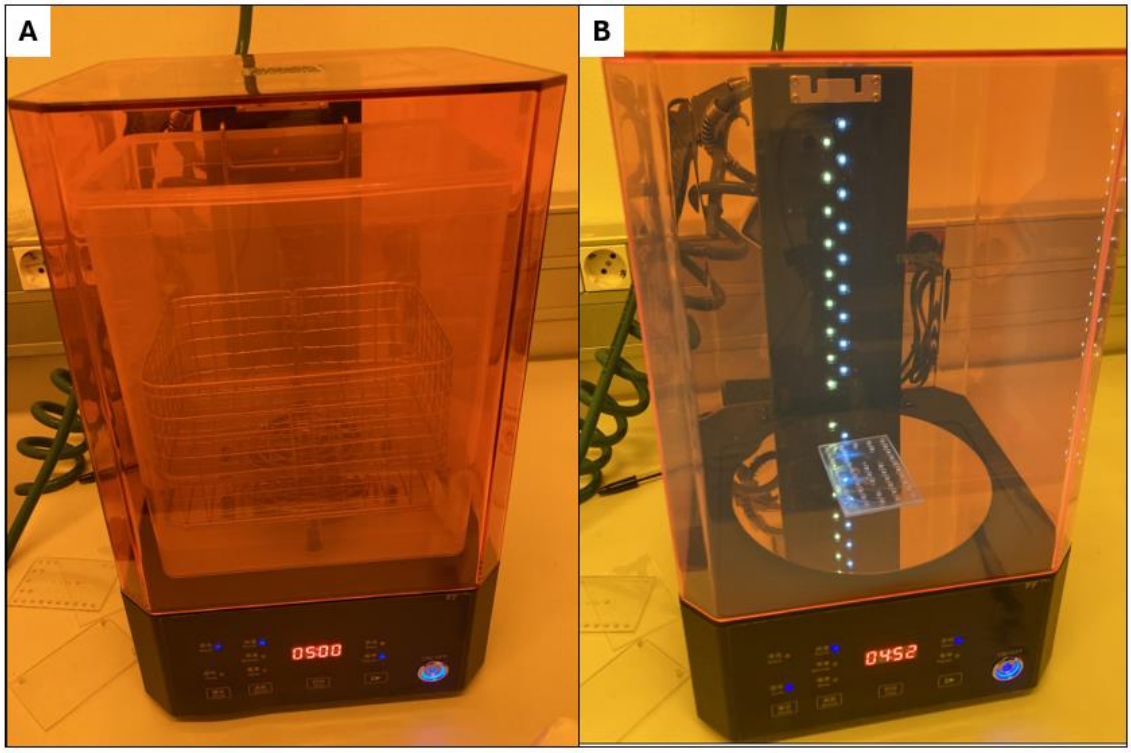


Figure 20: Washing and Curing Machine from CREALITY. (A) Washing mode, where the printed part is submerged in 2-Propanol (IPA) for cleaning. (B) UV curing mode, where the part is exposed to UV light for complete polymerization.

Throughout the post-processing, safety precautions were strictly followed, including the use of gloves and masks to avoid direct contact with the resin, which can be toxic and cause skin and eye irritation. The combination of thorough washing and precise UV curing was essential to ensure the robustness and functionality of the final device, making it ready for its intended microfluidic applications.

Throughout the printing process, the NanoDLP software allowed for remote monitoring by accessing the printer's IP address, enabling real-time observation and control without needing to enter the yellow-light room. A camera integrated into the system provided visual feedback, ensuring that the printing parameters were executed as expected and allowing immediate response to any issues that might arise.

In summary, careful preparation, precise parameter control, and thorough post-processing were critical to producing high-quality, reproducible microfluidic devices. Consistent temperature control, dose calibration for each resin type, and rigorous safety protocols ensured that the fabrication process was reliable and efficient, meeting the specific requirements for each printed design.

3.1.4 3D Printed Molds Fabrication and PDMS Replica

One of the most common approaches for fabricating microfluidic devices involved the use of 3D-printed molds to create PDMS replicas. This method leverages the precision of 3D printing to design molds with specific microchannel patterns, which are then replicated in PDMS, a silicon-based organic polymer known for its biocompatibility, optical clarity, and flexibility.

The process begins with the design and printing of the mold, where the desired channel relief is created as a raised pattern on a solid base. The mold is printed using standard DLP-SLA 3D printing techniques, but with one important adjustment: it is post-cured more extensively than typical printed parts. This extended post-curing process is crucial because it helps evaporate any residual substances that could interfere with the PDMS curing process. Without sufficient post-curing, these substances may prevent the PDMS from fully curing, particularly in the layers closest to the mold surface, leading to sticky or improperly formed channels.

Once the mold is prepared, the next step is to cover it with a mixture of PDMS. The PDMS is prepared using a ratio of 10:1 (base polymer to curing agent), which ensures the right balance of flexibility and durability in the final device. The mixture is thoroughly degassed to remove any trapped air bubbles that could cause defects, and then poured over the 3D-printed mold, making sure that the channels are fully filled. The mold covered with PDMS is placed in an oven at 85°C overnight, allowing the PDMS to cure completely. This curing step is critical for ensuring that the PDMS solidifies properly and takes on the precise shape and features of the mold.

After curing, the PDMS is carefully unmolded from the 3D-printed template, revealing a flexible and precise replica of the original design. The unmolding process must be done carefully to avoid tearing or distorting the fine features of the microchannels.

3.1.5 Bonding and chip manufacturing

Once removed from the mold, the PDMS replica is thoroughly cleaned, and the inlets and outlets holes of 1.0 mm were punched. Both the PDMS structure and the glass slides to which it will be bonded are cleaned with soap, water, ethanol, acetone, and 2-Propanol, ensuring that all surfaces are free of contaminants. Proper cleaning is essential to achieve a strong and leak-free bond between the PDMS and the glass.

The next step involves plasma activation to bond the PDMS to a glass slide, which serves as the base of the microfluidic device. The cleaned PDMS and glass slide are placed in a plasma cleaner (Harrick Plasma Cleaner, USA) set to 30 W and a pressure of 0.8 Torr, where they are exposed to plasma for 30

seconds. This treatment makes the surfaces hydrophilic, promoting a strong and durable bond between the two. Immediately after plasma treatment, the PDMS is aligned and pressed onto the glass slide to form a sealed microfluidic device. The process is shown in Figure 21.

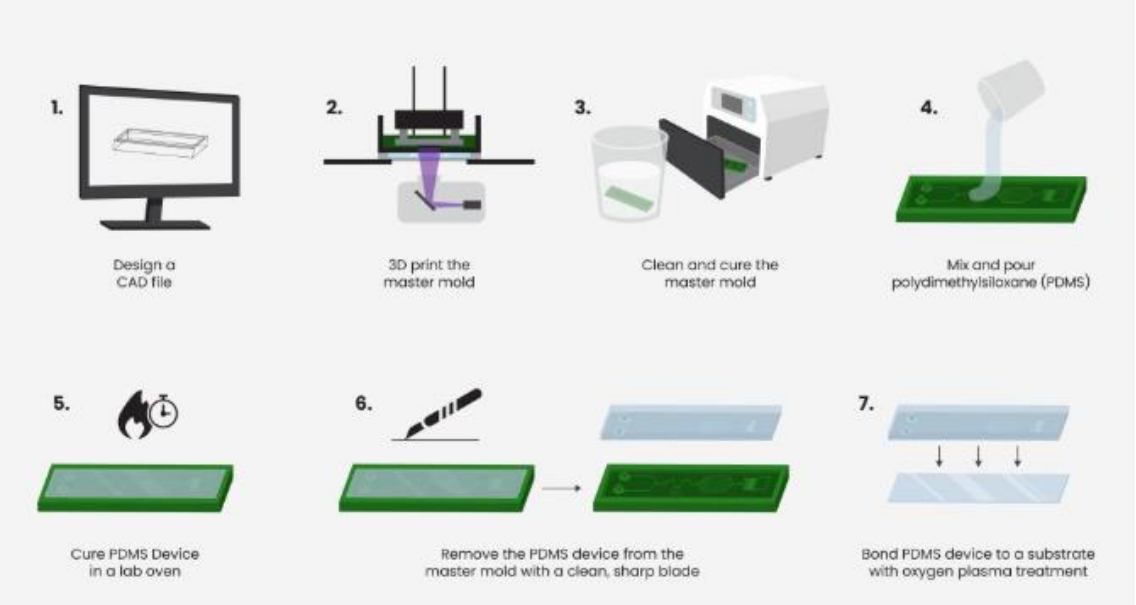


Figure 21: Step-by-step process for fabricating a PDMS device using a 3D-printed mold. (1) Design the mold using CAD software. (2) 3D print the master mold. (3) Clean and cure the mold. (4) Mix and pour PDMS into the mold. (5) Cure the PDMS device. (6) Carefully remove the cured PDMS device from the mold. (7) Bond the PDMS device to a substrate using oxygen plasma treatment. From (129)

The assembled device is then tested for leaks by flowing colored water through the channels. This quality control step ensures that the bonding is secure and that there are no unwanted gaps or weak points that could lead to leakage during actual use. Any detected issues are addressed by adjusting the bonding process or improving the cleanliness of the surfaces prior to plasma treatment.

The result is a microfluidic device that precisely mimics the architecture of the original 3D-printed mold, with the added benefits of PDMS's biocompatibility, optical transparency, and flexibility. This method allows for rapid prototyping and customization of microfluidic devices, making it an ideal choice for a wide range of applications in biomedical research and diagnostics.

3.1.6 Resins Used and Absorbance Test

Three commercial resins were selected for this study: FREEPRINT® ortho 385 nm from DETAX (130,131), KeyOrtho IBT from Keyprint (132), and PlasCLEAR from Asiga (133). Each resin was chosen based on its specific mechanical properties and compatibility with the DLP 3D printing process. According to the datasheets, the Detax and Asiga resins are classified as hard resins, exhibiting Young's

Modulus (E) of 1650 MPa and 1915 MPa, respectively, after curing. In contrast, the Keyprint resin remains flexible after curing, with an E value ranging between 15.5 MPa and 31 MPa.

The Detax and Asiga resins utilize the same photo-initiator, Diphenyl(2,4,6-trimethylbenzoyl)phosphine oxide (TPO), which triggers the polymerization process under UV light exposure. However, the Asiga resin contains a higher concentration of the absorber, resulting in an absorbance value at 385 nm that is 2.5 times greater than that of the Detax resin. In contrast, the Keyprint elastomeric resin has an absorbance coefficient similar to the Detax resin.

These three resins, commonly used in the dental industry, were selected not only for their mechanical properties but also for their biocompatibility, transparency, and compatibility with the 385 nm wavelength of the DLP projector used in the printing process. This selection ensured that the resins could meet the requirements for producing precise and functional microfluidic devices.

The absorbance test was performed using an Infinite M200 PRO Multimode Microplate Reader from Tecan to determine how each resin responded to UV exposure. For this experiment, 10 µL of each resin was pipetted into three separate wells of a 96-well plate, ensuring accurate dispensing despite the resins viscous nature. Absorbance measurements were taken three times for each resin, and an average value was calculated, subtracting the baseline obtained from a blank well to correct for any background interference. Given that the plate reader well fills the resin to a height of 320 µm, and considering the nominal height of the 3D-printed layers is 100 µm, the absorbance values were normalized by dividing by a factor of 3.2. This adjustment allowed for a more accurate comparison of how the resins would behave during the actual 3D printing process, ensuring consistent curing and layer formation.

3.1.7 Approaches for Printing Closed Channels and Integrating Internal Structures

One of the primary challenges in printing closed channels using DLP-SLA is controlling the extent to which the UV light cures the resin. During the printing process, the UV light can penetrate beyond the intended layer, leading to over-curing and potentially causing blockages or distortions within the channels. This issue is particularly pronounced when attempting to create enclosed or intricate internal structures.

A common approach to mitigate this problem is by customizing the resin with specific absorbent additives, which can limit the penetration of the UV light. However, when using commercial resins, this

level of customization is not always feasible. Therefore, achieving precise, closed channels relies heavily on the optimization of the printer's settings, specifically the exposure time and light intensity of the DLP projector. Through a series of calibration experiments, we were able to achieve these parameters, ensuring that each layer cures only to the desired depth without affecting the layers below.

By carefully controlling the exposure time and intensity, we can not only fabricate effective closed channels but also create additional structures within these channels. This capability opens possibilities for integrating complex internal designs, such as herringbone patterns or other flow-enhancing geometries, within enclosed spaces. This technique, once optimized, allows for versatile and precise control over the internal features of microfluidic devices, enhancing their functionality for a range of applications.

3.2 Dimensional Characterization

Dimensional characterization of the microfluidic devices was essential to ensure that the printed features adhered to the design specifications, both in terms of lateral and vertical accuracy. This section details the methods used to assess both lateral dimensions (width, length, and feature shape) and vertical dimensions (height, layer thickness, and roughness).

3.2.1 Lateral Dimensional Characterization

To measure the lateral dimensions, including width, length, and the shape of printed features, an optical microscope (Nikon Eclipse L150, Nikon, Tokyo, Japan) was used. This enabled high-resolution inspection of features such as triangles, circles, and squares, confirming their conformity to the intended design. Key features of the devices, such as microchannels and specific geometries, were measured to verify their dimensions, ensuring that the lateral resolution achieved by the 3D printer was within the specified tolerances. The optical microscope provided clear images that were analyzed to measure feature separations, widths, and shape fidelity, confirming that the microchannels and intricate designs adhered to the lateral dimensional requirements.

3.2.2 Vertical Dimensional Characterization

The vertical dimensions of printed structures, including the height of microchannels and other features, were characterized using a profilometer (DEKTAK XT, Bruker, Billerica, MA, USA). This tool provided nanometer-level precision to measure the vertical height of printed channels and structural elements, which is critical for ensuring the accuracy of 3D-printed microfluidic devices. The profilometer measured the total height of microchannels, allowing for verification of resin curing

consistency and the vertical resolution of the printing process. This confirmed that vertical structures, such as herringbone patterns, were formed with the intended height and dimensional fidelity.

3.2.3 Cross-Sectional Analysis

The cross-sectional dimensions of the microchannels were analyzed using an inverted microscope (Eclipse Ti, Nikon, Tokyo, Japan). This allowed for the inspection of the internal channel profiles and provided insights into the uniformity of the printed microchannels.

The inverted microscope provided detailed images of the cross-sections of the printed channels, allowing for the measurement of channel widths, heights, and internal shape. This ensured that the microchannels were free of obstructions or distortions that could affect their functionality.

3.2.4 Surface Roughness Characterization

Exterior surface roughness was calculated from atomic force microscopy (AFM) measurements performed on a Dimension 3100 AFM instrument (Veeco Instruments, Plainview, NY, USA) equipped with a rectangular silicon AFM tip (Budget Sensors, spring constant k = 40 N/m and a resonant frequency ν = 300 kHz) and operated in tapping mode at room temperature in air. Topographic images obtained from the scanning of 50 × 50 µm rastered areas were used for root-mean-square calculations performed with WSxM software (Nanotec Electrónica, Tres Cantos, Spain) (112). At least three positions were analyzed per sample.

3.2.5 Sidewall Roughness

In most additive manufacturing processes, the addition of discretized layers creates a sidewall roughness, which is inaccessible by AFM. To study the surface roughness of the sidewalls, we used a prediction model. According to ASME B46.1 (113), the surface quality can be described by the average surface roughness, which is defined as the summation of the peaks and valley areas divided by the evaluation length. This quality parameter can be calculated by the following Equation 13(113), and also shown in Figure 22, where the variables W and A for calculating the sidewall roughness are illustrated:

Equation 13: Sidewall Roughness.

$$R_\alpha = \frac{A}{W}$$

Where:

- $R_\alpha$represents the sidewall roughness,
- A is the uncured area between layers, and
- W is the thickness of each printed layer.



Figure 22: (A) Example of a 3D printed part and its sidewall roughness. (B) Zoom from 3 (A) where the thickness of the layer (W), and the uncured area in every layer (A) are described.

As shown in Figure 3, the sidewall roughness results from the uncured regions between each printed layer. This roughness affects the fluid dynamics inside the microchannels, making it important to characterize and optimize during the manufacturing process.

3.3 Design of Microfluidic Devices

The device designs utilized in this work were created using Autodesk Inventor, a highly versatile CAD software that allows for both 2D and 3D modeling. Autodesk Inventor can generate complex geometries with precise dimensions, which are critical for engineering applications. The software's flexibility enables the design of intricate devices, such as those shown in Figure 23 and Figure 24.

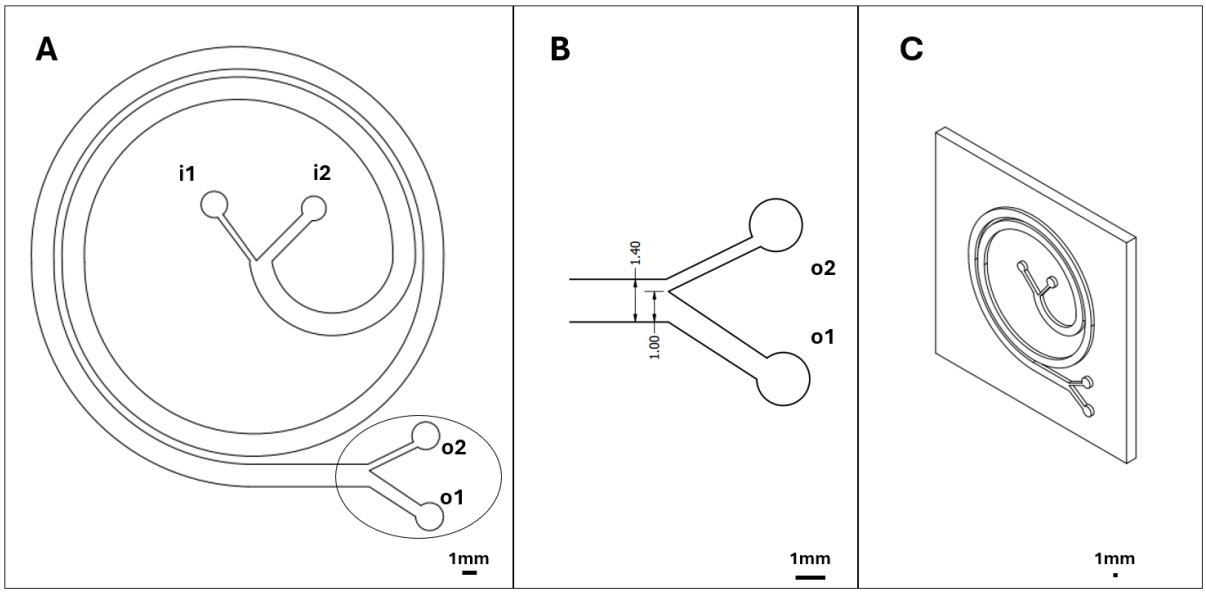


Figure 23: (A) Top view of the 3D spiral microfluidic device designed using Autodesk Inventor, highlighting the detailed geometry. i1 and i2 are the two inlets, and o1 and o2 the two outlets. (B) Zoom 2D view of the outlets, showing specific dimensions for fabrication. (C) Isometric view of the final 3D model, ready for being exported in STL format for 3D printing or further simulations.

The channels in the device have a rectangular cross section, measuring 1.4 mm in width and between 550 and 800 µm in height. Designed with a 2D geometry and extruded, the spiral's shape was specifically optimized to enhance particle separation with laminar flow conditions within the microfluidic channel.

This spiral channel completes 2 1/4 turns, each half turn increasing the radius, followed by a final quarter turn. To stabilize the flow and facilitate particle collection, a 7.55 mm straight segment is included at the end. To achieve a high-definition print of the spiral using DLP-SLA, it is essential to maintain a 500 µm gap between the two walls of the spiral, specifically, between the outer wall of the inner spiral and the inner wall of the outer spiral. The total internal perimeter of the spiral, including the straight segment, is 138.72 mm.

Table 2: Definitions of the spiral device.

Turn Segment	Radius (mm)	Perimeter (mm)
1st Half-Turn	3.80	12.00
2nd Half-Turn	9.65	30.25
3rd Half-Turn	10.6	33.18
4th Half-Turn	11.55	36.22
Final Quarter-Turn	12.45	19.52
Straight Segment	—	7.55

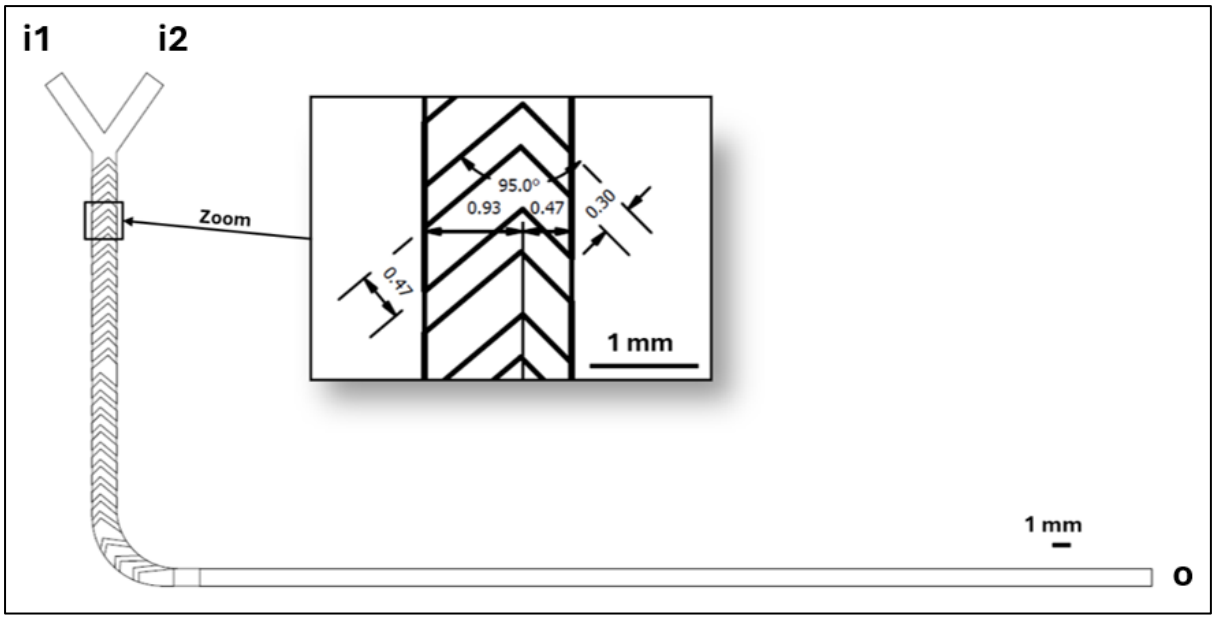


Figure 24: Detailed view of the herringbone structure within the microfluidic device. The zoomed section shows the specific geometric parameters, including the angles and spacing, essential for creating efficient fluid mixing. The overall channel width is also indicated. i1 and i2 are the two inlets, and o is the outlet.

The designs were exported in STL (Standard Triangle/Tessellation Language) format, a file type that represents the geometry of a 3D object using a mesh of interconnected triangles. This format is particularly suitable for 3D printing, as it simplifies the geometric data into triangles, allowing for easy processing by 3D slicing software.

Once exported in STL format, the files were imported into NanoDLP, a slicing software that converts the model into layers for 3D printing. NanoDLP processes the STL file by generating a series of thin layers that the printer can sequentially reproduce, ensuring precision in the final printed model.

Furthermore, the designs can be imported into COMSOL Multiphysics, a simulation software that enables finite element analysis on the same design geometries. This integration between Autodesk Inventor and COMSOL is particularly valuable for testing fluid dynamics and other physical properties within the designed structures.

3.4 Comsol Simulations

3.4.1 General Setup

For simulating both particle separation and fluid mixing, we utilized COMSOL Multiphysics, version 5.6, a robust tool for modeling and analyzing fluid dynamics in microfluidic devices. The simulations were

carefully set up to replicate the actual experimental conditions, reflecting the precise geometry of the microfluidic channels and incorporating the physical properties of both the fluids and the particles involved. For particle separation in the spiral structure, the Laminar Flow Module was used to model the flow behavior, while the Particle Tracing Module was employed to simulate particle trajectories within the laminar flow, accounting for forces such as drag and inertia that influence particle motion. This enabled us to visualize how particles of different sizes behaved and separated within the spiral geometry.

For the mixing of two fluids within the herringbone structures, the Laminar Flow Module was again used to simulate the fluid dynamics, while the Transport of Diluted Species Module modeled the transport and mixing of the two fluids. This module allowed us to analyze the concentration profiles of the fluids over time, considering both convection and diffusion effects. By utilizing these modules, we were able to gain insights into both the particle separation and fluid mixing processes, optimizing the designs for maximum efficiency.

3.4.2 Governing Equations

To accurately model the fluid dynamics and transport phenomena within the microfluidic devices, several fundamental equations were employed in the simulations. The Laminar Flow Module utilizes the Navier-Stokes equations and the Continuity equation to describe the behavior of fluid flow under laminar conditions, ensuring that the fluid's velocity and pressure fields are properly represented. For the fluid mixing simulation, the Transport of Diluted Species Module was used, which combines convection and diffusion effects through the Convection-Diffusion equation and Fick’s Law. These equations allowed us to model how different species were transported and mixed within the microchannels, while accounting for both diffusion and convective transport. The formulas used in each module are:

- **Laminar Flow Module**

This module applies the Navier-Stokes equations and the continuity equation to model fluid behavior under laminar flow conditions. The Navier-Stokes equation, which governs the motion of fluid particles, is represented in Equation 11. The continuity equation, which ensures mass conservation within the fluid system, is outlined in Equation 12.

- **Transport of Diluted Species Module**

This module describes the transport processes of a diluted chemical species within a fluid, integrating both diffusion and convection mechanisms. The governing equations include the Convection-Diffusion Equation, detailed in Equation 13, and Fick's Law, described in Equation 5. These equations collectively provide a framework for understanding how species are transported and distributed within the microfluidic environment.

3.4.3 Particle Separation Simulation in Spiral Structures

To predict particle behavior within the spiral microfluidic device and optimize the design, we used COMSOL Multiphysics® to simulate the separation process. Two modules were employed for this: the Laminar Flow Module, to simulate fluid flow within the spiral, and the Particle Tracing Module, to model the trajectories of particles of different sizes influenced by the fluid forces.

The simulations were based on the Navier-Stokes equations, which accurately describe fluid behavior in laminar conditions. The particle tracing allowed us to visualize how particles of different sizes were affected by the flow, predicting the points at which they would separate based on their size. Several parameters, including different channel heights and flow rates, were tested in the simulations to account for the variability inherent in the 3D printing process and the experimental conditions.

In these simulations, the inlets were set at a 1:9 flow rate ratio, with a sample with the particle suspension introduced in one inlet and the seath flow introduced in the other inlet. Table 2 presents the flow configurations tested.

A cutting plane was positioned at the outlet where the channel splits into two paths, providing a precise point to analyze particle distribution at the divergence. This allowed us to examine which particles were directed toward each outlet, offering a clear visualization of the separation efficiency. By using this method, we could directly observe how effectively the spiral device separated particles based on size.

The results of these simulations were compared with experimental data to validate the model, ensuring that the predictions aligned with the actual particle behavior observed during the experiments.

Table 3: Simulation Conditions for Particle Separation: Channel Heights (540 µm, 640 µm, 740 µm) and Flow Configurations with a 1:9 Flow Ratio, the '' means that contains the diluted particles. All values in µl/min.*

	Input 1	Input 2
Condition 1	760*	6840
Condition 2	6840	760*
Condition 3	700*	6300
Condition 4	6300	700*
Condition 5	670*	6030
Condition 6	6030	670*
Condition 7	655*	5895
Condition 8	5895	655*
Condition 9	640*	5760
Condition 10	5760	640*

3.4.4 Fluid Mixing Simulation in Herringbone Structures

We conducted two sets of experiments to investigate the effects of viscosity differences on mixing efficiency under laminar flow. In the first experiment, we mixed two fluids of equal viscosity: water and a fluorophore solution diluted in water. In the second experiment, we introduced fluids with different viscosities: dextran, a solution with viscosity similar to blood, and a fluorophore solution diluted in water. By visualizing the concentration profiles and velocity fields, we gained deeper understanding into the performance of the microfluidic devices, and we were able to optimize the design for better mixing efficiency.

Table 3 provides an overview of the key physical properties of water and dextran used in this study. These parameters, including density, viscosity, and diffusion coefficient, significantly impact the fluid behavior and mixing efficiency within the microfluidic channel.

Table 4: Physical properties of water and dextran used in simulations.

	Water	Dextran
Density [kg/m3]	997	1060
Viscosity [Pa*s]	8.9 e-4	4 e-3
Diffusion Coeficient [m2/s]	2 e-9	6 e-11

The inlets were set at a 1:10 flow rate ratio, with one inlet having a flow of 650 µl/min and a fluorophore concentration of 0 mol/m³, while the other inlet had a flow of 65 µl/min and a fluorophore concentration of 0.02 mol/m³.

In the simulation process, 30 lines were drawn along the channel, forming a matrix of 3 rows and 10 columns. These lines were used to analyze the fluorophore concentration along each line.

3.5 Particle Separation Experimental Validation

3.5.1 Device Setup and Preparation

The spiral microfluidic device used for particle separation was fabricated using DLP-SLA, both by printing the complete device in one single step and printing the mold to fabricate PDMS replicas.

The particle separation mechanism in this system is governed by the lateral migration of particles within the microfluidic channel, a process determined by the balance between drag and inertial lift forces. This balance dictates the equilibrium position of each particle along the channel, with distinct equilibrium positions based on particle size. For larger particles, the inertial lift force dominates, enabling them to achieve a stable position within the flow. On the other hand, smaller particles are more influenced by the drag force, which directs them toward different outlet paths, facilitating size based separation.

This flow configuration ensured consistent conditions throughout the experiment, optimizing separation efficiency based on particle size.

3.5.2 Particle Type and Characteristics

Fluorescent polystyrene microspheres were chosen for the separation experiments due to their well-defined sizes and optical properties, which facilitate precise visualization under a microscope. Four distinct particle sizes were selected to evaluate the separation performance of the spiral microfluidic device:

- 30 µm orange-fluorescen microspheres
- 50 µm green-fluorescen microspheres
- 75 µm red-fluorescen microspheres
- 100 µm green-fluorescen microspheres

These particle sizes span a range that allows for clear differentiation of trajectories during separation, and their fluorescent properties enable visualization under a microscope. The objective of the

experiments was to determine the separation point for each particle size as they traveled through the spiral. The particles density was consistent across all sizes to ensure that size was the primary factor driving separation.

To prepare the experiments, solutions of 10 mL containing approximately 1,000 particles each were created. This required using specific volumes from the stock solutions: 2 µL for the 30 µm particles, 8 µL for the 50 µm particles, 25 µL for the 75 µm particles, and 60 µL for the 100 µm particles. Intermediate dilutions were necessary for the preparation of the 30 µm and 50 µm solutions to ensure accurate particle concentrations. The concentration of particles in the final solution was calculated based on the sample flow rate, ensuring consistency and reproducibility during the experiments.

3.5.3 Fluid Properties and Experimental Conditions

The particle suspensions were prepared in MilliQ water. The experiments were set up with two inputs: one input for the particle suspension and another for MilliQ water acting as the sheath flow. Two experiments were performed for different channel heights and configurations, but always following the 1:9 ratio between the sample with particles and the seath flow. For the 540 µm channel height, the flow rate of the particle suspension was set to 760 µL/min, while the sheath flow rate was 6840 µL/min. In this configuration, the particle suspension and sheath flow entered through their designated inlets. For the 640 µm channel height, the flow rates were identical to the first experiment (760 µL/min for the particle suspension and 6840 µL/min for the sheath flow), but the inputs were reversed, with the particle suspension and sheath flow entering through opposite inlets. The flow setup in the spiral was carefully designed to maintain laminar flow conditions, with both inlets introducing fluid at precisely controlled rates using syringe pumps (Harvard Apparatus). The syringe containing the particle solution was either 10 or 20 mL, while the Milli-Q water syringe was 60 mL to ensure the experiment could run longer, allowing for stabilization of the separation process.

The separation of particles in this system relies on their lateral migration within the microfluidic channel, governed by the balance between drag and inertial lift forces. This balance determines the equilibrium position of each particle along the channel, with distinct equilibrium positions based on particle size. On one hand, for larger particles the inertial lift force dominates, enabling them to achieve a stable position within the flow. On the other hand, smaller particles are more affected by the drag force, which directs them toward different outlet paths, allowing for size-based separation.

In the spiral channel, additional forces due to the device's curvature further influence particle behavior. A neutrally buoyant particle experiences two primary lift forces: (1) the wall-effect lift force, which

pushes particles away from the walls, and (2) the shear-gradient-induced lift force, which directs particles toward the walls. These forces cause particles to migrate transversally across the flow direction until they reach equilibrium positions where opposing forces balance each other. The curved geometry of the channel enhances this effect by inducing a shear-gradient lift force that drives particles from the centerline toward the walls, while the wall-induced lift force repels them back toward the center. This dynamic interplay enables particles of varying sizes to settle into specific equilibrium positions, facilitating efficient size-based separation within the device.

This flow configuration ensured consistent conditions throughout the experiment, optimizing the separation efficiency based on particle size.

3.5.4 Validation and Separation Performance Analysis

The separation efficiency of the spiral device was validated through fluorescence microscopy. After flowing the fluorescent particles through the device, images were captured at the outlets using a fluorescence microscope to monitor the distribution of particles based on their fluorescent labeling. Each particle size was run separately to avoid overlap, allowing for clear visualization of particle distribution.

The images obtained were analyzed using the Fiji image processing platform, where a manual counting method was employed to quantify the number of particles in each outlet region. The analysis was performed to evaluate the degree of separation based on the size of the fluorescent particles (30 µm, 50 µm, 75 µm, and 100 µm), using one particle size per experiment.

Fluorescent microscopy and image processing provided a real-time method for assessing separation efficiency, ensuring that the separation performance could be systematically evaluated based on particle size and flow conditions.

3.5.5 Experimental Validation using Blood and Beads

Blood samples were obtained from healthy volunteers and acquired from the Blood and Tissue Bank in Barcelona (up to 36 h from its extraction). Blood samples were used as controls with the previous approval of the committee on research ethics with medicines and the commission of research projects of the Vall d'Hebron University Hospital.

Polystyrene particles of 70 µm conjugated with streptavidin (SPHEROTMSVP-800-4) were washed before use to remove the 0.02% NaN3 added as a preservative. First, the particles were resuspended by gently shaking the vial to obtain a homogeneous suspension. Then, 400 µL from the vial was added

to a 2mL Eppendorf tube. After, the tube was placed in a centrifuge at 1000 g for 20min. The supernatant was removed by aspiration, avoiding touching the particle pellet with the pipette tip. Subsequently, the pellet was resuspended in 1 mL of buffer solution (10 mMTris-HCl (pH7.5), 1 mMEDTAand2.0 MNaCI). Finally, the washing step was repeated and resuspended in 1 mL of PBS1X with CD45-Biotin (1:100) (Human Clone 5B1—LOTE 5190918251 de Miltenyi Biotec). The particles were incubated for 30 min at room temperature with gentle rotation. The particles coated with the biotinylated antibody CD45 were centrifuged two times at 1000 g for 20 min with PBS/BSA.

The particles coated with the biotinylated antibody CD45 were centrifuged at 1000 g for 20 min and resuspended in 1 mL of PBS1X with Goat Anti-Mouse IgG H&L Alexa Fluor 488 (1:100) (Thermo Fisher Scientific). The particles were incubated for 30 min at room temperature with gentle rotation. Thus, the presence of CD45 antibody onthe particles surface was checked by fluorescence microscopy (Nikon Eclipse Ti2). Moreover, particles incubated only with secondary antibody were considered as a negative control. The sample recovered from the first spiral device was stained with Hoechst (1:10.000) (Thermofisher −33342) and incubated with the particles coated with the biotinylated antibody CD45 for 30 min with gentle rotation. The Leukocytes binding to the polystyrene particles were checked by fluorescence (Nikon Eclipse Ti2) and quantified using ImageJ.

3.6 Mixing Analysis Experimental Validation

The experimental setup involved the injection of the two fluids into the microfluidic device, where the mixing efficiency was assessed by measuring the fluorescence intensity distribution along the channel. The images obtained from the experiment were processed using Fiji software to quantitatively analyze the mixing behavior. The experimental results demonstrated the effectiveness of the herringbone patterns in promoting mixing, confirming the accuracy of the simulations.

3.6.1 Device Setup and Experimental Conditions

The microfluidic devices were connected to a Harvard Apparatus syringe pump, which controlled the flow of two different solutions in separate experiments. In the first experiment, water was perfused through the left inlet, while the right inlet was perfused with a fluorescein solution (Sigma, #F6377) at a concentration of 0.1 mg/mL. In the second experiment, a viscous transparent solution, designed to mimic the viscosity of blood, was introduced through the left inlet. This solution was prepared by dissolving 3 g/mL Dextran from Leuconostoc spp (Sigma, #31392) to achieve a viscosity of 4 cP (0.04

dyn·s/cm²), facilitating the visualization of fluorescence. In both experiments, the solutions were perfused at carefully controlled rates through the microfluidic device for accurate analysis.

The two fluids were introduced into the device through a 1:10 mixing ratio between the two inlets. The left inlet, perfused with either water or the dextran solution, was set at a flow rate of 650 µL/min, while the right inlet, perfused with the fluorescein solution, was set at 65 µL/min. These flow rates were controlled precisely to ensure consistency between the two experiments and to evaluate the influence of different viscosities on the mixing efficiency. The combination of these experimental conditions enabled a systematic study of how fluid viscosity affects mixing behavior within the herringbone-patterned microfluidic channels.

3.6.2 Confocal Microscope Setup

To capture high-resolution images of the mixing process within the microfluidic devices, we used a Zeiss Axio Observer 7 microscope with an inverted stand, equipped with a Zeiss LSM 800 laser-scanning confocal module. The imaging was controlled using ZEN 2.3 (blue edition) software, and detection was enhanced by PTM Multi Alkali detector technology, providing the sensitivity needed for accurate fluorescence detection. To capture the full depth of the microfluidic channels, Z-stack imaging was employed with a 5x/0.16 M27 objective, capturing images at a resolution of 512 × 512 pixels, with a lateral resolution of 0.4007 pixels/µm and Z-slice spacing of 14 µm. This allowed for the complete visualization of fluid dynamics throughout the device.

Images were captured at strategic points along the microfluidic device, specifically between each herringbone pattern, to assess how fluid mixing progressed throughout the channel. The goal was to capture the distribution of fluorescein at key locations to monitor the effect of the herringbone structures on the mixing process. Using a resolution of 512 × 512 pixels, images were taken at multiple depths along the Z-axis of the channel, allowing for a detailed analysis of fluid behavior within the device.

To ensure that the entire depth of the microfluidic channels was analyzed, Z-stack imaging was employed. This technique involved capturing a series of images at different depths, with Z-slice spacing of 14 µm, covering the full height of the microfluidic channel. The use of Z-stacks allowed us to visualize the complete 3D structure of the fluid flow, ensuring no details were missed in regions that may have exhibited more complex mixing dynamics.

3.6.3 Image Processing and analysis with Fiji

Images captured during the confocal microscopy experiments were analyzed using Fiji, an open-source platform for image analysis (https://imagej.net/Fiji). The first step in the process involved enhancing each image to improve contrast, ensuring the fluorescein signal was clearly visible. This step was critical for accurate visualization of the fluid mixing patterns. A Region of Interest (ROI) was manually selected for each image, specifically focusing on the area between the herringbone patterns where fluid flow was observable.

After selecting the ROI, the image was divided into ten horizontal segments. This segmentation allowed for a more granular analysis of the distribution of the fluorescein across the width of the microfluidic channel. For each of these segments, the average fluorescence intensity per pixel was calculated, providing a precise measurement of how uniformly the dye was distributed. The goal was to quantify the degree of mixing along the channel. To simplify the data representation, the ten segments were grouped into five horizontal segments, each representing the average of two adjacent original segments. This approach provided a clearer overview of the distribution of fluorescence intensity across the channel, allowing for a more manageable and detailed evaluation of mixing efficiency at different points along the device.

To handle the large volume of images efficiently, a custom Fiji macro was developed and utilized for the systematic extraction of data. This macro enabled the sequential processing of multiple images, automatically extracting the mean fluorescence intensity for each ROI and segment. By automating these steps, the macro ensured consistency in the analysis across all images, reducing the possibility of human error and speeding up the process. The macro also allowed for the streamlined extraction of quantitative data, which was crucial for comparing mixing efficiency under different experimental conditions.

3.6.4 Mixing Efficiency Calculation/formula

The mixing efficiency in this study was calculated using a formula adapted from several key references on microfluidic mixing devices (7,102,120,134) , and uses the segments described in section 3.6.7 to define Li. The formula used is as follows:

Equation 14: Mixing Efficiency.

$$ME = 1 - \frac{1}{N-1} * \frac{\sum_{i=1}^{N} Lmax - Li}{Lmax}$$

Where:

- Lmax is the maximum fluorescence intensity observed among all segments within a single image.
- Li represents the fluorescence intensity in each segment.
- N is the total number of segments (or columns) into which the channel has been divided for analysis.

The formula used to calculate mixing efficiency assesses the degree of homogeneity in the distribution of the fluorescein dye within the microfluidic channel. By comparing the maximum fluorescence intensity Lmax with the intensity values of each segment Li, the formula evaluates how evenly the dye has mixed.

A mixing efficiency (ME) of 1 occurs when there is no variation in the intensity values across all segments (Li=Lmax for all segments). This result represents perfect mixing, where the dye is uniformly distributed throughout the channel. In this case, the summation term in the formula becomes zero, indicating no concentration differences.

In contrast, when there are significant differences in fluorescence intensity between the segments, the calculated ME approaches 0, reflecting poor mixing. In this scenario, the summation term increases as the differences between Li and Lmax are larger, indicating that the dye is unevenly distributed, with areas of high and low concentration within the channel.

One of the key aspects of this formula is its ability to normalize each image individually based on its own Lmax value. This normalization step is essential for maintaining consistency across images captured under different lighting conditions or imaging parameters, as it corrects for variations in image gain and exposure settings. By normalizing the fluorescence intensity to the maximum observed value in each image, we can directly compare the mixing efficiency across all captured images, ensuring accurate and consistent results.

The formula uses N−1 segments instead of N, as this approach guarantees that there will always be one segment where Li=Lmax. This ensures that we are not artificially inflating the mixing efficiency by including the segment with the maximum value in the calculation. This adjustment improves the reliability of mixing efficiency calculation and aligns with similar approaches in the literature.

The calculated mixing efficiency provides a quantitative measurement of the performance of the microfluidic device in mixing two fluids. This metric allows for a detailed comparison of how well the device can mix fluids with different viscosities or other properties under various flow conditions. By applying this formula across the different images and experimental conditions, we can evaluate the effectiveness of the herringbone patterns in promoting mixing and identify opportunities for design optimization.

Chapter4: 3D Printing Results and Discussion

4.1 Introduction to 3D Printing Performance in Microfluidics

This study aims to explore the capabilities of a customized DLP-SLA 3D printing setup to fabricate microfluidic devices with complex geometries, addressing the challenges associated with achieving high resolution and functional structures. The experimental focus is on evaluating the printer's ability to reliably produce microchannels while investigating critical factors such as resin selection, exposure settings, and calibration precision. By systematically assessing these variables, we seek to identify the conditions under which microchannels with specific dimensional requirements can be fabricated with minimal deviations from the design.

Surface roughness is hypothesized to be a key parameter affecting microfluidic performance, with the potential to disrupt fluid dynamics and influence outcomes in applications such as particle separation or mixing.

The fabrication of closed channels presents a particularly significant challenge, given the potential for over curing caused by UV light penetrating beyond the intended curing region. This work examines how exposure parameters and resin properties interact to maintain open channels while preserving dimensional fidelity. Resins with varying light absorbance properties are tested to determine their ability to prevent internal obstructions during the printing process.

Material compatibility is also a critical factor, particularly for applications requiring biocompatibility, transparency, and chemical resistance. Transparent materials are essential for real time observation of fluid flow and for validating device functionality.

The results of this investigation are expected to provide a comprehensive understanding of the current capabilities and limitations of DLP-SLA 3D printing for microfluidic device fabrication. By identifying areas for improvement and proposing potential solutions, this work aims to guide the development of optimized fabrication processes tailored to the demands of advanced microfluidic applications.

4.2 Projector Irradiance Calibration

At the initial setup of the 3D printer, projector irradiance calibration is conducted to evaluate the light output of the selected projector and determine the suitability of the fluorinated ethylene propylene (FEP) film for 3D printing. This process ensures that the FEP film does not excessively absorb irradiance, maintaining optimal conditions for precise layer curing.

Projector irradiance was measured using a Power and Energy meter USB interface with S302C Thermal Power Sensor (Bandwidth: $190\sim2500$ nm, Maximum 2 W, Sensor diameter 12 mm) from Thorlabs (Newton, NJ, USA). The sensor was fixed to the build platform adapter of the printer and brought to focus distance.

Measurements were performed at different projector pulse width modulation (PWM) setting value ($\mathrm{PWM} = 20, 45, 50, 70, 100, 150$). Irradiance was calculated for two different configurations: (i) no vat installed, (ii) vat with new FEP film, shown in Figure 42, where the irradiance of the DLP projector is shown. This calibration was essential to ensure optimal exposure and prevent over-curing during the 3D printing process.

As shown in Figure 25, the FEP absorbs more irradiance at higher values of LED intensity; however, the irradiance remains nearly linear within the range of 20-45 PWM. This stability in irradiance makes this range ideal for initiating our 3D printing experiments.

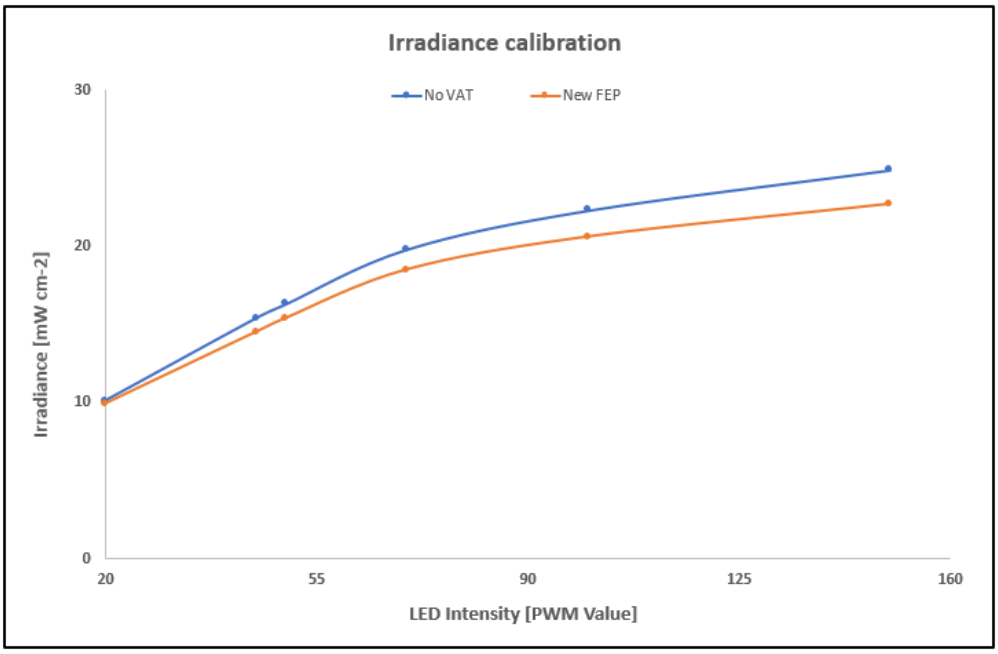


Figure 25: Irradiance calibration results depending on the LED intensity without vat and with a new FEP installed.

Figure 26 displays the VAT, which holds the liquid resin used during the printing process. The setup presents the mirror system, and the projector reflection located below the resin tray, which are essential components for directing UV light to cure the resin layer by layer.

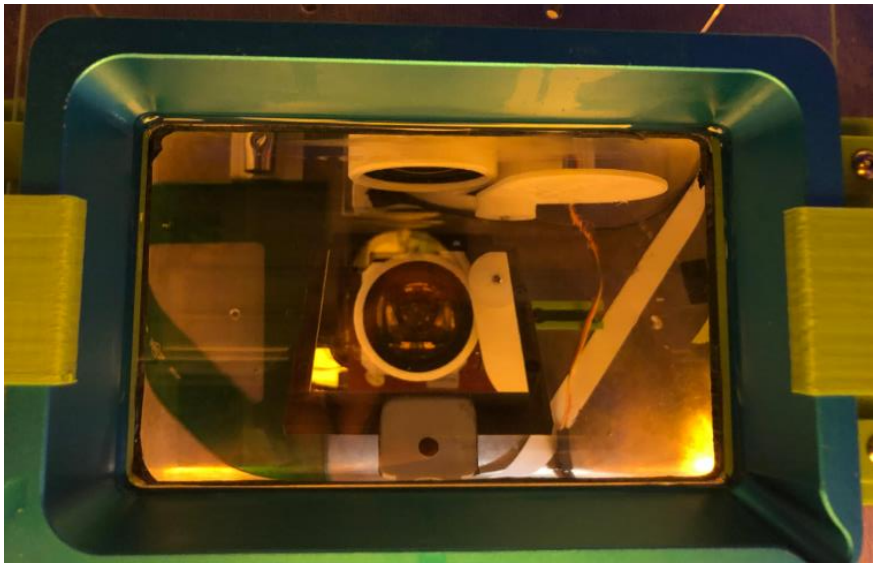


Figure 26: View of the VAT containing resin, with the mirror and projector reflection visible below the tray.

4.3 Absorbance Characterization of Resins

Absorbance testing is a fundamental step in optimizing 3D printing performance, as it directly impacts the energy absorption and polymerization efficiency of the resin layers during exposure to the DLP projector's UV light. The level of absorbance at the projector's peak wavelength determines how deeply the light penetrates the resin, influencing both the resolution and structural fidelity of the printed features. Resins with appropriate absorbance ensure that sufficient energy is delivered to cure each layer accurately without over curing or under curing adjacent layers. This is particularly critical for achieving fine resolution in complex microfluidic structures, where precise control of light penetration is essential to maintain dimensional accuracy and avoid occlusions in closed channels.

In this study, the absorbance spectra of three commercial resins (Detax, Asiga, and Keyprint) were measured to evaluate their compatibility with our DLP projector, which operates at a peak wavelength of 385 nm. The analysis provides insights into the curing dynamics of each resin, enabling the identification of optimal exposure settings to achieve uniform and controlled polymerization. By characterizing the absorbance properties, this step ensures that the selected resins are suitable for

producing high resolution microfluidic devices with minimal fabrication errors, setting a solid foundation for the subsequent optimization and printing processes.

As shown in Figure 27, the absorbance characteristics of each resin vary significantly:

- **Detax Resin**: This resin demonstrates an absorbance peak close to 385 nm, aligning well with our projector's emission peak. This suggests that the Detax resin is well-suited for polymerization, as it efficiently absorbs light at the projector's optimal wavelength, facilitating effective curing within the projected area.
- **Asiga Resin**: The Asiga resin displays a significantly higher absorbance: approximately 2.5 times greater than the Detax resin at 385 nm.
- **Keyprint Resin**: While the Keyprint resin does not exhibit a distinct peak at 385 nm, its absorbance level is similar to that of the Detax resin in the targeted range. Due to its comparable absorbance, Keyprint was also selected for testing as a potential candidate, given it may yield similar curing performance under the 385 nm light.

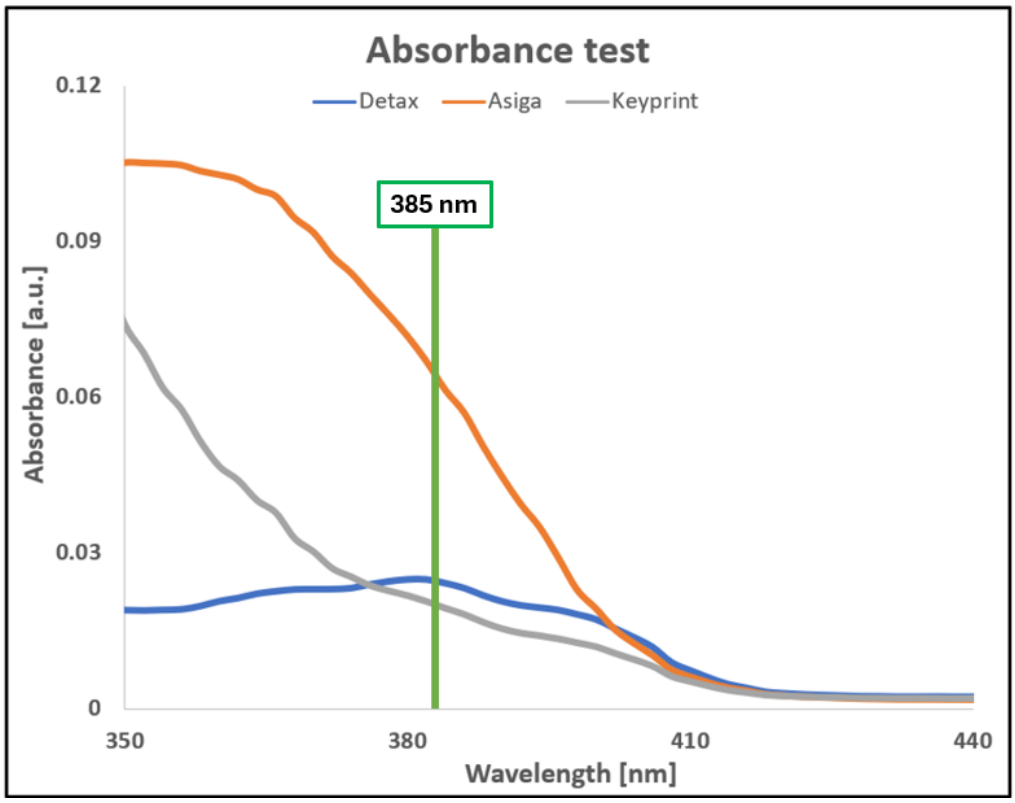


Figure 27: Graph presenting the absorbance for three commercial resins and its dependency with respect to the light wavelength, from 350 nm to 440 nm.

The absorbance results shown in Figure 43 provide essential guidance for determining the initial exposure times for each resin during 3D printing. Asiga resin, with the highest absorbance at 385 nm (2.5x higher than Detax and Keyprint), will require longer exposure times to deliver sufficient energy for complete layer polymerization. Its higher absorbance limits light penetration, necessitating more energy to ensure consistent curing throughout the layer. In contrast, Detax and Keyprint resins, which exhibit lower absorbance, allow light to penetrate more easily, potentially requiring shorter exposure times. As reported in (80), custom resins can achieve higher absorption than Asiga Plasclear resin, but on the same order of magnitude.

These differences in absorbance levels emphasize the importance of tailoring exposure times and light intensities to each resin, optimizing settings for different geometries and features. While all three resins demonstrated sufficient absorbance at 385 nm for further testing, the characterization underscores the need for precise adjustments to achieve successful layer-by-layer polymerization without over curing or insufficient curing. The next step involves refining exposure parameters for each resin to enable the accurate fabrication of complex microfluidic structures.

4.4 Optimization of Exposure Settings for 3D Printed Microstructures

Optimizing exposure settings is essential for achieving the precision required in 3D printing of microfluidic devices. Exposure time and light intensity directly influence the polymerization of resin layers, affecting both the resolution and structural fidelity of the printed features. Proper optimization ensures that each layer receives the necessary energy to cure without over curing adjacent layers, which is critical for maintaining the integrity of intricate geometries such as closed channels or high-aspect-ratio structures. This section outlines the systematic approach used to determine the ideal exposure settings for each resin, tailored to their unique absorbance characteristics and curing behavior.

4.4.1 Preliminary Exposure Range Test

Before testing individual settings for each resin, an initial range finding experiment was conducted using a parametric test structure. As shown in Figure 28 the design comprised six subgroups of squares, each containing five squares with dimensions of 100 µm, 200 µm, 300 µm, 600 µm, and 1000 µm, all with a height of 500 µm. For each layer, the DLP projector applied a unique exposure time to each subgroup, incrementally increasing the duration of exposure across the six subgroups. This allowed for the simultaneous evaluation of six different exposure times within a single experiment, with a fixed LED intensity. By repeating this process with different intensities and resins, a wide range of resin-intensity-time combinations were tested.

This approach aims to systematically explore how exposure duration influences the ability to accurately replicate features across different scales. Through these experiments, the goal is to identify the most optimal parameters for each resin.

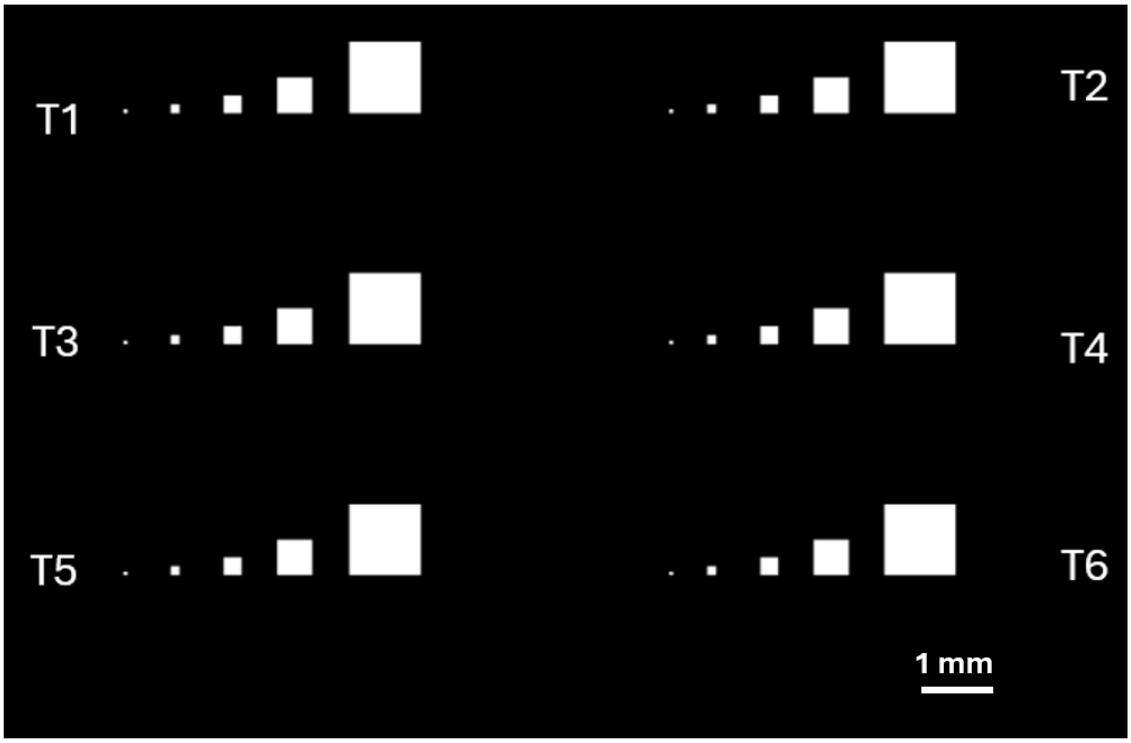


Figure 28: Top view of the designed test structure used to evaluate the effect of exposure time on dimensional accuracy. The design consists of six subgroups (T1–T6), each containing five squares with dimensions of 100 µm, 200 µm, 300 µm, 600 µm, and 1000 µm. Each subgroup is exposed to a unique exposure time, incrementally increasing from T1 to T6. This setup allows for the analysis of how varying exposure times influence the replication of features at different scales for a given resin and intensity.

The initial intensity values were chosen based on manufacturer specifications, literature values relevant to each resin type, and the results from Figure 26. This figure highlights that, for these intensity values, the FEP film does not absorb a significant amount of irradiance, ensuring efficient light transmission for the polymerization process. This preliminary test allowed for a quick visual assessment of suitable exposure times and intensities, helping identify ranges that would allow a correct curing. Shorter exposure times or lower intensities resulted in incomplete or under cured features, especially problematic for high aspect ratio structures that require adequate energy for proper formation. Conversely, longer exposure times or higher intensities led to over curing, causing closely spaced features to merge. This underscores the importance of identifying the minimum exposure times and intensities that ensure complete curing of the printed features.

From this initial test, a set of promising combinations of exposure time and intensity were identified, providing a foundation for further optimizations. These combinations were then

applied to different types of structures in subsequent tests to evaluate their effectiveness in achieving optimal print quality. This approach provided valuable insight into each resin's curing tolerance and helped establish practical exposure settings for the following iterative testing phase.

Table 5: Exposure times tested for each subgroup (T1–T6) in the parametric design. Times are listed for two layer thicknesses (50 µm and 100 µm) and for each resin (Detax, Asiga, and Keyprint). These exposure times were applied uniformly across all layers within each subgroup to evaluate their impact on feature replication and curing behavior.

	50 µm			100 µm		
	Detax	**Asiga**	**Keyprint**	**Detax**	**Asiga**	**Keyprint**
T1	0.5 s	2.5 s	0.5 s	1 s	5 s	1 s
T2	1.25 s	5 s	1.25 s	2.5 s	10 s	2.5 s
T3	2 s	10 s	2 s	4 s	20 s	4 s
T4	2.75 s	15 s	2.75 s	5.5 s	30 s	5.5 s
T5	3.5 s	20 s	3.5 s	7 s	40 s	7 s
T6	4.25 s	25 s	4.25 s	8.5 s	50 s	8.5 s

The results of the exposure range tests are summarized in six tables, corresponding to the combinations of layer thickness (50 µm and 100 µm) and resin type (Detax, Asiga, and Keyprint). Each table evaluates the curing behavior of the parametric design under varying exposure times and intensities. The data is color-coded for clarity: red indicates cases where 0–2 of the five structures were successfully printed, yellow marks conditions where 3–4 structures were produced, and green signifies conditions where all five structures were successfully replicated.

The analysis of the data reveals a consistent outcome across all tests. When only one structure is successfully cured (marked as "1"), it is always the largest square. When two structures are formed (marked as "2"), they are the two largest squares, and so on. This trend is attributed to the increased projected area of larger structures, which accumulates more energy from the projector during curing. As a result, larger structures polymerize more easily under conditions of lower exposure time and intensity, while smaller structures require higher energy input to achieve complete curing.

The six tables provide a comprehensive overview of how the combination of exposure time, intensity, and resin type influences the ability to replicate features of varying sizes. These results set the foundation for further analysis and optimization of printing parameters to achieve

consistent and accurate 3D printed structures, with subsequent sections focusing on specific findings and their implications.

Table 6: Summary of exposure conditions for Detax with 50 µm layers: number of successfully replicated structures under different PWM levels and exposure time combinations.

PWM	0.5 s	1.25 s	2 s	2.75 s	3.5 s	4.25 s
20	0	3	4	5	5	5
25	0	3	4	5	5	5
30	1	4	5	5	5	5
35	1	5	5	5	5	5
40	2	5	5	5	5	5
45	2	5	5	5	5	5

Table 7: Summary of exposure conditions for Detax with 100 µm layers: number of successfully replicated structures under different PWM levels and exposure time combinations.

PWM	1 s	2.5 s	4 s	5.5 s	7 s	8.5 s
20	1	3	4	5	5	5
25	1	4	5	5	5	5
30	2	5	5	5	5	5
35	2	5	5	5	5	5
40	2	5	5	5	5	5
45	2	5	5	5	5	5

Table 8: Summary of exposure conditions for Asiga with 50 µm layers: number of successfully replicated structures under different PWM levels and exposure time combinations.

PWM	2.5 s	5 s	10 s	15 s	20 s	25 s
20	0	0	2	4	5	5
25	0	1	3	4	5	5
30	0	1	4	5	5	5
35	0	1	4	5	5	5
40	0	2	5	5	5	5
45	0	2	5	5	5	5

Table 9: Summary of exposure conditions for Asiga with 100 µm layers: number of successfully replicated structures under different PWM levels and exposure time combinations.

PWM	5 s	10 s	20 s	30 s	40 s	50 s
20	0	1	2	4	5	5
25	0	1	3	4	5	5
30	0	2	4	5	5	5
35	0	2	5	5	5	5
40	0	2	5	5	5	5
45	0	2	5	5	5	5

Table 10: Summary of exposure conditions for Keyprint with 50 µm layers: number of successfully replicated structures under different PWM levels and exposure time combinations.

PWM	0.5 s	1.25 s	2 s	2.75 s	3.5 s	4.25 s
20	0	1	2	3	4	5
25	0	1	3	4	5	5
30	0	2	3	5	5	5
35	0	2	4	5	5	5
40	0	2	4	5	5	5
45	0	2	5	5	5	5

Table 11: Summary of exposure conditions for Keyprint with 100 µm layers: number of successfully replicated structures under different PWM levels and exposure time combinations.

PWM	1 s	2.5 s	4 s	5.5 s	7 s	8.5 s
20	0	1	2	4	5	5
25	0	1	3	4	5	5
30	0	2	4	5	5	5
35	0	2	5	5	5	5
40	0	2	5	5	5	5
45	0	2	5	5	5	5

The results of the exposure range tests reveal a logical and predictable trend across all resins and layer thicknesses. At lower energy levels, characterized by low intensity and short exposure times, all resins exhibit under cured structures. This occurs because the total energy received by the resin is insufficient to initiate or complete polymerization, resulting in incomplete or non-formed structures. As energy increases, the results show that only the largest structures form successfully. This is consistent with the fact that larger features accumulate more energy due to their greater projected area, enabling polymerization under lower energy conditions. Beyond a certain threshold of energy, all five structures are consistently formed, indicating that the exposure parameters are sufficient to fully cure even the smallest features. However, at very high energy levels, over curing becomes apparent, as adjacent features begin to merge due to excessive polymerization, compromising the dimensional fidelity of the printed structures.

When comparing results for the same resin between 50 µm and 100 µm layer thicknesses, an interesting pattern emerges. For the 100 µm layer thickness, using double the exposure time relative to the 50 µm layers, the structures form successfully under a wider range of energy conditions. Specifically, for the 100 µm layer thickness, more combinations of intensity and time result in the successful formation of all five structures, compared to the 50 µm layers. This suggests that increasing the layer thickness allows for faster and more consistent curing across multiple feature sizes.

These results emphasize the importance of finding the right balance in exposure parameters to ensure accuracy in the printed structures, while avoiding issues like under curing and over curing. The results highlight how feature size, energy input (intensity of the UV light and time exposure), and resin properties influence the success of the printing process. Based on these findings, the next set of experiments will start with a fixed parameter to reduce variability: the PWM will be set to 35 with an intensity of 7.2 A. The exposure times will begin at 1.25 s for Detax with 50 µm layers, 2.5 s for Detax with 100 µm layers, 15 s for Asiga with 50 µm layers, 20 s for Asiga with 100 µm layers, 2.75 s for Keyprint with 50 µm layers, and 4 s for Keyprint with 100 µm layers. These parameters will be used as a starting point to print more complex structures, iterating the exposure time to achieve optimal results, as will be detailed in the following section.

From the data presented in Tables 6 through 11, we can empirically analyze the minimum illumination time conditions (tic) necessary to replicate all the designed structures successfully. Using the irradiance calibration graph in Figure 25 to derive the irradiance values corresponding to different LED intensities, the tic values for each resin and configuration were consolidated into Table 12.

Table 12: Minimum ilumination time conditions.

	Detax 50	Detax 100	Asiga 50	Asiga 100	Keyprint50	Keyprint100
10 mWcm-2	2,75 s	5,5 s	20 s	40 s	4,25 s	7 s
11 mWcm-2	2,75 s	4 s	20 s	40 s	3,5 s	7 s
12 mWcm-2	2 s	2,5 s	15 s	30 s	2,75 s	5,5 s
13 mWcm-2	1,25 s	2,5 s	15 s	20 s	2,75 s	4 s
14 mWcm-2	1,25 s	2,5 s	10 s	20 s	2,75 s	4 s
15 mWcm-2	1,25 s	2,5 s	10 s	20 s	2,0 s	4 s

Using the equation 1 from Chapter 1, about Dose Control, we can consider that the polymerization efficiency (EFF) to obtain all the printing structures will be proportional to D(z,t). In this sense:

Equation 15: Polymerization Efficiency.

$$EFF = \delta * D(z, t_{ic})$$

with Delta (δ) being a parameter depending of each resin and z=50 µm or 100 µm. If we apply logarithms:

Equation 16: Ln Polymerization Efficiency.

$$Ln(EFF) = Ln(\delta) + Ln(t_{ic} * I_0) - z/h_a$$

We can calculate the main values for each resin using the previous table

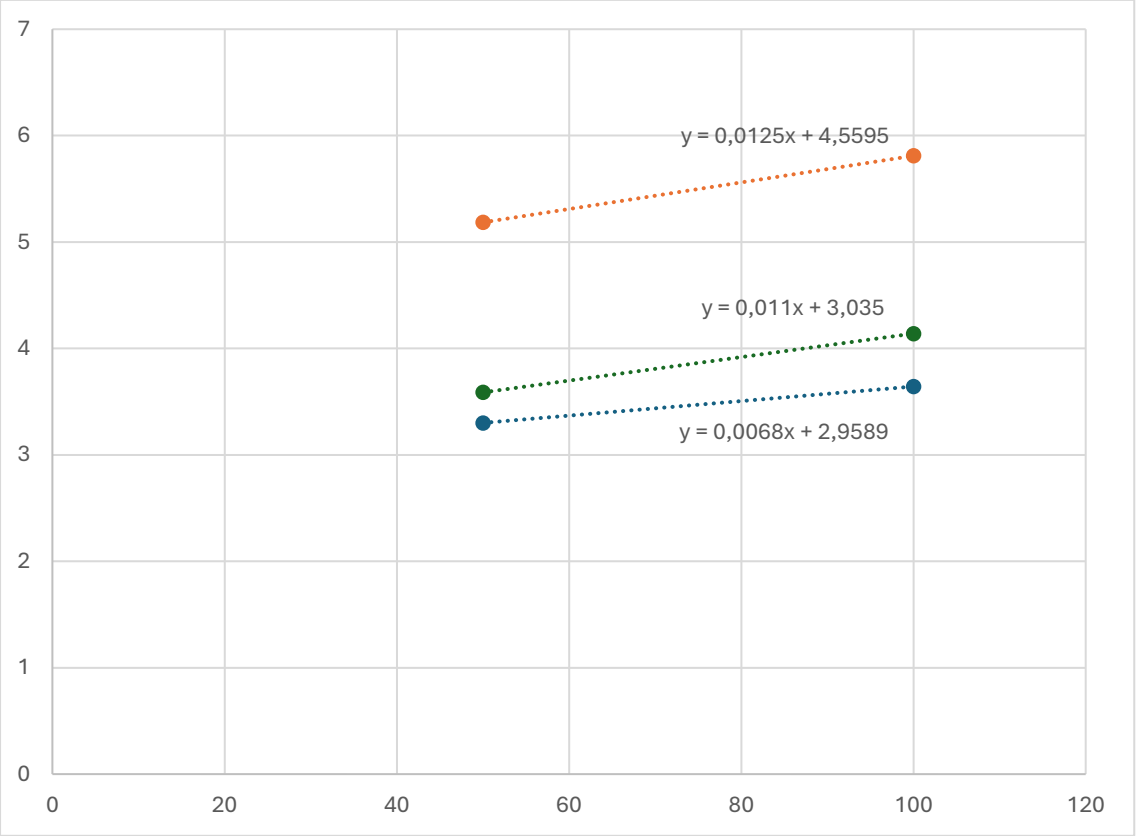
Table 13: Polymerization Efficiency Calculation

	Detax 50	Detax 100	ASIGA 50	ASIGA 100	Keyprint 50	Keyprint 100
Ln ($t_{ic}*I_0$)	3,30 ±0,12	3,70±0,22	5,19±0,18	5,81±0,21	3,59±0,12	4,14±0,15
n	3 (1)	6	6	6	6	6

(1) The minimum t values (1,25) introduce too much error so they are discarded

The values corresponding to 1.25 s for Detax 50 µm were excluded from the analysis because they were deemed to introduce the highest level of error.

For each resin using the values for 50 µm and 100 µm, we can estimate the value of Delta and the value of h_a.



Ln (δ) can be obtained as the 0-intercept and h_a from the inverse of the slope .

Table 14: Alpha and ha.

		Detax	Asiga	Keyprint
Alpha	exp(intercept)	19,3	95,5	20,7
	normalized to Detax	1,0	5,0	1,1
h_a	1/slope	146	80	91

The results for h_a align with the absorbance values presented in Figure 27, where Asiga demonstrates the highest absorbance among the tested resins. However, despite Detax and Keyprint exhibiting similar absorbance levels, their h_a values differ significantly. Additionally, it was determined that Asiga requires approximately five times more energy than Detax to achieve the same level of structure polymerization. Keyprint, on the other hand, requires only about 1.1 times more energy than Detax, underscoring Detax as the most energy-efficient resin for achieving polymerization.

4.4.2 Iterative Adjustment of Printing Parameters

Based on the results from the previous tests, this phase begins with a defined starting point for exposure parameters of a PWM of 35. The goal is to refine exposure times to enhance the resolution and accuracy of printed microstructures, adapting the settings for a broader range of feature sizes and designs.

Following the preliminary range finding experiment, a series of iterative tests were performed to refine the exposure time and intensity settings specific to each resin. One of the primary structures used for these tests, shown in Figure 29, included a range of feature types and dimensions to evaluate the printer's performance across various geometric configurations. This structure comprised cylinders ranging from 100 µm to 500 µm in diameter, with aspect ratios from 1 to 5, created both as extrusions above the surface and as recesses within the material. Additionally, square features with side lengths from 100 µm to 500 µm were printed, also with aspect ratios varying up to 5. Rectangular features of different sizes and separations, ranging between 100 µm and 500 µm, were incorporated to assess the minimum achievable spacing and dimensional accuracy.

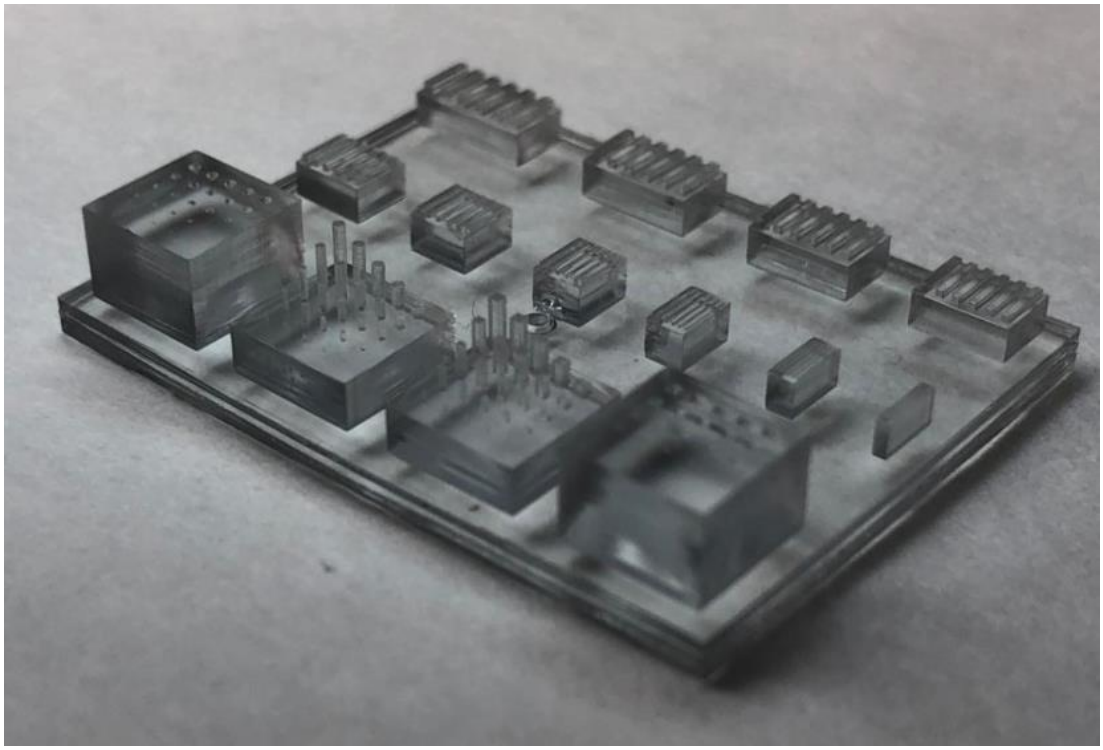


Figure 29: Test structure used to optimize exposure settings, featuring various geometries for resolution assessment. The structure includes cylindrical features with diameters ranging from 0.1 mm to 0.5 mm and aspect ratios from 1 to 5, both as extrusions and recessed holes. Square features, also ranging from 0.1 mm to 0.5 mm per side with similar aspect ratios, are included alongside rectangular features with varying dimensions and separations between 0.1 mm and 0.5 mm. This configuration allowed evaluation of achievable resolution, spacing, and fidelity across different shapes and aspect ratios.

These specific feature variations allowed us to systematically assess the impact of exposure settings on different types of microstructures, including isolated extrusions, recessed details, and elements with varying aspect ratios. By adjusting the exposure time and intensity in incremental steps, we were able to observe how closely spaced or high-aspect-ratio features responded to different curing conditions. This iterative approach enabled us to establish optimal parameters that could be further adapted based on the structural requirements of each resin.

During the iterative adjustment phase, it was observed that the Asiga resin's higher absorbance necessitated extended exposure times for adequate curing of fine details, while Detax and Keyprint allowed for shorter curing cycles but faced challenges in maintaining separation between closely spaced features. Fine features below 200 µm were particularly sensitive to over curing, emphasizing the importance of precise parameter calibration for each resin.

This process ultimately led to the identification of final settings that provided a balance between achieving high resolution and minimizing over curing effects, ensuring structural fidelity for each resin type. The insights gained from Figure 29, among other test geometries, contributed significantly to defining the practical limits of the DLP-SLA printing process in producing precise microfabricated structures.

As previously explained, the optimal 3D printing parameters for each resin (Detax, Asiga, and Keyprint) were established through a systematic, empirical adjustment of layer thickness, exposure time, and light intensity. The goal was to achieve the highest resolution and structural fidelity with minimal fabrication errors across various feature sizes and configurations. The final optimized parameters, as summarized in Table 11, present the settings that yielded the best results for each resin.

Table 15: Optimal settings empirically determined for the different resins tested.

Variable	Detax		Asiga		Keyprint	
Layer thickness (µm)	50	100	50	100	50	100
Exposure time for burn in layer (s)	4	6	30	40	5	7
Exposure time for normal layer (s)	1.25	2	12.5	20	2.5	4
Light power (PWM)	35	35	35	35	35	35

For layer thickness, both 50 µm and 100 µm layers were tested. Exposure times were optimized separately for burn-in and normal layers: extended exposure for burn-in layers ensured strong adhesion to the glass substrate, forming a stable base for subsequent layers, while shorter exposure times for normal layers helped maintain precision and avoid over curing. The light power, set at 35 PWM for consistency, was further explored in preliminary tests to evaluate each resin's response under varying intensities.

Each resin demonstrated unique curing characteristics, necessitating specific adjustments in exposure times to meet its critical energy (Ec) threshold, which is the minimum amount of energy required to form a solid layer during 3D printing. The Ec value varies depending on several factors, including the type and concentration of photoinitiators in each resin, as well as the resin's absorbance properties. Resins with higher absorbance require more energy to achieve polymerization due to reduced light penetration. Additionally, properties such as viscosity, which can influence light scattering, and refractive index, which affects how light interacts within the resin, also play a role in determining the critical exposure energy. These combined factors must be carefully considered when optimizing exposure parameters for precise and reliable 3D printing.

The optimized parameters allowed for successful fabrication of complex microstructures with minimal over curing issues. Excessive exposure or high intensities led to over curing, causing adjacent structures to merge or small holes to clog, while insufficient exposure compromised the formation of smaller features or high-aspect-ratio elements. Through this controlled iterative process, stable and reproducible printing conditions were established for each resin.

In summary, this optimization process emphasizes the critical balance between exposure time, intensity, and layer thickness to achieve high resolution, prints in DLP based microfabrication. These findings provide a robust protocol for employing Detax, Asiga, and Keyprint resins in applications that demand precise microstructural features.

With the optimal exposure settings established, the focus shifted towards evaluating the dimensional accuracy achieved under these parameters. Section 4.5 examines the width and Z-dimension fidelity of printed features, essential for assessing the reproducibility and practical applicability of the chosen settings in producing complex microfluidic structures.

The optimized exposure parameters identified in this study are fundamental for the correct use and functionality of the 3D printer. Moreover, minimizing defects like over curing enhances the reliability and reproducibility of the fabrication process, ensuring that the devices consistently

meet the requirements for advanced applications. This optimization was a critical step for the successful implementation of 3D printed microfluidic systems in experimental and practical settings.

4.5 Dimensional Accuracy

This section presents a detailed analysis of dimensional accuracy, a critical parameter in microfluidic applications where precise channel dimensions are essential for controlling fluid flow and ensuring device functionality. Dimensional fidelity in both horizontal (XY) and vertical (Z) measurements directly influences the performance and reliability of microfluidic devices, as even minor deviations can result in inconsistent flow rates or structural defects. By focusing on the evaluation of dimensional accuracy across different resins, this study aims to provide the capabilities and limitations of the 3D printing process. This analysis was based on the parameters established in previous sections to evaluate the precision of structures with varying feature sizes, aspect ratios, and separations. The findings will clarify the capabilities of this 3D printing technique, providing a comprehensive understanding of its potential to fabricate reliable and precise microfluidic devices tailored to specific applications.

4.5.1 Width Dimensioning

To determine the XY resolution of our custom build DLP 3D printer, a parametric design model was employed, fabricated with three commercial resins: Detax Freeprint Ortho, Asiga PlasCLEAR, and Keyprint KeyOrtho IBT. Each resin was printed at three target heights (200 µm, 400 µm, and 600 µm), to assess the influence of height on the printing accuracy and resolution capabilities. Figure 30A illustrates the digital model designed in Autodesk Inventor, and Figure 30B presents an example of the 3D-printed output using the Asiga resin at 600 µm height.

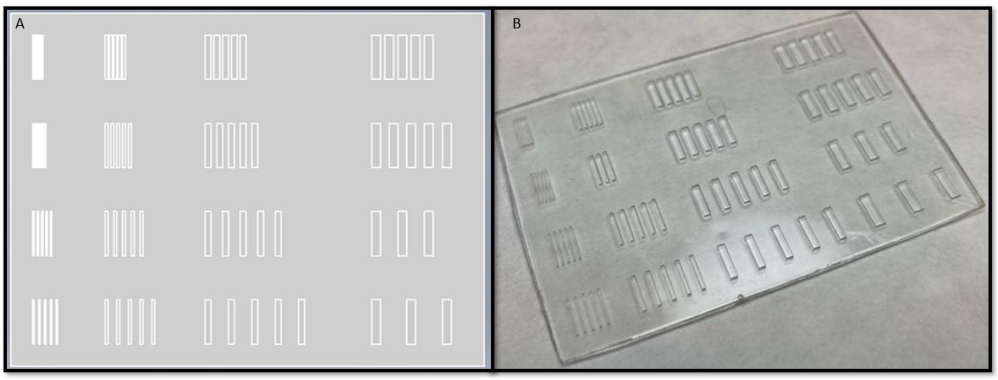


Figure 30: (A) Figure of the parametric design made with Inventor from Autodesk. (B) Picture of one of the 3D printed piece obtained, for the design of 600 µm height and the resin from Asiga.

The parametric design consists of an array of pillars with systematically varied widths and separations, providing a comprehensive assessment of each resin's capacity to resolve fine features. The model introduces three key variable parameters: pillar height, pillar width, and separation between pillars. These parameters were selected to determine the types of features achievable with each resin and to evaluate the printing resolution. In each print, the pillar height remains constant, while the width and separation vary depending on the row and column. Sixteen subgroups of pillars are arranged in a 4 × 4 grid, allowing a structured analysis of print quality and dimensional accuracy across a range of feature sizes and spacings.

Specifically, the width of each pillar is set to be a multiple of its height, progressing from half the height in the first column to three times the height in the last column. From left to right in Figure 5a, column 1 has pillars with widths set to half the height, column 2 matches the width to the height, column 3 doubles the width relative to the height, and column 4 triples it. Similarly, the separation between pillars increases down each row, starting with a separation of half the pillar width in row 1, matching the width in row 2, doubling the width in row 3, and tripling it in row 4. There were three designs, including three pillar heights (600 µm, 400 µm, and 200 µm), resulting in the largest pillars having a width of 1800 µm and the smallest a width of 100 µm. All pillars are 6 mm in length, creating a consistent basis for comparing feature resolution across resins. This structured variation enables a detailed analysis of each resin's dimensional fidelity and the overall effectiveness of the printing technique.

Using the parameters shown in Table 12, the smallest features achieved with each resin are reported in Figure 31, where the smallest structure obtained with a good definition and a good separation between features is shown. Additionally, the structure where the features start to have an imperfect separation is shown.

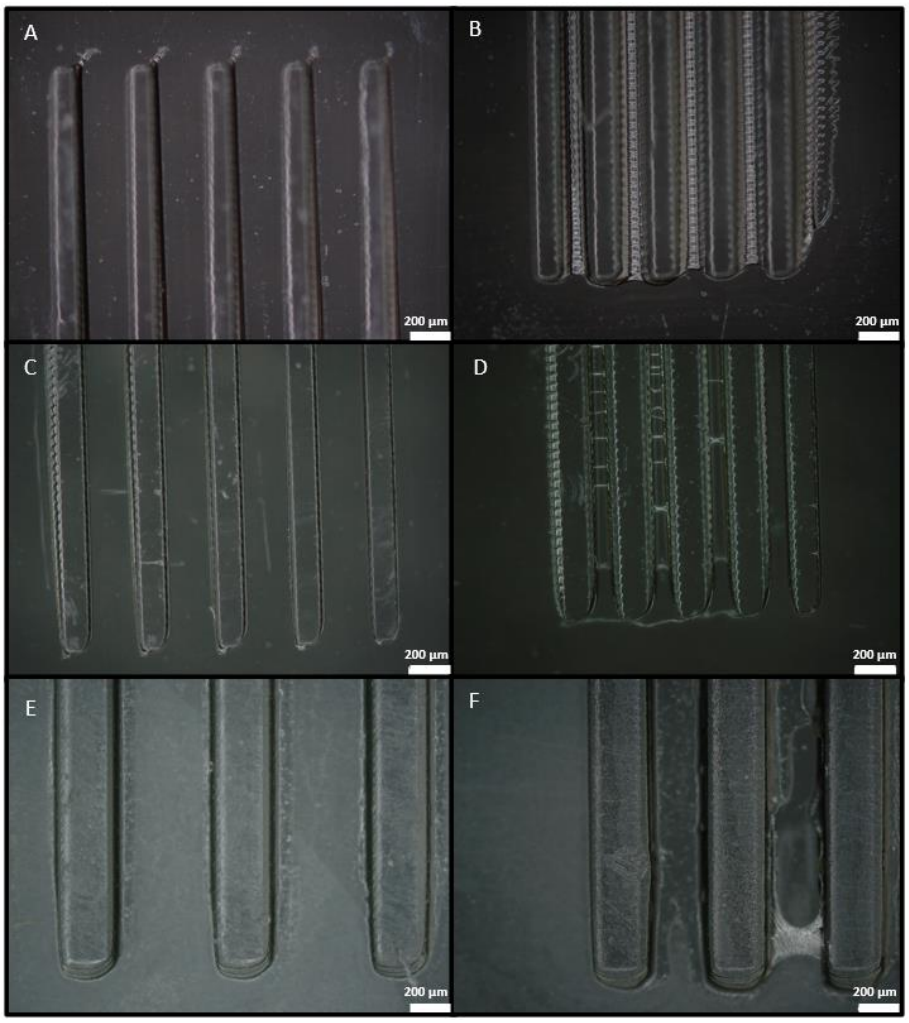


Figure 31: (A) Picture of the part printed with Detax, with a designed height of 200 µm, a width of 100 µm with a separation of 300 µm. (B) Picture of the part printed with Detax, with a designed height of 200 µm, a width of 100 µm with a separation of 200 µm. (C) Picture of the part printed with Asiga, with a designed height of 200 µm, a width of 100 µm with a separation of 300 µm. (D) Picture of the part printed with Asiga, with a designed height of 200 µm, a width of 100 µm with a separation of 200 µm. (E) Picture of the part printed with Keyprint, with a designed height of 400 µm, a width of 200 µm with a separation of 600 µm. (F) Picture of the part printed with Keyprint, with a designed height of 400 µm, a width of 200 µm with a separation of 400 µm. The figures in (A,C,E) are the ones obtained with the minimum height for each resin, the width being half the weight and the separation being three times the width and with a correct definition. The figures in (B,D,F) are the ones obtained with the minimum height for each resin, the width being half the weight and the separation being two times the width, and it can be appreciated that the separation of the structures starts being imperfect. The scale bar for all figures is 200 µm.

The width error was studied for the three resins for all the different structure configurations and a clear trend was identified. The presented error was obtained measuring the size of the objects in the printed result and comparing the result with the designed size. As seen in the following graphs shown in Figures 32, 33 and 34, the resolution error increases as the size of the structure and the separation between them decrease. In the graphics shown in Figures 32, 33 and 34, the X-axis corresponds to the width of the feature, going from half the height in the left to three times the height in the right. The Y-axis instead corresponds to the separation between the features, going from half of the width in the front to three times the width in the back. The Z-axis represents the

error calculated in the height of the features in percentage.The results obtained for the three resins with the designs of 600 µm height is shown in Figure 32.

For the Detax resin, the error goes from 0.40% in the worst case to 0.01% in the optimum scenario. For the Asiga resin, the error goes from 9.83% to 0.02%. For the Keyprint resin, the error goes from 1.99 % to 0.15%.

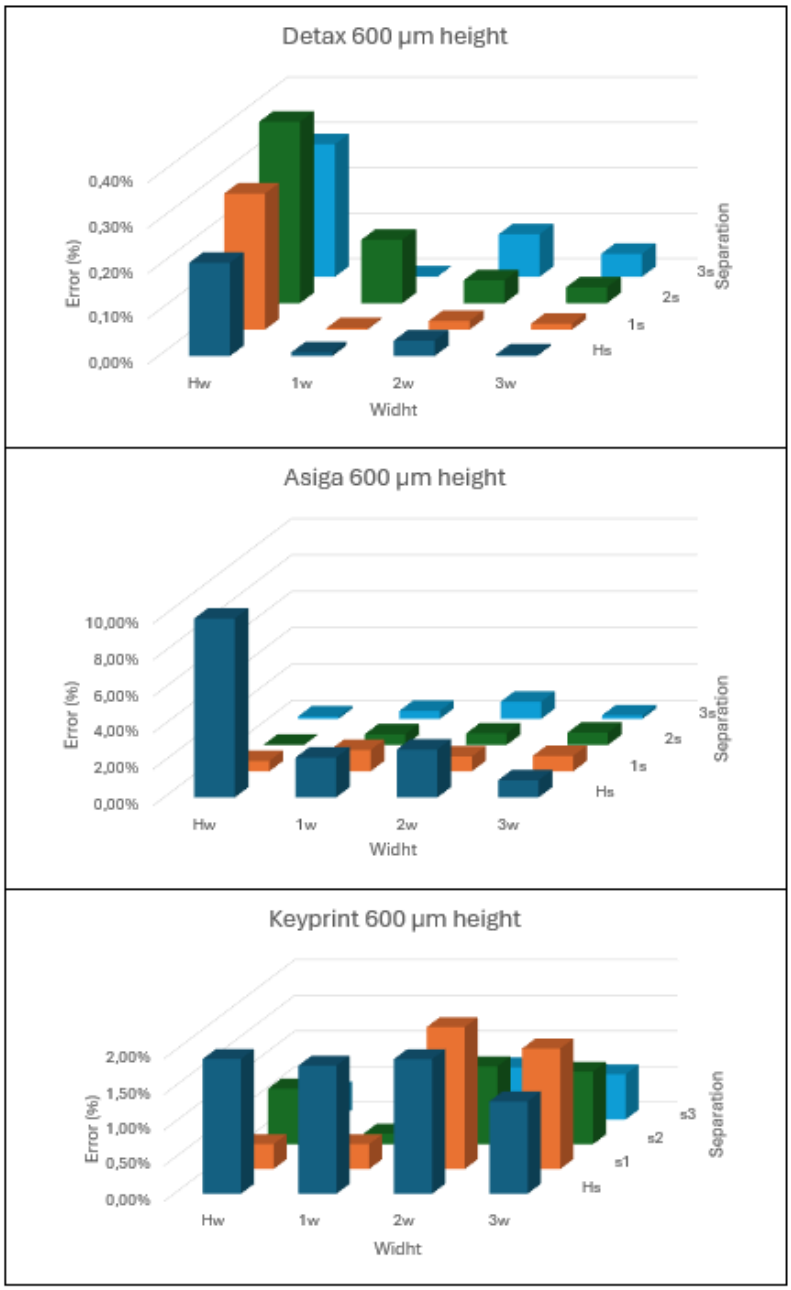


Figure 32: (A) Graphic from the error obtained printing the Detax part of 600 µm height. (B) Graphic from the error obtained printing the Asiga part of 600 µm height. (C) Graphic from the error obtained printing the Keyprint part of 600 µm height. In all (A,B,C), the X-axis corresponds to the width of the feature, going from the half of the height in the left to three times the height in the right. The Y-axis instead corresponds to the separation between the features, going from the half of the width in the front to three times the width in the back. The Z-axis represents the error calculated in the height of the features in percentage.

The results obtained for the three resins with the designs of 400 µm height is shown in Figure 33.

For the Detax resin, the error goes from 0.65% in the worst case to 0.02% in the optimum scenario. For the Asiga resin, the error goes from 15.08% to 0.69%. For the Keyprint resin, the error goes from 16.45% to 0.23%.

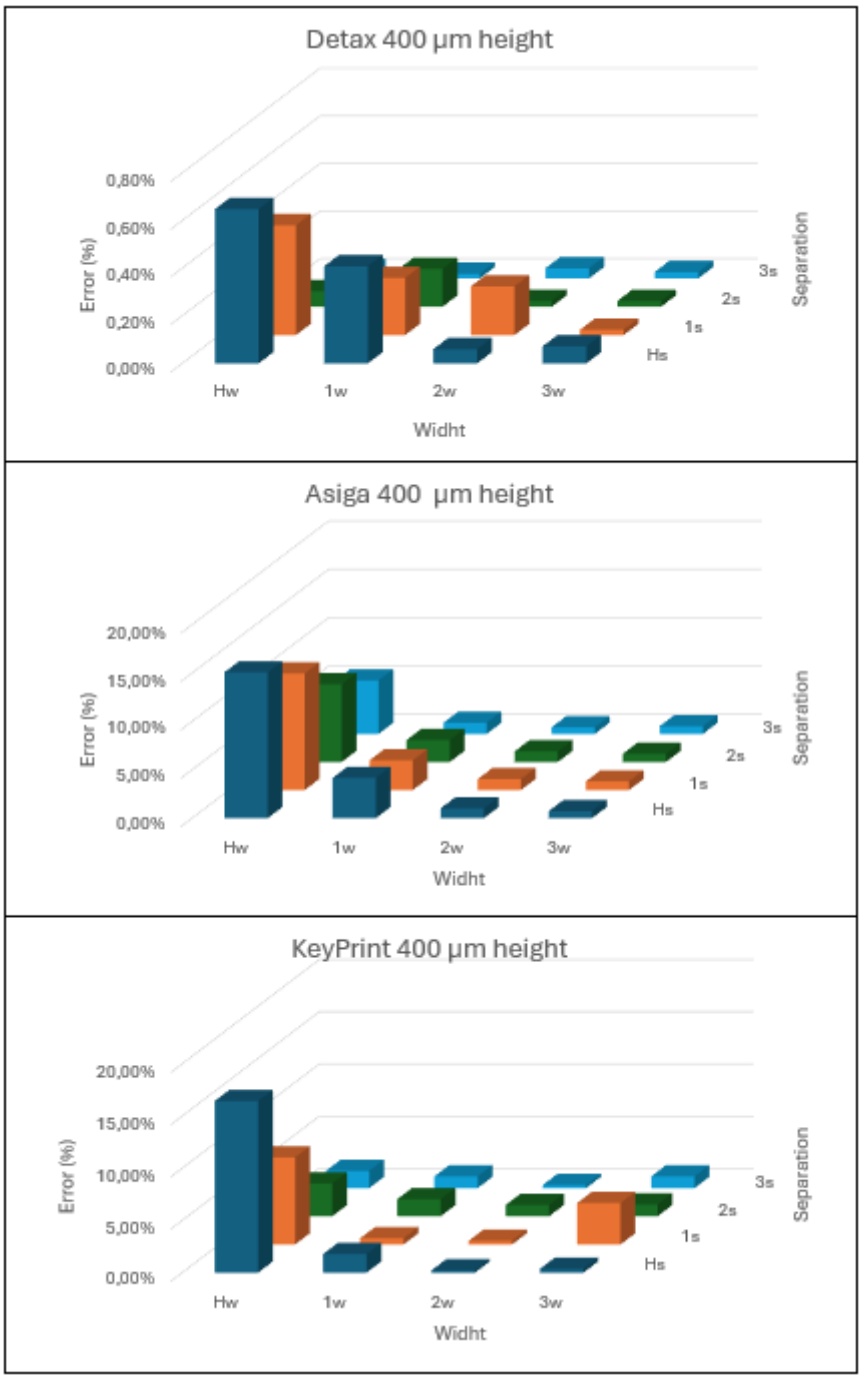


Figure 33: (A) Graphic from the error obtained printing the Detax part of 400 µm height. (B) Graphic from the error obtained printing the Asiga part of 400 µm height. (C) Graphic from the error obtained printing the Keyprint part of 400 µm height. In all (A,B,C), the X-axis corresponds to the width of the feature, going from the half of the height in the left to three times the height in the right. The Y-axis instead corresponds to the separation between the features, going from the half of the width in the front to three times the width in the back. The Z-axis represents the error calculated in the height of the features in percentage.

The results obtained for the Detax and Asiga resins with the designs of 200 µm height is shown in Figure 34. Keyprint results are not included as features were not properly printed.

For the Detax resin, the error goes from 6.08% in the worst case to 0.11% in the optimum scenario. For the Asiga resin, the error goes from 45.63% to 5.00%.

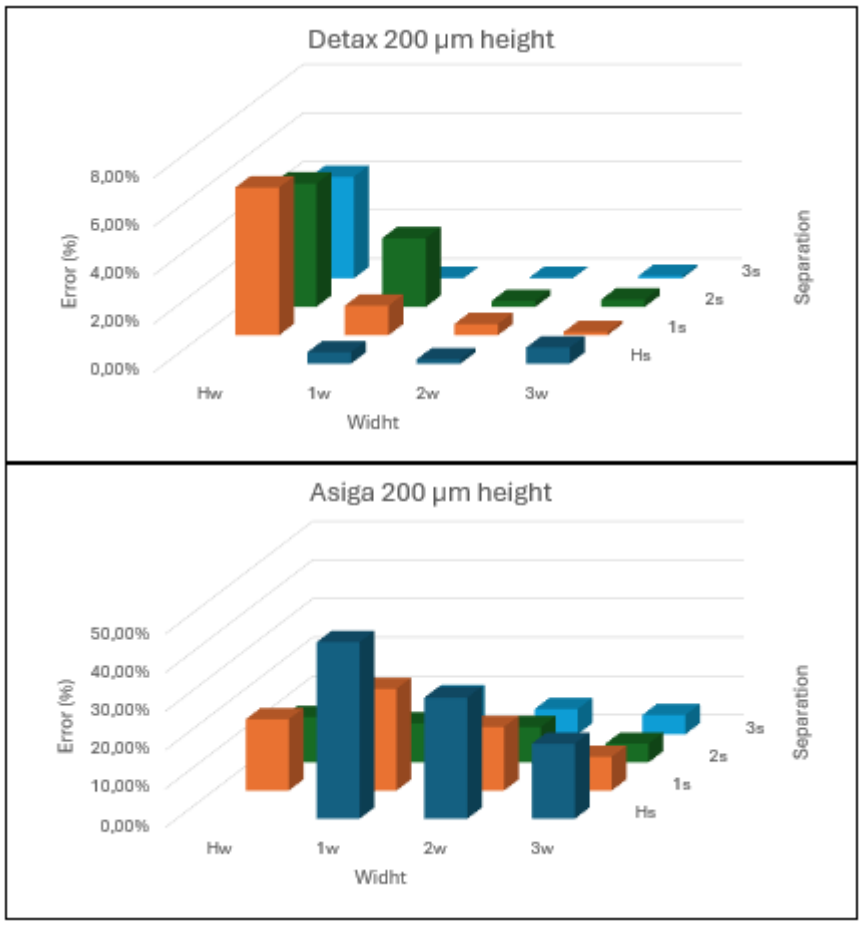


Figure 34: (A) Graphic from the error obtained printing the Detax part of 200 µm height. (B) Graphic from the error obtained printing the Asiga part of 200 µm height. In all (A,B), the X-axis corresponds to the width of the feature, going from the half of the height in the left to three times the height in the right. The Y-axis instead corresponds to the separation between the features, going from the half of the width in the front to three times the width in the back. The Z-axis represents the error calculated in the height of the features in percentage.

To conclude, the dimensional accuracy observed across different resins highlights significant variations linked to each resin's unique curing characteristics. Detax demonstrated the highest fidelity in maintaining the intended dimensions, particularly in smaller structures, whereas Keyprint exhibited greater deviations, especially in designs with reduced height. These findings emphasize that resin choice is crucial when high precision is required, particularly in applications where dimensional integrity directly impacts fluid flow control.

While the X-Y dimensional analysis has provided insight into the planar accuracy achievable with each resin, vertical dimensional fidelity is equally critical for ensuring the functionality of microfluidic channels and other 3D features. The results are contrastable by (74) where it is presented than the features are printed bigger as the exposure time increases, resulting in a decrease of the gap between features. Thus, the following section investigates the Z-dimension accuracy, analyzing height definition and assessing the performance of each resin in achieving the intended vertical specifications.

4.5.2 Z-Dimensioning

To further assess the dimensional accuracy of the 3D-printed structures, we analyzed their Z-dimension fidelity, focusing on height accuracy. This evaluation utilized the same parts depicted in Figures 30 and 31, enabling a consistent comparison across various structural features. Each feature's height was measured using a profilometer, providing precise measurements of vertical dimensions. The average height obtained from these measurements was then compared to the designed height, allowing for a calculation of height error. The results, summarized in Table 13, offer insight into each resin's ability to maintain Z-dimension accuracy.

Table 16: Height error for every resin type and every different height design.

Resin	Designed Height (μm)	Average Height Error
Detax	600	7.14%
	400	9.35%
	200	22.32%
Asiga	600	16.73%
	400	17.39%
	200	27.25%
Keyprint	600	34.43%
	400	46.38%

As shown in Table 13, there is a clear trend where the percentage error in height increases as the designed height decreases. This suggests that achieving dimensional accuracy is more challenging at smaller heights, likely due to limitations in the layer-by-layer resolution and polymerization depth control of the DLP printing process. Detax demonstrates the lowest height error across all tested dimensions, indicating a higher degree of precision and stability in maintaining the designed Z-dimension, which is crucial for applications requiring strict dimensional fidelity. Asiga shows a moderate increase in error, which is still relatively controlled compared to Keyprint. Keyprint exhibits the highest error percentages, particularly at smaller heights, with the 200 µm design proving unreachable.

These findings highlight the variability in performance between resins and suggest that Detax may be more suitable for applications demanding finer Z-dimension accuracy, especially in microfluidic and precision-based structures. In contrast, Keyprint's higher error rates could limit its use in applications where dimensional precision is paramount.

Additionally, we present in Figure 35 the profilometric analysis of a 200 µm design structure fabricated with Detax, illustrating the vertical profile captured across the surface. This measurement was conducted using a profilometer, a device that utilizes a fine needle tip to scan the surface topography. As the tip moves across the structure, it detects changes in height by gradually ascending and descending according to the surface features.

The graph shows inclined walls on the structures, which result from the profilometer’s scanning mechanics. As the needle progresses, it begins to ascend the side of the structure, moving forward as it rises. Similarly, when it reaches the peak and starts to descend, it continues to advance, producing the observed sloped profile along the walls. Reducing the tip's advance speed could improve the accuracy of this profile; however, this adjustment carries the risk of the tip getting stuck, potentially damaging the profilometer.

Two shaded regions, marked in red and green, indicate specific reference zones used to calculate the height difference between the base and the peak of the structure. The red-shaded area represents the baseline on the lower surface, while the green-shaded area marks the reference point on the top of the feature. By measuring the height difference between these two zones, we obtain an accurate assessment of the vertical resolution achieved in the printed structure, allowing us to evaluate the print’s dimensional fidelity relative to the intended design dimensions.

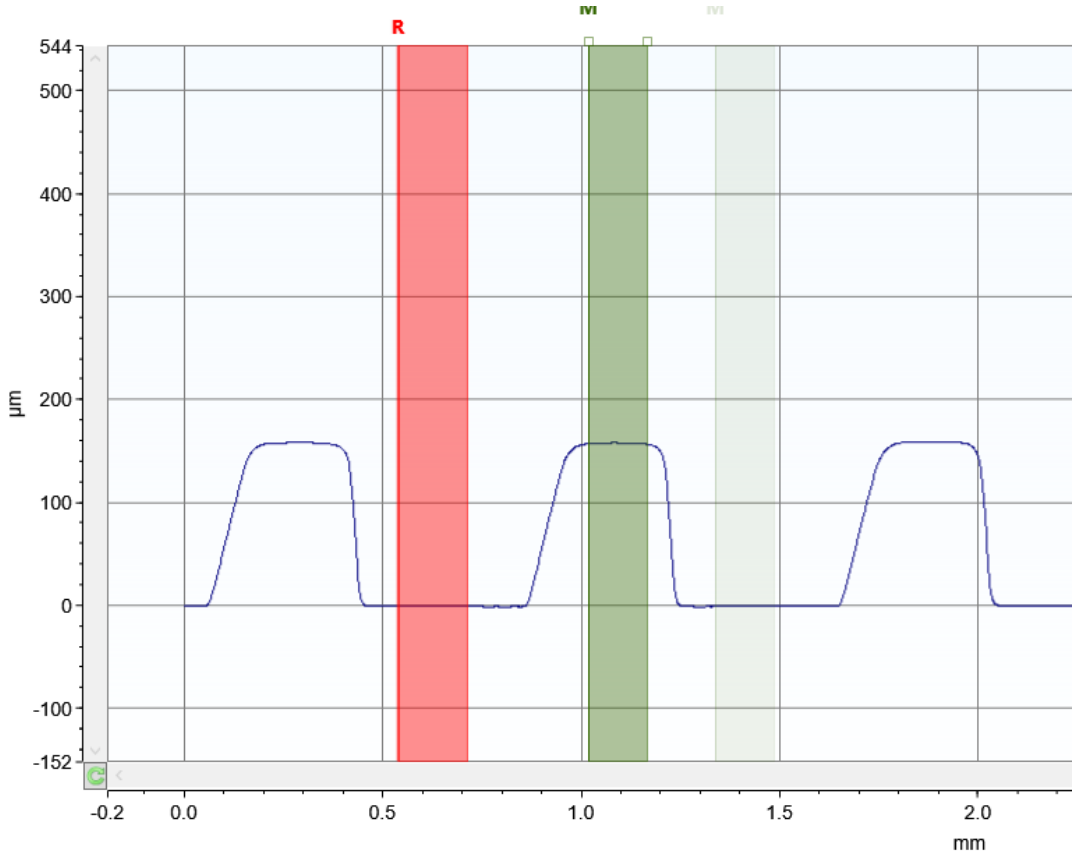


Figure 35: Profilometric analysis of a 3D-printed structure designed with a height of 200 µm. The graph illustrates the vertical profile across the structure, highlighting the inclined walls resulting from the profilometer's needle movement as it ascends and descends the feature. The red and green shaded regions mark the reference zones for calculating the height difference between the base (red) and the top (green) of the structure, providing a quantitative measure of Z-dimension accuracy.

4.6 Closed Channel Fabrication

Following the analysis of dimensional accuracy and resolution in previous sections, the focus here shifts to the challenge of over curing in closed channel fabrication, a crucial aspect in microfluidic applications where maintaining open and defined channels is essential. Over curing, a phenomenon caused by UV light penetrating beyond the intended layer, can lead to unwanted polymerization in surrounding areas, risking channel closure and loss of functionality. Addressing this challenge requires careful consideration of resin properties, layer thickness, and exposure parameters to optimize the fabrication process.

The relationship between resin absorbance and UV exposure time is crucial in understanding over-curing during closed channel fabrication, making this experiment particularly interesting. Higher absorbance resins, such as Asiga, limit light penetration depth, which reduces the risk of polymerizing unintended areas and helps keep channels open. However, their higher absorbance also requires longer exposure times to fully cure each layer, increasing the cumulative energy delivered. This additional energy could paradoxically enable light to penetrate deeper into the

resin, potentially causing polymerization within the channels. On the other hand, resins with lower absorbance, such as Detax and Keyprint, allow UV light to penetrate more easily, increasing the risk of over curing within the channels. However, they require shorter exposure times, reducing the total energy delivered. This combination between absorbance and exposure time creates a balance where one factor favors preventing over curing, while the other increases the risk, making the experimental results both curious and valuable for understanding the behavior of each resin.

Layer thickness also influences the extent of over curing. Thinner layers, like 50 µm, require more layers to complete the print, leading to increased cumulative UV energy exposure, which can generate over curing, particularly in low absorbance resins. Conversely, thicker layers, such as 100 µm, reduce the number of required layers and cumulative exposure, potentially mitigating over curing effects. We started the experiment using 100 µm layers because we hypothesized that thicker layers would result in less over curing. Thicker layers require fewer overall layers, reducing the total energy exposure during printing and decreasing the likelihood of unwanted polymerization inside the channels. This approach ensures better control over the printing process while maintaining the strength of the printed structures.

To evaluate how resin properties, cover thickness, and geometry affect the fidelity of printed microfluidic channels, two distinct designs were tested: rectangular channels and a stepped 'roof' design with a staircase profile (Figure Y). Both designs featured a channel height of 500 µm and a width of 1 mm, with cover layer thicknesses of 200 µm, 400 µm, 600 µm, and 800 µm, created using 1, 2, 4, and 8 layers of 100 µm each. The stepped 'roof' design included "staircases" composed of increments of 100 µm by 100 µm, resulting in a maximum height of 900 µm at the highest point of the channel. These experiments aimed to understand how variations in cover thickness and stepped geometries influence over-curing and channel openness.

The structures were fabricated using the three tested resins (Detax, Asiga, and Keyprint) under exposure times and intensities optimized from preliminary experiments to ensure consistent conditions across all designs. The printed results, shown in Figure 36, highlight the practical outcomes for both rectangular and stepped roof designs with varying cover thicknesses. Optical microscopy was used to analyze the structural integrity and dimensional accuracy of the printed channels, with a particular focus on over curing effects and layer fidelity.

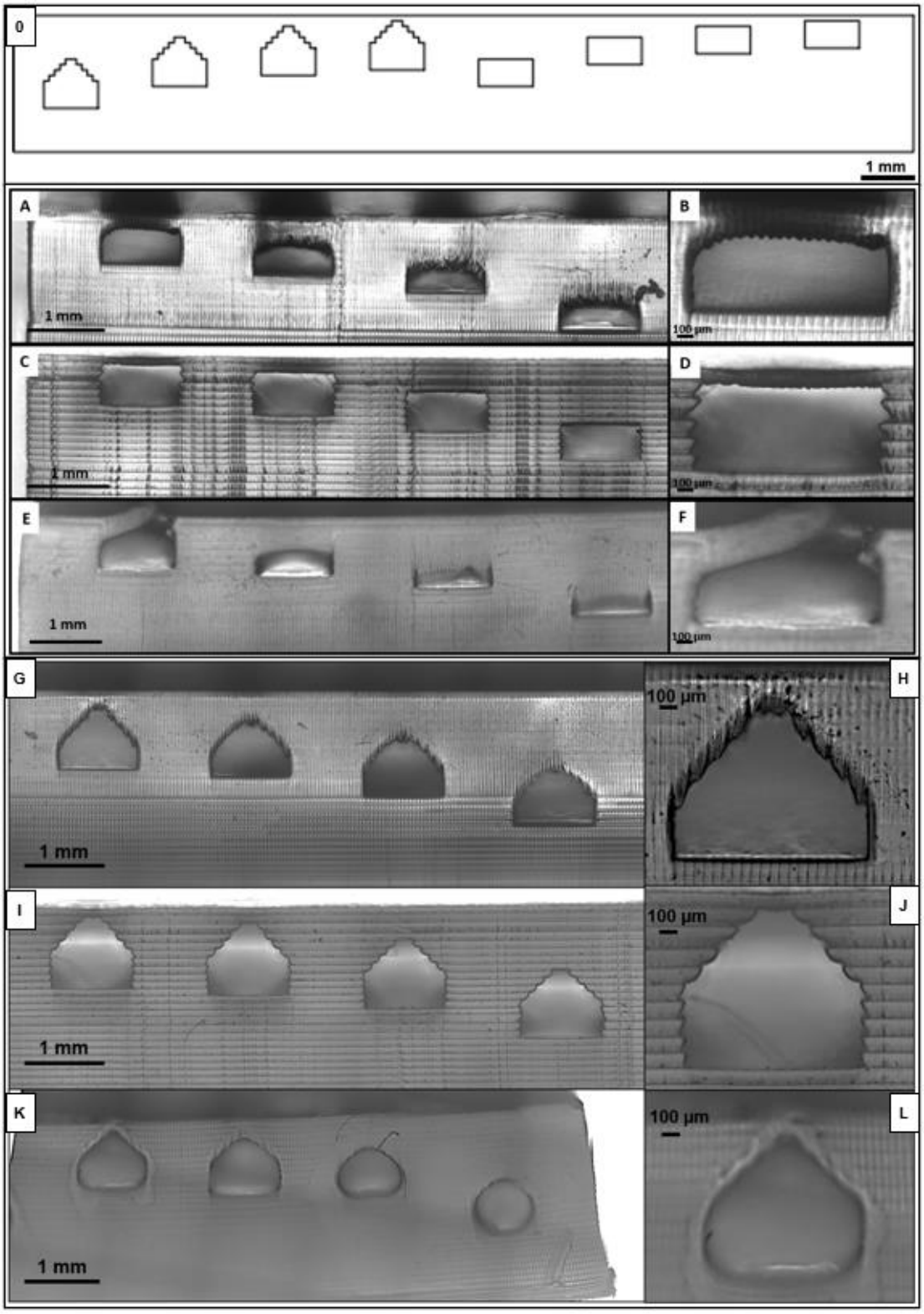


Figure 36: The top panel (0) depicts the design of the printed channels, including two geometries: rectangular and stepped-roof profiles. Both geometries maintain a consistent channel height of 500 µm, while the cover height varies across four values: 100 µm, 200µm, 400 µm, and 800 µm (left to right). Panels A–F correspond to the rectangular geometry, with A–B showing channels printed with Detax, C–D with Asiga, and E–F with Keyprint resins. Panels G–L present the stepped-roof geometry, with G–H representing Detax, I–J representing Asiga, and K–L representing Keyprint. For each resin, full channel views are shown on the left (A, C, E, G, I, K), and detailed zoomed-in views of the channels covered with 100 µm layers are shown on the right (B, D, F, H, J, L). The zoomed-in images provide a closer look at the quality and dimensional fidelity of the channels with the thinnest cover layer.

The results presented in Figure 36 provide a comprehensive analysis of channel performance for the three tested resins (Detax, Asiga, and Keyprint) evaluated across two distinct channel designs: rectangular and stepped “roof” profiles. These designs were fabricated to explore the effects of resin properties, channel geometry, and cover thickness on maintaining open and functional channels while minimizing over curing.

For rectangular channels (Panels A–F in Figure 36), the performance varied significantly depending on the resin used. For Detax resin (Panels A and B), channels with covers of one or two layers (100–200 µm) remained fully open and functional. However, increasing the cover thickness to four or eight layers (400–800 µm) led to partial obstruction of the channels. This result highlights how the lower absorbance of Detax resin allows UV light to penetrate deeper, causing unintended polymerization within the channel. Thinner covers effectively maintained channel openness, while thicker covers amplified over curing effects, posing challenges for achieving functionality.

In contrast, Asiga resin (Panels C and D) delivered superior results, with all channels remaining open and unobstructed across all tested cover thicknesses (100–800 µm). Even with the thickest cover (eight layers), the channels maintained their structural integrity. This performance is attributed to Asiga’s higher absorbance, which restricts UV light penetration, minimizing unintended polymerization. These results demonstrate the resin’s suitability for applications requiring precise closed channels with consistent dimensions.

For Keyprint resin (Panels E and F), significant limitations were observed. The channels with a one-layer cover (100 µm) were fragile and broke during cleaning process, as seen in Panel F. Additionally, channels with covers of more than one layer (200–800 µm) were fully obstructed by polymerized resin, reflecting the resin’s low absorbance and susceptibility to over curing. These challenges make Keyprint less viable for closed channel fabrication.

When moving to stepped “roof” channels (Panels G–L in Figure 36), which feature an additional 400 µm of channel height compared to the rectangular channels, clear improvements were observed in maintaining unobstructed channels. For Detax resin (Panels G and H), all channels remained fully open and unobstructed across all cover thicknesses (100–800 µm). This improvement suggests that the increased channel height effectively reduces over curing, even when thicker covers are used, demonstrating the potential of this design to enhance fabrication outcomes for Detax resin.

Similarly, Asiga resin (Panels I and J) continued to deliver excellent results. All channels across all cover thicknesses remained fully open and functional, maintaining the consistency observed with the rectangular design. This reinforces the resin's ability to prevent unintended polymerization through its high absorbance and precise curing properties, making it a reliable option for stepped "roof" designs as well.

For Keyprint resin (Panels K and L), the stepped design resulted in marginal improvements compared to the rectangular channels. Channels with covers of one and two layers (100–200 µm) remained open and unobstructed. However, channels with covers of four and eight layers (400–800 µm) exhibited partial obstruction due to over curing.

Overall, the stepped "roof" design demonstrated significant advantages on over curing over the rectangular channels, particularly for Detax and Keyprint resins. The increased channel height played a critical role in mitigating over curing, enabling more consistent results. Detax resin showed a marked improvement with the stepped design, achieving unobstructed channels even with thick covers. Asiga resin, as expected, maintained excellent performance across both designs and all cover thicknesses, confirming its reliability and precision. Keyprint resin, while showing some improvement with the stepped design, remained less suitable due to persistent issues with over curing and structural integrity at higher cover thicknesses.

These results emphasize the importance of considering resin properties, channel geometry, and cover thickness in closed channel fabrication. This analysis offers valuable insights for optimizing fabrication processes, enabling the selection of suitable materials and designs for advanced microfluidic applications.

The thickness of the covers was also measured for all resins, as shown in Figure 36, and compared against the designed dimensions. While Asiga and Detax resins closely matched the intended thickness, Keyprint showed significant deviations, further underscoring its limitations.

Table 17: The values of the thickness of the covers of the channels showed in Figure 36.

	Designed	Detax Rectangle	Asiga Rectangle	Keyprint Rectangle	Detax Roof	Asiga Roof	Keyprint Roof
1	100,0	207,2	114,5	259,1	164,8	107,0	168,0
2	200,0	404,2	212,3	435,0	292,2	200,8	293,0
4	400,0	637,4	448,9	690,4	512,3	436,9	519,0
8	800,0	1019,6	857,6	1131,8	906,1	832,3	911,0

The values presented in Table 14 are graphically represented in Figure 37. This figure compares the measured cover thickness with the number of designed layers, highlighting the differences between the materials tested: Detax, Asiga, and Keyprint in rectangular and roof configurations.

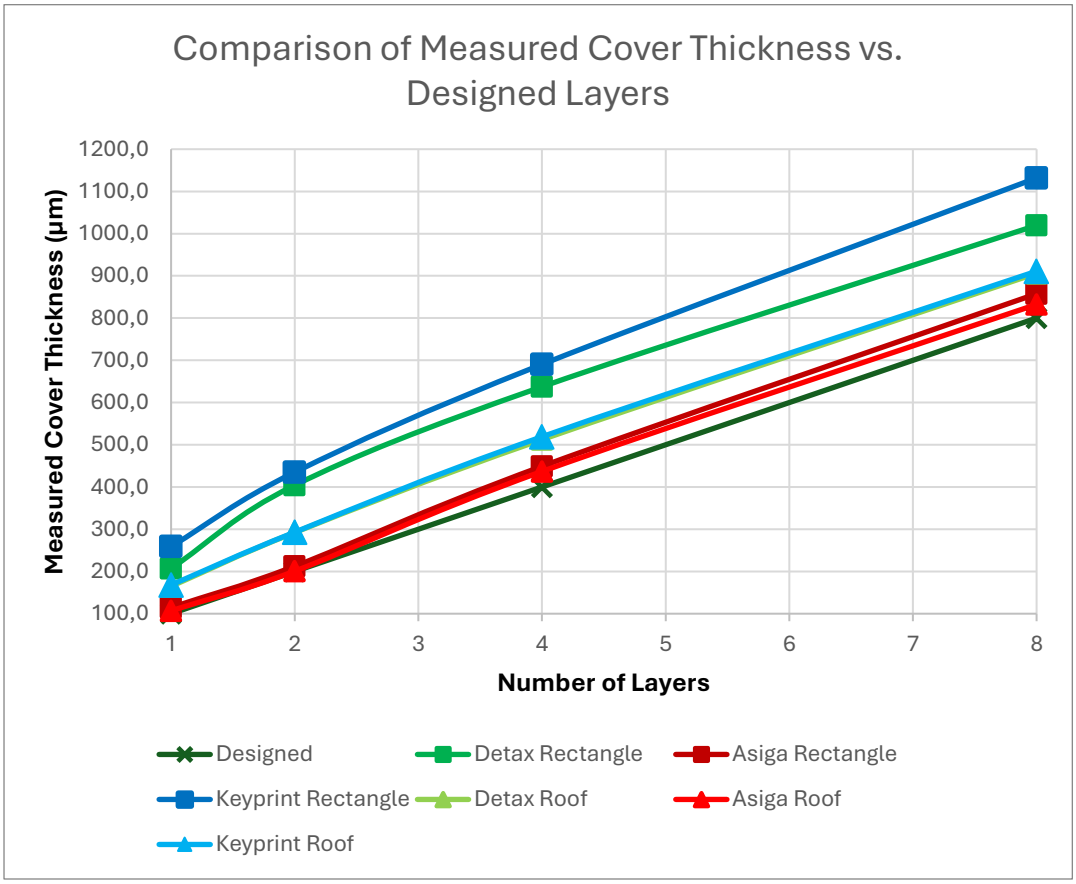


Figure 37: This graphic shows the thickness of the cover of every channel printed with the Asiga, Detax, and Keyprint resins vs. the design file values for one, two, four, and eight layers, respectively. The designed cover had a nominal thickness of 100 µm, 200 µm, 400 µm, and 800 µm.

From Figure 37, and as reported in (80), we can observe that the final thickness of the top layer of the channel is strongly influenced by the absorbance of the resin. The data highlights three distinct subgroups with similar error patterns. First, the Detax and Keyprint resins for rectangular channels form a group, with Keyprint showing slightly more pronounced deviations from the designed thickness. Second, Detax and Keyprint for stepped roof channels present almost identical values, indicating that the stepped geometry helps mitigate the effects of resin properties on over curing. Lastly, Asiga resin demonstrates the most accurate results for both rectangular and stepped roof designs, with very similar values across both geometries.

To further investigate the effects of channel size, layer thickness, and cover dimensions, the study transitioned from an initial experiment involving open channels fabricated with three resins to a focused analysis using Detax resin. This transition was motivated by the consistent performance of Detax in terms of dimensional accuracy and its compatibility with a wide range of exposure parameters, making it a reliable choice for detailed evaluations.

In this phase, rectangular channels with varying heights of 100 µm, 200 µm, 300 µm, 400 µm, and 500 µm were printed, combined with covers of 100 µm, 200 µm, 300 µm, and 400 µm. These experiments were conducted with layer thicknesses of 50 µm and 100 µm to evaluate how different printing settings influenced curing and structural outcomes. By analyzing the dimensions of the channels, this study aims to understand how resin optical properties and cover layer thickness interact to influence over-curing and overall dimensional accuracy.

Figure 38 presents the design and results of the rectangular channels experiment. Panel A illustrates the CAD design used, consisting of channels with varying dimensions and covers of different thicknesses. Panels B, C, D, and E show the printed results for 50 µm layer thickness, while panels F, G, H, and I correspond to the same design printed with 100 µm layer thickness. All channels were fabricated using the Detax resin, with the number of layers forming the covers varying across each row. The experiment was conducted to evaluate the impact of channel dimensions, cover thickness, and layer height on the accuracy and structural integrity of closed channels.

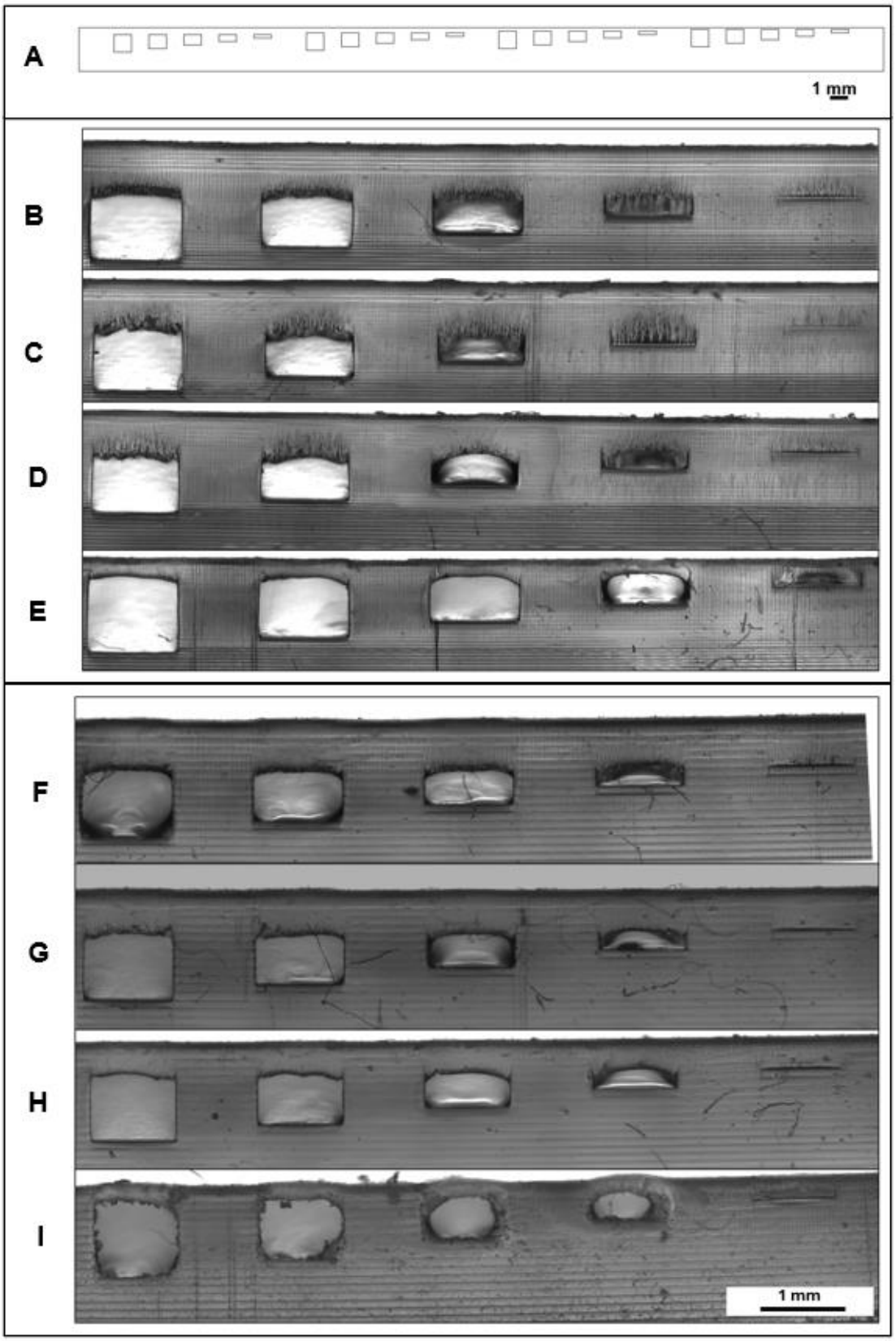


Figure 38: CAD design (A) and results of printed rectangular channels with varying dimensions and cover thicknesses using Detax resin. Panels B-E correspond to channels printed with 50 µm layer thickness, while panels F-I represent channels printed with 100 µm layer thickness. Each row demonstrates channels with cover thicknesses of 100 µm (B, F), 200 µm (C, G), 300 µm (D, H), and 400 µm (E, I), showcasing the effect of cover layer variation on channel integrity and dimensional accuracy. The scale bar shown in Figure I applies to all images from B to I.

The results presented in Figure 38 reveal distinct trends in the behavior of rectangular channels based on channel height, cover thickness, and layer settings. Channels with a height of 100 µm are consistently blocked under all conditions, indicating that this height is insufficient to remain open. For channels with a height of 200 µm, a cover thickness of up to 200 µm allows for open channels when printed with 50 µm layers. However, with 100 µm layers, these channels can tolerate a cover thickness of up to 300 µm, although the channels are not fully open and exhibit some degree of obstruction.

Notably, the covers printed with 50 µm layers exhibit less definition and higher surface roughness compared to those printed with 100 µm layers, which show significantly improved smoothness and dimensional fidelity. Interesting results are observed for channels with heights of 300 µm or more when printed with 100 µm layers, providing well-defined and functional structures. However, channels with covers of 100 µm thickness appear fragile, compromising their mechanical stability. As a result, channels printed with 100 µm layers and covers of 200 µm thickness are selected as the optimal configuration, balancing structural integrity and functionality.

To further analyze the impact of cover thickness on channel performance, a study was conducted to evaluate the average thickness of printed covers across different theoretical values for both 50 µm and 100 µm layer settings. The table below summarizes the results, showcasing the theoretical cover thicknesses alongside the measured average values obtained from the prints.

Table 18: Cover sizes as a function of layer thickness and channel size. All values in µm.

Layer Thickness	50				100			
Designed Dimensions	400.0	300.0	200.0	100.0	400.0	300.0	200.0	100.0
Measured Dimensions	579.8	567.7	438.5	221.3	573.9	456.5	375.6	220.5

The results highlight that, for both 50 µm and 100 µm layer thicknesses, the measured cover thickness consistently exceeds the theoretical values. This over-curing effect is more pronounced for larger theoretical thicknesses, particularly when using 50 µm layers. For 100 µm layers, the measurements demonstrate closer alignment with the theoretical values, underscoring improved dimensional fidelity when thicker layers are used. Notably, covers with theoretical thicknesses of 100 µm could not be reliably measured or analyzed.

In summary, this comprehensive analysis deepens our understanding of the interplay between cover thickness, layer settings, and over-curing dynamics in DLP based 3D printing. The findings highlight the critical balance required to maintain channel openness while minimizing unintended polymerization. The results observed with 100 µm layer settings and a cover thickness of 200 µm demonstrate a reliable approach for achieving robust and functional microfluidic structures. These configurations provide a solid foundation for accurate and reproducible channel fabrication. In the next section, these findings will be applied to assess the functionality of printed channels in operational microfluidic systems.

4.6.1 Printing of Inclined Closed Channels

Having established the feasibility of fabricating closed channels using DLP-SLA 3D printing, the next step is to evaluate whether it is possible to create channels with height variations or inclined channels with a constant cross-section. These inclined geometries would enable the integration of multiple working planes within a single chip, significantly enhancing the versatility and functionality of microfluidic devices.

This represents a critical advancement, as such features are currently challenging to achieve using traditional methods like soft lithography. Inclined channels could prepare the way for developing more versatile chips capable of performing multiple tasks within the same device, such as fluid mixing, particle separation, or sequential reactions across different planes. The ability to incorporate these features in a single microfluidic platform would allow for increased design flexibility and multifunctionality, all while maintaining a compact and efficient layout.

Figure 39 shows three images illustrating designs for 3D printed microfluidic components. These include 3D printed microfluidic channels, and an inclined microfluidic channel, enabling operation in two different planes.

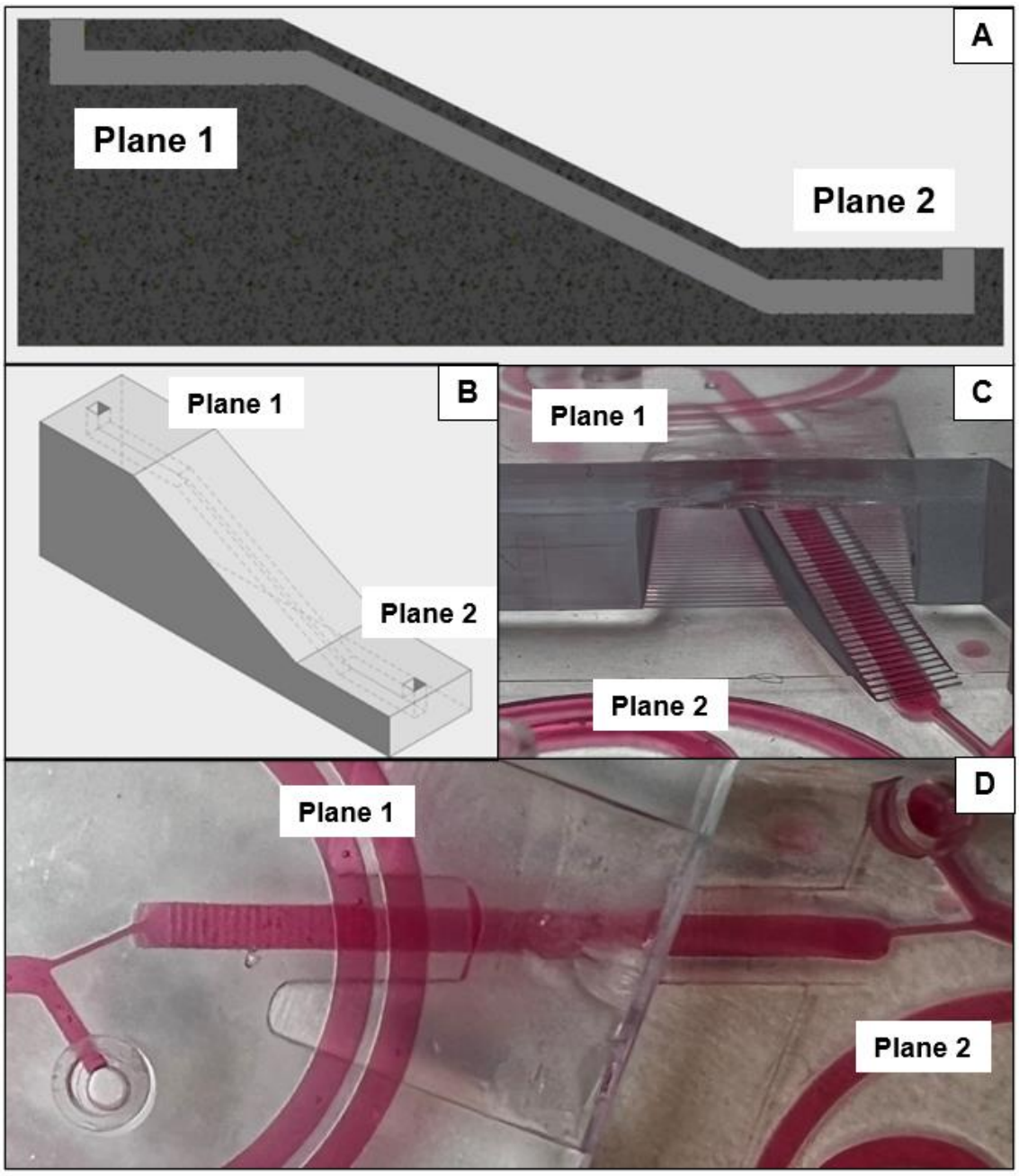


Figure 39: Designs and experimental results for the inclined channel configuration, enabling the transition from working Plane 1 to Plane 2. (A) Cross-sectional design of the inclined channel. (B) 3D schematic representation illustrating the transition between the two planes. (C, D) Experimental validation showing the fabricated channel filled with red-dyed water to enhance visibility of the channel structure and confirm functionality.

The focus of this study will be on assessing whether DLP-SLA 3D printing can achieve the required precision to fabricate these complex geometries without compromising the integrity of the channel structure. Success in this attempt would highlight the unique potential of DLP-SLA printing in advancing microfluidic device design beyond the capabilities of conventional fabrication techniques.

4.6.2 Integration of Input and Output Ports in One-Step Printed Channels

To enable the inclusion of input and output ports in microfluidic channels fabricated in a single printing step, it was necessary to introduce a 200 µm gap above the channel, as illustrated in Figure 40 This gap prevents the complete closure of the channel when the cylindrical adapter is inserted, ensuring that the channel remains functional. Without this design modification, the channel would become blocked due to excessive light projection directly above the channel during printing.

These cylindrical adapters, which serve as connectors to external tubing, can be customized in size to accommodate specific tubing requirements or standardized to fit common Luer connectors. This adaptability allows for a broad range of applications, enhancing the versatility of the printed microfluidic devices.

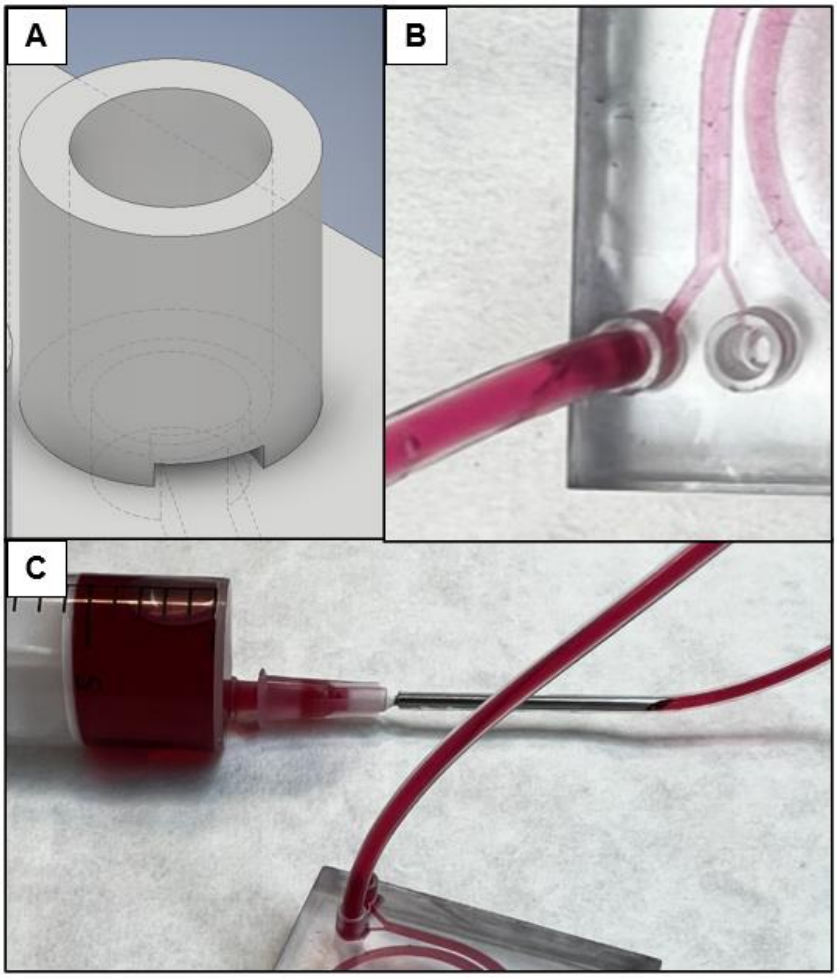


Figure 40: (A) 3D model of a cylindrical adapter designed for input/output integration in microfluidic devices. The design features a 200 µm gap above the microfluidic channel to prevent blockage during the printing process. The adapter fits securely into the microfluidic device without obstructing the channel and is designed to connect tubing for compatibility with syringes or other fluid delivery systems. (B, C) Experimental results showing the fabricated adapter connected to tubing, with red-dyed water flowing through the system.

4.7 Surface Roughness Characterization

4.7.1 Horizontal Surface Roughness

Horizontal as-printed surface roughness was calculated from atomic force microscopy (AFM) with topographic images obtained from the scanning of 50 × 50 µm areas as explained in Section 3.2.4. The test was done on 3D printed pieces with a flat surface. After analyzing a 50 × 50 µm area for the Asiga design, the roughness result was 40±1 nm. Instead, the Detax result for the same test was 66±1 nm, while the Keyprint one was 179±1 nm. As an example, the image obtained with the AFM for the Asiga resin is shown in Figure 41, which provides a visual reference for the quality of the surface finish achieved with this resin.

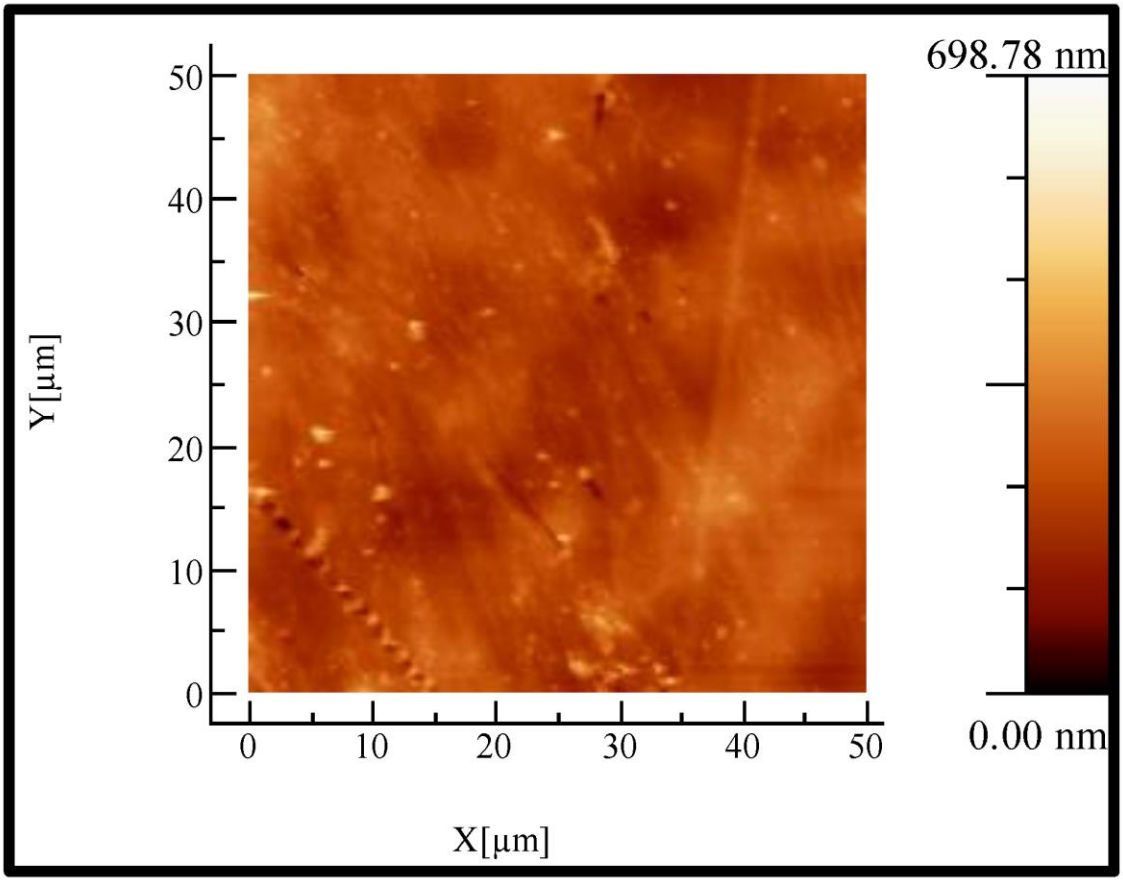


Figure 41: Fi gure obtained with the AFM, from a 3D printed object with the Asiga resin. In the right a heights histogram can be observed indicating the height difference in a 50 × 50 µm area.

4.7.2 Internal Channel Roughness

The internal superior part of the cover channel is also analyzed for roughness, as part of the overall surface quality evaluation. In this case, Asiga has the smoother roughness while having the higher absorbance. For the Asiga superior part of the channel, the roughness is 5 µm. For the lower absorbance resins the roughness is higher, with the Detax resin the roughness is 20 µm, and for the Keyprint resin it is 25 µm. Figure 42 presents a detailed view of the superior internal part of the cover channel fabricated with Detax resin, presenting the internal superior surface roughness.

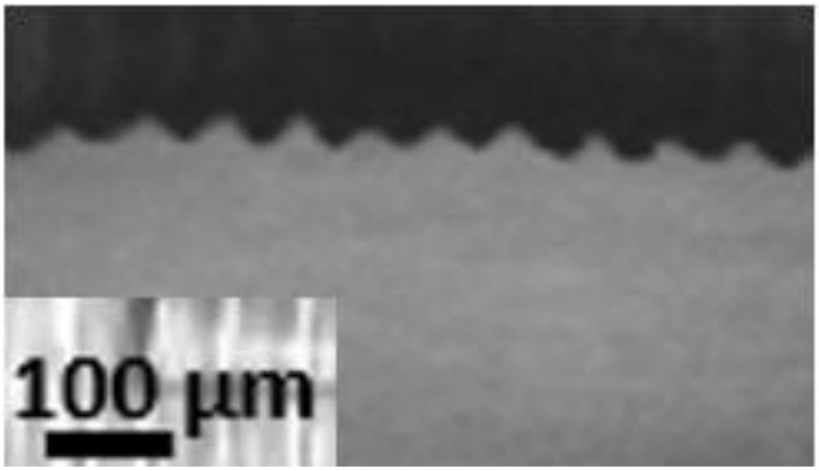


Figure 42: Zoomed image of the superior internal part of the cover channel fabricated using Detax resin with 100 µm layers, showing the surface roughness. Scale bar 100 µm.

The surface roughness observed in Figure 42 can be explained using the theoretical models proposed by Mostafa et al. and Gong et al., which describe the interplay between curing light diffraction and material properties during 3D printing processes. According to Mostafa et al., the micromirrors in the Digital Micromirror Device (DMD) act as micro-apertures, causing the reflected light to diffract. This diffraction results in an irradiance profile across the micromirrors that resembles a Gaussian distribution. Consequently, the accumulated irradiance on inclined or vertical surfaces, such as the superior part of the cover channel shown in Figure 42, exhibits characteristic roughness patterns.

The DMD device, composed of a 2D array of micromirrors, creates a superposition of irradiance profiles that collectively influence the curing process. As described in the theoretical model, the total irradiance is determined by the summation of Gaussian profiles from individual

micromirrors, where the pitch between micromirrors and the Gaussian radius significantly impact the uniformity of the irradiance distribution. The variations in irradiance intensity contribute to uneven curing across the surface, resulting in the roughness patterns observed in Figure 42.

Furthermore, the energy accumulation model proposed by Gong et al. expands upon the constant irradiance model to incorporate the effects of diffraction and energy penetration into successive layers. The energy received by a specific layer is a combination of direct exposure and energy penetrating from subsequent layers, with the penetration depth of the resin playing a critical role. The non-uniform energy distribution caused by diffraction effects leads to microstructural inconsistencies on the cured surface.

Based on the presented hypothesis, it is understandable that Detax and Keyprint resins exhibit greater horizontal roughness within the interior of the channel compared to Asiga resin. As shown in Figure 27, Asiga resin has a significantly higher absorbance than the other two resins, which likely contributes to its improved curing uniformity and smoother surfaces. This suggests that the optical properties of the resin, particularly its absorbance, play a crucial role in mitigating roughness induced by the diffraction effects of the printing process.

4.7.3 Lateral Roughness

To analyze lateral roughness, it is essential to consider the effects of irradiance distribution and energy accumulation during the photopolymerization process. Figure 43 illustrates the relationship between irradiance, accumulated energy, and the cured depth for varying layer thicknesses and exposure times. The irradiated affected zone represents the maximum number of previously cured layers that receive a portion of the exposure energy from the current layer. This interplay between irradiance and accumulated energy directly impacts the lateral roughness observed in DLP-SLA 3D-printed structures, as uneven energy distribution can lead to variations in the polymerization process across the layer.

By examining the accumulated energy profiles for 10 µm, 25 µm, and 50 µm layer thicknesses, as shown in Figure 43(a), Mostafa et al. demonstrated how energy distribution broadens with increasing layer thickness and exposure time(113). Additionally, the cured depth profiles depicted in Figure 43(b) highlight the influence of critical energy on the polymerization process, showcasing how material properties and exposure conditions affect the final layer dimensions. This analysis, conducted by Mostafa et al., provides critical insights into how the photopolymerization process contributes to lateral roughness in DLP-SLA printed microfluidic channels.

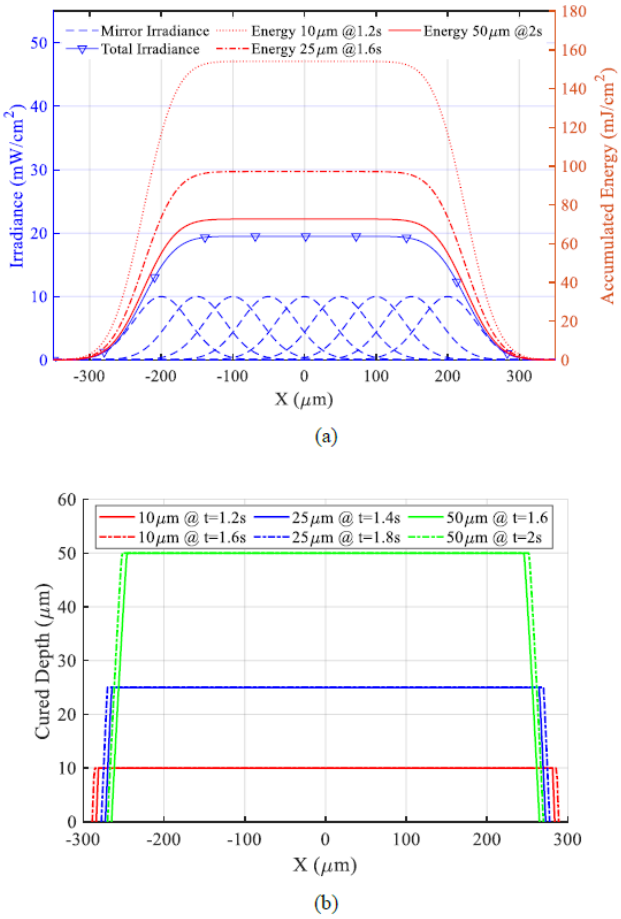


Figure 43: (a) Plot of the individual mirror irradiance, total irradiance, and accumulated energy for different layer thickness values, (b) Plot of the cured shapes at different exposure times and layer thickness values.

As shown in Figure 36, the only resin with a pronounced sidewall roughness is Asiga. Following Equation 13 from section 3.2.5, the Asiga sidewall roughness is 27.64 µm. On the other hand, for the Detax and Keyprint resins, we appreciate very smooth sidewalls, because of their lower absorbance. We calculated a sidewall roughness under 3 µm for both Detax and Keyprint resins.

The analysis of the roughness results reveals key insights into the relationship between layer thickness, resin properties, and the resulting roughness in DLP-SLA printed microfluidic devices. When thinner layers are used during printing, the total irradiance received by each layer increases due to the cumulative exposure of successive layers. This phenomenon is particularly significant in the Detax resin, which is the most efficient in polymerizing. The roughness observed in the inner surface of the channel cover in Detax likely stems from the 45° diamond orientation of the micromirrors in the DMD system, as hypothesized by authors studying surface profiles in the X

direction. This orientation amplifies the cumulative polymerization effect, aggravating the nominal error and contributing to increased roughness.

Mostafa et al. further observed that the impact of this nominal error becomes more pronounced when the layer thickness is reduced, as thinner layers are more susceptible to the cumulative over-curing effect. In contrast, the lateral roughness in Asiga is more clearly observed due to its higher absorbance and lower nominal error. This indicates a reduced number of overexposed layers and a more direct influence of the Gaussian distribution of irradiance produced by the micromirrors.

These findings suggest that lateral roughness and the roughness in the inner surface of the channel cover are two opposing effects influenced by the resin's polymerization efficiency and absorbance. In resins like Detax, where polymerization efficiency is high but cumulative effects dominate, roughness is heavily influenced by the over-curing of successive layers. Conversely, in Asiga, the higher absorbance and lower nominal error reduce the cumulative effects, making the irradiance profile’s Gaussian distribution the primary contributor to roughness.

Considering all the results obtained so far, the Detax resin stands out as the most attractive option for our objectives. This decision is based on its superior lateral surface roughness, a crucial factor for the fabrication of microfluidic channels, as well as its good precision in both XY and Z dimensions. In contrast, the Keyprint resin demonstrated lower performance across all evaluated parameters, making it unsuitable for the high standards required in this application.

Although the Asiga resin is a strong alternative due to its good precision in XY and Z dimensions and its high absorbance, which helps reduce overcuring, the lateral surface roughness of the channels produced with this resin was considered less favorable. Since achieving smooth channel walls is critical for ensuring optimal microfluidic performance, this factor ultimately influenced the decision to prioritize Detax resin.

Moreover, the shorter exposure times required by the Detax resin compared to Asiga were not considered a decisive factor in the selection process but do offer the practical advantage of faster prototyping. This benefit is particularly useful for iterative design and testing. With these considerations, the focus will now center on exploring the capabilities of Detax resin in detail and evaluating its performance in fabricating functional microfluidic devices.

4.8 Dimensional Error Analysis for Microfluidic Features Inside Channels

The capability to fabricate closed microfluidic channels with 3D printing represents a significant advancement in the field of microfluidics, as discussed in the previous chapter. In this section, we will evaluate the capability of fabricating internal structures within closed microfluidic channels and assess the precision with which these features can be produced. These structures are critical for enabling advanced functionalities within microfluidic devices, and the focus here will be to determine whether they can be successfully integrated into the channels and the level of accuracy achievable with the chosen fabrication techniques.

Traditionally, the creation of internal features within closed microfluidic devices has been challenging due to limitations in conventional fabrication methods such as soft lithography. These methods often require intricate multi-step processes involving bonding and alignment, which can introduce dimensional limitations and design restrictions. In contrast, 3D printing enables the simultaneous fabrication of channels and embedded structures in a single manufacturing step, offering a more versatile and efficient solution. This capability not only simplifies device fabrication but also allows for the integration of complex geometries that were previously unattainable.

The importance of internal microstructures lies in their ability to tailor the functionality of microfluidic devices to specific applications. For instance, engineered features within channels can promote chaotic advection for enhanced mixing, create particle traps for separation processes, or modify flow profiles to achieve precise control over reaction conditions. Such capabilities are critical in fields like biomedical diagnostics, where rapid and efficient mixing of reagents is essential.

In this chapter, we explore the feasibility and accuracy of fabricating internal microstructures within closed microfluidic channels using 3D printing. By leveraging the insights gained from the fabrication of closed channels, we evaluate the ability to produce intricate geometries while maintaining dimensional fidelity.

4.8.1 Experimental Design and Methodology

To investigate the feasibility of fabricating internal microstructures within closed microfluidic channels, a systematic experimental approach was designed, focusing on various geometries

and dimensions that are relevant to microfluidic applications. This study exclusively used the Detax resin, selected for its demonstrated suitability in achieving high dimensional accuracy with a moderate lateral roughness, as evidenced in previous closed channel experiments.

The experiment centered on fabricating three fundamental shapes for internal microstructures: squares, circles, and triangles. These shapes were chosen due to their broad applicability within microfluidic devices, where they can serve different purposes, such as promoting mixing, trapping particles, and redirecting flow. By evaluating these basic geometries, we could assess the printing precision across diverse designs. Each shape was printed in various sizes, targeting feature dimensions of 100 µm, 200 µm, and 300 µm, with separations between features ranging from 100 µm to 500 µm. This selection of dimensions covers the range commonly used in microfluidic applications, making the findings relevant for a wide array of device configurations.

Printing was conducted using a layer thickness of 100 µm, a setting determined to offer an optimal dimensional accuracy. The decision to use Detax resin stemmed from its favorable performance in closed-channel tests, where it demonstrated an acceptable level of over curing with optimized settings, and superior roughness quality relative to the other resins.

The resulting printed microstructures were examined with optical microscopy to measure dimensional accuracy. For each shape and size, multiple internal structures were fabricated and analyzed, allowing us to compute average dimensions and assess consistency. Dimensional error was quantified by comparing the actual printed dimensions on the Y axis to the design specifications, with results expressed as a percentage error. This characterization establishes a benchmark for the dimensional fidelity attainable with DLP-SLA based 3D printing.

4.8.2 Dimensional Accuracy of Printed Microstructures

In the analysis of dimensional accuracy for printed microstructures, a set of Detax resin-based samples was examined to evaluate the precision of fabricated features within closed microfluidic channels. Three primary geometries (squares, circles, and triangles) were printed at various dimensions and separations, as shown in Figure 44 it provides a visual representation of the printed microstructures, illustrating the diversity of shapes and dimensions examined. Close-up images of each geometry highlight the crispness and definition of edges, offering qualitative evidence of the printing accuracy achieved with Detax resin. These images demonstrate the feasibility of producing a range of internal structures within closed channels, maintaining the functional integrity of the microfluidic environment.

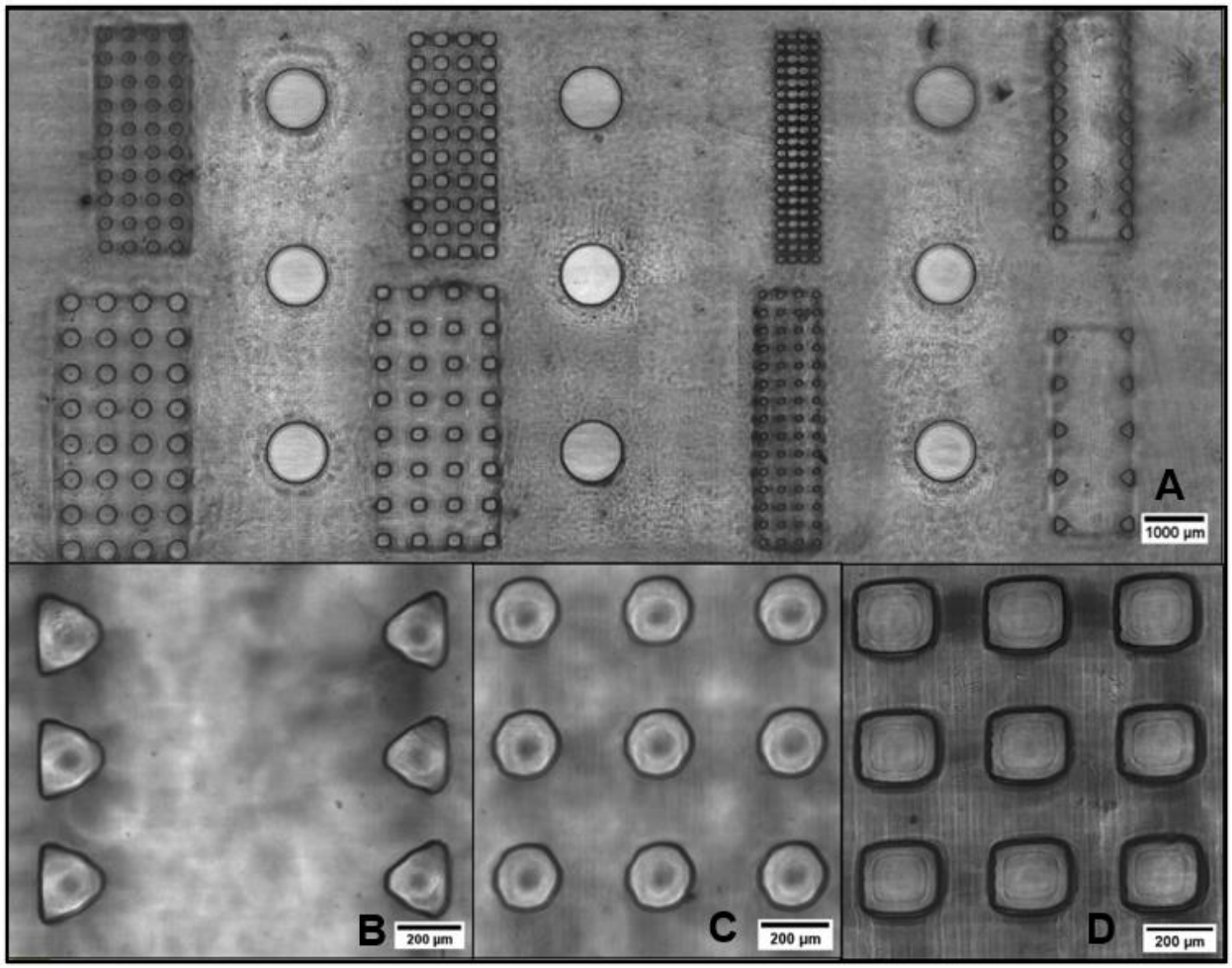


Figure 44: (A) The figure shows a 3D printed part created using Detax resin. The part features a microfluidic channel within which various structures can be observed. These structures include circles with diameters of 200 and 300 µm, separated by a distance equal to their diameter; squares with sides measuring 100 and 200 µm, separated by distances equal to and double their size respectively; and triangles with sides measuring 300 µm, separated by distances of 100 and 500 µm. The figure highlights the precise control over the dimensions and placement of the structures within the microfluidic channel, which can be used for various applications. (B) The figure shows 300 µm triangles with a separation of 100 µm vertically and 1 mm horizontally. (C) The figure shows circles with a diameter of 200 µm and a separation of also 200 µm. (D) The figure show squares with a side of 200 µm and a separation of 200 µm.

Panel A displays an array of microfluidic structures encapsulated within a channel created using Detax resin, highlighting the precision of stereolithography in microscale fabrication of varied geometric shapes. Triangles, circles, and squares are featured with different dimensions and spacing. Panel B focuses on triangular structures, each side measuring 300 µm, spaced 100 µm apart vertically and 1 mm horizontally. Panel C highlights circles with diameters of 200 µm, uniformly spaced 200 µm apart. Panel D presents squares with each side measuring 200 µm, also separated by 200 µm.

Table 16 summarizes the dimensional errors for each feature, providing a quantitative insight into the consistency and reliability of the printing process from all the features shown in the previous Figure 44.

Table 19: Dimensional errors for the microfluidic features fabricated using DLP-SLA 3D printing. The table lists the error percentages for different shapes and separations, highlighting the precision of the printing process.

Feature	Error (%)
100 µm Square (100 µm separation)	5.00
100 µm Square (200 µm separation)	3.60
200 µm Square (200 µm separation)	2.25
200 µm Square (400 µm separation)	0.85
200 µm Circle (200 µm separation)	0.66
300 µm Circle (300 µm separation)	0.77
300 µm Triangle (100 µm separation)	4.82
300 µm Triangle (500 µm separation)	1.95

The results indicate that the dimensional accuracy varies with both the geometry of the feature and its separation from adjacent structures. Smaller features with tighter separations (such as the 100 µm squares with 100 µm spacing) exhibited the highest dimensional error, with a deviation of approximately 5.0%. This higher error rate is likely due to the limitations of the printing resolution and the over curing effects in regions with minimal spacing, where light diffusion and scattering within the resin can impact the precision of feature boundaries. As the feature size and spacing increased, the dimensional error decreased significantly. For example, the 200 µm square with a 400 µm separation exhibited an error as low as 0.85%, while the 200 µm circle with 200 µm separation demonstrated an even lower error of 0.66%. These findings underscore the capability of DLP-SLA 3D printing to produce larger microstructures with high dimensional fidelity.

Notably, the circular features displayed the most consistent accuracy across all sizes and spacings, with dimensional errors consistently below 1.0% for features with 200 µm or more spacing. This suggests that circular geometries may be inherently less susceptible to over-curing and edge distortion effects, possibly due to their symmetric nature and reduced perimeter complexity compared to squares and triangles. Triangular features, in contrast, exhibited more variability, with errors ranging up to 4.82% in tightly spaced arrangements, likely due to their pointed edges and higher complexity, which may increase susceptibility to minor inaccuracies during the curing process.

4.8.3 Capabilities and Challenges of DLP-SLA 3D Printing for Internal Microfluidic Features

The comparative analysis between DLP-SLA 3D printing and traditional fabrication techniques, such as soft lithography and injection molding, highlights the distinct advantages of DLP-SLA printing for creating internal microstructures within closed channels. Traditional methods, while well-established, face significant challenges when it comes to fabricating intricate geometries or customizing designs for advanced microfluidic applications.

Soft lithography, for example, is highly effective for producing open channel devices with simple planar geometries. However, incorporating internal structures or closed channels requires additional bonding and alignment steps, which increase the risk of inaccuracies. These challenges become even more pronounced when dealing with complex 3D features, where misalignments during bonding can compromise functionality. The planar limitations of soft lithography also restrict its ability to rapidly customize designs or produce multi-level internal geometries, making it less adaptable for iterative prototyping or intricate device fabrication.

Injection molding offers exceptional precision and scalability, making it an ideal choice for mass production of straightforward, repetitive designs. However, the process involves high tooling costs and lengthy mold fabrication times, which are impractical for prototyping or the production of devices with intricate internal features. The rigidity of molds further restricts the ability to modify designs or include complex geometries, limiting the technique's utility for applications requiring rapid design iteration or custom internal structures.

In contrast, DLP-SLA 3D printing provides a versatile, single-step fabrication process that eliminates many of these challenges. By enabling the integration of internal features within closed channels, DLP-SLA printing reduces the errors associated with multi-step methods like soft lithography. Its ability to customize designs rapidly and fabricate geometrically complex structures, including non-planar and multilevel features, offers a level of design flexibility that is difficult to achieve with traditional methods. This flexibility is particularly advantageous for microfluidic devices that demand complex 3D specialized designs.

The results presented in this study provide valuable observations into the dimensional accuracy of DLP-SLA printed structures, highlighting key factors that influence precision. Dimensional discrepancies were observed, particularly in smaller structures or those with minimal spacing between features. These variations, as shown in Table 16, reflect characteristics peculiar in DLP-SLA printing process and demonstrate the importance of understanding how specific parameters affect printed outcomes. Over curing, caused by UV exposure exceeding the targeted regions,

was identified as the biggest challenge that influences dimensional fidelity. This effect is particularly relevant for closely spaced geometries where light penetration can lead to slight feature expansion, resulting in the fusion of contiguous features. These findings illustrate the complexity of achieving precision across diverse geometries and provide a clear understanding of which internal features can be reliably incorporated within closed channels and the level of accuracy achievable. Understanding and addressing these limitations is essential for ensuring that DLP-SLA 3D printing can meet the stringent requirements of advanced microfluidic applications.

In summary, DLP-SLA 3D printing demonstrates significant potential for fabricating internal structures within closed microfluidic channels, offering unmatched flexibility and customization compared to traditional methods. These findings provide valuable insights into the capabilities and current limitations of DLP-SLA printing for advanced microfluidic device fabrication.

Chapter 5: Spiral Microfluidic devices

5.1 Introduction

Microfluidics has revolutionized the manipulation of particles and cells at the microscale, offering precise control over fluid dynamics and enabling advanced separation techniques. Among the innovative approaches, spiral microfluidic devices have emerged as a powerful tool for particle separation based on size. These devices leverage the unique interplay of inertial lift forces and drag forces, which govern the lateral migration of particles within microchannels. This chapter explores the foundational principles and methodologies used to study particle separation in spiral microfluidic devices fabricated using advanced 3D printing techniques.

The separation mechanism in spiral microfluidic devices is primarily driven by the balance between inertial lift forces and drag forces. Inertial lift forces are generated by the interaction between velocity gradients and particle inertia. These forces push particles away from regions of high shear, such as near the channel walls, toward stable equilibrium positions. Larger particles, due to their greater inertia, experience stronger inertial lift forces, enabling them to migrate more effectively to equilibrium positions closer to the walls. In contrast, smaller particles are less influenced by inertial lift forces and are more affected by drag forces. Drag forces, caused by the viscous interaction between the particle and the surrounding fluid, act along the direction of flow and dominate the behavior of smaller particles. This interplay between the two forces ensures that particles of different sizes are directed to distinct paths within the channel, enabling efficient separation based on size.

Additionally, the curved geometry of the spiral induces secondary flows known as Dean flows, which further influence particle behavior. These secondary flows arise from centrifugal forces acting on the fluid, generating counter-rotating vortices within the cross-sectional plane of the channel. The combination of Dean drag forces and inertial lift forces creates a dynamic environment where particles migrate to size-specific equilibrium positions. The goal of this work is to achieve effective particle separation based on size by leveraging the interplay between inertial lift forces and Dean drag forces. Larger particles, predominantly influenced by inertial lift forces, are expected to migrate toward the inner walls of the spiral, while smaller particles, more susceptible to Dean drag forces, should be directed toward the outer walls. The optimization of flow rate, channel dimensions, and fluid properties is hypothesized to play a crucial role in refining this separation mechanism, making spiral microchannels a versatile platform for diverse applications.

The ability to manipulate these forces by adjusting channel dimensions, fluid properties, and flow rates makes spiral microchannels highly versatile for a wide range of applications. Altering the channel radius, height, and width can influence the strength and interaction of inertial and Dean forces, enabling the separation of particles with specific size thresholds. Differences in size and density among particles affect their response to these forces, enabling simultaneous sorting based on multiple criteria.

Separating cells from blood presents significant challenges due to the wide range of cell sizes and the similarities between certain cell types. While separating circulating CTCs from red blood cells (RBCs) is relatively straightforward due to the substantial size difference—CTCs are generally larger than RBCs—differentiating CTCs from leukocytes (white blood cells, WBCs) is more complex. Leukocytes often overlap in size with CTCs, which can lead to lower separation efficiency and increased contamination. To address this challenge, an effective approach involves binding leukocytes to beads, thereby increasing their overall size. This size augmentation enables better differentiation between leukocytes and CTCs during size-based separation processes, improving the specificity and reliability of microfluidic separation systems.

In 2015, Warkiani et al developed three staked spiral microfluidic devices based on previous optimization studies for the separation of CTCs ≥15 μm from blood cells (RBC, platelets, and WBC) with a diameter between 3μm to 15μm. The device designed is composed by two inlets, two outlets, channel width of 500 μm, and height of 170 μm as well as ~1 cm in radius of curvature (135). The proposed device allows the recovery of cancer cells ~85% and the depletion of white blood cells ~ 99.99% from a lysed blood sample (136). Overall, the separation microfluidic systems based on size can overcome the limitations of other approaches such as clogging, low recovery, and cell viability, which are some of the most relevant aspects to translating these applications into clinical applications (16).

Spiral microfluidic devices use both the inertial lift forces and the Dean drag force to separate cells. The Dean drag force is generated in curved channels, where the fast-moving fluid experiences a strong centrifugal force, leading to an unstable stratification. As a result, the high-velocity field in the center of the channel moves outward, creating two counter-rotating regions known as Dean vortices. These vortices contribute to the separation of cells in the microfluidic device (117).

In spiral-shaped microchannels, the present cells and particles are influenced by these Dean vortices and by the inertial lift forces. How much particles are affected by Dean force or by lift force depends on the particle's diameter. Di Carlo et al. demonstrated in their research that

particles did not follow the fluid streamlines but migrated across the streamlines in a continuous and predictable manner that can be used to separate particles at the outlets. By taking advantage of the unique characteristics of inertial lift force and Dean force, researchers can develop microfluidic devices that can efficiently and accurately separate and sort particles for various applications (110).

The spiral microfluidic devices employed in our study were fabricated with a rectangular cross-section, and the device includes a 2¼-turn spiral followed by a straight segment to stabilize the flow, ensuring reliable particle separation. The channel dimensions and geometries were varied, particularly in height, to explore their influence on particle separation efficiency under laminar flow conditions.To systematically investigate the effects of key parameters on particle separation, both experimental and computational methodologies were employed. Fluorescent polystyrene microspheres of varying sizes were used as model particles. Simulations performed using COMSOL Multiphysics® allow to compare with the experimental work, enabling detailed analysis of particle trajectories under varying channel heights, flow rates, and particle sizes. The Laminar Flow and Particle Tracing modules were employed to model the complex interactions between fluid dynamics and particle behavior, providing valuable insights into the separation process and guiding experimental design.

This chapter aims to present the methodologies and observations referred to particle separation in spiral microfluidic devices. The results will focus on understanding how channel dimensions, flow rates, and particle sizes influence separation efficiency, laying the groundwork for optimizing device performance and to enhance the understanding of size-based particle separation and its potential applications in biomedical and industrial contexts.

5.2 Spiral Design for Leveraging Lift and Dean Forces

The spiral microfluidic device was specifically designed to enable size-based particle separation by leveraging the interplay between lift and Dean forces. These forces are fundamental in determining the trajectories and equilibrium positions of particles within the channel, providing the basis for efficient separation. The device's geometry was carefully engineered to create flow conditions where these forces act synergistically, allowing particles of different sizes to migrate to distinct positions under laminar flow.

The spiral microfluidic device design consists of inf multiple turns with progressively increasing radius, culminating in a straight segment to stabilize the flow before the outlets. As detailed in Table 3 from Chapter 3.5 of Materials and Methods, the channel features a width of 1.4 mm and varying heights between 550 µm and 800 µm. The first half-turn of the spiral has a radius of 3.8

mm, while the second half-turn increases to a radius of 9.65 mm. This progression continues with the third and fourth half-turns, which have radius of 10.55 mm and 11.55 mm, respectively. The spiral concludes with a final quarter-turn, featuring a radius of 12.45 mm, and a straight segment at the end ensures stabilized fluid flow and particle trajectories before exiting the device. These carefully designed dimensions play a critical role in maintaining laminar flow and enabling particle separation. To ensure successful fabrication and functionality, the design incorporates a 500 µm gap between adjacent spiral walls. This gap is critical for avoiding fabrication defects during 3D printing and for maintaining the structural integrity of the device. The increased channel height, made possible thanks to 3D printing, was a premeditated design choice to accommodate higher flow rates and larger particles (≥50 µm in diameter). These larger particles, which can be beads, are particularly relevant for biomedical applications where functionalized particles may be used to selectively bind and remove specific cell types, such as leukocytes, with size similar to the circular tumor cells (CTC). With this "trapping methodology" is possible to increase the purity of CTCs patient blood samples by removing leukocytes adhered to the beads coated with CD45+ receptor antibodies (137) .

DLP-SLA 3D printing enables the design of microfluidic devices with dimensions that are particularly useful for concentrating purified CTCs from blood samples. Traditional lithography spiral methods can make it difficult to separate CTCs from leukocytes due to their similar size. With SL 3D printing, we can create microfluidic devices with features that enhance CTCs separation, enabling more effective purification. This approach has the potential to significantly improve CTC isolation and analysis for a range of research and clinical applications, allowing for the concentration of purified CTCs from blood samples.

Figure 45 provides an overview of the design and manufacture of the spiral microfluidic device. Panel A shows the schematic of the spiral device, which consists of two inlets (sample input and PBS 1X) and two outlets (CTCs Outlet and Beads+Leukocytes Outlet). The microchannels feature dimensions of 1.4 mm in width and 540 µm in height. Panel B presents the master design created in AutoCAD, while Panel C shows the master fabricated using 3D printing. Panels D and E validate the proper development of the microfluidic channels through optical microscopy, confirming their suitability for subsequent replication in PDMS. Panels F and G highlight the fluorescence validation of the spiral device stained with fluorescein, demonstrating a strong bonding between the PDMS and glass substrate.

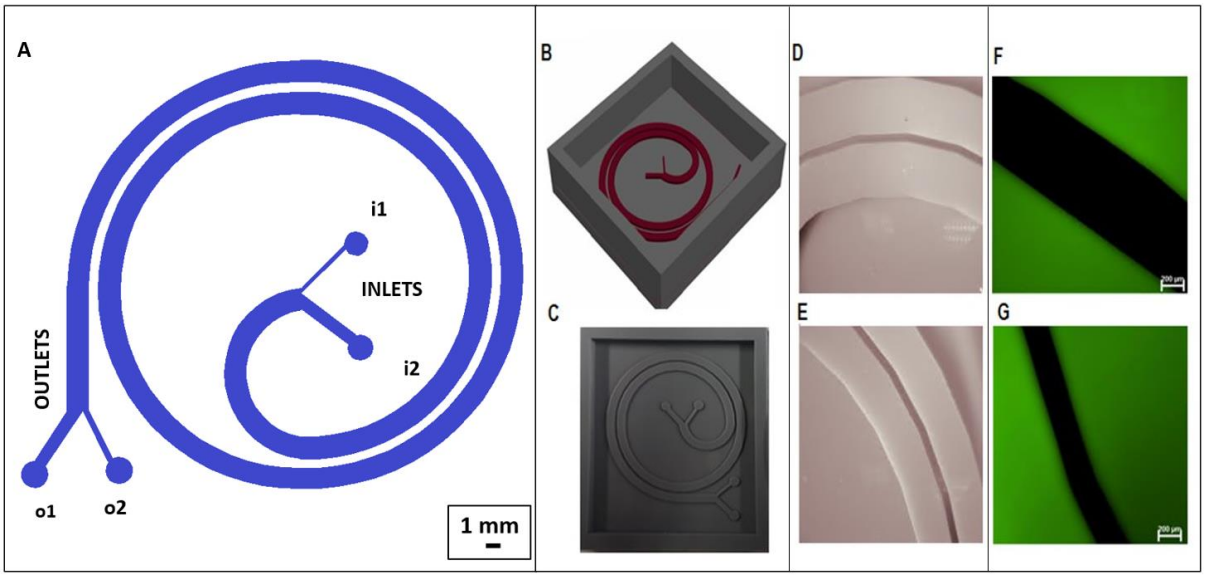


Figure 45: Design and manufacture of the spiral microfluidic device: (A) Schematic of the spiral design with two inlets (sample input and seath flow) and two outlets (CTCs Outlet and Beads+Leukocytes Outlet). (B) Master designed in AutoCAD. (C) Master fabricated by 3D printing. (D-E) Optical microscopy images validating the microfluidic channels' proper development for subsequent PDMS replication. (F-G) Fluorescence images of the spiral device stained with fluorescein, demonstrating good bonding between the PDMS and glass substrate. Scale bars: 1 mm (A), 200 µm (F, G).

5.3 Particle Separation Simulations

To evaluate the separation efficiency of the 3D-printed spiral microfluidic device, the theoretical cutoff diameter for particle separation was first calculated and subsequently compared to results obtained through COMSOL simulations. The cutoff diameter represents the particle size threshold at which the device effectively separates particles, directing larger particles toward one outlet while smaller particles are directed toward another.

The theoretical cutoff was determined using a criterion based on the ratio of the particle diameter (ap) to the hydraulic diameter (Dh) of the channel. According to (138)(0, effective particle focusing occurs when:

Equation 17: Theoretical Cuttoff for Particle Separation.

$$\frac{ap}{D_h} \geq 0.07$$

Here, D_h is the hydraulic diameter, defined as: is the hydraulic diameter, defined as:

Equation 18: Hydraulic Diameter.

$$D_h = \frac{4A}{P} = \frac{2*w*h}{w+h}$$

where A is the cross-sectional area of the channel, P is the wetted perimeter, w is the width and h the height. This relationship emphasizes the dependency of separation performance on the channel geometry. The theoretical cutoff diameter calculated using this formula serves as a benchmark for evaluating particle separation performance in the designed spiral channel.

To simulate how particles behave inside the spiral, the Computational Fluid Dynamics (CFD) module and Particle Tracing module were used. The CFD module enables simulating a continuous flow field inside the device, and the Particle Tracing module was used to solve several discrete trajectories. Hence, the device was utilized to simulate and monitor the actions of CTCs and "Leukocytes+Particles" which is expected to have a total size higher than 70 µm. Hence, the size threshold was ranging from 75 to 100 microns to eliminate bead-trapped leukocytes.

The simulations of the laminar flow demonstrated the Dean Flow effect on a transversal plane as indicated in Figure 46 (arrows in the sections). The in-plane velocity magnitude was plotted in this plane together with the in-plane velocity vectors. As a result, the in-plane vectors indicate two symmetrical recirculating zones in the upper and bottom part of the channel, characteristic of the secondary Dean flow (Figure 46 B-E). Figures 46 B-E show a comparison of the different channel height considered, meanwhile the sample flow rate was fixed to 700 µL/min and the sheath flow to 6.300 µL/min. The results show that the Dean velocities increase when the cross-sectional area of the channel also increases, leading to a stronger Dean force. This enhanced Dean force leads to more efficient separation of particles, resulting in a higher separation ratio.

After the stationary solution for the flow was obtained, the particles trajectories were calculated in a time-dependent study. The simulations were done considering a one-way coupling between the fluid and the particles. The equilibrium position for each particle was calculated along the microfluidic device, it is expected that the balance between the drag and lift force generates different equilibrium position of the particles depending on their size. Thus, the lift force is stronger for the "Particles+leukocytes", meanwhile the CTCs are mainly affected by the drag force, which allows being able to separate them, since they take different outputs in the microfluidic device. (Figure 46).

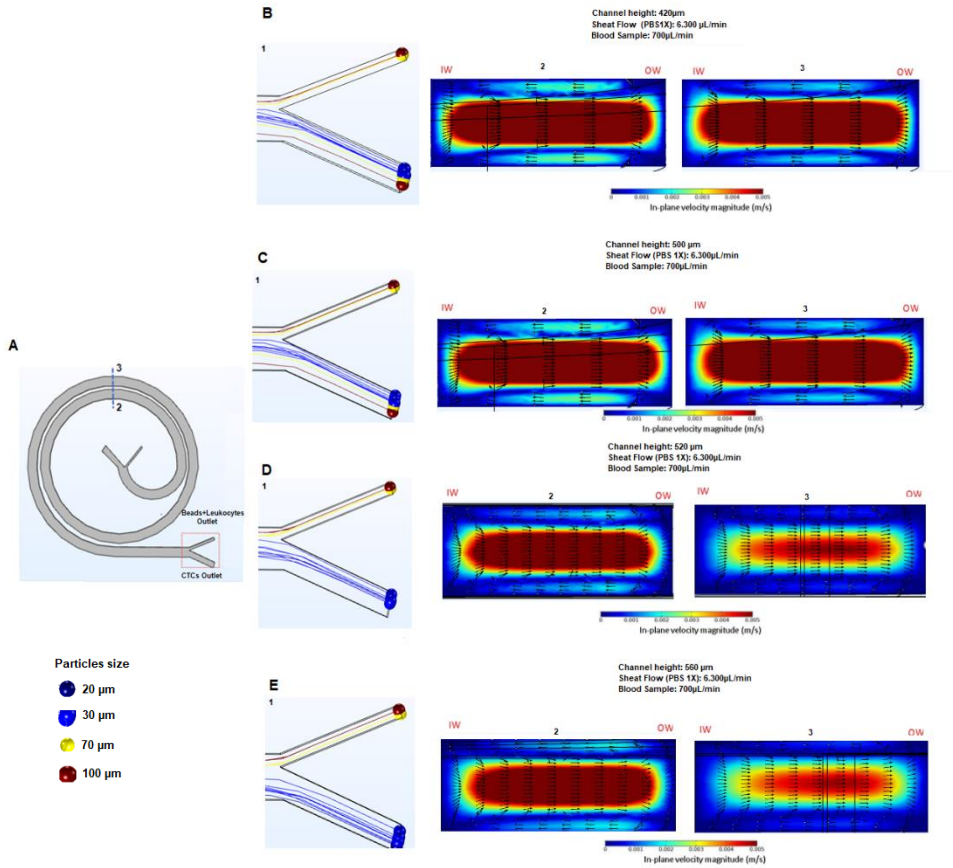


Figure 46: Results obtained in COMSOL. The figure shows a 2D view of a COMSOL simulation of the spiral microfluidic device with particles of different sizes introduced into the system, represented by different colors with a fixed sample flow rate of 700 µL/min and a sheath flow of 6.300 µL/min. The simulation is used to analyze the behavior of the particles as they flow through the spiral channel. By tracking the trajectories of the particles, the efficiency of the device in separating particles of different sizes can be studied.

For this study, theoretical calculations were performed for channel heights of 550 µm, 600 µm, 700 µm, and 800 µm. The interplay between Dean Drag and inertial lift forces is critical, as Dean drag is predominant near the channel walls, while inertial lift forces govern particle motion toward equilibrium positions.(138,139)

Figure 47 illustrates the comparison between theoretical particle separation diameters, calculated using Equation 17, and simulated separation diameters obtained through COMSOL simulations, across different channel heights. The figure highlights the dependency of particle separation performance on the channel geometry. As the channel height increases from 550 µm to 800 µm, both theoretical and simulated separation diameters increase, reflecting the enhanced influence of Dean forces on particle trajectories. The simulated values are consistently higher than the theoretical predictions, likely due to the interplay of additional factors, such as localized flow disturbances and secondary forces not accounted for in the simplified theoretical

model. This comparison serves to validate the theoretical results while providing an understanding of the device's separation behavior under various geometrical conditions.

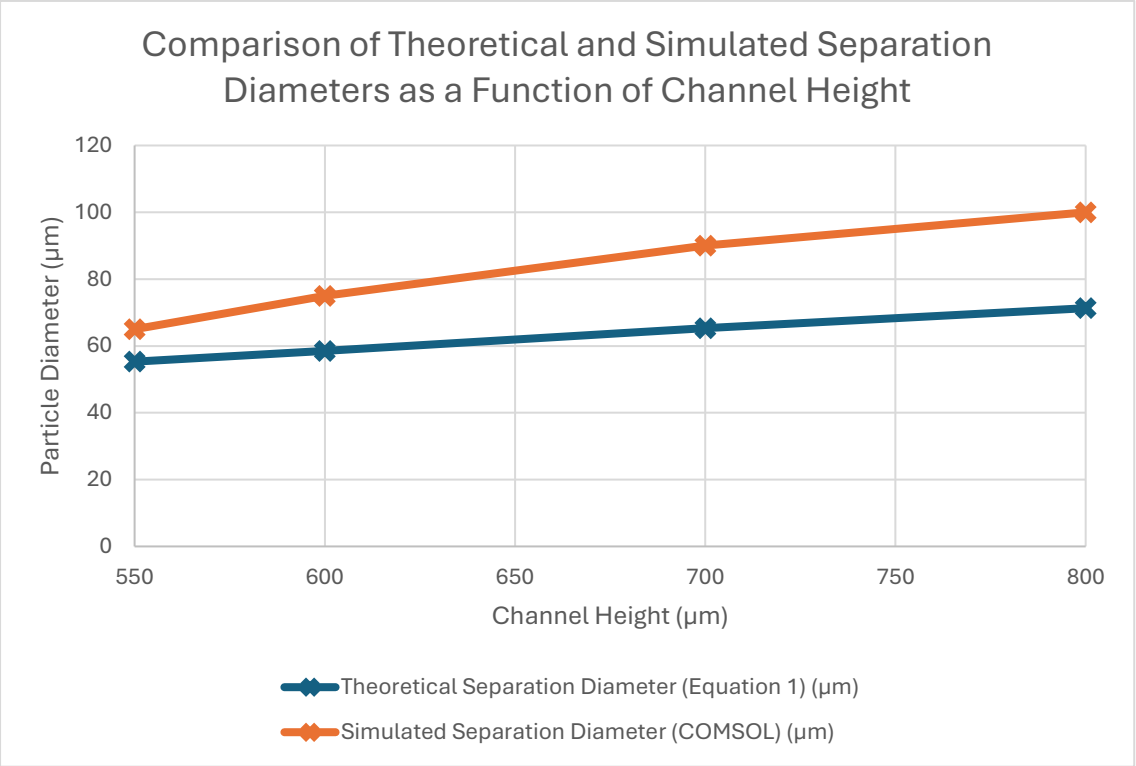


Figure 47: Comparison of theoretical particle separation diameters calculated using Equation 1 and simulated separation diameters obtained through COMSOL for channel heights of 550 µm, 600 µm, 700 µm, and 800 µm and a fixed sample flow rate of 700 µL/min and a sheath flow of 6.300 µL/min. The graph demonstrates the relationship between channel height and separation efficiency, with larger channel heights yielding increased separation diameters. Simulated values consistently exceed theoretical predictions, reflecting additional effects not captured by the theoretical model.

Following the theoretical calculations and general simulations to estimate the particle separation cutoff points across various channel heights, the focus now shifts to simulating specific channel heights that align with our experimental capabilities: 540 µm, 640 µm, and 740 µm. These simulations were designed to evaluate the influence of different flow rates and channel geometries, enabling the identification of the most promising conditions for subsequent experimental validation.

For each channel height, simulations were conducted at five different flow rates, introducing the particle-containing flow through each of the two inputs alternately. In all simulations, the flow rate ratio between the particle-containing flow and the sheath flow was maintained at 1:9, consistent with prior studies to ensure optimal particle focusing(25). This dual-input

configuration results in two simulations per flow rate, effectively exploring both input configurations for a total of 10 simulations per channel height. By analyzing these simulations, we aim to determine the optimal flow conditions and input configurations that maximize separation efficiency, thereby guiding the design of the most informative and feasible experiments. Table 2, in the Materials and Methods Chapter, summarizes the ten simulation conditions done for the channel heights of 540 µm, 640 µm and 740 µm, always following the 1:9 ratio between the particle sample and the seath flow.

The Reynolds numbers were calculated and presented in the table, all the values are within the appropriate range for conducting particle separation experiments under laminar flow conditions, with values between 100 and 150 being ideal for this purpose. The data demonstrates how both flow rate and channel height influence the Reynolds number. Higher flow rates and smaller channel heights result in increased Reynolds numbers, while lower flow rates and larger channel heights reduce them.

Table 20: Reynolds Numbers for Simulated Channel Heights and Flow Rates.

	760 + 6840 $\mu l/min$	700 + 6300 $\mu l/min$	670 + 6030 $\mu l/min$	655 + 6895 $\mu l/min$	640 + 5760 $\mu l/min$
540 µm	130,52	120,21	115,05	112,47	109,90
640 µm	124,12	114,31	109,41	106,96	104,51
740 µm	118,32	108,97	104,30	101,96	99,63

For each simulated channel height, a table is presented to comprehensively analyze the particle separation performance. The table summarizes the percentage of particles of each size directed toward the inner outlet (the smaller outlet of the spiral microfluidic device, referred to as "i2" in Figure 45) under the given simulation conditions. These numerical results provide clear insights into the separation behavior, allowing for a detailed comparison of particle distribution across different channel heights and flow conditions.

To obtain these results, COMSOL Multiphysics was used to simulate the particle trajectories within the spiral microfluidic channel. As demonstrated in Figure 46, the simulations track the movement of particles of varying sizes as they flow through the spiral. In COMSOL, a plane was defined at the section where the spiral channel bifurcates into two outlets, allowing the software to count the particles exiting each outlet. By analyzing this data, the percentage distribution of

particles for each size between the two outlets was determined. Figure 48 illustrates the particle behavior and separation achieved within the spiral microfluidic device. Panel A provides a top view of the device, showing the trajectories of particles of various sizes as they traverse the spiral. Panel B presents an isometric view of the outlet section, clearly displaying the two outputs: the Outer Outlet (OO) and the Inner Outlet (IO), as well as the distribution of particles between them. Finally, Panel C offers a cross-sectional view at the bifurcation point, highlighting the allocation of particles to each outlet, demonstrating the efficiency of size-based separation.

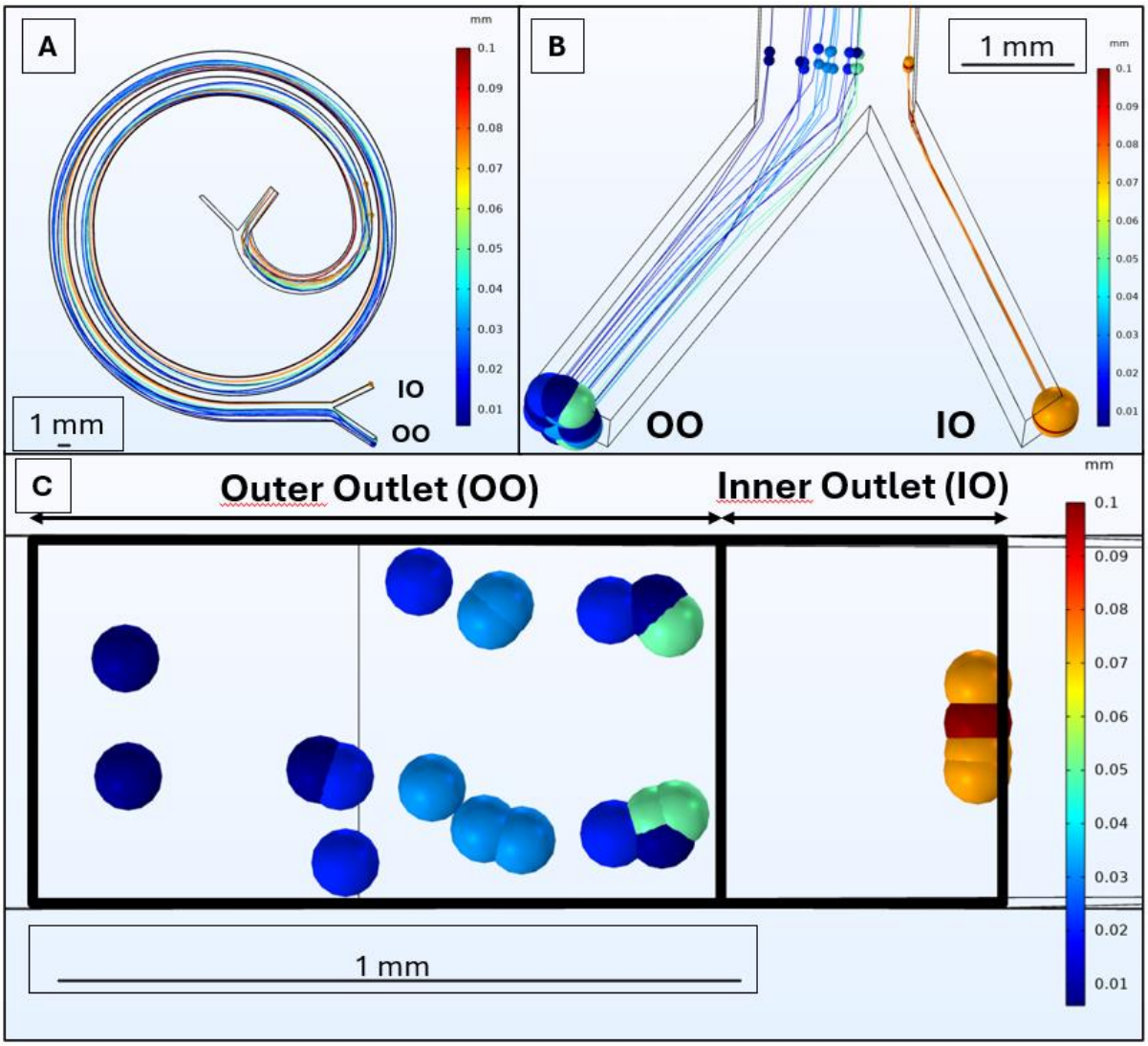


Figure 48: Particle trajectories and separation in the spiral microfluidic device. (A) Top view showing particle trajectories within the spiral channel. (B) Isometric view of the outlet section, displaying the distribution of particles between the Outer Outlet (OO) and the Inner Outlet (IO). (C) Cross-sectional view at the bifurcation point, illustrating the allocation of particles to each outlet based on their size. Scale bar: 1 mm.

Channel Height: 540 µm

The table for this channel height shows the percentage of particles of sizes 6 µm, 20 µm, 30 µm, 50 µm, 75 µm, and 100 µm exiting through the inner outlet. The data highlights how smaller particles are predominantly directed toward the outer outlet, while larger particles are more likely to exit through the inner outlet, reflecting the particle size-based separation achieved at this height.

Table 21: Percentage of particles of each size exiting through the Inner Output for various flow conditions and channel height of 540µm. The remaining percentage corresponds to particles exiting through the Outer Output.

Height: 540 µm	Particle size	100	75	50	30	20	6
Flow 760 6840	% Inner Output	100	100	0	0	0	20
Flow 760 6840 Reverse	% Inner Output	100	100	0	0	40	60
Flow 700 6300	% Inner Output	100	100	0	0	20	0
Flow 700 6300 Reverse	% Inner Output	100	100	0	40	40	40
Flow 670 6030	% Inner Output	100	100	20	40	20	100
Flow 670 6030 Reverse	% Inner Output	100	100	0	0	0	40
Flow 655 5895	% Inner Output	100	100	0	20	20	40
Flow 655 5895 Reverse	% Inner Output	100	100	0	0	0	0
Flow 640 5760	% Inner Output	100	100	0	20	20	60
Flow 640 5760 Reverse	% Inner Output	100	100	0	0	0	0

Channel Height: 640 µm

The table for this channel height presents similar data, showing the particle distribution percentages for the inner outlet. With the increased channel height, variations in particle behavior are observed, particularly for intermediate particle sizes, as the Dean and lift forces act differently compared to the 540 µm channel.

Table 22: Percentage of particles of each size exiting through the Inner Output for various flow conditions and channel height of 640µm. The remaining percentage corresponds to particles exiting through the Outer Output.

Height: 640 µm	Particle size	100	75	50	30	20	6
Flow 760-6840	% Inner Output	100	0	0	80	60	80
Flow 760 – 6840 Reverse	% Inner Output	100	40	0	0	0	0
Flow 700 – 6300	% Inner Output	100	0	0	20	20	40
Flow 700 – 6300 Reverse	% Inner Output	100	0	0	0	0	0
Flow 670 – 6030	% Inner Output	100	0	0	0	0	25
Flow 670 – 6030 Reverse	% Inner Output	100	50	0	20	40	40
Flow 655 – 5895	% Inner Output	100	0	0	0	0	25
Flow 655 – 5895 Reverse	% Inner Output	100	0	0	0	60	60
Flow 640 - 5760	% Inner Output	100	0	0	0	0	25
Flow 640 - 5760 Reverse	% Inner Output	100	0	0	40	60	60

Channel Height: 740 µm

The table for the 740 µm channel height demonstrates how the largest channel geometry affects separation behavior. Larger particles exhibit greater separation efficiency due to enhanced Dean forces, while smaller particles show differing distribution trends compared to the smaller channel heights.

Table 23: Percentage of particles of each size exiting through the Inner Output for various flow conditions and channel height of 740µm. The remaining percentage correspond to particles exiting through the Outer Output.

Height: 740 µm	Particle size	100	75	50	30	20	6
Flow 760 6840	% Inner Output	100	0	0	40	80	80
Flow 760 6840 Reverse	% Inner Output	0	0	0	0	0	20
Flow 700 6300	% Inner Output	100	0	0	20	40	40
Flow 700 6300 Reverse	% Inner Output	0	0	0	0	0	40
Flow 670 6030	% Inner Output	100	0	0	40	40	40
Flow 670 6030 Reverse	% Inner Output	0	0	0	0	60	80
Flow 655 5895	% Inner Output	100	0	0	40	20	40
Flow 655 5895 Reverse	% Inner Output	0	0	0	40	80	80
Flow 640 5760	% Inner Output	100	0	0	40	40	0
Flow 640 5760 Reverse	% Inner Output	50	0	0	40	80	80

We can use the results of simulation to determine the device capacity to distinguish between large diameter beads (75µm and 100 µm) and low diameter beads (50 µm, 30µm, 20 µm, 6µm) considering that our interest in to separate large beads that will trap the leukocytes from the CTC existing in the sample.

We can define some approximative quality factors from the different heights and flow considering the percentage of recovery of large beads and the percentage of “contamination” with small beads (number of small beads present versus number of large beads recovered).

Table 24: Percentage of 100 µm and 75 µm particles recovered at the Inner Output and contamination levels for different flow rates for the Device of 540 µm.

	100 µm	75µm	Contamination
760	100%	100%	10%
700	100%	100%	10%
670	100%	100%	90%
655	100%	100%	40%
640	100%	100%	50%

Table 25: Percentage of 100 µm and 75 µm particles recovered at the Inner Output and contamination levels for different flow rates for the Reverse Device of 540 µm.

	100 µm	75µm	Contamination
760	100%	100%	50%
700	100%	100%	60%
670	100%	100%	20%
655	100%	100%	0%
640	100%	100%	0%

Table 26: Percentage of 100 µm and 75 µm particles recovered at the Inner Output and contamination levels for different flow rates for the Device of 640 µm.

	100 µm	75µm	Contamination
760	100%	0%	220%
700	100%	0%	80%
670	100%	0%	25%
655	100%	0%	25%
640	100%	0%	25%

Table 27: Percentage of 100 µm and 75 µm particles recovered at the Inner Output and contamination levels for different flow rates for the Reverse Device of 640 µm.

	100 µm	75µm	Contamination
760	100%	40%	0%
700	100%	0%	0%
670	100%	10%	70%
655	100%	0%	120%
640	100%	0%	160%

Table 28: Percentage of 100 µm and 75 µm particles recovered at the Inner Output and contamination levels for different flow rates for the Device of 740 µm.

	100 µm	75µm	Contamination
760	100%	0%	200%
700	100%	0%	100%
670	100%	0%	120%
655	100%	0%	100%
640	100%	0%	80%

Table 29: Percentage of 100 µm and 75 µm particles recovered at the Inner Output and contamination levels for different flow rates for the Reverse Device of 740 µm.

	100 µm	75µm	Contamination
760	0%	100%	50%
700	0%	100%	25%
670	0%	100%	20%
655	0%	100%	0%
640	50%	100%	0%

These results illustrate how channel height, flow rates, and the initial distribution of input particles influence separation efficiency within the spiral microfluidic device. It is shown that the device height significantly affects the separation cutoff point; in a 540 µm channel, particles of both 100 µm and 75 µm are directed to the inner outlet. Conversely, in a 640 µm channel, all 100 µm particles go to the inner outlet but some of the 75 µm particles vary in their trajectory, while in a 740 µm channel, there is even a loss of 100 µm particles. Additionally, the chosen flow rate within a specific channel height impacts the percentage of contamination, thus highlighting the importance of selecting the appropriate device and flow rate according to the desired objective. This detailed and clear analysis of particle behavior across different channel geometries is crucial for determining optimal conditions for effective particle separation and deciding on the most efficient experiments to conduct.

In conclusion, the simulation results provide valuable insights into the separation performance of the spiral microfluidic device for different channel heights and flow rates. Based on the findings, the flow rate of 760 µL/min will be tested experimentally for the 540 µm channel height, and the flow rate of 760 µL/min (rotated input configuration) for the 640 µm channel height. These cases demonstrated a promising level of particle separation efficiency in the simulations, indicating the potential for effective experimental validation. The experimental testing will serve to confirm the separation behavior observed in the simulations and further evaluate the device's performance under real conditions.

5.4 Fabrication of the Spiral Microfluidic Device

5.4.1 Mold-Based PDMS Devices

The mold-based fabrication of spiral microfluidic devices combines the precision of 3D printing with the flexibility and biocompatibility of PDMS, making it a widely used approach for creating microfluidic systems. This method involves several steps, from designing and fabricating the mold to replicating the microchannel structure in PDMS and assembling the device. By using 3D printing, detailed molds with extruded channel structures can be created, enabling consistent and reliable replication of complex geometries.

The drawing for the molds used for PDMS replication were designed using Autodesk Inventor software, allowing precise control over the spiral geometry, including radius, channel widths, and

heights. The designed channel width was 1.4 mm and the heights had a range from 550 µm to 800 µm. The molds were fabricated via a DLP-SLA process using three different resins: Detax Freeprint Ortho 385, Asiga PlasClear and Keyprint KeyOrtho IBT. The 3D printing process creates a raised (extruded) spiral structure on the mold, which ensures that the features correspond to the channel geometry of the final PDMS replica. The design ensures a 500 µm gap between adjacent spiral walls to prevent fabrication errors during 3D printing, minimizing the risk of resin overcuring and ensuring reproducibility of the mold geometry.

The replication process starts by preparing PDMS in a standard 10:1 ratio of base polymer to curing agent, ensuring a balance between flexibility and mechanical stability. The mixture is thoroughly degassed in a vacuum chamber to remove air bubbles that could compromise the quality of the channels. The degassed PDMS is poured over the mold, ensuring complete coverage of the spiral structure. This step is crucial for replicating the intricate details of the channel geometry. The mold-PDMS assembly is placed in an oven at 85°C for at least 12 hours to cure the PDMS fully. After curing, the PDMS layer is carefully peeled off the mold, taking care to preserve the structural integrity of the spiral channels. Once the PDMS replica is obtained, inlet and outlet holes are punched with a diameter of 1.0 mm to allow fluid entry and exit during experiments.

The PDMS replica is bonded to a glass substrate to create a closed microfluidic system. This process involves oxygen plasma treatment of both the PDMS and glass surfaces to generate reactive groups that form a strong and permanent bond upon contact. Plasma exposure is applied for 30 seconds, and the two surfaces are aligned and pressed together immediately to ensure uniform adhesion. Figure 49 shows the equipment used for the bonding using plasma cleaner.



Figure 49: Plasma cleaner used for the oxygen plasma treatment of PDMS and glass surfaces prior to bonding.

The bonded device is inspected for leaks using dye-based flow tests. Colored dye is injected into the microchannels to verify the integrity of the bonds. This step is essential for ensuring the functionality of the device in subsequent experiments.

Mold-based PDMS devices are widely used in microfluidic research due to their optical transparency, chemical compatibility, and flexibility, making them ideal for applications such as particle separation, mixing, and biological assays. The transparency of PDMS and glass facilitates real time visualization of fluid and particle motion under a microscope, which is particularly advantageous for fluorescence-based studies. The use of 3D printed molds ensures consistent replication of intricate channel geometries, enabling the rapid and cost-effective production of multiple PDMS replicas, thereby providing scalability for experimental studies. Additionally, the reusability of molds adds efficiency to the production process, while the biocompatibility and optical clarity of PDMS make it highly suitable for biological and imaging applications.

Despite these advantages, the method does have limitations. The process involves multiple steps, including mold fabrication, PDMS replication, and bonding, which can be time consuming. Overall, the mold-based PDMS fabrication method is a robust and versatile approach for creating microfluidic devices with precise geometries and excellent performance. By leveraging the

accuracy of 3D printed molds and the flexibility of PDMS, this method enables the production of devices suitable for a variety of experimental and practical applications.

Figure 50a shows the extrusion to create an open channel, which is used for creating PDMS molds and can be observed in Figure 50b. Figure 50b shows the PDMS replica bonded to glass and tested with dyes for further confirmation of the absence of leakage between the channels.

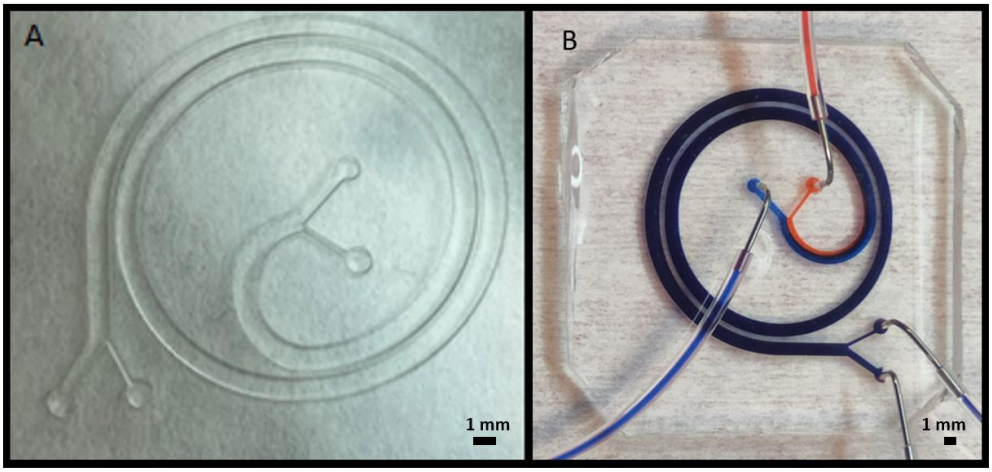


Figure 50: (A) 3D printed result with Detax resin of the extruded spiral, with a designed channel width of 1.4 mm and height of 600 µm. (B) Picture of the microfluidic system created with the PDMS replica based on the 3D printed part of (A).

5.4.2 Embossed 3D-Printed Devices with Direct Assembly

The fabrication of spiral microfluidic devices using embossed 3D-printed channels provides an alternative to mold-based methods, enabling rapid prototyping while simplifying the assembly process. In this approach, the spiral microchannel is printed directly as an open channel recessed into the base of the part, and the open channel is sealed with a complementary 3D printed cover.

The same dimensions from the mold-based method were used, channel width of 1.4 mm and heights ranging from 550 µm to 800 µm. Also the same resins were used, Detax Freeprint Ortho 385, Asiga PlasClear, and Keyprint KeyOrtho IBT.

To close the open channels and create a sealed microfluidic system, a second 3D printed piece was used as a cover. This cover was fabricated to match the geometry of the base and included integrated inlets and outlets for fluid management. Among the resins tested, KeyOrtho IBT was

particularly effective for sealing purposes. This resin retains a sticky surface even after printing, providing a natural adhesion that facilitates bonding with the embossed base.

The sealing process involved aligning the cover with the embossed base and applying mechanical pressure, typically using clamps or tweezers, to ensure a tight bond. The assembly was then post-cured under UV light, a process that activated the residual stickiness of the KeyOrtho IBT resin and securely bonded the two components. This approach eliminated the need for additional adhesives. This post-curing step also ensured full polymerization of the resin, enhancing the mechanical stability and durability of the device.

Leak tests were performed using dyed fluids to confirm the integrity of the sealed channels, as seen in Figure XX. This step verified the bonding quality and ensured that the device was ready to use.

Compared to mold-based methods, the embossed channel approach with direct sealing offers several advantages. It reduces fabrication time, eliminates intermediate steps like PDMS casting, and allows for the integration of additional features, such as built-in connectors or multi-level designs. However, it also requires careful handling during assembly to ensure precise alignment and consistent bonding, especially when dealing with smaller channel dimensions, and it is more propense to leakages.

We used the open channel shown in Figure 51a and attached a 3D printed cover with connectors, as shown in Figure 51b, to have a closed microfluidic channel. Moreover, the devices were tested using syringe pumps and two different dyes were passed through the channel confirming the absence of leakage as seen in Figure 51c.

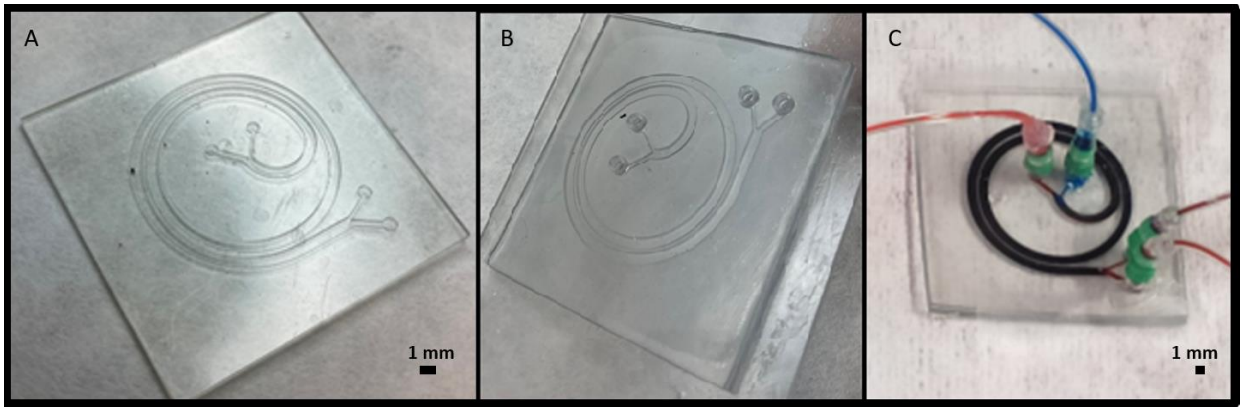


Figure 51: (A) 3D printed result with Detax resin of the embossed spiral, with a designed channel width of 1.4 mm and height of 600 µm. (B) Assembly of an open spiral and a cover printed separately, with Keyprint resin. (C) Microfluidic system consisting of two inputs and two outputs, used to separate particles by their size.

5.4.3 Dimensional Accuracy: Resin and Method Comparison

Dimensional accuracy is a critical factor in ensuring the performance and reliability of microfluidic devices. As shown in the table, the dimensional deviations for width and height are greater in embossed features compared to extruded ones, regardless of the resin used. This highlights a consistent trend where the embossed process introduces higher errors.

In Table 27, height and width errors are presented for the designs shown in Figures 8a and 9a, for each type of resin.

Table 30: Width and height error for extruded and embossed spiral printed with the three different types of resin.

Resin	Feature Type	Width Error	Height Error
Detax	Extrusion	0.14%	0.94%
	Embossed	0.30%	3.62%
Asiga	Extrusion	0.24%	0.93%
	Embossed	0.31%	4.98%
Keyprint	Extrusion	0.34%	3.40%
	Embossed	1.43%	4.67%

Among the three resins tested, Detax emerges as the resin with the highest precision, achieving the lowest errors in both width (0.14% for extrusion, 0.30% for embossed) and height (0.94% for extrusion, 3.62% for embossed). This superior accuracy makes Detax particularly suitable for applications requiring tight dimensional tolerances. Furthermore, as discussed in the previous chapter, Detax also exhibited reduced lateral roughness, contributing to smoother channel walls and improved fluid flow characteristics.

In contrast, embossed features, while advantageous in terms of simplifying the sealing process, exhibit significantly higher errors. This fabrication method also introduces additional challenges, such as alignment inaccuracies during assembly and a higher propensity for leaking, particularly when dealing with complex geometries or high-pressure flow systems. These drawbacks make embossed methods less favorable for precise experimental setups, despite their faster and easier manufacturing process.

Given these findings, the PDMS mold-based method is considered the optimal approach for producing microfluidic devices for experimental studies. The use of Detax resin in the mold fabrication process further ensures the highest dimensional accuracy and device performance,

making it the preferred choice for creating reliable and reproducible microfluidic channels. This combination of PDMS replication and Detax molds provides a robust solution for achieving both precision and functionality in experimental microfluidics.

5.4.4 Microfluidic Devices Fabrication Using 3D Printed Closed Channels

The direct fabrication of microfluidic devices with closed channels using 3D printing represents an innovative and efficient method for device production. In this approach, the channels were printed fully enclosed, eliminating the need for subsequent sealing or assembly processes. Devices with channel heights of 600 µm, 700 µm, and 800 µm, with a cover thickness of 200 µm, were successfully fabricated. However, attempts to produce closed-channel designs with smaller dimensions were unsuccessful, due to over curing problems and difficulties removing the uncured resin from the channels. Only the Detax resin was tested in this section, as we considered the lateral roughness of the device a critical factor.

This fabrication method incorporates inlets and outlets directly into the printed device. Once the device is printed, the only additional steps required are cleaning and post curing. The result is a ready-to-use microfluidic device that requires no additional assembly or preparation. This integration of inlets and outlets is particularly advantageous, as it reduces potential alignment errors and minimizes leakage risks commonly associated with assembly.

The methodology used to achieve these closed channel designs builds upon the technique outlined in the previous results chapter. By carefully optimizing printing parameters, including resin selection and curing protocols, it was possible to ensure dimensional accuracy and structural integrity of the enclosed channels. This method represents a significant advancement in microfluidic device fabrication, offering a rapid, reliable, and assembly-free alternative for creating devices with enclosed channels.

Figure 52 showcases a spiral microfluidic device fabricated in a single step using DLP-SLA 3D printing. The device integrates both inputs and outputs within the same printing process, eliminating the need for additional assembly steps. The microchannels exhibit a width of 1.4 mm and a height of 600 µm.

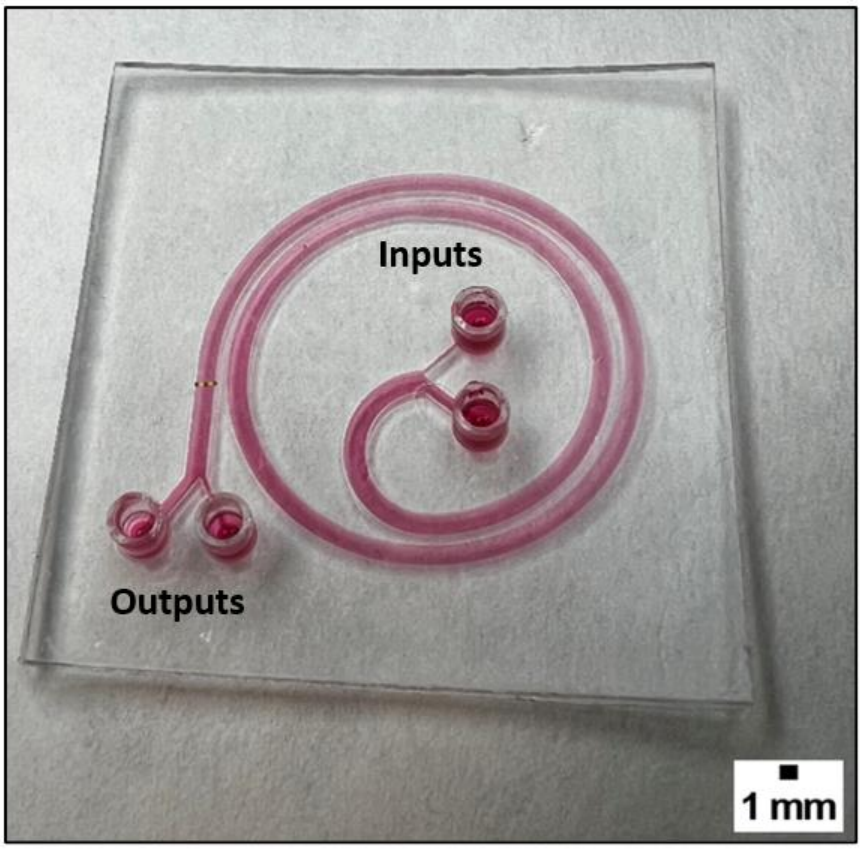


Figure 52: The picture shows a 3D printed device, which consists of a spiral with a channel of 1.4 mm width and 600 µm height.

5.5 Experimental Results

Based on the simulation results discussed in Section 5.3, a series of experiments were designed to validate the functionality of the spiral microfluidic device. These experiments aimed to confirm that the device performs as expected under the defined configurations. Fluorescent polystyrene particles with diameters of 30 µm, 50 µm, 75 µm, and 100 µm were used to analyze the particle distribution between the inner and outer outlets at specific channel heights and flow rates.

The experimental setup included the 540 µm device tested at a flow rate of 760 µL/min for the four particle sizes. Additionally, the 640 µm device was tested at the same flow rate (760 µL/min) but with a rotated particle input configuration compared to the 540 µm setup.

Experiments were conducted using a fluorescence microscope equipped with a high-speed camera capable of capturing particle traces. Fluorescence filters specific to the particle type

were applied: a red fluorescence filter for 30 µm and 75 µm particles, and a green fluorescence filter for 50 µm and 100 µm particles. Experimental parameters were carefully defined to ensure consistent data acquisition, with each experiment lasting 2 minutes and images captured at intervals determined by an exposure time of 100 ms.

As detailed in the methods section, the fluids were introduced into the device using syringe pumps, and the outlets were directly connected to waste containers. Although no cytometry analysis was performed on the outlet samples, the waste from both outlets was collected separately to allow for potential future analysis. These experiments provide a crucial step toward experimentally validating the simulated separation performance of the spiral microfluidic device.

To analyze the results of the experiments, the particles exiting through each output are manually counted. This process involves dividing the video, which consists of a series of time-varying stacks, into subsets of stacks. This division simplifies the task of counting the number of particles directed to each outlet. The counting process is carried out using ImageJ software, which allows precise visualization and analysis of the particle trajectories. An example of the processed stack subsets and particle trajectories is shown in Figure 53, highlighting the approach used to quantify the distribution of particles across the inner (left) and outer (right) outlets.

Figure 53 provides an example of the processed stack subsets and particle trajectories. The fluorescence microscopy images illustrate the distribution of fluorescent polystyrene particles exiting through the inner (left) and outer (right) outlets, allowing the quantification of the spiral microfluidic device in separating particles based on their size. In these examples, red fluorescence (A) corresponds to 30 µm particles, while green fluorescence (B) represents 100 µm particles.

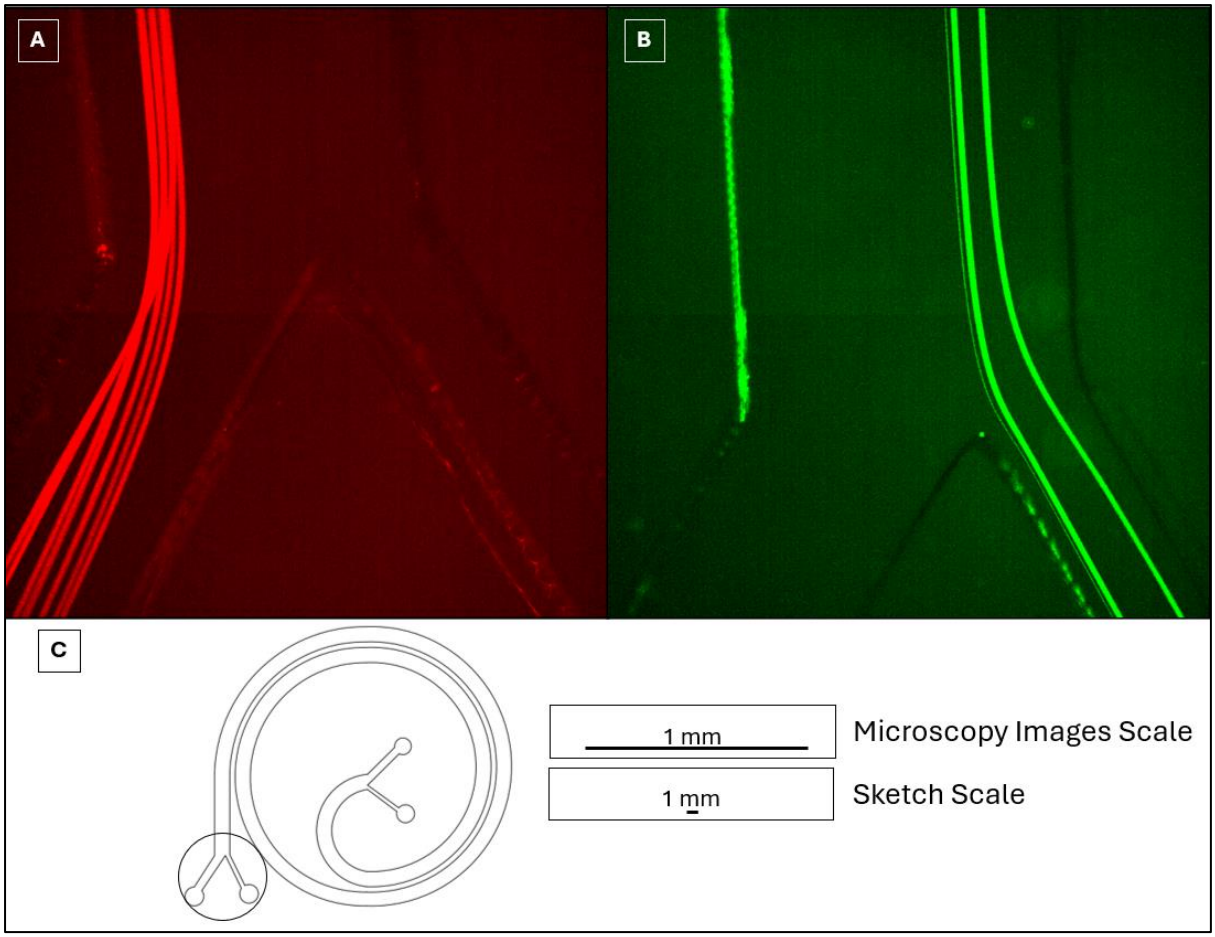


Figure 53: Processed stack subsets and fluorescence microscopy images showing particle trajectories in the spiral microfluidic device. (A) Fluorescent polystyrene particles of 30 µm diameter, directed toward the outer outlet. (B) Fluorescent polystyrene particles of 100 µm diameter, directed toward the inner outlet. (C) Sketch of the spiral microfluidic device with an inset indicating the analyzed region. Scale bars: 1 mm.

Table 31: Experimental Results for Channel Height: 540 µm. Sample with Particles 760 ul/min and Seath Flow 6840 ul/min.

540 um	Particle size	100	75	50	30
Flow 760 6840	% Inner Output	88,24%	87,50%	0,00%	0,00%
	% Outer Output	11,76%	12,50%	100,00%	100,00%

The comparison between the experimental and simulated results for the 540 µm channel height reveals both alignments and discrepancies. For larger particles, such as those with diameters of 100 µm and 75 µm, the simulated results indicate that 100% of these particles exit through the inner outlet, reflecting an ideal separation scenario. However, experimental results show slightly lower percentages, with 88.24% of 100 µm particles and 87.50% of 75 µm particles directed toward the inner outlet, while the remaining fractions exit through the outer outlet. This deviation highlights the fact that experimental results may not be as ideal as simulations due to inherent variations in real-world conditions, such as minor flow instabilities or particle behavior that cannot be perfectly replicated in a simulation.

For smaller particles, such as those with diameters of 50 µm and 30 µm, both experimental and simulated results align, showing that 100% of these particles are directed toward the outer outlet. This consistency confirms that the device performs effectively in separating smaller particles under these conditions. It is important to note that the experimental setup did not include particles of 20 µm or 6 µm, which were included in the simulations. Therefore, no direct comparison can be made for these particle sizes.

Overall, the experimental results demonstrate that the device with these specific conditions can effectively isolate a large proportion of particles larger than 75 µm. While experimental outcomes may exhibit slight deviations from ideal simulations, they confirm the device's utility for size-based particle separation and its suitability for practical applications requiring the isolation of larger particles.

Table 32: Experimental Results for Channel Height: 640 µm. Sample with Particles 760 ul/min and Seath Flow 6840 ul/min. Reverse Configuration.

640 um	Particle size	100	75	50	30
Flow 760 6840 INVERSE	% Inner Output	93,55%	14,29%	0,00%	0,00%
	% Outter Output	6,45%	85,71%	100,00%	100,00%

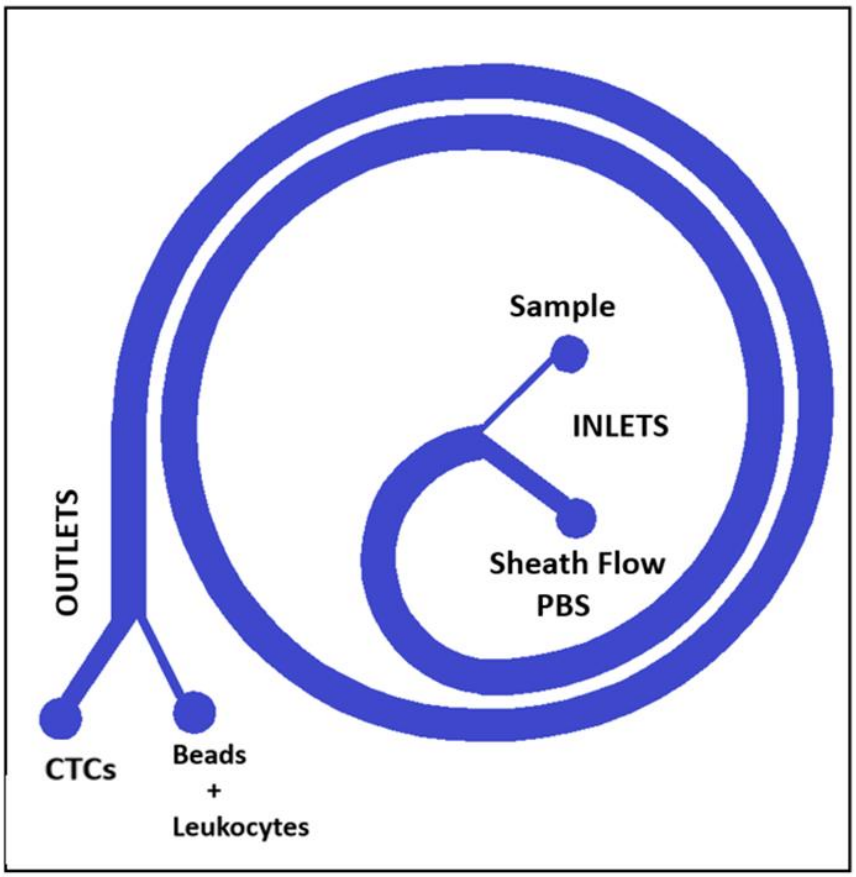
The comparison between the experimental and simulated results for the 640 µm channel height provides important insights into the performance of the spiral device. In the simulated results, particles with diameters of 100 µm exit through the inner outlet, achieving separation efficiency Particles of 75 µm, however, show a distribution where 40% are directed toward the inner outlet and 60% toward the outer outlet, which is not useful for applications requiring strict separation. Smaller particles (50 µm and 30 µm) are fully directed to the outer outlet in the simulations, demonstrating effective separation for these sizes. It is important to note that particles of 20 µm and 6 µm were not included in the experimental part of this study.

Experimentally, the results align well with the objectives for this channel height. The 100 µm particles show good separation, with 93.55% directed toward the inner outlet and only 6.45% to the outer outlet. This validates the device's ability to effectively separate particles of this size. For the 75 µm particles, experimental results show that only 14.29% exit through the inner outlet, while 85.71% are directed to the outer outlet. While this deviates from the simulated values, it is a favorable outcome, as it ensures that the inner outlet predominantly contains particles larger than 75 µm. This distinction allows the device to serve as a reliable threshold for separating particles into two categories: those larger than 75 µm and those smaller.

The experimental results confirm that this device and configuration can be used effectively to isolate 100 µm particles with high precision. Furthermore, the reduced presence of 75 µm particles in the inner outlet enhances the device's utility in applications requiring strict separation between larger and smaller particles. The ability to achieve such clear differentiation supports the device's potential for practical applications where precise size-based particle separation is critical.

5.5.1 EXPERIMENTAL RESULTS OBTAINED IN COLLABORATION

Figure 54 illustrates the design of the single spiral microfluidic device. This device is designed to separate CTCs from a blood sample and subsequently purify the isolated CTCs, effectively reducing leukocyte contamination. The innovative spiral design leverages centrifugal forces to stratify cellular components based on size and density, facilitating precise separation through dual outputs.



enrichment.

Figure 54: Design of the single spiral. The spiral design is used for standard lithography and for 3D printing, a microfluidic device that enables first the separation of CTCs from a blood sample and second the purification of the obtained CTC sample reducing the separation of CTCs from a blood sample and second the purification of the obtained CTC sample reducing the concentration of Leukocytes. The blood sample is introduced into one of the device's two inputs and then flows through the spiral channel. As the blood flows through the spiral, it is subjected to centrifugal forces, which causes the CTCs to migrate towards the outer wall of the spiral while the other components such as beads and leukocytes move towards the center. This separation is then facilitated by the device's two outputs, with the CTCs being directed towards one output while the beads and leukocytes are directed towards the other. This design allows for the efficient and precise separation of CTCs from a blood sample, which can then be used for various diagnostic and therapeutic applications.

Characterization of spiral device with 70 µm particles-Leukocytes and 20 µm particles as CTCs model

Therefore, as previously mentioned, new enrichment methods are needed to purify CTCs and reduce the leukocyte background, which is a key requirement for performing cancer gene mutation analysis using contamination-sensitive technologies, such as real-time PCR and next generation sequencing (140,141). For that purpose, the single 3D spiral device previously developed could help to increase the leukocyte depletion. For this, a blood sample without cancer cells was processed through another spiral device obtained by the doctoral thesis of Jessica Sierra (142). The sample obtained from CTCs outlet, which would correspond to the leukocytes that could contaminate the CTCs sample, was incubated with 70 µm diameter microspheres conjugated with Biotin-CD45 antibodies and secondary antibody as a control (Figure 56A-C). The surface antibody coverage and the total number of particles required to maximize the leukocyte capture was calculated based on the assumption that in heterogeneous interactions with an excess of target capture interact with a limited concentration of capture probe on the surface, estimated to be around 30%(143).

The developed microfluidic setup, presented in Figure 55, utilizes a spiral microfluidic device to separate CTCs from leukocytes bound to beads, leveraging size-based differentiation. By conjugating leukocytes with beads to increase their effective size, the system enables efficient separation of CTCs and leukocyte-bead complexes based on inertial forces.

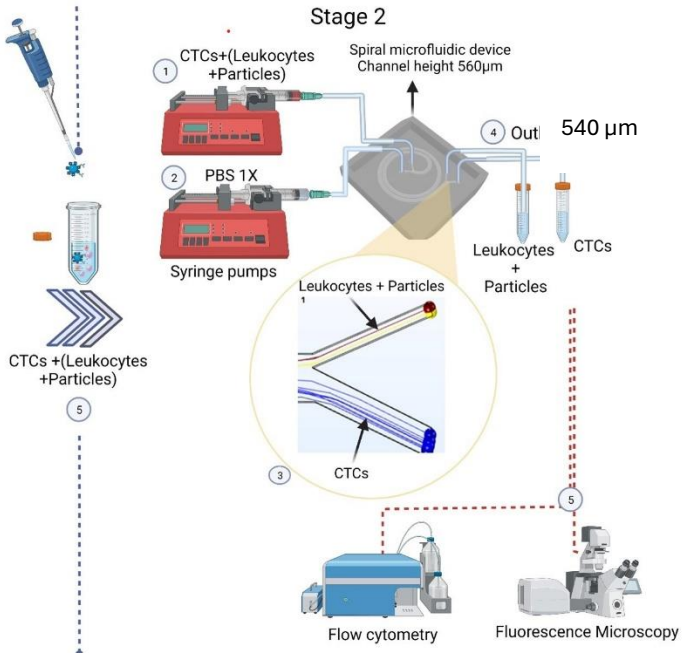


Figure 55: Microfluidic setup for the separation of CTCs from leukocyte-bead complexes.

The results revealed that around 48% of leukocytes were captured by the beads (Figure 56 D, E). Moreover, through the capture of microscope fluorescent images was possible to demonstrated that most of the 70 µm particles without leukocytes bonded could be separated and take the "Leukocytes+beads outlet". It may be the same case for the particles with the leucocytes bonded, since the total size of the particles would be bigger, and as the simulation results demonstrated that this device allows separate particles bigger than 70µm. Limitations in the quantification of 70 µm particles recovered were encountered using flow cytometry due to clogging caused by the particles size and recording videos due to the time recording time possible per sample. Despite the limitations exposed the number of 70 µm particles recovered were quantified by microscopy, and the results shows a recovery rate of 75±17% (Figure 56G,). Moreover, particles of 20 µm as CTCs model were pass through the spiral and as result 100% were successfully recovered (Figure 56F)

Hence, based on the preliminary optimization based on the percentage of leukocytes captured by the beads, as well as the separation of the particles observed by microscope images; we hypothesize that this device could separate smaller particles which correspond to cancer cells or CTCs (>12µm) from streptavidin particles coated with CD45 and leukocytes. Nonetheless, further work is needed to develop reliable quantification methods for the easy implementation of this system and the validation of the complete system with blood samples spiked with cancer cells, as well as blood samples from cancer patients.

Finally, thanks to the devices developed is not needed to perform extra sample centrifugations, which increases the risk of losing CTCs. In contrast, our system could represent a new approach to CTC separation by combining inertial forces microfluidic devices, antibody binding approaches, and 3D printing methods that have not been widely reported until now, which could allow higher leukocyte and erythrocyte depletion rates.

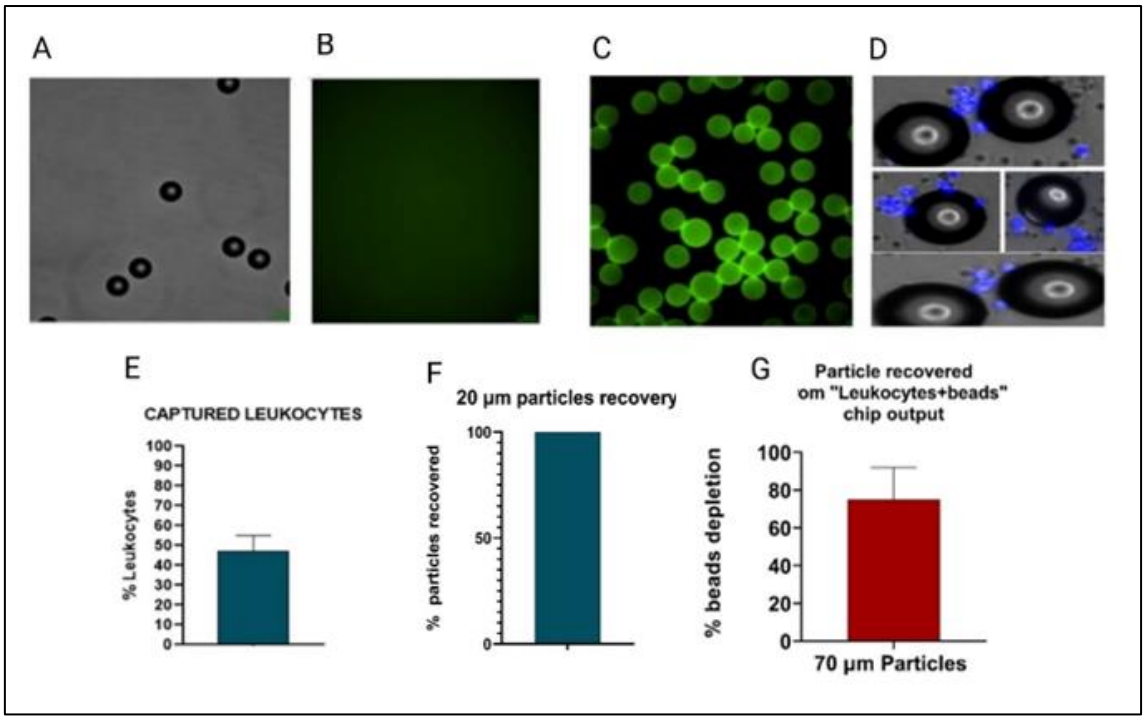


Figure 56: Characterization of polystyrene particles binding to CD45-antibody: A) Polystyrene particles of 70um in Bright field (BF). (B) Negative control for Biotin-CD45. C) Polystyrene particles binding with biotin-CD45 antibody and secondary antibody AlexaFluor 488. D). Polystyrene particles are binding with leukocytes (nucleus stained in blue). E) Quantification of particles binding to leukocytes with an efficiency around 48%. F) Quantification of 20 µm depleted from the sample (100%) G) Quantification of 70 µm depleted from the sample (75±17%). Values and error bars represent mean ± S.E.M.

5.6 Design and fabrication of two spiral microfluidic devices to increase the separation efficiency

In order to further enhance the purification capability of our spiral microfluidic devices combined with beads, we have developed a design compatible with 3D printing that features two interconnected spirals, as shown in Figure 57. This new approach involves the fabrication of two different spirals, each 3D printed in different planes, that work in tandem to maximize CTCs purification. Furthermore, channels can be printed on different planes, that is one of the benefits of 3D printing.

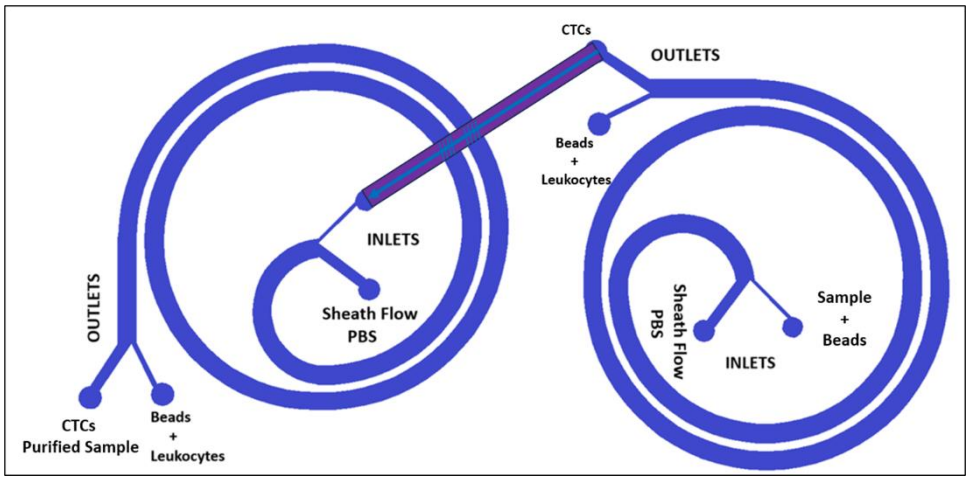


Figure 57: Design of the two interconnected spirals. The two blue spirals are placed in different planes; thus, the red channel is inclined. The new design is a double spiral microfluidic device that can be 3D printed thanks to its inclined channel, which enables double filtration of the blood sample.

The device shown in Figure 52 was modified by adding a second spiral in a different plane, as shown in Figure 58. To ensure the inclined channel was not obstructed while printing the channel height was fixed to 800 µm. This novel design leverages the purified CTCs obtained from the first spiral device as the input for the second spiral device, thereby enhancing the separation efficiency. The use of 3D printing made this innovation feasible since the second spiral was printed on a different plane than the first one, which is not achievable with traditional lithographic fabrication techniques.

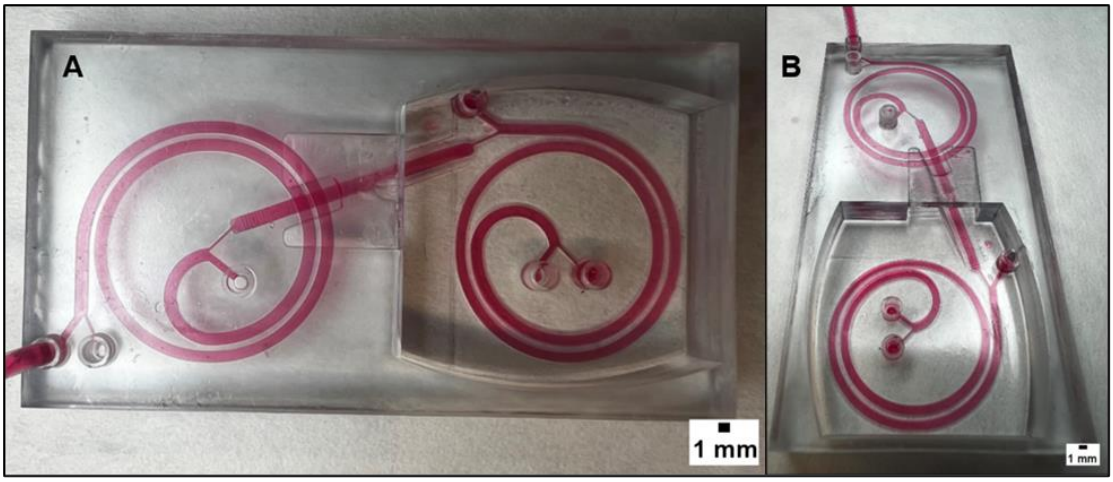


Figure 58: (A) Figure 6A displays the superior view of a microfluidic device that combines two spirals in order to enhance its performance. The device has two spirals in different planes, and this figure provides an overview of the device's structure and design. (B) Figure 6B provides a different point of view of the device. It can be observed that the two spirals are arranged in different planes and that there is an inclined channel that connects them. The realization of this design is possible thanks to the 3D printing technology, which offers the flexibility and precision necessary to create complex geometries that cannot be achieved with traditional manufacturing methods. The dimension of the channel is 1.4 mm in width with a height of 800 µm.

The dimensions of the channels within the microfluidic device were studied using test structures as shown in Figure 59. The results of the fabrication confirmed that the channel cover was slightly thicker than the intended design. This deviation in dimension is attributed to the UV radiation from the DLP-SLA printer, which penetrates the cover and enters the channel, curing a small amount of resin that should have remained uncured. The deviation in dimensions was found to have a minimal effect on the overall performance of the device, and further optimization of the printing process can be done to mitigate this issue.

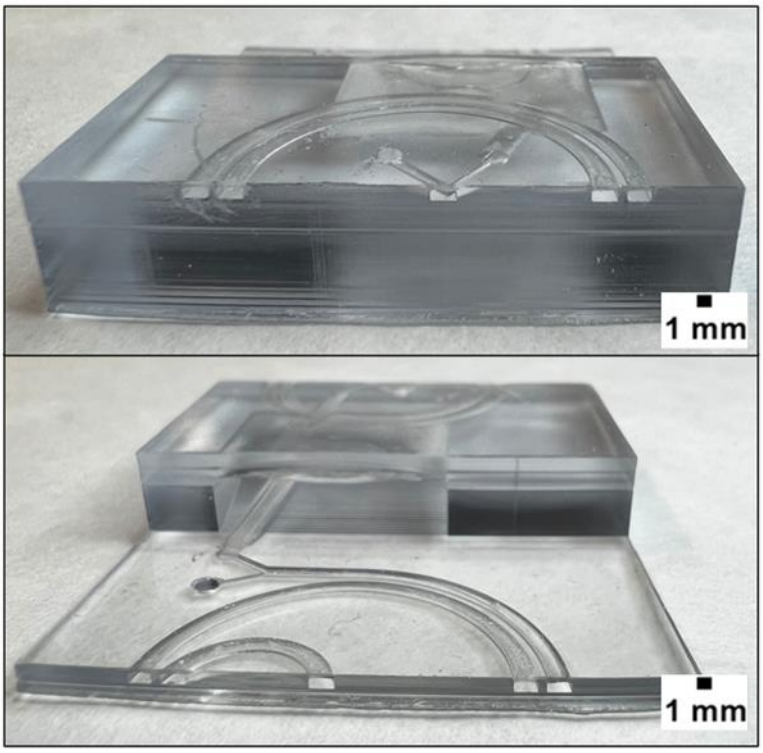


Figure 59: The figure shows two different views of the section of the double-spiral device, 3D printed with Detax resin. This has been created by using a slicing software to cut a portion of the complete device, to uncover the interior of the channels. It shows the printed dimensions of the channels, and any deviations from the intended design would be noticed.

With the sections of these 3D printed channels, their measurements were compared to the intended design. The cover of the upper spiral was observed to be 252 µm, which is 52 µm more than the intended 200 µm. This indicates that extra polymerization occurred due to the penetration of UV radiation from the DLP printer, meaning that the UV light cured a small amount of resin that should have remained uncured. As a result, the channel height ended up being 748 µm, instead of the intended 800 µm. Similarly, the cover of the lower spiral was observed to be 276 µm, indicating that a slight amount of extra cured material was present. This was because the lower spiral was printed before the upper spiral, and therefore received a higher dose of UV light energy directly or through diffusion. This resulted in the channel height being measured at 724 µm, rather than the 800 µm that was intended.

Chapter 6: Herringbone Mixer Results

6.1 Introduction

This chapter presents and discusses the results obtained in the development and evaluation of herringbone mixers fabricated using advanced 3D printing techniques. This work include both computational simulations and experimental validations, highlighting the effectiveness of these devices in enhancing mixing efficiency under laminar flow conditions. Using DLP 3D printing, the study explores the fabrication and performance of microfluidic devices with herringbone structures, looking into the capabilities and limitations of this innovative approach for microfluidics.

Efficient mixing in microfluidic systems is one of the most critical challenges in achieving functional and reliable LOC devices. Due to the inherent laminar flow in microfluidic channels, where fluid layers flow parallel with minimal interaction, mixing is typically governed by molecular diffusion. However, diffusion is a slow process that becomes increasingly insufficient at the microscale, limiting the utility of microfluidic systems in applications requiring rapid or homogeneous mixing. To address this limitation, herringbone mixers have been introduced as a design innovation. These mixers leverage staggered groove patterns along the walls or floor of microchannels to induce chaotic advection, creating secondary flows and vortices that disrupt the laminar profile and significantly enhance mixing.

Herringbone mixers are particularly advantageous in low Reynolds number flows, where inertial forces are negligible, and viscous forces dominate. By splitting, folding, and recombining fluid layers, these mixers introduce chaotic dynamics into an otherwise orderly laminar system. This allows for faster and more efficient mixing compared to reliance on molecular diffusion alone. Their utility extends to a variety of applications, including chemical synthesis, diagnostic assays, drug delivery, and biological reactions, where precise and rapid mixing is critical for functionality.

The fabrication of herringbone mixers using traditional methods, such as soft lithography, is labor-intensive and faces several limitations. These methods rely on photolithographic techniques to define the microstructures, followed by etching and bonding steps to assemble the device. While effective for simple planar designs, these approaches are poorly suited for fabricating complex three-dimensional structures, such as staggered herringbone grooves within closed microfluidic channels. Additionally, traditional methods struggle to create devices with large aspect ratios or increased channel heights, which are crucial for handling larger fluid volumes. This limitation makes soft lithography less suitable for applications requiring higher

throughput or larger-scale fluid manipulation. Furthermore, soft lithography requires cleanroom facilities and specialized equipment, increasing costs and reducing accessibility. The limited design flexibility of traditional fabrication methods further restricts innovation in microfluidic device fabrication, particularly when complex geometries and higher fluid capacities are required.

Recent advancements in additive manufacturing, particularly DLP-SLA 3D printing, have addressed many of these limitations, offering a transformative approach to microfluidic device fabrication. DLP-SLA uses UV light to cure liquid resin into solid structures with high precision, enabling the direct creation of complex geometries layer by layer. This technique not only reduces fabrication time and costs but also allows for the integration of intricate internal features, such as herringbone grooves, within closed channels. Furthermore, the development of biocompatible and transparent resins has expanded the applicability of DLP-SLA printed microfluidic devices in biomedical fields, enabling real-time observation of fluid behavior through microscopes.

Herringbone mixers fabricated using DLP-SLA provide significant advantages over those created with traditional methods. The flexibility of 3D printing allows for rapid prototyping and customization of groove geometry, size, and placement, enabling the optimization of mixing performance for specific fluid viscosities and flow rates. Additionally, the ability to integrate mixing structures directly into enclosed channels in a single printing step ensures high fidelity and reduces the risk of misalignment or defects during assembly.

In this work, DLP-SLA was utilized to fabricate microfluidic devices with integrated herringbone structures designed to enhance mixing efficiency. Fabricated devices were characterized for their ability to create secondary flows and chaotic advection. Both computational and experimental approaches were employed to evaluate the performance of these devices. Simulations were necessary to work into the mixing dynamics, vortex formation, and efficiency at different flow rates and viscosities.

This chapter is organized as follows: First, the design and fabrication of the herringbone mixers are described, detailing the geometry and DLP-SLA printing process. Next, the results of computational simulations are presented, showcasing the flow patterns, vortex dynamics, and predicted mixing efficiencies. Finally, the experimental results are presented, comparing observed mixing efficiencies with the simulations.

6.2 Design

The herringbone mixer design developed in this study focuses on enhancing mixing under laminar flow conditions by leveraging chaotic advection. The design incorporates staggered grooves, each 0.3 mm wide and angled at 95°, arranged in two series of 12 herringbones patterned along the superior surface of the microchannel. These features are designed to induce secondary flows, disrupting the laminar flow profile and significantly improving fluid interaction. The channel configuration includes two inlets that converge just before the herringbone-patterned region, facilitating fluid mixing before their exit through the channel's outlet, as illustrated in Figure X of the Methods section.

The design process was carried out using Autodesk Inventor, a Computer-Aided Design (CAD) software, which allowed precise specification of the key parameters used in this work, such as the inclination angle of 95°, the number and dimensions of the grooves, and their alignment. The alignment of the herringbones ensures interaction between fluid streams and the structured surfaces, with the tips positioned one-third (0.47 mm) from one wall and two-thirds (0.93 mm) from the opposite wall. After the first 12 herringbone grooves, the alignment is reversed to maintain flow disruption and mixing consistency.

The last three herringbone structures are integrated into a curved segment of the channel, followed by a long straight section. This design choice was made to address the limitations of our 3D printer, which has a maximum printable area of 75 mm x 50 mm. Without incorporating the curved segment, the total length of the herringbone structure would exceed these dimensions, making it impossible to fabricate using our 3D printing setup. By leveraging the design flexibility provided by 3D printing, the herringbone structure was adapted to include a curve, ensuring it remains within the printable dimensions while maintaining its mixing efficiency. Additionally, the straight section after the herringbone provides a region for observing and analyzing the resultant mixed fluid, enabling effective downstream analysis. After the mixing region, the channel height transitions from 1.2 mm to 0.5 mm at the outlet segment, compressing the fluid and facilitating downstream analysis.

The staggered grooves of the herringbone structures are particularly advantageous in low Reynolds number conditions, where laminar flow dominates, and molecular diffusion alone is insufficient for effective mixing. By splitting, folding, and recombining fluid layers, these grooves create chaotic advection, allowing faster mixing than diffusion-based approaches. Their ability to induce secondary flows and vortices makes them versatile for a variety of applications, including diagnostic assays and chemical synthesis.

Fabrication of the herringbone mixers employed DLP-SLA 3D printing techniques, which offer significant advantages for creating complex geometries. DLP-SLA printing allowed the direct integration of intricate herringbone patterns into enclosed microchannels in a single printing step. This approach reduced fabrication time and assembly complexity while ensuring geometric fidelity. The use of biocompatible and transparent resins enabled real-time observation of fluid behavior under a microscope, facilitating the evaluation of mixing performance. Additionally, the printing method minimized potential defects such as misalignment or bonding failures commonly associated with traditional fabrication methods.

The dimensions and parameters used in this design were specifically tailored to the requirements of the study. The combination of staggered grooves, carefully selected dimensions, and a robust fabrication process demonstrates the effectiveness of the herringbone mixer in achieving efficient fluid mixing under laminar flow conditions. These features highlight the potential of this design for diverse applications while leaving room for future optimization and adaptation to other microfluidic challenges.

6.3 Fabrication

6.3.1 Mold-Based PDMS Devices

The fabrication process for herringbone microfluidic devices using PDMS molds involved several steps to ensure precision and reproducibility. Molds were produced with DLP-SLA 3D printing using the resin Detax Freeprint Ortho 385. This process enabled the creation of detailed molds with extruded structures corresponding to the channel geometry with the herringbone features engraved.

Once printed, the molds were post-cured under UV light to enhance mechanical strength and eliminate residual monomers, making them suitable for repeated use. The PDMS replication process began by mixing a 10:1 ratio of base polymer to curing agent, ensuring the right balance of flexibility and durability. The mixture was degassed in a vacuum chamber to eliminate air bubbles, poured over the mold, and cured at 85°C for 12 hours. After curing, the PDMS was carefully peeled off the mold to preserve the structural integrity of the replicated features.

Inlet and outlet holes, 1 mm in diameter, were punched into the PDMS layer to allow fluid entry and exit. To create closed microfluidic systems, the PDMS replicas were bonded to glass substrates using oxygen plasma treatment. Both surfaces were exposed to plasma for 30 seconds, generating reactive groups that formed a strong, permanent bond upon contact. The

bonded devices were inspected for leakage using dye-based flow tests to ensure functionality during experiments.

This method provides microfluidic devices with optical transparency, ideal for real-time observation of fluid dynamics. Additionally, the reusable molds allowed for the efficient production of multiple devices, making this approach cost-effective and scalable. However, the fabrication process involved multiple steps, which, although robust, required careful execution to ensure consistent results.

6.3.2 Directly Printed Closed-Channel Devices

Fully enclosed herringbone devices were fabricated directly using DLP-SLA 3D printing with Detax Freeprint Ortho 385 resin. This approach bypassed the need for additional sealing or assembly steps, streamlining the manufacturing process. The printed devices included integrated inlets and outlets, avoiding alignment and the risk of leaks.

The printing process required precise optimization of parameters to ensure dimensional accuracy and structural integrity. Challenges such as over-curing and removing uncured resin were addressed by carefully adjusting exposure times and resin handling procedures. Post-printing, the devices underwent thorough cleaning to remove any residual resin and UV post-curing to enhance their mechanical properties.

The inclusion of a curved segment in the herringbone structure allowed the device to fit within the maximum printable area of the 3D printer (75 mm x 50 mm), without compromising its functionality. This curved segment was followed by a long straight section, providing a region for observing and analyzing the resultant mixed fluid in downstream applications.

While this fabrication method eliminated many of the assembly challenges associated with traditional approaches, it was not without limitations. Smaller channel dimensions proved difficult to achieve due to over-curing, restricting the range of applications. Nonetheless, the directly printed devices demonstrated excellent reproducibility and robustness, offering a rapid and efficient solution for producing enclosed microfluidic systems.

6.4 Computational Simulations

Figure 3 shows the concentration profiles distribution of a water-based fluorophore (mol/m³) in two separate experiments conducted in the microfluidic channel. The first experiment involves the mixing of water with the water-based fluorophore solution (Figure 3A and 3B), while the second experiment examines the mixing of dextran with the water-based fluorophore solution (Figure 3C). These simulations represent the progression of fluorophore concentration as the fluids pass through the herringbone structures within the channel. The sections shown in Figure 3A are taken at intervals corresponding to every two herringbones along the channel. Figures 3B and 3C present magnified views of the same sections depicted in Figure 3A for the water-water and dextran-water experiments, respectively. The images in Figures 3B and 3C are arranged in order from left to right and then top to bottom, corresponding to their positions along the channel. The herringbone design successfully generates vortices throughout the channel, which are visible in the slices taken at regular intervals along the length of the device.

These vortex formations are the result from the interaction between the fluids and the internal herringbone structures, which are designed to create secondary flows within the microchannel. In both simulations, the vortices are well-developed and consistently present along the length of the channel. This indicates that the herringbone geometry effectively disrupts the otherwise stable laminar flow, generating controlled chaotic mixing regions. These vortices enhance the interaction between fluid layers, significantly improving the homogenization of the fluorophore concentration across the channel.

The orientation of Figure 60 has been intentionally rotated for visualization purposes. While in the actual microfluidic device the herringbone structures are located on the upper surface of the channel, the device is shown in Figure 60 with the herringbones appearing on the bottom. This rotation was applied to enhance the clarity of the sections depicted in Figure 60A, making it easier to illustrate the progression of the concentration profiles as the fluids flow through the channel. This adjustment does not alter the interpretation of the results but facilitates a more straightforward analysis of the mixing efficiency across the cross-sectional planes.

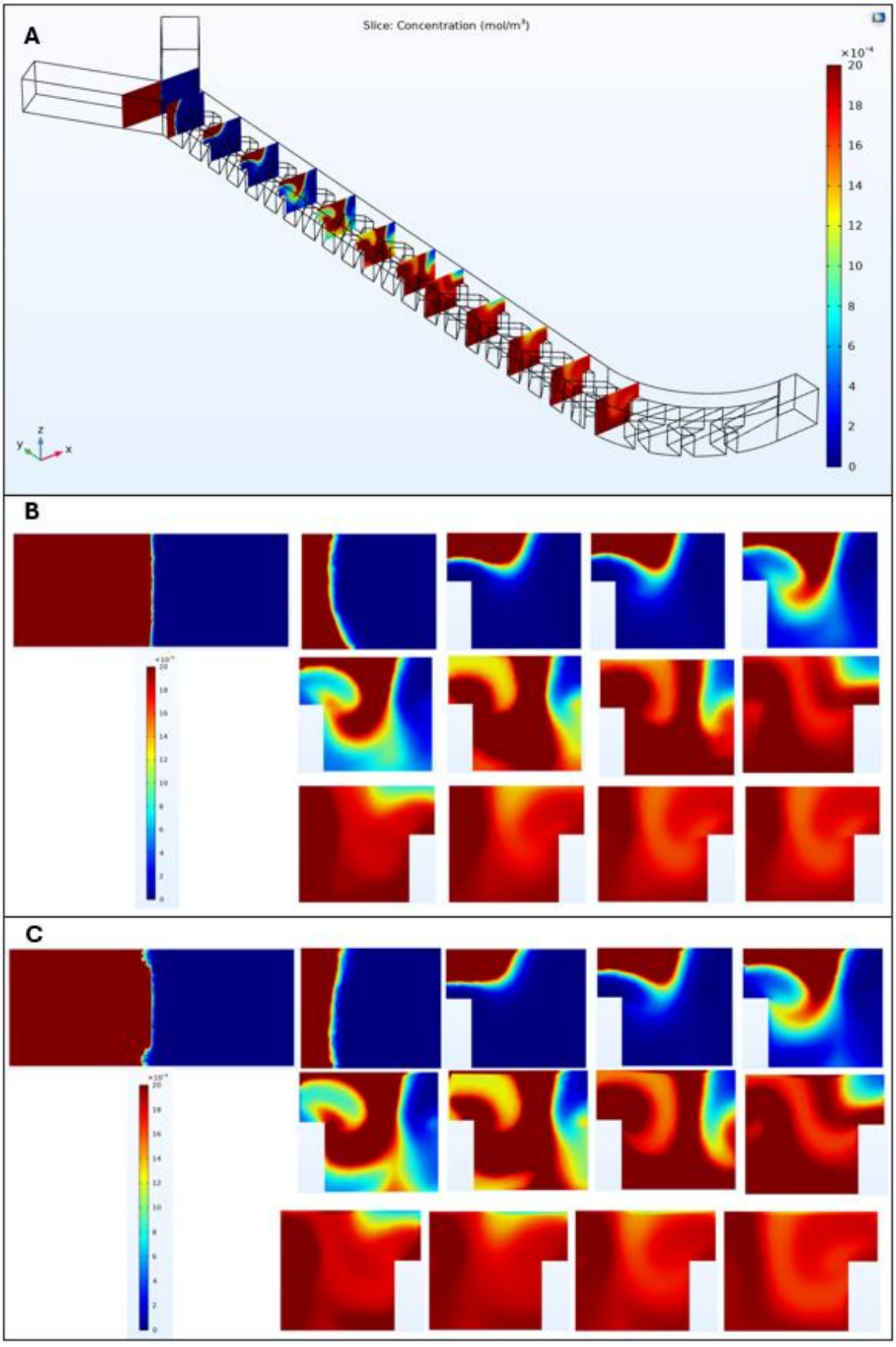


Figure 60: (A) Concentration distribution of water-based fluorophore (mol/m^3) with water in the microfluidic channel, showing the mixing of fluids as they pass through the herringbone structures. The color scale represents the concentration of the fluorescent dye, where red indicates higher concentrations and blue

indicates lower concentrations. The sections in (A) are taken at intervals corresponding to every two herringbones. (B) Cross-sectional views of the concentration profiles for the water and water-based fluorophore solution, magnified from the sections shown in (A) and ordered from left to right, then top to bottom. (C) Cross-sectional views for the dextran and water-based fluorophore solution, also with the same sequence as (A). It is remarkable to note that Figure 60B and 60C represent two fluids with different viscosities, yet the overall vortex patterns remain similar without significative differences.

In the simulation, fluorophore concentration was monitored along 10 regions placed across the channel's width at three different heights: one near the herringbone structures, one at the bottom of the channel, and one at mid-height. To simplify the analysis and enhance clarity, the data from every two regions were averaged, yielding five distinct regions.

Figure 61 provides a schematic representation of the region where the herringbone structures begin, just after the convergence of the two inlets. The diagram illustrates how concentration measurements were organized across the microchannel to evaluate the mixing efficiency. The channel is divided into five distinct regions along its width, each represented by a colored section. These regions extend through the entire depth of the channel, encompassing the full 3D volume of the microfluidic flow within each section.

The mixing efficiency graphs derived from these measurements represent the fluorophore concentration throughout the entire volume of each colored region. This approach ensures a comprehensive analysis of the mixing behavior across the channel, capturing both lateral and vertical concentration gradients.

In the subsequent experimental results, data will be presented and organized using the same schematic framework. This consistency enables a direct comparison between simulation and experimental outcomes, providing deeper insights into the mixing dynamics and performance of the herringbone structures.

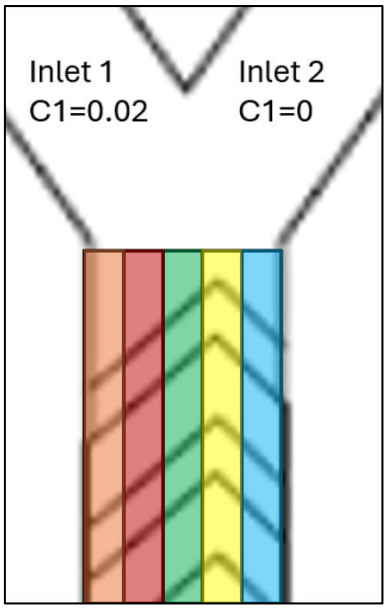


Figure 61: Schematic representation of the concentration measurement zones within the microchannel.

The device is divided into five distinct vertical regions (colored bands) spanning the full depth of the channel. Inlet 1 introduces a solution with a concentration of C1 = 0.02, while Inlet 2 introduces a solution with C1 = 0. The colored regions represent areas where fluorophore concentration profiles are analyzed to assess mixing efficiency. This organization enables a consistent framework for comparing simulation and experimental results.

The graphs in Figure 62 present the concentration profiles at two critical regions of the channel: the bottom (Figures 62A and 62C) and near the herringbone structures (Figures 62B and 62D), for both experiments of mixing water and dextran with the water-based fluorophore. These profiles highlight the different mixing behaviors of water-based fluorophore with water (Figures 62A and 62B) and water-based fluorophore with dextran (Figures 62C and 62D), providing valuable insights into the effects of fluid properties on the mixing process. These results complement the vortex patterns previously observed in the simulations and experimental images, allowing for a comprehensive evaluation of the microfluidic mixing performance.

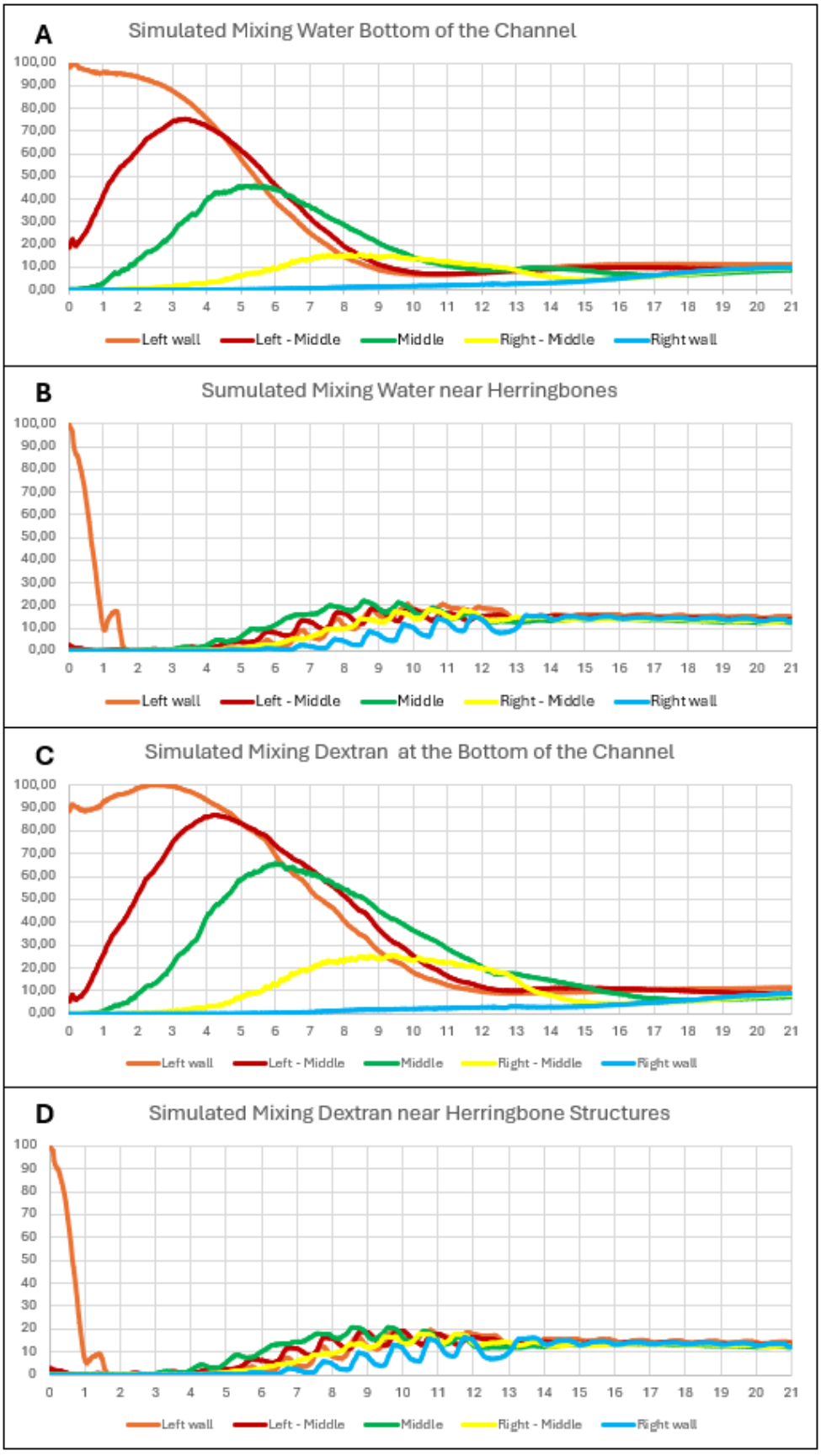


Figure 62: Simulated mixing profiles for water and dextran with a water-based fluorophore at two distinct locations within the microfluidic channel: near the herringbone structures and at the bottom of the channel . The top row shows the mixing efficiency for water with water-based fluorophore near the herringbones (A) and

at the bottom (B). The bottom row illustrates the mixing profiles for dextran with water-based fluorophore near the herringbones (C) and at the bottom (D). Faster mixing and stabilization, with smoother transitions can be observed when the interface is formed with two water streams. However, slower mixing, with more pronounced peaks it is shown for a water-dextran interface, due to its higher viscosity.

The herringbone design generates zones of turbulence and chaotic flow, particularly at the edges of the structures. These zones are where the angle and elevation of the grooves disrupt the otherwise laminar flow, causing the fluid to deviate from its typical layered path.

The chaotic flow increases the interaction surface between the two fluids, promoting mechanical agitation that helps break down the laminar layers commonly seen in microfluidic channels. This agitation results in a more homogenous mixture, as the secondary flows generated by the herringbone grooves facilitate rapid mixing across the entire channel. The 1:10 ratio was arbitrary chosen to observe how the mixing behaves when one fluid has a flow rate an order of magnitude higher than the other.

6.5 Experimental Analysis

6.5.1 Experimental Setup

The experimental approach, detailed in the Methods section, is designed to evaluate the performance of the fabricated herringbone mixers under realistic conditions. A dual-inlet configuration was used, where a transparent fluid was introduced through one inlet and a fluorescent fluid through the second inlet at a flow rate ratio of 10:1, specifically, the flow rate was 65 µL/min for the water-based fluorophore and 650 µL/min for the water or the dextran solution. This setup allows for the visualization of mixing dynamics within the herringbone-patterned region by leveraging the fluorescent fluid to capture concentration gradients and vortex formation. High-resolution confocal microscopy was employed to image the mixing process, providing the data required for both qualitative and quantitative analysis. These experiments are essential for validating the effectiveness of the herringbone design and understanding its capability to disrupt laminar flow and enhance mixing through chaotic advection.

The evaluation process will also incorporate computational simulations performed using COMSOL Multiphysics. These simulations will analyze fluid dynamics within the device and help elucidate how the herringbone geometry and flow parameters influence mixing performance. By comparing experimental data with simulation predictions, the study aims to validate the design and refine it further to optimize performance for various microfluidic applications. This

comprehensive approach enables an in-depth understanding of how herringbone mixers function and how 3D printing can be leveraged to produce efficient and scalable mixing devices.

This chapter begins the exploration of these results, focusing on the design rationale, fabrication process, and the experimental and computational analyses that will ultimately guide the optimization of herringbone mixers for advanced microfluidic applications.

To provide a comparison between the two mixing experiments, we calculated the Reynolds number for each experiment, as it is a critical parameter in characterizing fluid flow regimes within microfluidic channels. The Reynolds number helps differentiate between laminar and turbulent flow, directly impacting mixing efficiency and flow patterns. Given that the two experiments involve fluids with different viscosities, water and a water-based fluorophore solution in the first experiment, and dextran mixed with a water-based fluorophore solution in the second, it is important to calculate Re for each case separately.

For both experiments, the Reynolds number was calculated using Equation 4.

The table below presents the Reynolds number calculations for the two different fluid combinations used in our experiments: water mixed with a fluorophore solution, and dextran mixed with a fluorophore solution. The Reynolds number was calculated using the equation provided above, considering the density, dynamic viscosity, and the hydraulic diameter of the microfluidic channel for both fluid combinations. As shown in the table, the flow for water-based experiments results in a higher Reynolds number compared to the dextran-based experiments due to the lower viscosity of water. These values confirm that both experiments are conducted within the laminar flow regime, with a more significant reduction in Re when using dextran due to its higher viscosity. Additionally, the viscosity and density for the water + dextran mixture were calculated using the proportional values of each component, ensuring accuracy in representing the fluid properties of the mixture.

Table 33: Reynolds number (Re) comparison for two different fluid combinations: water + water (fluorophore solution) and dextran + water (fluorophore solution).

	Water + Water	Dextran + Water	
ρ	997	1054,27	kg /m3
v	9,93E-03	9,93E-03	m/s
D_h	1,09E-03	1,09E-03	m
μ	8,90E-04	3,72E-03	Pa*s
Re	12,14	3,07	

6.5.2 Experimental Results

Figure 63 illustrates the device, which is fabricated in one single 3D printing step and demonstrates the mixing of fluorescein and water, introduced using syringe pumps. The internal herringbone structures, clearly visible in the figure, are intended to create vorticity and promote efficient mixing as the fluid moves through the channel.

Figure 63A provides an overview of the device, showcasing the microchannel and connected syringe pumps used to introduce the fluids into the system. The connected tubing ensures a controlled flow rate for both solutions. Figure 63B zooms into the start of the channel, where the two inlets converge. At this stage, the two fluids remain distinct, creating a heterogeneous distribution within the channel. Instead, Figure 63C focuses on the end of the channel, where there is a homogeneous distribution of the fluorescent dye and water thanks to the mixing induced by the herringbone.

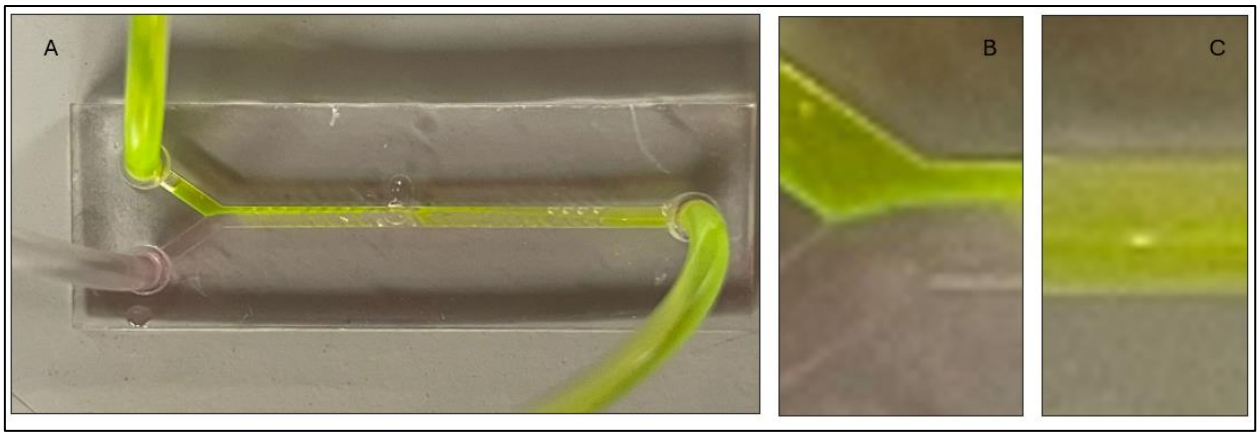


Figure 63: (A) shows a fully 3D-printed herringbone device used for fluid mixing. The device features a herringbone structure that facilitates the mixing of a fluorescent dye with water. The fluids are introduced into the microchannel using syringe pumps, as indicated by the connected tubing. (B) Start of the channel, where the two inlets get together, two different fluids can be easily differentiated in a heterogeneous distribution. (C) End of the channel, both fluids are mixed in a homogeneous result.

Using an inverted confocal microscope, two separate experiments were conducted to analyze the fluorescence distribution and vortex formations under identical experimental conditions. The first experiment examined the mixing behavior of a water-based fluorophore solution with water, while the second analyzed the same fluorophore solution mixed with dextran. The flow rate was maintained at 65 µL/min for the water-based fluorophore and at 650 µL/min for the water or the dextran solution. These experiments aimed to capture the real experimental vortex within the microchannel, as shown in Figure 64, providing detailed insights into the flow dynamics and enabling a direct comparison to the simulated results. The fluorescence signal highlights the fluid motion and mixing efficiency induced by the herringbone structures, offering a comprehensive understanding of the mixing process.

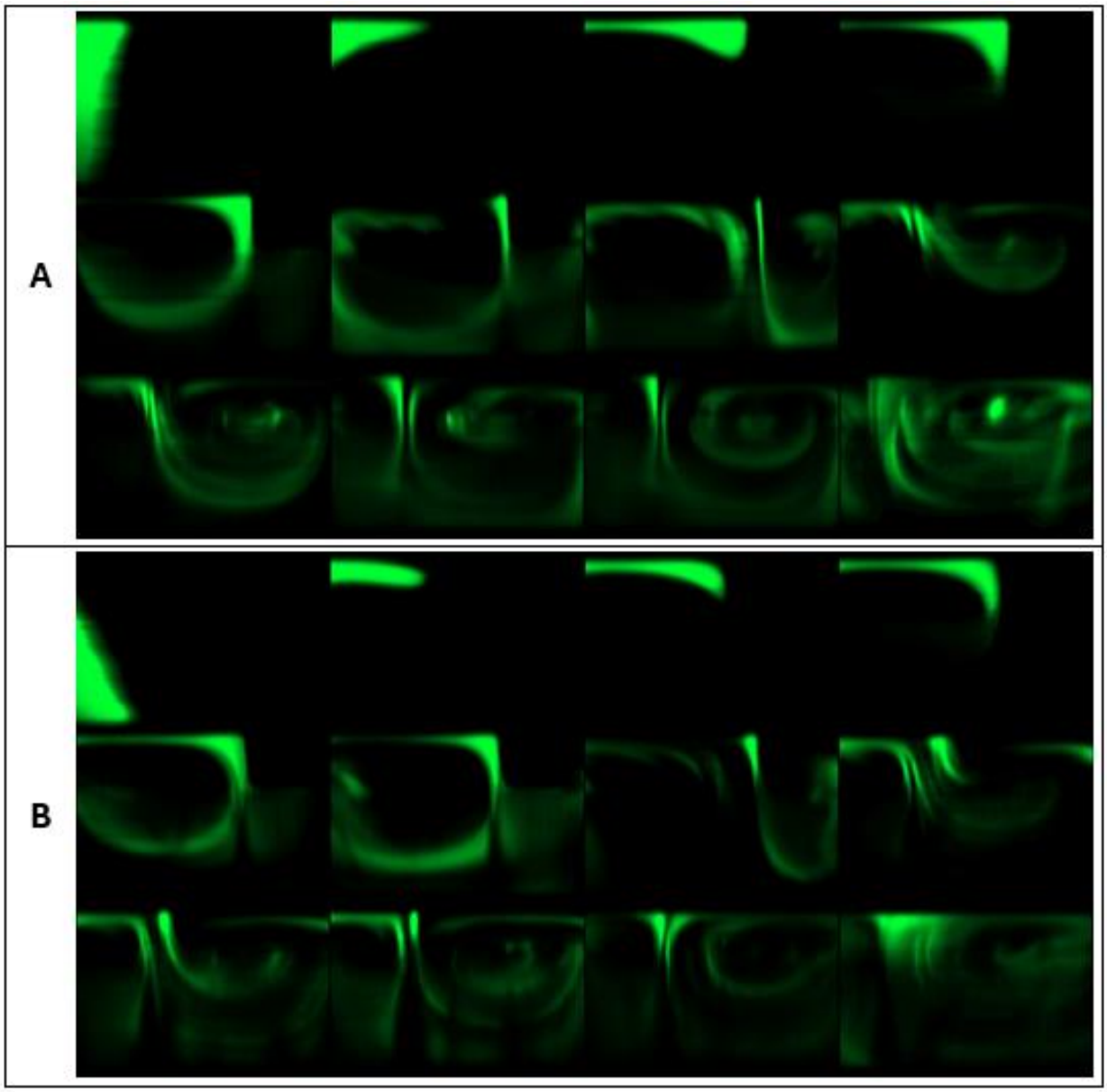


Figure 64: Experimental vortex formations observed using inverted confocal microscopy. (A) Vortices formed during the mixing of a water-based fluorophore solution with water. (B) Vortices formed during the mixing of the same fluorophore solution with dextran. The images show cross-sectional slices of the microfluidic channel, taken perpendicular to the flow direction. Each section corresponds to a location between two consecutive herringbone structures, and are taken every two herringbones, allowing visualization of the vortices across the entire channel depth. The green fluorescence highlights the areas of fluid motion and mixing, emphasizing the effectiveness of the herringbone geometry in disrupting laminar flow and enhancing mixing efficiency. The flow rate was maintained at 65 µL/min for the water-based fluorophore and at 650 µL/min for the water or the dextran solution. This setup enables a detailed study of the mixing behavior between the two fluids.

In these experiments, a water diluted fluorescent dye is initially introduced into the channel on one inlet, at a 1:10 flow rate ratio with respect to the other inlet, which is filled with either water (Figure 64A) or dextran solution (Figure 64B) depending on the experiment. The herringbone geometry disrupts the laminar flow and pushes the fluorescent liquid towards the lower part of the channel. This lateral movement of the fluid creates recirculation zones, pulling the fluorescent dye towards the outer regions of the channel.

As the fluid progresses along the channel, the induced vortices redistribute the fluorescent liquid, leading to effective mixing across the channel's cross-section. In the case of mixing water with the water-based fluorophore, Figure 64A, the distribution of dye shows a rapid and even spreading of the fluorescence, reflecting the mixing dynamics predicted by the simulations. Similarly in the mixing of dextran water with the water-based fluorophore, Figure 64B, despite the higher viscosity, the herringbone structure also successfully facilitates a redistribution of the fluorescent dye, resulting in significant mixing along the channel.

The experimental results closely align with the simulated vortex patterns, however a delay in the vortex formation is observed in the dextran experiments compared with the ones mixing water, showing an influence of viscosity.

Experimentally, at the bottom of the channel, the mixing profiles for both experiments of mixing water and dextran with the water-based fluorophore, display peaks that progressively shift between consecutive columns. These peaks correspond to the lateral displacement of the fluorescent dye, driven by the vortices induced in the herringbone region. As the fluid progresses along the channel, the intensity of these peaks diminishes, reflecting the more uniform distribution of the dye across the channel width, ultimately resulting in enhanced mixing. This pattern is comparable with Figure 62, consistent with the vortex dynamics observed in the lower section of the channel, where the fluorescent fluid is laterally transported, producing pronounced intensity peaks. Notably, in the case of mixing dextran, the peaks exhibit higher concentrations of fluorophore, indicating that the higher viscosity of dextran makes difficult the diffusion process. However, the herringbone structures continue to generate sufficient secondary flows, enabling the fluid mixing even though the slower diffusion rate associated with the more viscous fluid.

The experimental results for fluorescein concentration profiles in the mixing of water and dextran with the water-based fluorophore are shown in Figure 65. These profiles were captured using an inverted confocal microscope and illustrate the distribution of the fluorescent dye across five regions spanning the entire depth of the microchannel, from the left wall to the right wall. The plots provide insights into the mixing efficiency by representing the distribution of the dye, highlighting the impact of the herringbone structures on fluid dynamics and mixing progression.



Figure 65: (A) Experimental results of fluorescein mixing water with the water-based fluorophore within a herringbone microchannel, normalized, showing concentration changes across five columns: Left Wall, Left - Middle, Middle, Right - Middle, and Right Wall. (B) Experimental results of fluorescein mixing dextran with the water-based fluorophore within the same microchannel, also normalized and representing the same five columns. The results were obtained using an inverted confocal microscopy.

In both the water and dextran experiments, we observe initial strong peaks in the concentration profiles. These peaks are directly aligned with the pronounced peaks observed in the simulated data near the bottom of the channel. Such behavior is expected, the high shear regions near the bottom, combined with the action of the herringbone structures, generate vortices that push the fluid laterally, leading to a pronounced concentration of dye in localized regions. As the fluids advance, the intensity of these peaks diminishes, representing the redistribution of the fluorescence and the gradual homogenization of the flow.

As the dominance of the lower layers in the fluorescence signal decreases, fluctuations near the herringbone structures become more noticeable. These fluctuations result from the disruption of laminar flow caused by the herringbones, which are designed to generate chaotic advection and secondary flow patterns. This process enhances the redistribution of the fluorescent liquid throughout the entire channel depth. As the fluid progresses through the device, the pronounced peaks in the bottom region gradually give way to more evenly distributed fluctuations, signaling the effective homogenization of the fluorescence across the channel. Both experimental and simulated results confirm that efficient mixing is achieved as the fluorescence signal from the bottom layer diminishes, while recirculating vortices generated by the herringbones redistribute the fluorescent dye throughout the channel.

Figure 66A shows the mixing efficiency as defined in the methods section, for the water mixing with the water-based fluorophore, while Figure 66B presents the results for the mixing of dextran, comparing both simulation and experimental data. As observed, the simulated mixing efficiency for the water mixture reaches 85%, while the experimental data settles at 65%. Similarly, dextran's mixture mixing efficiency is slightly lower, with 82% in the simulation and 47% in the experiment.

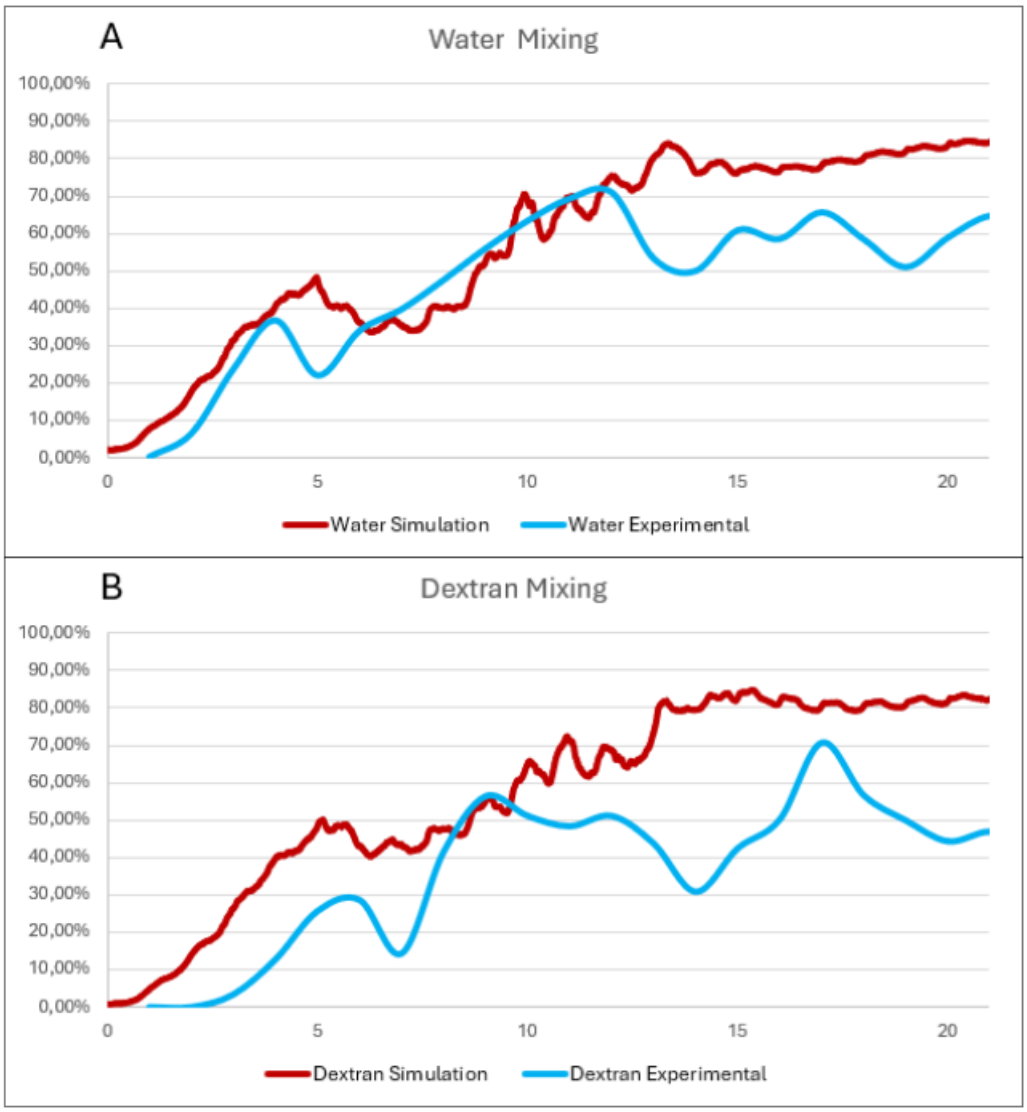


Figure 66: (A) illustrates the comparison between the simulated and experimental mixing of water with a water-based fluorophore in a herringbone microchannel. The simulation (red line) shows a rapid increase in mixing efficiency, stabilizing at 85%, whereas the experimental data (blue line) peaks at 65%, indicating slower homogenization and higher variability. (B) compares the simulated and experimental mixing of dextran with a water-based fluorophore. The simulation (red line) achieves 82% mixing efficiency, while the experimental data (blue line) shows a lower mixing efficiency of 47%, highlighting greater difficulty in achieving homogeneity due to dextran's higher viscosity.

Chapter 7: General Discussion

7.1 Evaluation of Printing Parameters and Resolution

The results presented in Chapter 4 demonstrate significant advancements in the fabrication of microfluidic devices using our custom-made DLP-SLA 3D printer, addressing critical challenges such as over curing, dimensional accuracy, and the integration of internal features within closed channels. These findings highlight not only the potential of DLP-SLA based techniques to overcome limitations associated with traditional fabrication methods but also their transformative impact on the design and application of microfluidic devices.

The absorbance study revealed that the resins Detax and Keyprint exhibit similar absorbance levels, while Asiga shows an absorbance 2.5 times higher. Based on these observations, printing parameters were iteratively optimized to reduce variability. Initial experiments fixed the PWM to 35, with exposure times set according to resin and layer thickness. For instance, Detax required 1.25 s for 50 µm layers and 2.5 s for 100 µm layers, while Asiga demanded significantly higher exposure times, such as 15 s for 50 µm layers and 20 s for 100 µm layers, 2.75 s were needed for Keyprint with 50 µm layers, and 4 s for Keyprint with 100 µm layers. After multiple iterations with different structures, the finalized optimal printing parameters were determined for each resin. For Detax, the optimal exposure times were 1.25 seconds for normal layers and 4 seconds for the burn-in layer with a layer thickness of 50 µm, and 2 seconds for normal layers and 6 seconds for the burn-in layer with a layer thickness of 100 µm. For Asiga, the exposure times were 12.5 seconds for normal layers and 30 seconds for the burn-in layer with 50 µm layers, and 20 seconds for normal layers and 40 seconds for the burn-in layer with 100 µm layers. For Keyprint, the optimal exposure times were 2.5 seconds for normal layers and 5 seconds for the burn-in layer with 50 µm layers, and 4 seconds for normal layers and 7 seconds for the burn-in layer with 100 µm layers. Across all experiments, the light power was consistently set at a PWM of 35. These optimized parameters provided a strong foundation for subsequent experiments with more complex geometries and ensured consistent print quality across all tested resins.

Dimensional accuracy results revealed average z-dimension errors as follows: for Detax, errors were 7.14% for 600 µm height, 9.35% for 400 µm height, and 22.32% for 200 µm height; for Asiga, errors were 16.73%, 17.39%, and 27.25%, respectively; and for Keyprint, errors were 34.43%, 46.38%, and 50.2% for the same heights. These results indicate that Detax consistently outperformed the other resins in z-dimension accuracy across various

layer thicknesses and heights. In terms of xy-plane accuracy, Detax exhibited average errors of approximately 1.5% across all tested features, while Asiga showed higher variability, with errors ranging from 2% to 5%, likely due to its higher absorbance affecting lateral precision. Keyprint demonstrated the largest xy-plane errors, averaging 6%.

For rectangular channels, Detax was able to maintain unobstructed channels with cover thicknesses up to 200 µm, but increasing the thickness to 400 µm or more led to partial obstructions due to over curing. Asiga demonstrated exceptional performance, with all channels remaining fully open and functional across all tested cover thicknesses, benefiting from its higher absorbance, which effectively minimizes light penetration into undesired areas. Conversely, Keyprint exhibited significant limitations, with channels remaining open only up to 200 µm cover thickness, while thicker covers resulted in complete obstruction. For stepped roof designs, the increased channel height of 400 µm improved results across all resins, particularly for Detax, which achieved fully open channels even at 800 µm cover thickness. Asiga maintained its excellent performance across all thicknesses, while Keyprint showed some improvement compared to the rectangular design, with channels remaining open up to 200 µm but partially obstructed at higher cover thicknesses. These findings underscore the critical relationship between resin absorbance, channel geometry, and cover thickness in the successful fabrication of closed microchannels. Resin absorbance plays a pivotal role in controlling the polymerization process, as higher absorbance reduces over-curing by limiting light penetration to adjacent layers.

Sidewall roughness measurements provided additional insight into resin performance. Asiga achieved superior results for closed channel fabrication due to its higher absorbance, allowing for better definition and reduced over-curing. However, sidewall roughness values showed significant variability among the resins. Asiga exhibited an average sidewall roughness of 27.64 µm, which, while functional for closed channels, limits its suitability for applications requiring precise lateral smoothness. In contrast, both Detax and Keyprint demonstrated much smoother sidewalls, with roughness under 3 µm, attributed to their lower absorbance properties. This smoothness is critical for applications involving fluid flow and cells or particle handling inside the microfluidic channels, where lateral roughness can disrupt laminar flow and reduce device performance.

The roughness observed in DLP-SLA printed microfluidic devices highlights the complex interplay between resin properties, layer thickness, and polymerization dynamics. Thinner

layers result in increased cumulative irradiance, amplifying over-curing effects, particularly in resins like Detax, which exhibit high polymerization efficiency. This leads to increased roughness on internal surfaces, driven by the diamond orientation of micromirrors in the DMD system and cumulative polymerization. Conversely, in resins like Asiga, higher absorbance and lower nominal error mitigate over-curing, resulting in smoother surfaces but higher lateral roughness more directly influenced by the Gaussian irradiance profile. These findings underscore the critical role of resin properties in balancing surface quality and dimensional accuracy during microfluidic device fabrication.

Given these results, Detax was ultimately selected for the majority of subsequent experiments. While Asiga performed better for closed channels in isolation, the priority of minimizing sidewall roughness for improved flow dynamics led to the choice of Detax. Its balanced performance in dimensional accuracy and roughness provided the necessary reliability and precision for advancing the fabrication of complex microfluidic devices.

Detax, with its relatively smoother surface profiles, enabled the successful fabrication of closed channels with embedded internal features, including squares, triangles, and circles, with dimensional errors maintained below 5%. The results from the dimensional characterization of the printed devices confirm the reliability of DLP-SLA 3D printing for microfluidic applications. The accuracy of the larger features, such as the 200 µm and 300 µm circles, was remarkable, with deviations below 1%, highlighting the precision of this technique. Although smaller features like the 100 µm squares exhibited slightly higher deviations, this level of precision was still effective for structure formation. These results demonstrate that 3D printing is a viable and precise method for creating functional microfluidic devices, even with complex geometries like herringbone grooves.

These achievements validate DLP-SLA 3D printing's capability to produce intricate microstructures within closed geometries.

The study also demonstrated the ability to fabricate inclined channels and microfluidic connectors, marking a notable innovation in the design of 3D printed microfluidic devices.

DLP-SLA printing offers unique advantages over traditional methods like soft lithography and injection molding. Soft lithography, while effective for planar designs, struggles with closed channels and embedded features due to its multi-step processes. Injection molding is precise but lacks the flexibility and cost-efficiency needed for prototyping. DLP-SLA printing overcomes these limitations with a single-step, versatile process that enables the creation of complex internal features efficiently.

In conclusion, this work establishes a robust foundation for the use of DLP-SLA 3D printing in microfluidic device fabrication. By addressing critical challenges and demonstrating the feasibility of fabricating closed channels, inclined geometries, and embedded internal structures, this study underscores the transformative potential of DLP-SLA printing as a versatile and precise fabrication method.

7.2 Study of Spiral Device for size-based Particle Separation

The comparison between simulation and experimental results has provided valuable insights into the performance of the spiral microfluidic devices fabricated using both mold-based PDMS and directly assembled embossed-channel methods. Among these, the mold-based PDMS devices have proven to be more reliable for experiments involving particle separation. This method ensures greater dimensional precision, resulting in devices with structurally robust channels and fewer experimental failures. In contrast, the embossed-channel method, while faster and easier to fabricate, has shown limitations, including higher misalignment rates during assembly and increased leakage, making it less suitable for high-precision experiments. Furthermore, the mold-based PDMS method allowed for tighter control over spiral dimensions, which is critical for achieving accurate separation results.

The spiral devices were designed based on simulations performed in COMSOL Multiphysics®, which predicted particle separation behavior under varying channel heights and flow conditions. Particles of 100 µm, 75 µm, 50 µm, 30 µm, 20 µm and 6 µm were used in simulations, and particles of 100 µm, 75 µm, 50 µm, 30 µm were tested in experiments. The devices tested experimentally included channels with heights of 540 µm, 640 µm, and 740 µm, using a particle-laden flow of 760 µL/min introduced through one inlet and a sheath flow of 6840 µL/min through the opposite inlet. The 540 µm channel demonstrated effective separation of 75 µm and 100 µm particles through the inner outlet, with over 87% of these particles exiting as predicted by the simulations. For the 640 µm channel, the optimal configuration required reversing the inlet for the particle-laden flow compared to the 540 µm setup. This adjustment ensured better separation of larger particles, with the experimental results showing a clear threshold above 75 µm for particles exiting through the inner outlet. Interestingly, while simulations for the 640 µm channel predicted 40% of 75 µm particles exiting through the inner outlet, experiments showed only 14% doing so. This deviation is advantageous, as it ensures a cleaner separation of particles above 75 µm, allowing the inner outlet to exclusively collect larger particles.

These devices have the added benefit of being fabricated in a single printing step, achieving channel designs with nominal heights of 600 µm, 700 µm, and 800 µm. Post-curing and dimensional adjustments result in actual channel heights of 540 µm, 640 µm, and 740 µm, respectively, maintaining excellent consistency with the designed parameters. This single-step manufacturing process significantly reduces production complexity, making it highly efficient for practical applications. However, in the case of the double-spiral design, the minimum channel height achieved is currently 800 µm, resulting in a final dimension of 740 µm. Further optimization of the design and printing process is needed to fabricate inclined channels with smaller dimensions, enabling their use in more precise separation applications.

The results demonstrate that these 3D-printed spiral devices are particularly suited for an initial separation step, effectively isolating larger particles from smaller ones with a separation threshold typically around 75 µm. Devices with a channel height of 540 µm group particles of 75 µm and larger through the inner outlet, while the 640 µm device offers a bigger particle separation, isolating only particles larger than 75 µm. This capability makes these devices ideal for applications requiring an initial size-based sorting step. Once the larger particles are separated, subsequent processing can involve devices with smaller channels, typically fabricated through photolithography. These smaller devices, with smaller channel dimensions, are more suitable for fine separations of smaller particles, as demonstrated by Kuntaegowdanahalli et al. (2009) and Özbey et al. (2018) (138,139).

The ability to fabricate 3D-printed microfluidic devices that achieve reliable particle separation marks a significant advancement in the field. By optimizing the flow conditions and channel geometry, these devices provide a practical and efficient solution for applications requiring size-based particle separation. The combination of a robust initial separation using 3D-printed devices, followed by finer separations using lithography-based devices, establishes a comprehensive and scalable approach to particle sorting.

7.3 Study of Herringbone Device for Fluid Mixing under Laminar Flow

The study presented in Chapter 6 successfully demonstrates the potential of 3D printing technology, specifically DLP-SLA, in fabricating microfluidic devices with complex internal geometries like herringbone structures to enhance fluid mixing. As discussed in the introduction, traditional fabrication techniques such as soft lithography are limited in creating intricate, three-dimensional internal structures that are essential for chaotic

advection and improved mixing. DLP-SLA 3D printing overcomes these limitations, enabling rapid prototyping and the creation of precise, reproducible geometries.

Through 3D printing, we have successfully fabricated microfluidic devices with a channel height of 1200 µm, and herringbone structures sized at 700 µm. This represents a significant increase compared to typical dimensions reported in the literature (124,125,144), where herringbone heights usually range between 75 µm and 200 µm. The ability to produce devices with such large structures allows handling greater fluid volumes, an advantage that was previously limited by traditional fabrication techniques such as photolithography. 3D printing has enabled us to surpass these conventional manufacturing constraints, offering increased flexibility in device design and allowing for the creation of larger microfluidic systems. This development is key to extending the use of microfluidics, especially for applications that need to handle larger volumes.

The simulations and experiments realized present a clear representation of the influence of the 3D printed herringbone microchannel, the results visually demonstrate the distinct flow patterns and mixing behavior within the channel. The successful mixing of fluorescein confirms the practical effectiveness of the herringbone design in promoting fluid mixing. The chaotic advection generated by the grooves disrupts the otherwise laminar flow, leading to enhanced mixing between the two inlet streams.

The integration of herringbone structures into the microfluidic channels played a crucial role in generating the necessary secondary flows to improve mixing in both water and dextran while mixing with a water-based fluorophore solution. In low Reynolds number environments, such as the ones used in this study, laminar flow conditions typically dominate, meaning fluids flow in parallel layers with minimal natural mixing. The herringbone grooves disrupt this flow, generating transverse movements and vortex formation that promote chaotic advection, thereby enhancing mixing. Both the simulated and experimental results show vortex patterns like those reported in the literature, despite the use of bigger channels in this study. This similarity confirms that even at augmented scales, the herringbone design maintains its effectiveness in generating the chaotic flows required for efficient mixing.

In the simulations, both mixings of water-based fluorophore solution with water and dextran demonstrated the expected formation of vortices near the herringbone structures, which is critical for inducing chaotic mixing. The simulated mixing efficiency for water with water-based fluorophore solution reached 85%, stabilizing more quickly than the mixing of

dextran with the water-based fluorophore solution, which had a final simulated efficiency of 82%. The rapid initial drop in concentration for the water experiment, particularly near the bottom of the channel, indicated faster and more efficient mixing due to its lower viscosity. The mixing patterns for the water mixing experiment showed smoother, less pronounced peaks as the fluid became homogeneously distributed throughout the channel. In the experimental setup, the water-based experiment had a Reynolds number of 12.14, similar to the device used by Yang et al., which reported a mixing index of 15%. Their device featured two sets of six herringbone structures over a total length of 1.7 mm. In contrast, our device, with a total length of over 20 mm and a more extensive herringbone pattern, allowed for greater fluid interaction and enhanced mixing. The increased channel length in our setup likely contributed to the higher mixing results.

The experiment mixing dextran, on the other hand, exhibited a slower initial drop in concentration due to its higher viscosity, which resisted the secondary flows generated by the herringbones. Despite this, the simulated efficiency still reached 82%, illustrating that the herringbone structures significantly enhanced mixing for this more viscous fluid. The simulations also showed more pronounced peaks in the concentration profiles, particularly in the middle sections of the channel, reflecting the slower homogenization process.

When comparing the experimental results with the simulations, the water-water experiments consistently demonstrated faster and more efficient mixing in both cases. However, experimental water mixing reached 65%, lower than the simulated result. These discrepancies highlight the inherent challenges of translating idealized simulations into practical applications, but also affirm the overall effectiveness of the design. The experimental water mixing profiles revealed more fluctuations compared to the simulations, likely due to flow irregularities, but still achieved homogeneity toward the end of the channel.

For the mixing of dextran with the water-based fluorophore, the experimental mixing efficiency was significantly lower than the one from mixing water, at 47%, as expected due to its higher viscosity. However, the herringbone structures still played a crucial role in improving mixing compared to what would be expected in a laminar flow without such features. The experimental results also showed more pronounced fluctuations in the mixing profiles, particularly in the middle and later sections of the channel, reflecting the difficulty in achieving homogeneous mixing for high viscosity fluids. While the experimental dextran

results were lower than the simulations, they still demonstrate the efficacy of the device in promoting mixing in challenging conditions.

These results show a clear trend: the mixing of water with the water-based fluorophore solution stabilizes faster and achieves a higher level of mixing in both simulation and experimental settings. In contrast, the mixing of dextran with a water-based fluorophore solution, due to its higher viscosity, exhibits slower mixing and lower efficiency. This behavior is consistent with the vortex dynamics discussed earlier.

Overall, this study highlights the power of integrating herringbone structures into microfluidic devices using 3D printing to enhance mixing efficiency, even in challenging conditions like low Reynolds number flows and high viscosity fluids. The successful formation of vortices and the improved mixing profiles observed in both simulations and experiments underscore the effectiveness of this design approach. Moving forward, there is potential to optimize the geometry of the herringbone structures, adjusting groove angles and depths to further improve mixing, particularly for more viscous fluids like dextran.

By leveraging the precision and flexibility of DLP-SLA 3D printing, this study not only addresses key challenges in microfluidic mixing but also paves the way for further innovations in device design and fluid manipulation. The results obtained here have important implications for a range of applications, from biomedical diagnostics to chemical engineering, where efficient fluid mixing is essential for performance.

Chapter 8: Conclusions

1. The work presented in this thesis confirmed the utility of DLP-SLA 3D printing for microfluidic applications, demonstrating its reliability in fabricating both molds for PDMS replication and fully enclosed microchannels. Using commercially available resins, it was possible to achieve complex geometries with a high degree of precision, expanding the possibilities for microfluidic device fabrication.
2. The dimensional accuracy analysis shows that error decreases as feature size and separation increase, while smaller sizes and closer separations result in higher errors. Detax resin demonstrated the best performance, with XY errors below 1% for structures larger than 400 µm and approximately 5% for structures with dimensions of 200 µm.
3. An in-depth analysis of over curing effects confirmed the successful fabrication of closed channels and highlighted the critical role of resin absorbance. The study demonstrated that resins with higher absorbance significantly reduce over curing, leading to smaller dimensional errors in the channel cover.
4. The successful fabrication of internal structures within the microchannels, including circles, squares, and triangles, was achieved. A detailed analysis of dimensional accuracy revealed minimal errors, consistently below 5%, validating the precision of the fabrication process and demonstrating the potential for creating intricate geometries in microfluidic devices.
5. The analysis of surface and lateral roughness highlights the intricate interplay between resin properties, layer thickness, and cumulative energy exposure in DLP-SLA 3D printing. Detax resin emerged as the most balanced option for microfluidic device fabrication, offering superior lateral roughness and high precision in XY and Z dimensions. However, its efficiency in polymerizing layers contributed to increased roughness on the inner surface of channel covers due to over-curing effects. Conversely, Asiga resin's higher absorbance and lower nominal error reduced over-curing but resulted in more pronounced lateral roughness due to the Gaussian irradiance profile. These findings underscore the importance of selecting resins that align with specific fabrication requirements, balancing polymerization efficiency and surface quality to optimize microfluidic channel performance.

6. The integration of computational simulations into the design process significantly enhanced the development of microfluidic devices. Simulations provided critical guidance, reducing experimental trial-and-error while aligning closely with real-world performance.

7. The spiral microfluidic devices developed in this work successfully achieved particle separation, particularly for particles above 75 µm. Experimental results closely aligned with computational simulations, demonstrating the device ability to operate under low Reynolds number conditions.
8. Leukocytes were successfully captured using 70 µm beads conjugated with CD45 antibodies, enabling their size-based separation from CTCs. This approach demonstrates the potential of combining antibody binding and size-based microfluidic separation for efficient leukocyte depletion and CTC isolation.
9. The generation of vortex by the herringbone structures was successfully analyzed and compared through both simulations and experimental validations. The results demonstrated how these vortices effectively disrupt the laminar flow, redistributing the fluid and enabling mixing.
10. Efficient mixing of two fluids was achieved under laminar flow conditions, even for systems with different viscosities, such as dextran-water solutions. This highlights the versatility and robustness of the herringbone mixers for challenging fluid systems.

Statement of Originality

The author of this thesis, Francesc Subirada Blanco, considers it to be original and that it complies with the ethical codes and good practices without containing plagiarism.

Then, I declare the following elements of this thesis to be considered a contribution to knowledge:

- Subirada, F.; Paoli, R.; Sierra-Agudelo, J.; Lagunas, A.; Rodriguez-Trujillo, R. & Samitier, J. (2022). *Development of a Custom-Made 3D Printing Protocol with Commercial Resins for Manufacturing Microfluidic Devices*. (Polymers 2022,14,2955)
  https://doi.org/10.3390/polym14142955

- Sierra-Agudelo, J.*; Subirada, F.*; Hendriks, M.; Rodriguez-Trujillo, R ; & Samitier, J. (2023). *Low-cost 3D printed inertial flow micro fluidic devices for cellular isolation in liquid biopsies*. (November), 1–16. https://doi.org/10.3389/frlct.2023.1175668
  *Both considered 1st Author
  (Frontiers in Lab on a Chip Technologies, Vol.2 2023)

- 3D-Printed Herringbone Patterns for Enhanced Fluid Mixing in Microfluidic Devices (article is pending submission for review)

Bibliography

1. Zare RN, Kim S. Microfluidic platforms for single-cell analysis. Vol. 12, Annual Review of Biomedical Engineering. 2010. p. 187–201.
2. Whitesides GM. The origins and the future of microfluidics. Vol. 442, Nature. 2006. p. 368–73.
3. Lee CS. Grand Challenges in Microfluidics: A Call for Biological and Engineering Action. Frontiers in Sensors. 2020;1.
4. Chen X, Chen H, Wu D, Chen Q, Zhou Z, Zhang R, et al. 3D printed microfluidic chip for multiple anticancer drug combinations. Sens Actuators B Chem. 2018 Dec 10;276:507–16.
5. Frenea-Robin M, Marchalot J. Basic Principles and Recent Advances in Magnetic Cell Separation. Magnetochemistry. 2022 Jan 1;8(1).
6. Zilionis R, Nainys J, Veres A, Savova V, Zemmour D, Klein AM, et al. Single-cell barcoding and sequencing using droplet microfluidics. Nat Protoc. 2017 Jan 1;12(1):44–73.
7. Tiboni M, Tiboni M, Pierro A, Del Papa M, Sparaventi S, Cespi M, et al. Microfluidics for nanomedicines manufacturing: An affordable and low-cost 3D printing approach. Int J Pharm. 2021 Apr 15;599.
8. Rodríguez CF, Andrade-Pérez V, Vargas MC, Mantilla-Orozco A, Osma JF, Reyes LH, et al. Breaking the clean room barrier: exploring low-cost alternatives for microfluidic devices. Vol. 11, Frontiers in Bioengineering and Biotechnology. Frontiers Media S.A.; 2023.
9. Palacio-Castañeda V, Velthuijs N, Le Gac S, Verdurmen WPR. Oxygen control: the often overlooked but essential piece to create better in vitro systems. Vol. 22, Lab on a Chip. Royal Society of Chemistry; 2022. p. 1068–92.
10. Kasahara K, Leygeber M, Seiffarth J, Ruzaeva K, Drepper T, Nöh K, et al. Enabling oxygen-controlled microfluidic cultures for spatiotemporal microbial single-cell analysis. Front Microbiol. 2023;14.
11. Baptista LS, Porrini C, Kronemberger GS, Kelly DJ, Perrault CM. 3D organ-on-a-chip: The convergence of microphysiological systems and organoids. Vol. 10, Frontiers in Cell and Developmental Biology. Frontiers Media SA; 2022.
12. Nasiri R, Zhu Y, de Barros NR. Microfluidics and Organ-on-a-Chip for Disease Modeling and Drug Screening. Vol. 14, Biosensors. Multidisciplinary Digital Publishing Institute (MDPI); 2024.
13. Au AK, Lee W, Folch A. Mail-order microfluidics: Evaluation of stereolithography for the production of microfluidic devices. Lab Chip. 2014;14(7):1294–301.
14. Au AK, Huynh W, Horowitz LF, Folch A. 3D-Printed Microfluidics. Angewandte Chemie - International Edition. 2016;55(12):3862–81.

15. Sharafeldin M, Jones A, Rusling JF. 3D-printed biosensor arrays for medical diagnostics. Micromachines (Basel). 2018;9(8):1–22.

16. Esmaeilsabzali H, Beischlag T V., Cox ME, Parameswaran AM, Park EJ. Detection and isolation of circulating tumor cells: Principles and methods. Vol. 31, Biotechnology Advances. 2013. p. 1063–84.

17. Knowlton S, Yu CH, Ersoy F, Emadi S, Khademhosseini A, Tasoglu S. 3D-printed microfluidic chips with patterned, cell-laden hydrogel constructs. Biofabrication. 2016 Jun 21;8(2).

18. FAN YQ, WANG HL, GAO KX, LIU JJ, CHAI DP, ZHANG YJ. Applications of Modular Microfluidics Technology. Chinese Journal of Analytical Chemistry [Internet]. 2018;46(12):1863–71. Available from: http://dx.doi.org/10.1016/S1872-2040(18)61126-0

19. Aladese AD, Jeong HH. Recent Developments in 3D Printing of Droplet-Based Microfluidics. Vol. 15, Biochip Journal. SpringerOpen; 2021. p. 313–33.

20. Behera PP, Kumar N, Kumari M, Kumar S, Mondal PK, Arun RK. Integrated microfluidic devices for point-of-care detection of bio-analytes and disease. Vol. 2, Sensors and Diagnostics. Royal Society of Chemistry; 2023. p. 1437–59.

21. Deiana G, Smith S. 3D Printed Devices for the Separation of Blood Plasma from Capillary Samples. Micromachines (Basel). 2024 Mar 1;15(3).

22. Chu PY, Hsieh CH, Wu MH. The Combination of Immunomagnetic Bead-Based Cell Isolation and Optically Induced Dielectrophoresis (ODEP)-Based Microfluidic Device for the Negative Selection-Based Isolation of Circulating Tumor Cells (CTCs). Front Bioeng Biotechnol. 2020 Aug 6;8.

23. Chung AJ. A Minireview on Inertial Microfluidics Fundamentals: Inertial Particle Focusing and Secondary Flow. Vol. 13, Biochip Journal. SpringerOpen; 2019. p. 53–63.

24. Cima I, Wen Yee C, Iliescu FS, Min Phyo W, Hon Lim K, Iliescu C, et al. Label-free isolation of circulating tumor cells in microfluidic devices: Current research and perspectives. Biomicrofluidics. 2013 Feb 4;7(1).

25. Hou HW, Warkiani ME, Khoo BL, Li ZR, Soo RA, Tan DSW, et al. Isolation and retrieval of circulating tumor cells using centrifugal forces. Sci Rep. 2013;3.

26. Scott SM, Ali Z. Fabrication methods for microfluidic devices: An overview. Vol. 12, Micromachines. MDPI AG; 2021.

27. Gale BK, Jafek AR, Lambert CJ, Goenner BL, Moghimifam H, Nze UC, et al. A review of current methods in microfluidic device fabrication and future commercialization prospects. Vol. 3, Inventions. MDPI Multidisciplinary Digital Publishing Institute; 2018.

28. Nguyen T, Sarkar T, Tran T, Moinuddin SM, Saha D, Ahsan F. Multilayer Soft Photolithography Fabrication of Microfluidic Devices Using a Custom-Built Wafer-Scale PDMS Slab Aligner and Cost-Efficient Equipment. Micromachines (Basel). 2022 Aug 1;13(8).

29. Mukherjee P, Nebuloni F, Gao H, Zhou J, Papautsky I. Rapid prototyping of soft lithography masters for microfluidic devices using dry film photoresist in a non-cleanroom setting. Micromachines (Basel). 2019;10(3).

30. Attia UM, Marson S, Alcock JR. Micro-injection moulding of polymer microfluidic devices. Vol. 7, Microfluidics and Nanofluidics. 2009. p. 1–28.

31. Sollier E, Murray C, Maoddi P, Di Carlo D. Comparison of rapid prototyping polymers for high pressure injections. 15th International Conference on Miniaturized Systems for Chemistry and Life Sciences. 2011;1825–7.

32. Alexandre-Franco MF, Kouider R, Kassir Al-Karany R, Cuerda-Correa EM, Al-Kassir A. Recent Advances in Polymer Science and Fabrication Processes for Enhanced Microfluidic Applications: An Overview. Micromachines (Basel). 2024 Sep 6;15(9):1137.

33. Karimi K, Fardoost A, Mhatre N, Rajan J, Boisvert D, Javanmard M. A Thorough Review of Emerging Technologies in Micro- and Nanochannel Fabrication: Limitations, Applications, and Comparison. Micromachines (Basel) [Internet]. 2024 Oct 21;15(10):1274. Available from: https://www.mdpi.com/2072-666X/15/10/1274

34. Akbari Z, Raoufi MA, Mirjalali S, Aghajanloo B. A review on inertial microfluidic fabrication methods. Vol. 17, Biomicrofluidics. American Institute of Physics Inc.; 2023.

35. Prabhakar P, Sen RK, Dwivedi N, Khan R, Solanki PR, Srivastava AK, et al. 3D-Printed Microfluidics and Potential Biomedical Applications. Vol. 3, Frontiers in Nanotechnology. Frontiers Media S.A.; 2021.

36. Su R, Wen J, Su Q, Wiederoder MS, Koester SJ, Uzarski JR, et al. A P P L I E D S C I E N C E S A N D E N G I N E E R I N G 3D printed self-supporting elastomeric structures for multifunctional microfluidics [Internet]. Vol. 6, Sci. Adv. 2020. Available from: http://advances.sciencemag.org/

37. Yazdi AA, Popma A, Wong W, Nguyen T, Pan Y, Xu J. 3D printing: an emerging tool for novel microfluidics and lab-on-a-chip applications. Microfluid Nanofluidics. 2016 Mar 1;20(3):1–18.

38. Su R, Wang F, McAlpine MC. 3D printed microfluidics: advances in strategies, integration, and applications. Vol. 23, Lab on a Chip. Royal Society of Chemistry; 2023. p. 1279–99.

39. Mehta V, Rath SN. 3D printed microfluidic devices: a review focused on four fundamental manufacturing approaches and implications on the field of healthcare. Vol. 4, Bio-Design and Manufacturing. Springer; 2021. p. 311–43.

40. Rogers CI, Qaderi K, Woolley AT, Nordin GP. 3D printed microfluidic devices with integrated valves. Biomicrofluidics. 2015 Jan 13;9(1).

41. Tasoglu S, Folch A. Editorial for the special issue on 3D printed microfluidic devices. Micromachines (Basel). 2018;9(11):3–5.

42. Valentin Romanov,†,∇ Raheel Samuel,†,‡,∇ Marzieh Chaharlang,† Alexander R. Jafek,† Adam Frost,§,∥,⊥,# and Bruce K. Gale* †. FDM 3D Printing of High-Pressure, Heat-Resistant, Transparent Microfluidic Devices Valentin.pdf. 2019.

43. Niculescu AG, Chircov C, Bîrcă AC, Grumezescu AM. Fabrication and applications of microfluidic devices: A review. Vol. 22, International Journal of Molecular Sciences. MDPI AG; 2021. p. 1–26.

44. Chen C, Mehl BT, Munshi AS, Townsend AD, Spence DM, Martin RS. 3D-printed microfluidic devices: fabrication, advantages and limitations - a mini review. Vol. 8, Analytical Methods. Royal Society of Chemistry; 2016. p. 6005–12.

45. Ukita Y, Takamura Y, Utsumi Y. Direct digital manufacturing of autonomous centrifugal microfluidic device. In: Japanese Journal of Applied Physics. Japan Society of Applied Physics; 2016.

46. Parker B, Ghosh S, Abdulla R, Wang Z, Kim K, Samanipour R. A simple and high-resolution stereolithography-based 3D bioprinting system using visible light crosslinkable bioinks. Biofabrication [Internet]. 2015;7(4):045009. Available from: http://dx.doi.org/10.1088/1758-5090/7/4/045009

47. He Y, Wu W Bin, Fu JZ. Rapid fabrication of paper-based microfluidic analytical devices with desktop stereolithography 3D printer. RSC Adv [Internet]. 2015;5(4):2694–701. Available from: http://dx.doi.org/10.1039/C4RA12165A

48. Kim YT, Folch A, Kuo AP, Parra-Cabrera C, Bhattacharjee N. Desktop-Stereolithography 3D-Printing of a Poly(dimethylsiloxane)-Based Material with Sylgard-184 Properties. Advanced Materials. 2018;30(22):1800001.

49. Eng H, Maleksaeedi S, Yu S, Choong YYC, Wiria FE, Tan CLC, et al. 3D Stereolithography of Polymer Composites Reinforced with Orientated Nanoclay. Procedia Eng. 2018;216(2017):1–7.

50. https://www.custompartnet.com/wu/stereolithography. 2024.

51. Li Z, Wang C, Qiu W, Liu R. Antimicrobial Thiol–ene–acrylate Photosensitive Resins for DLP 3D Printing. Photochem Photobiol. 2019;2.

52. Zhao T, Yu R, Li S, Li X, Zhang Y, Yang X, et al. Superstretchable and Processable Silicone Elastomers by Digital Light Processing 3D Printing. ACS Appl Mater Interfaces. 2019;11(15):14391–8.

53. Bae SU, Kim BJ. Effects of cellulose nanocrystal and inorganic nanofillers on the morphological and mechanical properties of digital light processing (DLP) 3D-Printed photopolymer composites. Applied Sciences (Switzerland). 2021 Aug 1;11(15).

54. https://www.creality.shop/es/blogs/news/what-is-uv-resin-3d-printer-and-what-is-it-work-for. 2024.

55. Otuka AJG, Tomazio NB, Paula KT, Mendonça CR. Two-photon polymerization: Functionalized microstructures, micro-resonators, and bio-scaffolds. Polymers (Basel). 2021 Jun 2;13(12).

56. Paula KT, Tomazio NB, Salas OIA, Otuka AJG, Almeida JMP, Andrade MB, et al. Femtosecond-laser selective printing of graphene oxide and PPV on polymeric microstructures. J Mater Sci. 2021 Jul 1;56(19):11569–77.

57. Ahmad NN, Wong YH, Ghazali NNN. A systematic review of fused deposition modeling process parameters. Vol. 2, Soft Science. OAE Publishing Inc.; 2022.

58. Carrell CS, McCord CP, Wydallis RM, Henry CS. Sealing 3D-printed parts to poly(dimethylsiloxane) for simple fabrication of Microfluidic devices. Anal Chim Acta. 2020 Aug 8;1124:78–84.

59. Walczak R, Adamski K. Inkjet 3D printing of microfluidic structures - On the selection of the printer towards printing your own microfluidic chips. Journal of Micromechanics and Microengineering. 2015 Aug 1;25(8).

60. https://www.custompartnet.com/wu/fused-deposition-modeling. 2024.

61. https://www.custompartnet.com/wu/ink-jet-printing. 2024.

62. https://www.custompartnet.com/wu/selective-laser-sintering. 2024.

63. Leonards H, Engelhardt S, Hoffmann A, Pongratz L, Schriever S, Bläsius J, et al. Advantages and drawbacks of Thiol-ene based resins for 3D-printing. 2015;9353:93530F. Available from: http://proceedings.spiedigitallibrary.org/proceeding.aspx?doi=10.1117/12.2081169

64. Serex L, Bertsch A, Renaud P. Microfluidics: A new layer of control for extrusion-based 3D printing. Micromachines (Basel). 2018 Feb 16;9(2).

65. Lee YS, Bhattacharjee N, Folch A. 3D-printed Quake-style microvalves and micropumps. Lab Chip. 2018;18(8):1207–14.

66. Rothbauer M, Eilenberger C, Spitz S, Bachmann BEM, Kratz SRA, Reihs EI, et al. Recent Advances in Additive Manufacturing and 3D Bioprinting for Organs-On-A-Chip and Microphysiological Systems. Vol. 10, Frontiers in Bioengineering and Biotechnology. Frontiers Media S.A.; 2022.

67. Carvalho V, Gonçalves I, Lage T, Rodrigues RO, Minas G, Teixeira SFCF, et al. 3d printing techniques and their applications to organ-on-a-chip platforms: A systematic review. Vol. 21, Sensors. MDPI AG; 2021.

68. Bhattacharjee N, Urrios A, Kang S, Folch A. The upcoming 3D-printing revolution in microfluidics. Lab Chip. 2016;16(10):1720–42.

69. Microfluidics for Biological Applications.

70. Mosadegh B, Mazzeo AD, Shepherd RF, Morin SA, Gupta U, Sani IZ, et al. Control of soft machines using actuators operated by a Braille display. Lab Chip. 2014 Jan 7;14(1):189–99.

71. Boaks M, Roper C, Viglione M, Hooper K, Woolley AT, Christensen KA, et al. Biocompatible High-Resolution 3D-Printed Microfluidic Devices: Integrated Cell Chemotaxis Demonstration. Micromachines (Basel). 2023 Aug 1;14(8).

72. Ding L, Razavi Bazaz S, Asadniaye Fardjahromi M, McKinnirey F, Saputro B, Banerjee B, et al. A modular 3D printed microfluidic system: a potential solution for continuous cell harvesting in large-scale bioprocessing. Bioresour Bioprocess. 2022 Dec 1;9(1).

73. Guttridge C, Shannon A, O'Sullivan A, O'Sullivan KJ, O'Sullivan LW. Biocompatible 3D printing resins for medical applications: A review of marketed intended use, biocompatibility certification, and post-processing guidance. Vol. 5, Annals of 3D Printed Medicine. Elsevier Inc.; 2022.

74. Beauchamp MJ, Gong H, Woolley AT, Nordin GP. 3D printed microfluidic features using dose control in X, Y, and Z dimensions. Micromachines (Basel). 2018 Jun 28;9(7).

75. Kardar P, Ebrahimi M, Bastani S. Influence of temperature and light intensity on the photocuring process and kinetics parameters of a pigmented UV curable system. J Therm Anal Calorim. 2014 Oct 1;118(1):541–9.

76. O'Neill PF, Kent N, Brabazon D. Mitigation and control of the overcuring effect in mask projection micro-stereolithography. In: AIP Conference Proceedings. American Institute of Physics Inc.; 2017.

77. Li F, MacDonald NP, Guijt RM, Breadmore MC. Multimaterial 3D Printed Fluidic Device for Measuring Pharmaceuticals in Biological Fluids. Anal Chem. 2019;91(3):1758–63.

78. Sanchez Noriega JL, Chartrand NA, Valdoz JC, Cribbs CG, Jacobs DA, Poulson D, et al. Spatially and optically tailored 3D printing for highly miniaturized and integrated microfluidics. Nat Commun. 2021 Dec 1;12(1).

79. Gross B, Lockwood SY, Spence DM. Recent advances in analytical chemistry by 3D printing. Vol. 89, Analytical Chemistry. American Chemical Society; 2017. p. 57–70.

80. Gong H, Beauchamp M, Perry S, Woolley AT, Nordin GP. Optical approach to resin formulation for 3D printed microfluidics. RSC Adv [Internet]. 2015;5(129):106621–32. Available from: http://dx.doi.org/10.1039/C5RA23855B

81. Bagheri A, Jin J. Photopolymerization in 3D Printing. ACS Appl Polym Mater. 2019;1(4):593–611.

82. Layani M, Wang X, Magdassi S. Novel Materials for 3D Printing by Photopolymerization. Advanced Materials. 2018;30(41):1–7.

83. Li F, Macdonald NP, Guijt RM, Breadmore MC. Increasing the functionalities of 3D printed microchemical devices by single material, multimaterial, and print-pause-print 3D printing. Lab Chip. 2019;19(1):35–49.

84. Voet VSD, Strating T, Schnelting GHM, Dijkstra P, Tietema M, Xu J, et al. Biobased Acrylate Photocurable Resin Formulation for Stereolithography 3D Printing. ACS Omega. 2018;3(2):1403–8.

85. Hua Gong, a Bryce P. Bickham, a Adam T. Woolley b and GPN. Custom 3D printer and resin for 18 μm × 20 μm mi- crofluidic flow channels. 2017;(i):8–10.

86. Taormina G, Sciancalepore C, Bondioli F, Messori M. Special resins for stereolithography: In situ generation of silver nanoparticles. Polymers (Basel). 2018;10(2).

87. Macdonald NP, Cabot JM, Smejkal P, Guijt RM, Paull B, Breadmore MC. Comparing Microfluidic Performance of Three-Dimensional (3D) Printing Platforms. Anal Chem. 2017 Apr 4;89(7):3858–66.

88. Dang B Van, Charlton AJ, Li Q, Kim YC, Taylor RA, Le-Clech P, et al. Can 3D-printed spacers improve filtration at the microscale? Sep Purif Technol. 2021 Feb 1;256.

89. Ligon-Auer SC, Schwentenwein M, Gorsche C, Stampfl J, Liska R. Toughening of photo-curable polymer networks: A review. Polym Chem. 2016;7(2):257–86.

90. Ligon SC, Liska R, Gurr M, Mu R, Gmbh HBFD, Bleiche ADR, et al. Polymers for 3D Printing and Customized Additive Manufacturing. 2017;

91. Kuo AP, Bhattacharjee N, Lee YS, Castro K, Kim YT, Folch A. High-Precision Stereolithography of Biomicrofluidic Devices. Adv Mater Technol. 2019;1800395:1–11.

92. Voet VSD, Schnelting GHM, Xu J, Loos K, Folkersma R, Jager J. Stereolithographic 3D Printing with Renewable Acrylates. Journal of Visualized Experiments. 2018;(139):1–6.

93. Subirada F, Paoli R, Sierra-Agudelo J, Lagunas A, Rodriguez-Trujillo R, Samitier J. Development of a Custom-Made 3D Printing Protocol with Commercial Resins for Manufacturing Microfluidic Devices. Polymers (Basel). 2022 Jul 1;14(14).

94. Aloui F, Lecamp L, Lebaudy P, Burel F. Refractive index evolution of various commercial acrylic resins during photopolymerization. Express Polym Lett. 2018;12(11):966–71.

95. Goh WH, Hashimoto M. Fabrication of 3D Microfluidic Channels and In-Channel Features Using 3D Printed, Water-Soluble Sacrificial Mold. Macromol Mater Eng. 2018 Mar 1;303(3).

96. Goh WH, Hashimoto M. Dual sacrificial molding: Fabricating 3D microchannels with overhang and helical features. Micromachines (Basel). 2018;9(10).

97. Hagemann C, Bailey MCD, Carraro E, Lionello VM, Khokhar N, Suklai P, et al. SOL3D: Soft-lithography on 3D vat polymerised moulds for fast, versatile, and accessible high-resolution fabrication of customised multiscale cell culture devices with complex designs [Internet]. 2022. Available from: http://biorxiv.org/lookup/doi/10.1101/2022.02.22.481424

98. Waheed S, Cabot JM, Macdonald NP, Lewis T, Guijt RM, Paull B, et al. 3D printed microfluidic devices: Enablers and barriers. Vol. 16, Lab on a Chip. Royal Society of Chemistry; 2016. p. 1993–2013.

99. Khoo H, Allen WS, Arroyo-Currás N, Hur SC. Rapid prototyping of thermoplastic microfluidic devices via SLA 3D printing. Sci Rep. 2024 Dec 1;14(1).

100. Hagemann C, Bailey MCD, Carraro E, Stankevich KS, Lionello VM, Khokhar N, et al. Low-cost, versatile, and highly reproducible microfabrication pipeline to generate 3D-printed customised cell culture devices with complex designs. PLoS Biol. 2024 Mar 1;22(3).

101. Britel A, Tomagra G, Aprà P, Varzi V, Sturari S, Amine NH, et al. 3D printing in microfluidics: experimental optimization of droplet size and generation time through flow focusing, phase, and geometry variation. RSC Adv. 2024 Mar 5;14(11):7770–8.

102. Battat S, Weitz DA, Whitesides GM. Nonlinear Phenomena in Microfluidics. Vol. 122, Chemical Reviews. American Chemical Society; 2022. p. 6921–37.

103. Xia HM, Wu JW, Zheng JJ, Zhang J, Wang ZP. Nonlinear microfluidics: Device physics, functions, and applications. Vol. 21, Lab on a Chip. Royal Society of Chemistry; 2021. p. 1241–68.

104. Ferreira G, Sucena A, Ferrás LL, Pinho FT, Afonso AM. Hydrodynamic entrance length for laminar flow in microchannels with rectangular cross section. Fluids. 2021 Jul 1;6(7).

105. Klein AK, Dietzel A. A Primer on Microfluidics: From Basic Principles to Microfabrication. In: Advances in Biochemical Engineering/Biotechnology. Springer Science and Business Media Deutschland GmbH; 2022. p. 17–35.

106. Suh YK, Kang S. A review on mixing in microfluidics. Vol. 1, Micromachines. 2010. p. 82–111.

107. Saravanakumar SM, Cicek PV. Microfluidic Mixing: A Physics-Oriented Review. Vol. 14, Micromachines. Multidisciplinary Digital Publishing Institute (MDPI); 2023.

108. Di Carlo D. Inertial microfluidics. Vol. 9, Lab on a Chip. Royal Society of Chemistry; 2009. p. 3038–46.

109. Zhang J, Yan S, Yuan D, Alici G, Nguyen NT, Ebrahimi Warkiani M, et al. Fundamentals and applications of inertial microfluidics: A review. Vol. 16, Lab on a Chip. Royal Society of Chemistry; 2016. p. 10–34.

110. Carlo D Di, Irimia D, Tompkins RG, Toner M. Continuous inertial focusing, ordering, and separation of particles in microchannels [Internet]. 2007. Available from: www.pnas.orgcgidoi10.1073pnas.0704958104

111. Amini H, Lee W, Di Carlo D. Inertial microfluidic physics. Vol. 14, Lab on a Chip. Royal Society of Chemistry; 2014. p. 2739–61.

112. Horcas I, Fernández R, Gómez-Rodríguez JM, Colchero J, Gómez-Herrero J, Baro AM. WSXM: A software for scanning probe microscopy and a tool for nanotechnology. Review of Scientific Instruments. 2007;78(1).

113. Mostafa KG, Nobes DS, Qureshi AJ. Investigation of Light-Induced Surface Roughness in Projection Micro-Stereolithography Additive Manufacturing (PμSLA). In: Procedia CIRP. Elsevier B.V.; 2020. p. 187–93.

114. Musharaf HM, Roshan U, Mudugamuwa A, Trinh QT, Zhang J, Nguyen NT. Computational Fluid–Structure Interaction in Microfluidics. Vol. 15, Micromachines. Multidisciplinary Digital Publishing Institute (MDPI); 2024.

115. Shayor AA, Kabir MdE, Rifath MdSA, Rashid A Bin, Oh KW. A Synergistic Overview between Microfluidics and Numerical Research for Vascular Flow and Pathological Investigations. Sensors. 2024 Sep 10;24(18):5872.

116. O'Connor J, Day P, Mandal P, Revell A. Computational fluid dynamics in the microcirculation and microfluidics: What role can the lattice Boltzmann method play? Vol. 8, Integrative Biology (United Kingdom). Royal Society of Chemistry; 2016. p. 589–602.

117. Kalpakli A, Örlü R, Alfredsson PH. Dean vortices in turbulent flows: Rocking or rolling? Vol. 15, Journal of Visualization. Springer Verlag; 2012. p. 37–8.

118. Rajendran J, Esfandyarpour R. Revolutionizing Personalized Health: The Frontier of Wearable Biomolecule Sensors Through 3D Printing Innovation. Biomedical Materials and Devices. Springer Nature; 2024.

119. Shafique H, Karamzadeh V, Kim G, Shen ML, Morocz Y, Sohrabi-Kashani A, et al. High-resolution low-cost LCD 3D printing for microfluidics and organ-on-a-chip devices. Lab Chip. 2024 Apr 19;24(10):2774–90.

120. Tsai CHD, Lin XY. Experimental study on microfluidic mixing with different zigzag angles. Micromachines (Basel). 2019 Sep 1;10(9).

121. Enders A, Siller IG, Urmann K, Hoffmann MR, Bahnemann J. 3D Printed Microfluidic Mixers—A Comparative Study on Mixing Unit Performances. Small. 2019;15(2):1–9.

122. Zhang J, Li W, Alici G. Inertial Microfluidics: Mechanisms and Applications. In 2017. p. 563–93.

123. Kee SP, Gavriilidis A. Design and characterisation of the staggered herringbone mixer. Chemical Engineering Journal. 2008 Aug 1;142(1):109–21.

124. Williams MS, Longmuir KJ, Yager P. A practical guide to the staggered herringbone mixer. Lab Chip. 2008;8(7):1121–9.

125. Channon RB, Menger RF, Wang W, Carrão DB, Vallabhuneni S, Kota AK, et al. Design and application of a self-pumping microfluidic staggered herringbone mixer. Microfluid Nanofluidics. 2021 Apr 1;25(4).

126. Williams S. A Absolute Pressure Pressure Absorption Photometer AC Dielectrophoresis Lab-on-Chip Devices.

127. Lee CY, Chang CL, Wang YN, Fu LM. Microfluidic mixing: A review. Vol. 12, International Journal of Molecular Sciences. 2011. p. 3263–87.

128. Braunger ML, Fier I, Rodrigues V, Arratia PE, Riul A. Microfluidic mixer with automated electrode switching for sensing applications. Chemosensors. 2020 Mar 1;8(1).

129. https://3dprintingindustry.com/news/innovations-in-microfluidics-fabricating-pdms-devices-with-3d-printed-master-molds-225459/. 2024.

130. https://www.detax.de/en/ueber-detax/zertifizierung.php.

131. https://sgdentalshop.com/wp-content/uploads/2019/03/DETAX-Freeprint-3D-catalogue-dental-materials-sgdentalshop.pdf. 2024.

132. https://keyprint.keystoneindustries.com/. 2024.

133. https://www.asiga.com/materials/.

134. Zhang Y, Tong X, Yang L, Yin R, Li Y, Zeng D, et al. A herringbone mixer based microfluidic device HBEXO-chip for purifying tumor-derived exosomes and establishing miRNA signature in pancreatic cancer. Sens Actuators B Chem. 2021 Apr 1;332.

135. Warkiani ME, Khoo BL, Wu L, Tay AKP, Bhagat AAS, Han J, et al. Ultra-fast, label-free isolation of circulating tumor cells from blood using spiral microfluidics. Nat Protoc. 2016;11(1):134–48.

136. Warkiani ME, Khoo BL, Tan DSW, Bhagat AAS, Lim WT, Yap YS, et al. An ultra-high-throughput spiral microfluidic biochip for the enrichment of circulating tumor cells. Analyst. 2014 Jun 3;139(13):3245–55.

137. Sierra Agudelo JN, Subirada F, Hendriks M, Rodriguez Trujillo R, Samitier J. Low-cost 3D printed inertial flow microfluidic devices for cellular isolation in liquid biopsies. Frontiers in Lab on a Chip Technologies. 2023 Nov 8;2.

138. Kuntaegowdanahalli SS, Bhagat AAS, Kumar G, Papautsky I. Inertial microfluidics for continuous particle separation in spiral microchannels. Lab Chip. 2009;9(20):2973–80.

139. Özbey A, Karimzadehkhouei M, Bayrak Ö, Koşar A. Inertial focusing of microparticles in curvilinear microchannels with different curvature angles. Microfluid Nanofluidics. 2018 Jun 1;22(6).

140. Onoshima D, Hase T, Kihara N, Kuboyama D, Tanaka H, Ozawa N, et al. Leukocyte Depletion and Size-Based Enrichment of Circulating Tumor Cells Using a Pressure-Sensing Microfiltration Device. ACS Measurement Science Au. 2023 Apr 19;3(2):113–9.

141. Diéguez L, Winter MA, Pocock KJ, Bremmell KE, Thierry B. Efficient microfluidic negative enrichment of circulating tumor cells in blood using roughened PDMS. Analyst. 2015;140(10):3565–72.

142. Sierra J, Samitier J. Development of microfluidic devices for cancer cell isolation .

143. Peterson AW. The effect of surface probe density on DNA hybridization. Nucleic Acids Res. 2001 Dec 15;29(24):5163–8.

144. Stroock AD, McGraw GJ. Investigation of the staggered herringbone mixer with a simple analytical model. Philosophical Transactions of the Royal Society A: Mathematical, Physical and Engineering Sciences. 2004 May 15;362(1818):971–86.